THREE DIMENSIONAL LIQUEFACTION ANALYSIS OF OFFSHORE FOUNDATIONS

Hossein Ali Taiebat, B.Sc., M.E.S.

A thesis submitted for the
Degree of Doctor of Philosophy

Department of Civil Engineering
The University of Sydney

March 1999

Dedicated to my dearest;

Giti & Dena

SYNOPSIS

This thesis presents numerical techniques which have been developed to analyse three dimensional problems in offshore engineering. In particular, the three dimensional liquefaction analysis of offshore foundations on granular soils is the main subject of the thesis.

The subject matter is broadly divided into four sections:

1) Development of an efficient method for the three dimensional elasto-plastic finite element analysis of consolidating soil through the use of a discrete Fourier representation of field quantities.

2) Validation of the three dimensional method through analyses of shallow offshore foundations subjected to three dimensional loading and investigation of the yield locus for foundations on purely cohesive soils.

3) Formulation of governing equations suitable for three dimensional liquefaction analyses of offshore foundations founded on granular soil, presentation of a method for liquefaction analyses, and application of the method in modified elastic liquefaction analyses of offshore foundations.

4) Application of a conventional elasto-plastic soil model in the liquefaction analyses of offshore foundations using the three dimensional finite element method.

The finite element method developed in this thesis provides a rigorous and efficient numerical tool for the analysis of geotechnical problems subjected to three-dimensional loading. The efficiency of the numerical tool makes it possible to tackle some of the problems in geotechnical engineering which would otherwise need enormous computing time and thus would be impractical. The accuracy of the numerical scheme is demonstrated by solving the bearing capacity problem of shallow foundations subjected to three-dimensional loading. The generalized governing equations and the numerical method for liquefaction analyses presented in this thesis provide a solid base for the analysis of offshore foundations subjected to cyclic wave loading where they are founded on potentially liquefiable soil. The practicability of the numerical scheme is also demonstrated by a modified elastic liquefaction analysis of offshore foundations. The liquefaction phenomenon is redefined in the context of the conventional Mohr-Coulomb model, so that a relatively simple and practical model for elasto-plastic liquefaction analysis is presented.

The three-dimensional finite element method together with the numerical scheme for liquefaction analysis and the elasto-plastic soil model provide a suitable practical engineering tool for exploring the responses of offshore foundations subjected to cyclic wave loading.

PREFACE

The candidate carried out the work described in this thesis during the period of his studies, 1995-1998, in the Department of Civil Engineering, the University of Sydney, under the supervision of Professor John P. Carter.

In accordance with the By-laws of the University of Sydney, a candidate shall state the sources from which his information is derived, the extent to which he has availed himself of the work of others, and the portion of the work which he claims as original. In this regard, the author claims originality for the entire work described in this thesis, less the information or ideas derived from the many references and sources which have been acknowledged in the text. In particular, originality of the following works is claimed:

The entire review of the current theoretical and experimental investigations of the liquefaction of granular soil and liquefaction analysis of offshore foundations, presented in Chapter 2.

The application of the discrete Fourier series in deriving a finite element formulation of consolidation and verification of the formulation and application of the method to the numerical examples, presented in Chapter 3.

The three dimensional finite element analyses of shallow foundations on cohesive soils, the presentation of the two and three dimensional yield locus for the foundations and the new bearing capacity equation suitable for foundations under combined three dimensional loading, the subjects of Chapter 4.

The development of the generalized governing equations for the stress-strain relationship of liquefiable soil, the presentation of a numerical scheme for liquefaction analysis, the application of the numerical method to modified elastic liquefaction analyses of offshore foundations, the entire investigation of the effects of various factors on the behaviour of the foundations, and the comparison of the results of analyses with the existing observed values, presented in Chapter 5.

The entire work on the elasto-plastic method for liquefaction analysis of offshore foundations and the application of the method to the numerical example considered in Chapter 6.

The entire studies on cyclic resistance of offshore foundations on granular soil, the investigation of the effects of various parameters on the cyclic responses of offshore foundations, and the presentation of a simple method for comparative studies, presented in Chapter 7.

The candidate used the powerful structure of the existing general finite element computer program of AFENA as the basis for his programming. However, incorporation of the discrete Fourier series and the pseudo force method in non-linear programming as well as the numerical scheme for liquefaction analysis into the finite element program are claimed to be original.

ACKNOWLEDGEMENTS

The work described in this thesis has been made possible through support and financial assistance provided to me during the course of study. I was the recipient of an Overseas Postgraduate Research Scholarship, a University Postgraduate Research Award, and the Centre for Geotechnical Research Scholarship, for which I am grateful.

I am indebted to many people for their interest and assistance during the course of this work. I have very much valued my time in the Department, I have learned a great deal and made some lifelong friends. In this regard, I would like to thank various members of the staff and the research students, in particular, Dr. David Airey, Associate Professor John C. Small, Dr. Tim Hull, Dr. Martin D. Liu, Mohammad K. Islam, Jiping Pan, Takashi Itakura, and Changxin Wang.

To Professor John P. Carter, the Head of the Department of Civil Engineering, I wish to express my deep gratitude and sincere thanks for his invaluable supervision, generous assistance, and continuous encouragement during my entire period of candidature.

Finally, the last four years would have been unbearably difficult without the continued support of my family. I cannot thank them enough for their love, understanding, sacrifices, and always being there for me. In appreciation of all that support, this thesis is dedicated to them.

March 1999 H. A. Taiebat

CONTENTS

NOTATION

All notation and symbols are defined where they first appear in the text. However, the most frequently used notations and their meanings are given here. Some symbols may have a different definition in different chapters. In these cases, the chapter numbers relevant to the definition are given in brackets preceding the definitions.

a_j Vector of nodal variables corresponding to wedge j

a Internal radius of a cylinder of soil

c' Cohesion

c_v Coefficient of one dimensional consolidation

e [4] Eccentricity of the load on a foundation

e [3][5][6] $(1,1,1,0,0,0)^T$

e_{cs} Critical void ratio at $p'=1$

f [4] Yield function

f [3] Force vector or right hand side vector, subscripts R and p correspond to body force and flow term respectively

f [3] Failure criterion in a constitutive model

g [2] Gravitational acceleration

g [3] Plastic potential function in a constitutive model

g_j Vector of applied forces at nodes on the cutting planes of wedge j

g'_j Vector of applied forces at nodes within wedge j

h Size of an element in a finite element mesh

k [3] [7] Coefficient of soil permeability, matrix of coefficient of permeability

k [4] Rate of increase in shear strength of a non-homogeneous soil

m_v Coefficient of volume compressibility

n Vector of generalized nodal variable, $(u, q)^T$

n_o Initial nodal variable

p [3] Pore water pressure

p [3] Horizontal uniform pressure

p' Mean effective stress, subscripts i, s, and f refer to the initial, the current, and the failure values of the mean effective stresses, respectively

p'_c Size of the yield locus in the Modified Cam-Clay model

q [3] Nodal pore water pressure, subscript t denotes time

q Deviatoric shear stress, subscripts i, s and f refer to the initial, the current, and the failure values of the deviatoric stresses, respectively

q_c Cyclic deviatoric shear stress

q_u Average pressure on the base of a foundation

r		Vector of generalized applied force, (f_R, f_p)
r_j		Vector of applied forces on wedge j
s_u		Undrained shear strength
s_{uo}		Undrained shear strength of non-homogeneous soil at the tip of a foundation
t		Time
u	[3]	Nodal displacement, subscripts r, z and θ denote displacements in the radial, vertical and circumferential directions respectively
u	[2][5][6][7]	Pore pressure
u_c	[2][5][6]	Pore pressure generated by cyclic loading
u_l	[5][6]	Limiting excess pore pressure
u_{max}	[2][5][6]	Maximum achievable pore pressure at a point in a soil
v		Superficial velocity of pore fluid, $(v_r, v_z, v_\theta)^T$
w_j		Field variables at nodes on the cutting planes of a wedge j
w'_j		Field variables at nodes within a wedge j
z		Depth
A	[3]	Hardening modulus
A	[4]	Contact area of a foundation
A	[6]	The difference between the initial and the current mean stresses, p_i'-p_s'
$\boldsymbol{A}_s$-$\boldsymbol{F}_s$		Component of partitioned $\boldsymbol{S}$ matrix
B	[4]	Breadth of a foundation
B	[6]	The difference between the initial and the failure mean stresses, p_i'-p_f'
B'		Breadth of fictitious effective area of a foundation
$\boldsymbol{B}$		Matrix of shape function derivatives
D		Diameter of circular footings
D_p		Pile diameter
D_r		Relative density
D_s		Diameter of the boundary of a cylinder of soil
$\boldsymbol{D}$		The material constitutive matrix, superscripts e and ep denote elastic and elasto-plastic constitutive matrices
DI		Damage index, $(S_i - S_s)/S_i$
E'		Drained Young's modulus
E		Young's modulus
E_u		Undrained Young's modulus
$\boldsymbol{E}$		$(\partial N/\partial r, \partial N/\partial z, \partial N/\partial \theta)^T$
G		Shear modulus
G_1		Shear modulus at the first cycle of loading
G_k		k^{th} Fourier coefficient of applied forces at nodes on the cutting planes of wedges

G'_k — k[th] Fourier coefficient of applied forces at nodes within wedges

H — Horizontal load

H_c — Horizontal cyclic load

H_{max} — Maximum tolerable horizontal load for a foundation under combined loading

H_u — Ultimate bearing capacity for a foundation under pure horizontal load

H_0 — Maximum horizontal load capacity for a foundation in the absence of moment

$\boldsymbol{I}$ — Identity matrix

$\boldsymbol{J}$ — $\begin{pmatrix} \boldsymbol{I} & \boldsymbol{0} & \boldsymbol{0} \\ \boldsymbol{0} & -\boldsymbol{I} & \boldsymbol{0} \\ \boldsymbol{0} & \boldsymbol{0} & \boldsymbol{I} \end{pmatrix}$

$\boldsymbol{K}$ — Stiffness matrix, $\int \boldsymbol{B}^T.\boldsymbol{D}.\boldsymbol{B}.dV$

K — Coefficient of lateral soil pressure in a simple shear test

K_o — Coefficient of lateral earth pressure for soil at rest

L' — Length of the fictitious effective area of a foundation

L^T — Isotropic pore pressure stiffness matrix, coupling matrix, $\int \boldsymbol{B}^T.e.N.dV$

M [2][4] — Overturning moment

M [3] — Strength parameter in the Modified Cam-Clay model

M_c — Cyclic moment

M_{max} — Maximum tolerable moment for a foundation under combined loading

M_u — Ultimate bearing capacity for a foundation under pure moment

M_0 — Maximum moment capacity for a foundation in the absence of horizontal load

M^* — Moment calculated at a reference point above the base of a foundation

N [2][5][6] — Number of cycles of load

N [3] — Shape Functions, subscripts p and d denote pore pressure and displacement

N [3] — Number of wedges in a cylindrical model

N_c — Bearing capacity factor

N_{eq} — Equivalent number of cycles

$\underline{N}_k$ — k[th] Fourier coefficient of generalized nodal variables

N_l — Number of cycles of load required for soil liquefaction

Q — Ultimate bearing capacity of a foundation

Q_k — k[th] Fourier coefficient of pore water pressures corresponding to the nodes on the cutting planes of wedges

Q'_k — k[th] Fourier coefficient of pore water pressures corresponding to the nodes inside wedges

R — Body forces

$\underline{R}_k$ — k[th] Fourier coefficient of nodal forces of right hand side vector

R_N — Equivalent cyclic ratio

$\boldsymbol{S}$		Consolidation stiffness matrix, $\begin{pmatrix} \boldsymbol{K} & -\boldsymbol{L}^T \\ -\boldsymbol{L} & -\Delta\, t.\beta.\boldsymbol{\Phi} \end{pmatrix}$
S_i		Extra shearing capacity of a soil at its initial state of stresses, q_{fi} - q_i
$\boldsymbol{S}_j$		Consolidation stiffness matrix of wedge j
S_s		Extra shearing capacity of a soil at its current state of stresses, q_{fs} - q_s
$\boldsymbol{S}_D$		Dyadic component of stiffness matrix, $(\boldsymbol{S}_T - \boldsymbol{S}_I)$
$\boldsymbol{S}_I$		Initial stiffness matrix
$\boldsymbol{S}_T$		Tangent stiffness matrix
$\underline{\boldsymbol{S}}_k$		k^{th} modal coefficient of consolidation stiffness matrix
$(\boldsymbol{S1}\text{-}\boldsymbol{S4})_k$		Components of partitioned $\boldsymbol{S}_k$ matrix
T_v		Non-dimensional time factor
U_k		k^{th} Fourier coefficient of displacements corresponding to the nodes on the cutting planes of wedges, subscripts r, z and θ denote radial, vertical and circumferential directions
U'_k		k^{th} Fourier coefficient of displacements corresponding to the nodes inside wedges, subscripts r, z and θ denote radial, vertical and circumferential directions
V	[3]	Volume
V	[4][2]	Vertical load
V_c	[2][7]	Vertical cyclic load
V_c	[4]	Compression capacity of a foundation
V_{max}		Maximum tolerable vertical load for a foundation under combined loading
V_t		Tension capacity of a foundation
V_u		Ultimate bearing capacity for a foundation under pure vertical load
W_k		k^{th} Fourier coefficient of field variables at nodes on the cutting planes of wedges
W'_k		k^{th} Fourier coefficient of field variables at nodes within wedges
$W_k^{T^*}$		k^{th} conjugate transpose of Fourier coefficient of field variables at nodes on the cutting planes of wedges
$W'^{T^*}_k$		k^{th} conjugate transpose of Fourier coefficient of field variables at nodes within wedges
α	[2][5][6][7]	Pore pressure generation parameter
α	[3]	Wedge angle of an axi-symmetric body, $2\pi/N$
α_1-α_5		Constant coefficients
β		A parameter corresponding to a particular integration rule
δ		Displacement, subscripts h and v refer to displacements in the horizontal and vertical directions, respectively
ε		Strain, subscripts r, z and θ denote the radial, vertical and circumferential direction, superscripts e and p denote elastic and plastic

ε^c	Cyclic strain
ε_v^c	Volumetric cyclic strain
ε^t	Total strain
ε^s	Strain resulting from application of stress
ε_v	Volumetric strain
ϕ', ϕ	Friction angle
γ_w	Unit weight of water
γ_{sat}	Saturated unit weight
η	$Cos(k\alpha)$
η'	$Cos(k\alpha/2)$
κ	Elastic consolidation parameter in the Modified Cam-Clay model
λ	Plastic consolidation parameter in the Modified Cam-Clay model
μ	$Sin(k\alpha)$
μ'	$Sin(k\alpha/2)$
ν', ν	Poisson's Ratio
θ	Rotation angle
σ	Total stress
σ'	Effective stress, subscripts *v* and *r* denote the vertical and the radial effective stress and subscripts *o* indicates the initial effective stress
σ'_{vi}	Initial vertical effective stress
τ_c	Cyclic shear stress
τ_i	Initial shear stress
τ_{max}	Maximum shear stress
ω	Load rate parameter
ζ_e	Eccentricity factor
ζ_i	Inclination factor
ζ_s	Shape factor
ψ	Dilation angle
Φ	Flow matrix; $\frac{1}{\gamma_w}\int E^T.k.E.dV$

Chapter 1

INTRODUCTION

1.1: NATURE OF THE PROBLEM

There are large reserves of hydrocarbons in many offshore regions around the world. The production of hydrocarbons generally involves the building of temporary or fixed platforms, which must support drilling machinery and production processing equipment. The successful exploitation of the reserves in most cases depends upon the ability to solve the many problems associated with the design and construction of offshore platforms in a hostile ocean environment. The stability of such structures depends in part on the successful performance of their foundations.

There are many similarities between the design of foundations for offshore structures and those for conventional onshore foundations. However, some important differences exist. In particular:

(a) Offshore foundations are usually subjected to lateral wave loads which are both large and cyclic in nature.

(b) Offshore structures must be located where hydrocarbons are found, unlike most onshore structures, where the choice of a suitable site is usually an essential stage in cost effective analysis of the structure. The seabed sites often consist of soft organic soil deposits.

(c) The scale of offshore foundations is usually many times larger than that of onshore foundations. This is due primarily to the large environmental loads and also to the unsuitable subsoil which often exhibits unusual or difficult behaviour.

(d) The huge costs of construction necessitate a more rigorous approach to the design of offshore foundations under combinations of vertical load, lateral load, and overturning moment. The conventional bearing capacity method used in the design of onshore foundations may be inadequate and inefficient.

(e) Design modifications during or after construction are likely to be very expensive, if not impossible. This also necessitates a thorough and accurate design procedure.

(f) If the structures are founded on granular soil, the potential for liquefaction of the seabed soil is another important geotechnical problem that must be considered in the design of offshore foundations. In many cases, the cyclic response of the seabed deposits governs the choice of foundation type.

(g) There are very few recorded data available on the response of seabed soil deposits under environmental loading. This has meant that most of the design approaches rely heavily on analytical methods rather than empirical ones.

Because of these differences, the methods used in the design of onshore foundations are often not directly applicable to the design of offshore foundations. As mentioned, there is always a tendency to utilize more rigorous analytical methods in the design procedure and rely less on empirical approaches for offshore foundations. This is not to say that safe design may not be achievable by using empirical methods together with engineering judgment and previous experience. However, in such an approach, the design obtained may well be found to be over-conservative, and therefore, expensive. Furthermore, when extrapolation beyond the boundaries of current experience in terms of size, type, and magnitude of loading is required, the uncertainty associated with the lack of proper understanding of the fundamental problem is a potential risk. This is the case for offshore foundations, which on many occasions go beyond previous experience.

Offshore structures are most often subjected to repeated loading. When a wave passes such a structure, the forces first act in one direction and a few seconds later in the opposite direction with almost the same magnitude. It is therefore not sufficient to check the stability of the structure for the maximum forces introduced by waves acting as static loads. It must also be considered that, before the maximum wave occurs, the structure has already been subjected to a great number of waves of smaller amplitude applying cyclic loading to the soil foundation. Under such cyclic loading conditions soil exhibits very significant dissipative and softening characteristics. The effects of cyclic loading are thus of great concern to determine to what extent the behaviour of soil under cyclic loading may influence the safety of these structures.

Experimental tests on soils under cyclic loading have revealed a behaviour which is considerably different from that during a single loading. Under repeated loading, strains increase steadily with each cycle and very large strain could result at a stress level less than the value required for static failure. Under undrained conditions, each load cycle is accompanied by an increase in pore pressure, which reduces the effective stress. As the

effective stress state approaches the failure envelope, deformation increases, which may eventually result in instability or a serviceability problem.

Most of the work on the response of soils to cyclic loading has been performed on sands and has been concentrated on the problem of sand liquefaction under repeated loading. Studies of the response of clays to repeated loading have shown that there are many similarities between the behaviour of sands and clays. Therefore, it may be possible to adopt a similar approach to tackle the problem of cyclic loading on soils. However, the studies presented in this thesis are concentrated on the cyclic response of sands.

Most of the present knowledge of the cyclic response of sands has been gained from studies of the liquefaction of sands under earthquake loading. There are numerous recorded data on the failure of foundations of modern structures due to earthquake cyclic loading. Under such conditions, loose sands under these foundations behave in a contractive manner. A low permeability or a confined drainage path may cause pore pressure to be generated in the sand. Increase in pore pressure reduces the shearing resistance of the sand and may trigger liquefaction. There are some differences between the cyclic loading generated by an earthquake and by storm waves. Earthquake cyclic loading has higher frequency, and therefore, may be considered more effective in generating pore water pressures. However, cyclic loading generated by an ocean storm has a relatively long period. The drainage paths for some parts of the sand under an offshore foundation may also be long enough to prevent instantaneous dissipation of pore pressure generated by each cycle of load. Therefore, the same principle which triggers liquefaction under earthquake loading may also cause failure of the offshore foundation.

The stability and safety of offshore foundations founded on liquefiable sands has always been a great concern for geotechnical practitioners. Over the last three decades or so, substantial achievements have been made in the development of theoretical methods of analysis of liquefaction under offshore foundations. In most cases, these methods are based on numerical predictions of pore pressures. In almost all numerical analyses of liquefaction, two-dimensional finite element methods have been used to model the soil and the flow of water in the soil. Considering the three-dimensional nature of the loading on offshore foundations, these methods necessarily involve some approximation in the analyses of liquefaction and result in uncertainty of the predictions obtained.

A fully three-dimensional finite element method allows rational consideration of the complex problem of soil-water-structure interaction in a liquefaction analysis. A realistic approach in liquefaction analysis should also take into account the generation as well as the dissipation of pore pressures during a storm period. This approach requires calculation of pore pressures generated due to the application of a single wave or a parcel of waves in a storm. The process

of generation and dissipation of pore pressures may need to be repeated many times in the analysis. Application of a non-linear model for soil can perhaps lead to a solution close to the true behaviour of sand under cyclic loading. However, so far, no such solution has been reported in the literature.

One of the most overwhelming barriers in developing a liquefaction analysis which takes into account the three-dimensional nature of the problem is the very large computational time involved in the numerical solution. This is particularly true when a non-linear model for soil is included in the analysis. Therefore, despite the availability of the three-dimensional finite element methods, applications of a fully three-dimensional liquefaction analysis are rare.

1.2: OBJECTIVES OF THE THESIS

The objectives of this thesis are as follows:

(a) To develop an efficient finite element method capable of analysing three-dimensional non-linear problems of consolidating soil.

(b) To illustrate the accuracy of the newly developed finite element algorithm, to demonstrate the power of the tool in the solution of non-linear problems, and to gain confidence in the use of the method for problems with unknown solutions.

(c) To present generalized governing equations for liquefaction suitable for three-dimensional finite element analyses.

(d) To apply the three-dimensional finite element method to modified elastic liquefaction analyses of offshore foundations and to demonstrate some of the problems associated with the modified elastic model.

(e) To propose a relatively simple, but practical, non-linear soil model suitable for liquefaction analysis, and to apply the model to the liquefaction analysis of an offshore foundation.

(f) To demonstrate the practicability of the proposed three-dimensional non-linear liquefaction model by conducting extensive parametric investigations.

In this thesis, a semi-analytical finite element method is adopted for formulation of the efficient method of analysis. In an extensive parametric study, the method is applied to the problem of the bearing capacity of shallow foundations subjected to three-dimensional loading. This study has produced three-dimensional failure surfaces for these foundations, as

well as confidence in the accuracy of the solution algorithm. The method is then applied to offshore foundations subjected to cyclic wave loading. The generalized equations of liquefaction are simplified for an elastic soil model and applied in order to analyse an offshore foundation. Deficiencies associated with the modified elastic model are demonstrated. A relatively simple elasto-plastic model, based on the elastic-perfectly-plastic Mohr-Coulomb model, is presented for liquefiable soil. The model is then applied to the liquefaction analysis of an existing offshore foundation and the results are compared with the observed behaviour of the foundation. Finally, the elasto-plastic model is applied in a parametric study of some offshore foundations and the resistance of the foundations to cyclic loading is compared.

1:3: OUTLINE OF THE THESIS

The thesis consists of eight chapters including this introduction and a summary presented in Chapter 8. The studies presented in this thesis can be broadly divided into three parts. The main part of the study is concentrated on the liquefaction analysis of offshore foundations, and consists of Chapters 2, 5, 6 and 7. This part covers a literature review, the mathematical formulation of liquefaction, the development of a method for liquefaction analysis, and the application of the method to the liquefaction analyses of offshore foundations. Development of the numerical tool is another important part of the study. This part is presented in Chapter 3, where a brief review of literature dealing with semi-analytical finite element methods will be presented. The verification of the numerical tool is carried out in Chapter 4, where a numerical solution is given to the problem of the bearing capacity of foundations on purely cohesive soils. Finally, a summary of the studies will be presented in Chapter 8.

A brief review of the subjects discussed in each chapter is presented below.

Chapter Two

This chapter is principally intended to provide a review of the literature on the methods used in liquefaction analysis of offshore foundations founded on granular soils which experience cyclic wave loading. First of all, the basic characteristics of offshore foundations are presented. The laboratory cyclic tests on sands, the effects of various factors on the cyclic behaviour of sands, and the various soil models available for characterising such a behaviour are also dealt with in this chapter. It is not possible to address, in detail, all of the experimental data and all the soil models which might be involved in a consideration of the liquefaction problem. However, attempts are made to provide a basic understanding of the cyclic response of granular soils and to address in detail some of the important subjects related

to liquefaction. A detailed chronological review of the research done on the analyses of offshore foundations is also presented.

Chapter Three

In this chapter, an efficient finite element formulation for consolidating soil, based on the use of a discrete Fourier series representation of the field quantities, is described. In this method, the original three-dimensional problem is effectively decomposed into several problems of smaller size. In this way the time required for the numerical analysis reduces to less than *5%* of the time required in a standard three-dimensional finite element analysis. A literature review of the semi-analytical finite element method is also presented in this chapter. The method is applied to analyses of consolidating soil and some of the results are compared with published data.

Chapter Four

Validation of the method presented in Chapter 3, and verification of its results in the analyses of three-dimensional problems are the primary subject of Chapter 4. A simple problem with a known theoretical solution, the bearing capacity of circular foundations on homogeneous cohesive soils, has been adopted for the verification. However, this chapter extends its goal further by analysing circular foundations for all imaginable combinations of loads and moment. A unique yield locus is developed which can be used for foundations on cohesive soils obeying the Tresca failure criterion subjected to three-dimensional loading.

Chapter Five

This chapter presents the first part of the numerical finite element analyses of liquefaction. A general form of the governing equations for liquefaction is presented in this chapter together with a general procedure for liquefaction analyses. The governing equations are then simplified for an elastic soil model. The model predicts an elastic response under static loading but incorporates the accumulation of excess pore pressure under repeated undrained loading. It is therefore referred to as a “modified elastic model”. The model is applied to the liquefaction analysis of an offshore foundation which was built in an ocean environment and has a history of numerical analysis as well as measured data from its performance during storms. The results of the analysis are compared with some published results and also with the measured data. The adequacy of the modified elastic liquefaction analysis in predicting the behaviour of the soil is discussed. Some of the deficiencies of the method are related to the elastic soil model. They reveal the significance of an appropriate elasto-plastic soil model in a liquefaction analysis.

Chapter Six

In this chapter, attempts are made to improve the method for liquefaction analysis presented in Chapter 5. A relatively simple elasto-plastic model is introduced for liquefaction analysis. In the proposed model, an elastic-perfectly-plastic soil model, the Mohr-Coulomb model, with its well-defined structure, defines the yield surface and the flow rule. The effects of cyclic loading are included in the model separately, using the results of laboratory tests on samples of soil. The elasto-plastic model is applied to solve the problem of liquefaction of the same offshore foundation studied in Chapter 5. It is shown that the new model improves the prediction of the behaviour of the foundation subjected to storm loading.

Chapter Seven

In this chapter the performance of the elasto-plastic model for liquefaction analysis is explored. The capabilities of the model are demonstrated through a comparative study of offshore foundations subjected to cyclic loading. Three different hypothetical foundations are considered in the study. The effects of cyclic loads with different amplitudes and different directions applied to the foundations are compared. The effects of the ambient load level on the performance of the foundations are also studied. A simple method is presented which may be used in comparative studies of offshore foundations subjected to cyclic loading. Some of the theoretical deficiencies associated with the elasto-plastic model and their effects on liquefaction analyses are discussed. Some of the difficulties observed during the numerical analyses are also presented.

Chapter Eight

This chapter offers a summary of the results of the studies performed in this thesis. Conclusions are drawn and some recommendations for further research are proposed.

To summarize, the aim of this thesis is to develop analytical techniques, and to apply them to the analysis of liquefaction problems of offshore foundations on granular soils, in an attempt to obtain a better understanding of some of the factors that affect the behaviour of these foundations. Emphasis has been placed on the practicability of the numerical techniques, and it is shown that they may be used to make realistic predictions of the cyclic responses of offshore foundations.

Chapter 2

REVIEW OF LIQUEFACTION OF GRANULAR SOIL AND LIQUEFACTION ANALYSES OF OFFSHORE FOUNDATIONS

2.1: INTRODUCTION

The soil mechanics literature does not show much evidence of liquefaction studies before 1964. However, the classical works of Casagrande (1936), as quoted by Seed (1976), and Terzaghi and Peck (1948) indicate that there was at least recognition that liquefaction could be induced by static loading. The enormous damage experienced in Anchorage and Niigata, where a number of buildings and apartment blocks tilted during the Alaska and Niigata earthquakes on 19 June 1964, played an important role in activating the geotechnical profession to study the liquefaction phenomenon induced in soil by earthquakes (Seed, 1976). The Niigata earthquake has been cited symbolically as the first event in the world where all kinds of modern infrastructure were destroyed by what came to be well known later as soil liquefaction (Ishihara, 1993). In addition, the records of major landslides (Seed, 1968), movements of bridge supports (Rose *et al.*, 1969), the failure of waterfront structures as a result of liquefaction, and the need to consider this problem in the design of offshore structures and nuclear power plants have also played a major role in the development of studies for evaluating the liquefaction potential of soil deposits.

Cyclic loading produced by earthquakes and ocean storms is the major cause of liquefaction of granular soil deposits. In an earthquake, soil elements may undergo a series of cyclic stress conditions which are considered to be primarily due to upward propagation of shear waves in the soil deposit. During an ocean storm, as a wave moves across an offshore gravity structure it exerts a lateral force on the structure, first along the direction of its movement and then in the opposite direction. This causes the foundation soil strata to experience a series of stress cycles in both the horizontal and vertical direction due to the horizontal forces and the overturning moments. The cyclic stress conditions are comparable to those induced by earthquake loading. However, some differences exist; ocean wave periods are longer than the period of earthquake cycles of shaking, an ocean storm duration is considerably longer than the duration of seismic shaking, and ocean wave loading is transmitted mainly from the

structure to the soil whereas some parts of earthquake loads are generated by the acceleration of the soil mass.

Most liquefaction studies have been concentrated on the effects of earthquakes. However, many of the same principles apply to liquefaction induced by wave actions, both on the ocean floor and below structures constructed on the ocean floor. Most of the knowledge of the liquefaction phenomenon has been obtained through experimental studies on samples of saturated sands in laboratories. The results of experimental studies have been used as the bases for analytical and numerical evaluation of liquefaction potential in sands.

Numerical analysis of liquefaction is not possible without a proper understanding of the liquefaction phenomenon. Therefore, the literature review in this chapter mainly focuses on material related to the explanation of liquefaction of granular soils and liquefaction of offshore foundations. The review is divided into seven parts. The basic characteristics of offshore foundations and wave loads are the subjects of the first part. The mechanism of liquefaction will then be presented followed by the laboratory modelling of liquefaction. These are followed by a brief review of the constitutive modelling of soils subjected to cyclic loading. A chronological review of liquefaction analyses of offshore foundations is the subject of another section. Some of the rare laboratory model tests on foundations subjected to cyclic loading will also be reviewed. A summary of the literature studies will be presented in the last part of this chapter, plus a conclusion which draws together a framework for the liquefaction analysis of offshore foundations.

2.2: SOME CHARACTERISTICS OF OFFSHORE FOUNDATIONS

Various types and shapes of offshore structures have been designed and constructed, including gravity structures, tension leg towers, guyed towers, caissons, etc. These offshore structures are subjected to a combination of environmental forces such as waves, currents, winds, and possibly earthquakes. Offshore structures are mainly supported by two types of foundations; spread footings resting on the seabed and deeply penetrating piled foundations.

One of the main characteristics of offshore foundations is that they are subjected to ocean storms which apply relatively large horizontal loads and overturning moments. The lateral load is usually a substantial fraction of the vertical load, and therefore, the overturning moment is also very large. Comparing an offshore foundation with a high-rise onshore building of the same height, Young *et al.* (1975) showed that the offshore foundation is subjected to a lateral load of about *25%* of its vertical load, while the lateral load for the high-rise building is only about *2%* of its vertical load. Wave loads have irregular amplitudes

and they are cyclic in nature. This characteristic makes the design of offshore foundations more complex in comparison to ordinary onshore foundations.

In this section, the nature of cyclic wave loads on offshore structures will be studied. Also discussed in this section are the typical wave composition and distribution in a storm, various types of loads on offshore foundations, the inertia effects of cyclic loads, and the distribution of stresses in the soil under the foundations.

2.2.1: Sea Waves

An ocean storm generates a complex mixture of waves of different periods, heights and directions. The speed of wave propagation depends on the period of the waves. Waves with a long period travel faster than waves with a short period. Waves of different periods are propagated independently of each other (Ewing, 1970). Wave energy grows proportionally with time until it is limited by wave breaking under steady wind conditions.

There seems to be very little understanding of the process of wave generation that can explain quantitatively the growth of waves and define a universally acceptable wave composition in a storm. The storm compositions used in design of offshore facilities are necessarily predictions often derived from short records taken at a proposed site and based on assumed probabilistic properties of wave parameters such as height and period. Since wave heights enter all design computations, the probabilistic distribution of wave heights becomes important. Based on statistical analyses of available data, obtained from observations of waves in any particular area, it is possible to give an approximate description for a severe storm. Such a description indicates that a storm of a certain duration would contain a specific number of waves of various heights.

The composition of waves in a storm, used in the analysis of the Ekofisk tank by Rahman *et al.* (1977), is given, as an example, in Table 2.1. The characteristics of the waves in term of periods and heights are also given. It is assumed that this particular storm has a return period of *100* years in the North Sea environment.

Table 2.1: Characteristics of waves and storm composition (Rahman *et al.*, 1977)

Wave group	Wave height (*m*)	Wave period (*sec.*)	Number of waves
1	*0.6*	*5.0*	*497*
2	*2.1*	*7.2*	*490*
3	*6.1*	*10.0*	*485*
4	*10.1*	*11.5*	*471*
5	*14.1*	*12.5*	*282*
6	*18.0*	*13.2*	*121*
7	*22.0*	*13.4*	*32*
8	*25.0*	*13.5*	*3*

An ocean storm may be considered to consist of an infinite number of trains of waves with different amplitudes and lengths. In analysing offshore foundations, the distribution of waves of different intensities within the design storm plays an important role in predicting the response of the foundations. Since the true distribution is usually not available, an ideal distribution is assumed for the waves in a storm. In an ideal distribution, the storm may be assumed to have a simple wave composition; waves of smaller height come first followed by higher and higher waves until the peak of the storm is reached at the highest wave(s). After the peak, the storm begins to subside and wave heights gradually decrease. A more realistic storm histogram can be obtained using a probabilistic function to define the occurrence and the number of waves of different heights during the storm. (Reese *et al.*, 1988)

2.2.2: Wave Induced Loading on Offshore Foundations

During a storm, the passage of waves creates lateral cyclic pressures and cyclic buoyancy forces on offshore structures. The magnitudes of the forces created by a wave depend on the height of the wave and the shape of the super-structure. The wave loading on a gravity structure is typically a horizontal force with an amplitude of the order of *1/3* of the structure weight and a smaller vertical force with an amplitude of *1/10* of the structure weight (Smith, 1982). The lateral load is transferred to the foundation soil strata together with its complementary moment.

In general, an offshore foundation is usually subjected to a combination of loads; a vertical load due to the submerged weight of the structure, V, a horizontal load due to current and wind, H, a moment resulting from the horizontal force and also due to the eccentricity of the vertical load, M, a cyclic horizontal load and a cyclic moment produced by waves, H_c and M_c, a cyclic vertical load due to the changing buoyancy, V_c, and a cyclic pressure across the sea floor due to the variation of the wave profile (Fig. 2.1).

The dynamic effects of the cyclic forces may also be required to be considered since wave loads are transferred to the soil within a relatively short time interval. The speed of the loading is certainly one of the main criteria characterising the dynamic phenomenon and the loading duration is also another important criterion. Other dynamic criteria depend on the properties of the soil. It is therefore difficult to establish conditions that can describe the importance of dynamic loading. Ishihara (1996) defined the duration of loading approximately as one quarter of the period of one loading cycle. Problems where the load application lasts more than tens of seconds are defined as static problems. Ishihara (1996) classified dynamic problems by the properties and the conditions of the various loadings, as presented in Fig. 2.2. Based on Ishihara's classification, the wave loading on offshore foundations can be considered as static loading.

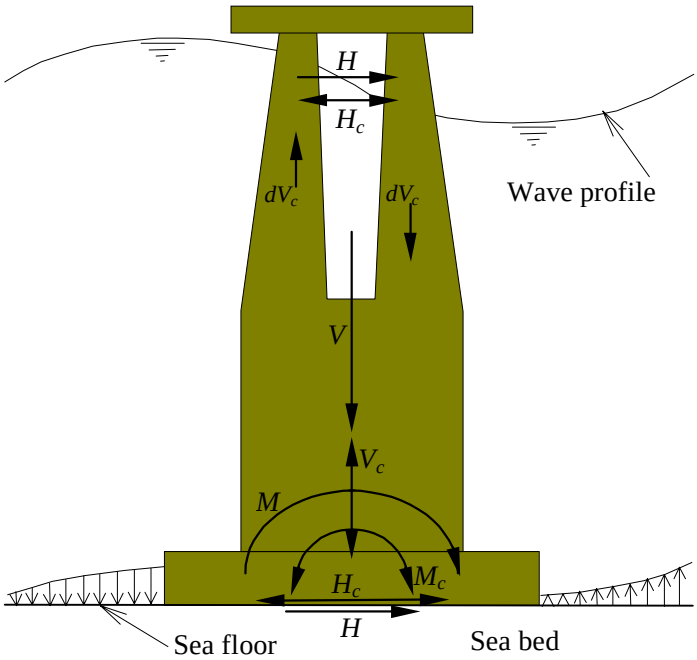

Fig. 2.1: Loads on a typical gravity offshore platform

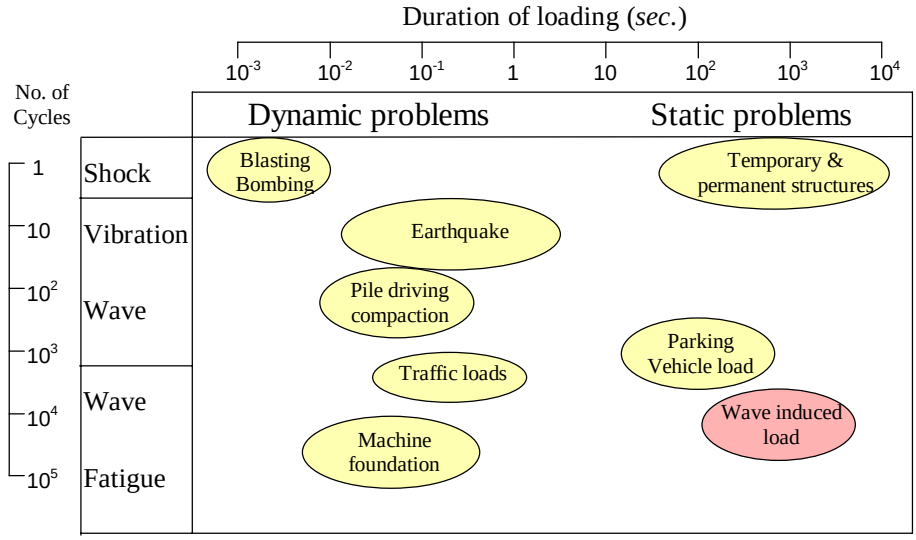

Fig. 2.2: Classification of dynamic problems (Ishihara, 1996)

O'Reilly and Brown (1991) indicated that the foundations of relatively flexible structures subjected to wind and wave loading must be designed with the possibility of dynamic amplification in mind. On the other hand, Zienkiewicz and Bettess (1982) demonstrated that for a typical seabed problem under the action of waves of periods no shorter than *10 sec* and in which the length of the drainage path for pore pressure dissipation is of the order of *10 m*, the dynamic effects can be entirely neglected.

Because of the conflicting recommendations, it is difficult to conclude definitively on the need for dynamic analysis of the response of offshore foundations. A dynamic analysis probably gives a more complete picture of the behaviour of offshore foundations under storm loading.

However, a dynamic analysis is usually very complex. Incorporation of the dynamic effects in a liquefaction analysis adds an extra degree of complexity to an already difficult and complex problem. As a first attempt to study such problems it is better to deal with liquefaction separately and neglect the effects of dynamic loading in the liquefaction analysis.

2.2.3: Cyclic Stresses Under Offshore Foundations

Various points in the soil under an offshore foundation are subjected to different combinations of normal and shear stresses, depending on the type of the foundation, the position of the points, and the type of loading. For example, stresses acting at two points in the soil under an offshore gravity platform, which is subjected to cyclic horizontal load and moment, are shown in Fig. 2.3.

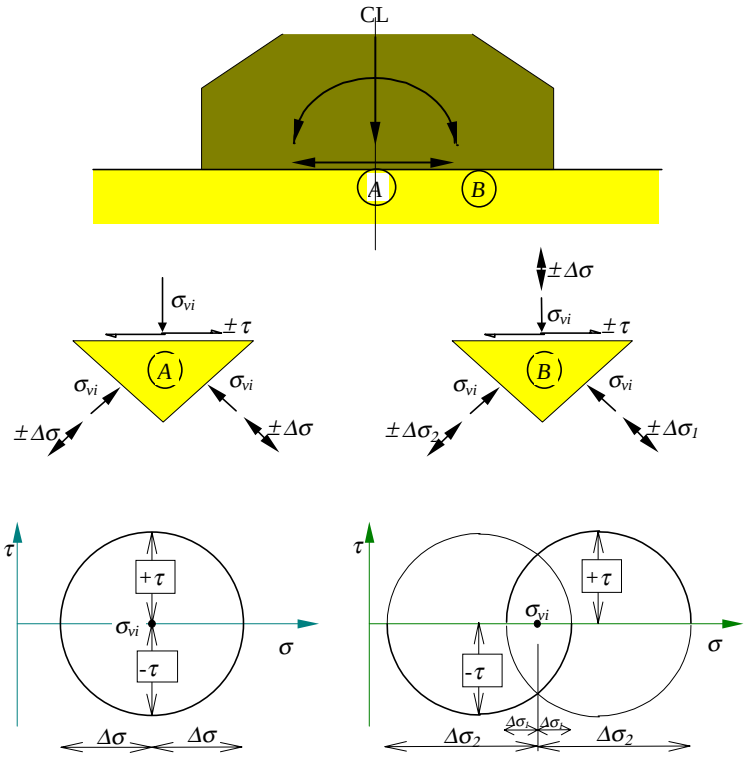

Fig. 2.3: Cyclic stresses under an offshore gravity platform

The cyclic loading creates a cyclic change in the shear stress at point (*A*), at the centre of the footing. At point (*B*), situated off centre, the vertical stress also changes. For simplicity, the initial stress due to the ambient loads is assumed to be isotropic at these points. Stresses at points (*A*) and (*B*) are plotted on the Mohr stress circle in Fig. 2.3. At point (*A*), the normal stress is constant while the shear stress changes its direction. This means that the shear stress is positive during one half of the load cycle and negative during the other half, when the horizontal force changes its direction. At point (*B*) there exists a change in the normal stress combined with a change in the direction of the shear stress.

2.3: LIQUEFACTION OF GRANULAR SOIL

2.3.1: Definition of Liquefaction

Liquefaction is a term used to describe the failure of saturated granular soils under certain conditions which generate high pore water pressures in the soil and result in large strains and continuous deformation.

Seed (1976) defined liquefaction as a condition where soil undergoes continuous deformation at a constant low residual strength or with no resistance, due to the build-up and maintenance of high pore water pressures. Pore pressure build-up leading to liquefaction of this type may be due to either static or cyclic stress application. Several other viewpoints have also been expressed concerning the mechanism of liquefaction by which masses of saturated cohesionless soil subjected to cyclic loading might experience excessive deformations (Whitman, 1985).

Although the term liquefaction may be applied to a wide range of failure conditions of saturated soil, this study limits the coverage mainly to the liquefaction of saturated granular soils due to cyclic loading.

2.3.2: Mechanism of Liquefaction

It is generally accepted that the basic cause of liquefaction of saturated cohesionless soil is the development of excess pore water pressures due to the application of cyclic stresses or strains on the soil. The basic mechanism of liquefaction has been explained from observation of the behaviour of sand samples under cyclic stresses in laboratories.

Being one of the first pioneers in liquefaction studies, H. Bolton Seed expressed the mechanism of liquefaction as follows (Seed, 1976). “As a consequence of the applied cyclic stresses, the structure of the cohesionless soil tends to become more compact with a resulting transfer of stress to the pore water and a reduction in stress on the soil grains. As a result, the soil grain structure rebounds to the extent required to keep the volume constant, and this interplay of volume reduction and soil structure rebound determines the magnitude of the increase in pore water pressure in the soil. As the pore water pressure approaches a value equal to the applied confining pressure, the sand begins to undergo deformations. If the sand is loose, the pore water pressure will increase suddenly to a value equal to the applied confining pressure, and the sand will rapidly begin to undergo large deformations. If the sand will undergo unlimited deformations without mobilising significant resistance to deformation, it can be said to be liquefied. If the sand is dense, it may develop a residual pore water pressure on the completion of a full stress cycle, which is equal to the confining pressure, but

when the cyclic stress is reapplied on the next stress cycle, the soil will dilate, the pore pressure will drop if the sand is undrained, and the soil will ultimately develop enough resistance to withstand the applied stress. However, it will have to undergo some degree of deformation to develop the resistance, and as the cyclic loading continues, the amount of deformation required to produce a stable condition may increase. Ultimately, for any cyclic loading condition, there appears to be a cyclic stress level at which the soil is able to withstand any number of cycles of a given stress without further deformation. This type of behaviour is termed *cyclic mobility* or *initial liquefaction with a limited strain potential"* (Seed, 1976).

Another picture of the liquefaction mechanism has been presented by Finn *et al.* (1977) as follows. Shear strains generated by cyclic loading cause slip at grain to grain contacts. This inter-granular slip, in dry sands, would lead to volumetric compaction. In saturated sands due to long drainage path or cyclic loads at high frequencies, the volumetric compaction is retarded because water can not drain instantaneously to accommodate the volume change. Consequently, the sand skeleton transfers some of its inter-granular or effective stresses to the pore water and the pore water pressures increase. Reduction in effective stresses leads to a structural rebound in the sand skeleton and reduces shearing resistance of the soil. In extreme cases, the pore water pressure developed during cyclic loading may increase until all the inter-granular or effective stresses acting on the soil skeleton are eliminated from the system. In this case the soil flows like a viscous liquid and liquefaction is said to have occurred.

Both loose sands and dense (thus dilating) sands have a potential for liquefaction (Chu, 1993). Even gravel specimens under cyclic triaxial tests may fail due to liquefaction (Evans, 1993 and Sirovich, 1996). Although gravels are usually considered to be completely free draining, a gravelly soil layer may be bounded by layers of soil with low permeability and drainage may be impeded. Evans and Harder (1993) showed several cases where gravelly soil liquefied in-situ. From these observations, it is reasonable to accept that any kind of granular soil, which is not at its highest possible density, has the potential for liquefaction under undrained conditions.

2.3.3: Liquefaction of Foundation Systems

For a system consisting of liquefiable soil and a foundation, all parts of the soil under the foundation do not necessarily liquefy instantaneously under cyclic loading. Depending on the magnitudes of the cyclic loads and initial loads, the boundary conditions and the drainage path, some parts of the soil may liquefy and lose all or part of their strength, while the rest of the soil may still maintain sufficient strength to resist the applied external load. The definition of liquefaction for a system consisting of a soil and a foundation needs further consideration. There seems to be no literature dealing with the definition of failure of foundation systems due to liquefaction.

For a foundation-soil system under cyclic loading, “total failure” can be described as the condition where the soil mass deforms continuously under the ambient and cyclic loads applied to the foundation. Such conditions cause instability or bearing capacity failure. The foundation system may reach equilibrium only after enormous displacements and removal of the cyclic component of the loading. “Partial failure” involves large permanent displacements during cyclic loading. Some elements of the soil liquefy and lose their strength, but overall, the soil mass remains stable following the cyclic loads. Permanent displacements can, if of sufficient magnitude, create serviceability problems for the structure involved. In this case, equilibrium is sustained due to redistribution of stresses and the resistance of some elements of the soil. Unless the soil is highly sensitive, the shearing resistance of the soil is restored after cyclic loading and drainage leading to dissipation of the excess pore pressures.

2.4: LABORATORY CYCLIC LOADING OF GRANULAR SOIL

Laboratory tests are used to determine the cyclic response of granular soils under loading conditions similar to those expected in the field. Various laboratory methods have been developed to characterise the liquefaction properties of granular soils. Seed and Lee (1966) were possibly the first to use samples of saturated sand in a triaxial test apparatus for cyclic loading tests. They set the samples under a confining pressure and subjected them to a sequence of uniform cyclic axial stresses under undrained conditions until the samples deformed to a certain level of axial strain. This has been considered as a useful procedure for producing meaningful data to assess the resistance of sand to liquefaction. Since then, various laboratory tests, including cyclic simple shear tests (Seed and Peacock, 1971), true triaxial tests (Ishihara and Yamada, 1981), cyclic torsional shear tests (Ishihara and Li, 1972), hollow cylinder tests, etc. have been developed and used to define the liquefaction characteristics of granular soils.

The laboratory apparatuses commonly used for cyclic load testing are briefly explained in this section. Some results of triaxial tests on samples of saturated sands are also described.

2.4.1: Cyclic Test Apparatus

Simple Shear Tests

In a cyclic simple shear test, the soil sample is first consolidated under an effective overburden pressure σ'_{vi} and a lateral pressure equal to $K\sigma'_{vi}$, where K is the coefficient of lateral soil pressure. The stress condition before application of the cyclic stresses is shown in Fig. 2.4.a. As a result of the application of a horizontal cyclic shear stress, τ_c, on the sample, the state of stresses changes to the condition shown in Fig. 2.4.b. It is assumed that the

application of cyclic shear stress does not alter the normal stresses in the vertical and horizontal planes. It was believed (Seed and Peacock, 1971) that this test can simulate the field stresses produced by an earthquake on a soil deposit with a level surface.

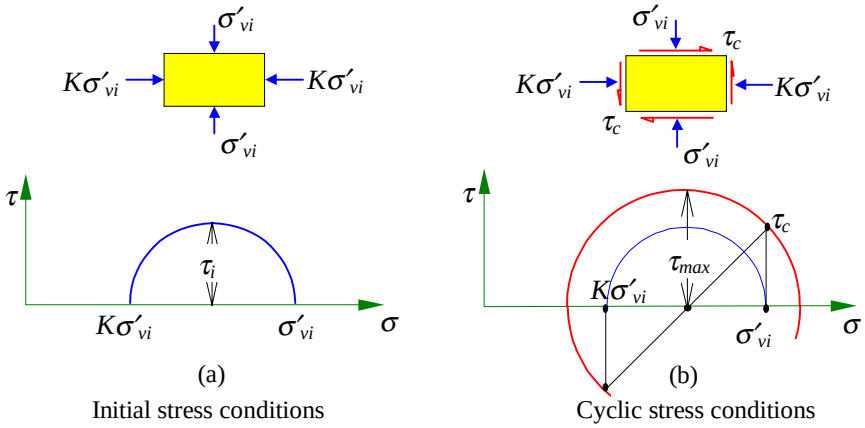

Fig. 2.4: Cyclic stresses in a simple shear test

In a simple shear test, the maximum shear stress in the sample at the initial conditions, τ_i, is usually not zero ($K \neq 1$). After application of cyclic shear stress, the maximum shear stress in the sample increases to:

$$\tau_{max} = \sqrt{\tau_c^2 + \left(\frac{\sigma'_{vi}\ (1-K)}{2}\right)^2}$$

There is a reorientation in the direction of the principal stresses; the direction of the major principal stress rotates progressively through a small angle on each side of the vertical (Seed and Peacock, 1971).

Cyclic loading causes an increase in pore water pressure under undrained conditions. When the magnitude of pore pressure exceeds the value of the initial vertical effective stress, σ'_{vi}, the soil loses its strength resulting in liquefaction (Seed and Peacock, 1971).

While in principle, it should be a relatively simple matter to reproduce these stress conditions on representative soil samples in the laboratory, difficulties are encountered in ensuring a uniform application of shear stress across the width of the sample, ensuring the development of a uniform shear strain throughout the height of the sample, enclosing test specimens to maintain constant volume, and ensuring the development of complementary shear stress along the vertical faces of the test specimen. The limitations of the test apparatus and the consequences of non-uniformities in stress conditions cause the samples to fail under lower applied stress conditions than those which would be required under corresponding field conditions (Seed and Peacock, 1971).

The response of a soil to cyclic loading is highly dependent on the initial stress conditions, particularly on the value of the over-consolidation ratio, OCR, and consequently the coefficient of soil lateral pressure, *K*. Fig. 2.5 shows the initial and cyclic stress conditions in the Mohr circle diagrams for two samples subjected to the same cyclic shear stress but having the initial values of $K=1$ and $K<1$. The measured effect of *K* on the liquefaction potential of a soil is presented in Fig. 2.6. This figure shows the relationship between the cyclic shear stress ratio, τ_c/σ'_{vi}, and the number of cycles required to cause liquefaction, N_l, for samples having the same void ratio, but different initial values of *K*. The cyclic stress required to cause failure after a given number of cycles increases with increasing value of *K*.

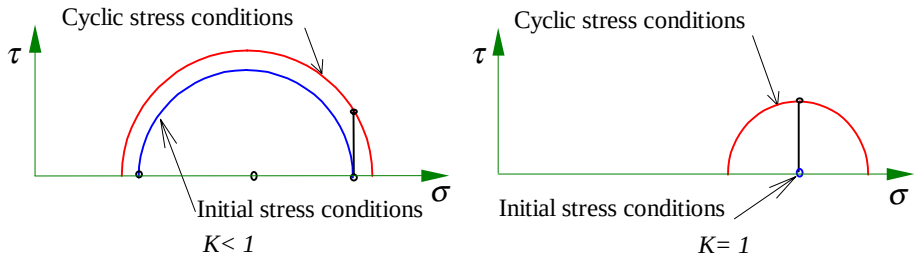

Fig. 2.5: Effects of initial stress conditions on stresses developed in cyclic simple shear tests.

The criterion for liquefaction in simple shear tests, that is when the excess pore pressure reaches the value of the initial vertical effective stress, cannot be justified in general. Based on this criterion, in cases where the coefficient of lateral soil pressure is less than one, at the onset of liquefaction the mean effective stress becomes less than zero, which is obviously unrealistic. There are no data available on stress paths during the tests, that might allow a better interpretation of liquefaction conditions. However, a more appropriate criterion for liquefaction can be adopted as the condition where the excess pore pressure reaches the value of the initial mean effective stress in the soil. This revised definition reduces the dependency of the liquefaction data on the initial horizontal stresses, or the value of *K*, as has been shown in Fig. 2.6.

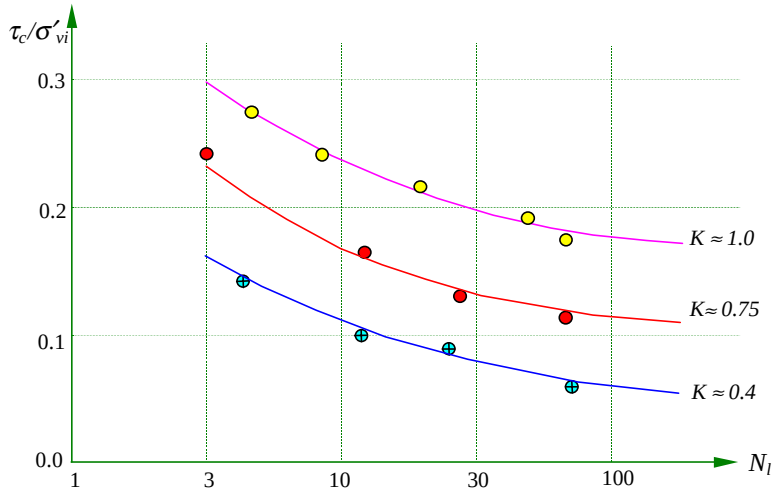

Fig. 2.6: Effects of initial principal stress ratio, *K*, on the liquefaction potential (Seed and Peacock, 1971)

Triaxial Tests

Triaxial tests are often used to evaluate the characteristics of saturated sands under cyclic loading because of the greater simplicity in testing procedures. In a standard cyclic undrained test, a sample is initially consolidated under a hydrostatic pressure p'_i, producing the stress conditions shown in Fig. 2.7.a. The sample is then subjected to a cyclic axial stress of q_c at constant lateral total pressure. In saturated samples, the effective stresses produced in this way are the results of an increase in the axial effective stress of $q_c/2$ and a decrease in the lateral effective stress of $q_c/2$. The normal stress in the sample on the plane at 45^o to the axial direction remains unchanged and a shear stress is developed on the plane equal to $\tau_c = q_c/2$ (Fig. 2.7b). The value of the intermediate principal stress is assumed equal to the major principal stress during one half of the loading cycle and to the minor principal stress during the other half. The direction of the major principal stress necessarily rotates through an angle of 90^o during each cycle.

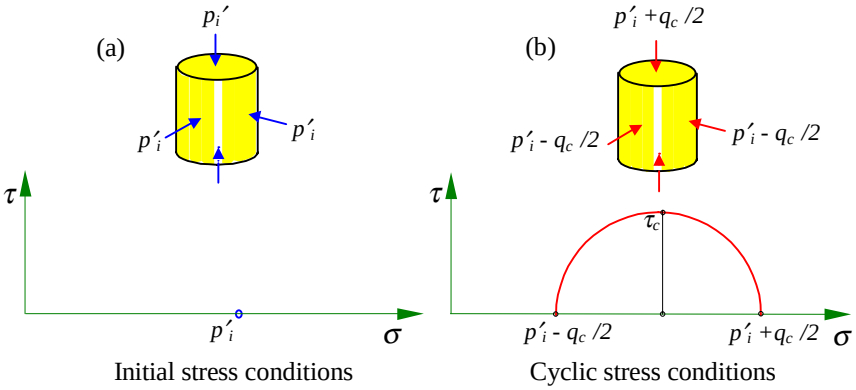

Fig. 2.7: Cyclic triaxial compression test

The results of undrained cyclic triaxial tests are usually expressed in terms of the ratio of applied deviatoric cyclic stress, q_c, to the initial hydrostatic pressure, p'_i, versus the number of cycles to cause liquefaction in the sample. The ratio of q_c/p'_i is often referred to as the "cyclic stress ratio". Fig. 2.8 shows typical results from cyclic triaxial tests.

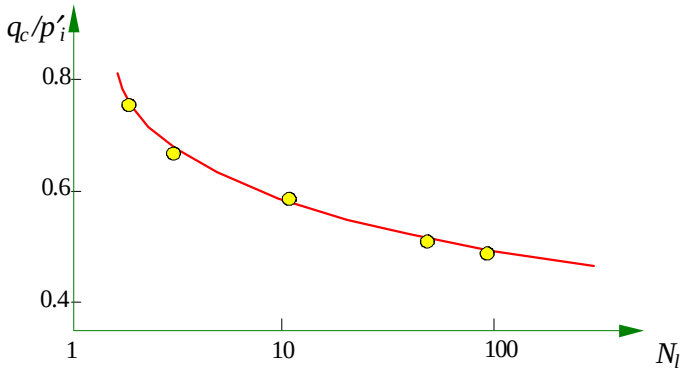

Fig. 2.8: Typical results from undrained cyclic triaxial test (Kaggwa, 1988)

Various stress paths, other than the standard one explained previously, can also be adopted in cyclic triaxial tests. Obviously, the results of tests with different stress paths are not similar. Jessberger and Jordan (1981) studied the influence of three different stress paths on the liquefaction resistance of a sand. The stress paths in their undrained triaxial tests are shown in Fig. 2.9. Stress path (*A*) represents a one-way cycling test in which the cell pressure is kept constant. Stress paths (*B*) and (*C*) are two-way cycling tests. The results of tests on sand following these stress paths are shown in Fig. 2.10. There exists a marked difference between the behaviour of the sand in the one-way cyclic tests and the two-way cyclic tests. This implies that application of the results of one-way cycling test in a liquefaction analysis may result in the possibility of liquefaction being underestimated. There also exists a small difference between the results of the two-way cyclic tests, however, the difference becomes negligible as the stress ratio reduces.

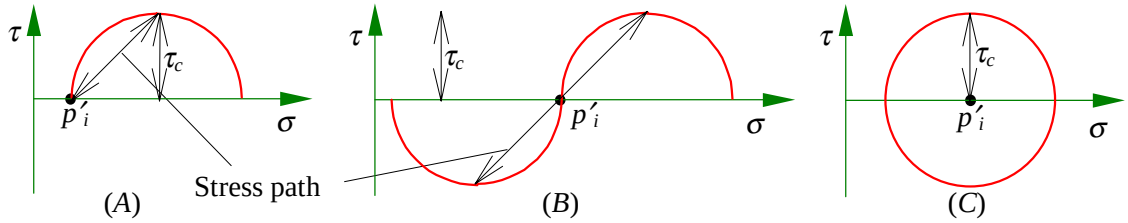

Fig. 2.9: Three different stress paths in cyclic triaxial tests

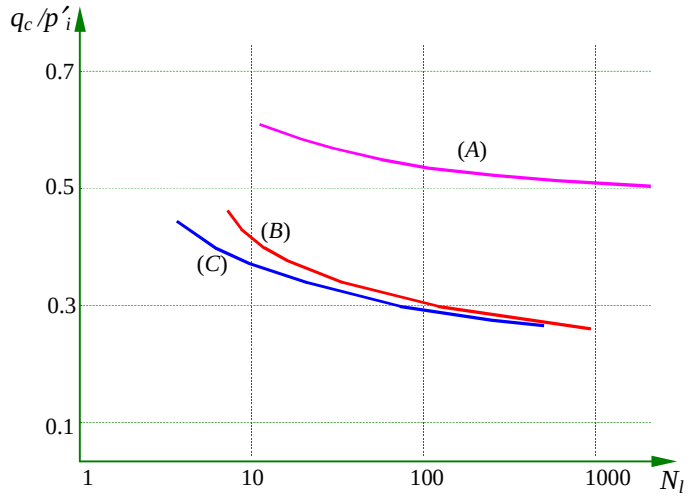

Fig. 2.10: Results of cyclic triaxial tests with various stress paths (Jessberger and Jordan, 1981)

It is often necessary to study the liquefaction resistance of a soil with a non-zero initial shear stress corresponding to an anisotropic initial consolidation condition. To do so, a static deviatoric stress is applied prior to cyclic loading. Also for some studies, it is convenient to perform strain-controlled tests by subjecting soil samples to cyclic strains of constant amplitude and recording the resulting changes in the pore pressures and stiffness of the soil.

In cyclic triaxial tests, the principal stress directions remain fixed during the initial state and the cyclic loading. However, field stress conditions are often different from those developed in triaxial tests in some respects. The initial stress conditions may be dissimilar to the triaxial stress conditions. In the field there is often a reorientation of the principal stress directions during cyclic loading. These field conditions may be approximated better in other types of tests such as torsional shear tests or true triaxial tests. However, cyclic triaxial tests are the most commonly used tests in liquefaction studies because of the greater simplicity in testing procedure.

Torsional Shear Test

A solid cylindrical or hollow cylindrical specimen can be tested in a torsional apparatus. The cyclic tests on hollow cylindrical specimens have an advantage in that the strain distribution is approximately uniform in the radial direction. In this apparatus four components of stress, i.e. vertical, torsional, inner cell pressure, and outer cell pressure can be applied independently to a sample. It is also possible to apply any combination of torsional and triaxial shear stresses to a sample. Therefore, any complex stress change involving rotation of the principal stress axes can be produced. The torsional apparatus is very useful for investigating the effects of seismic loading on a soil, since stress paths associated with seismic loading involve cyclic rotation of the principal stress directions and cyclic changes in the relative magnitude of the intermediate principal stress. Symes *et al.* (1985) examined the effects of stress path on liquefaction of loose granular materials by laboratory tests in a hollow cylinder apparatus. Cyclic principal stress rotation was shown to be an important factor in determining the likelihood of liquefaction.

True Triaxial Test

Cubical samples of saturated sands can be used in a true triaxial cyclic test apparatus to investigate the liquefaction characteristic of the sands subjected to cyclic stresses involving changes in amplitudes as well as in directions. The shear stress changes are simulated by changing the stresses on the octahedral plane within the cubical samples. Ishihara and Yamada (1981) performed a series of cyclic true triaxial tests on cubical sand samples. Several stress paths were examined. The cyclic load application started from a state of isotropic consolidation and stopped when the effective confining stress became zero. One type of test with a crisscrossing stress path employed two-directional cyclic loadings which were executed alternatively in two mutually perpendicular directions. The number of cycles required to cause initial liquefaction in this test reduced to about half the number obtained by uni-directional cyclic loading. This implies that the inclusion of additional cyclic loading in another direction can have an important influence on the liquefaction potential of sand. When cyclic loads were applied in all three perpendicular directions, the number of cycles required to cause liquefaction reduced by a factor of about *3.5* below the number required under uni-directional cycling.

2.4.2: Results of Experimental Tests on Granular Soils

In laboratory undrained tests on saturated granular soils, it is generally observed that pore water pressure builds up steadily during cyclic loading, and at sufficiently large cyclic stress levels it eventually approaches a value equal to the initial effective confining pressure in the cyclic triaxial tests, or to the initial vertical effective stress in the cyclic simple shear tests. High pore pressures are usually accompanied by large strains. The axial strains in cyclic triaxial tests rise to about *3%* (Jessberger and Jordan, 1981) or *5%* (Ishihara, 1993). Such a state has often been referred to as 'initial liquefaction' or simply 'liquefaction' (Ishihara, 1993). The criterion for initiation of liquefaction is traditionally considered as the state where the pore pressure generated due to cyclic loading rises to a value equal to the initial confining pressure (Seed and Lee, 1966). For loose sands, the initial liquefaction can certainly be taken as a state of softening. Infinitely large deformation is produced suddenly with complete loss of strength during or immediately following initial liquefaction (Fig. 2.11). For medium dense to dense sands, a state of softening is observed at an axial strain of about 5%, accompanied by a pore pressure almost equal to the initial confining pressure. However, the deformation does not thereafter increase indefinitely, and complete loss of strength does not take place in the sample (Ishihara, 1993). This behaviour is most often referred to as "cyclic mobility" (Seed, 1976). In silty sands or sandy silts containing some fines, it is often observed that pore water pressure does not develop fully, but it stops building up when it reaches a value of about *90% - 95%* of the initial confining stress. However, a significant amount of cyclic strain usually develops, indicating that considerable softening is taking place in the soil. Therefore, in the cyclic triaxial tests on medium to dense sands, or on the sands with a significant amount of fines, the occurrence of *5%* axial strain is often used as a practical criterion to define liquefaction (Ishihara, 1996).

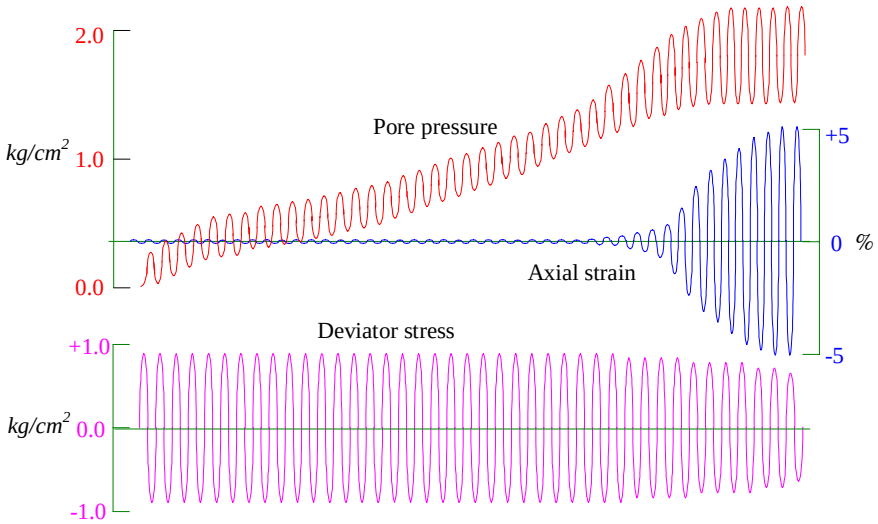

Fig. 2.11: Typical data from undrained cyclic triaxial tests on loose and medium dense sands (Finn *et al.*, 1971)

The results of undrained cyclic tests on saturated granular soils are usually expressed in terms of the number of cycles required for liquefaction and the cyclic load level (Fig. 2.12). The main conclusions derived from undrained cyclic test studies are that the larger the cyclic stresses, or the looser the samples, or the lower the confining pressures, the fewer the number of cycles required to cause liquefaction.

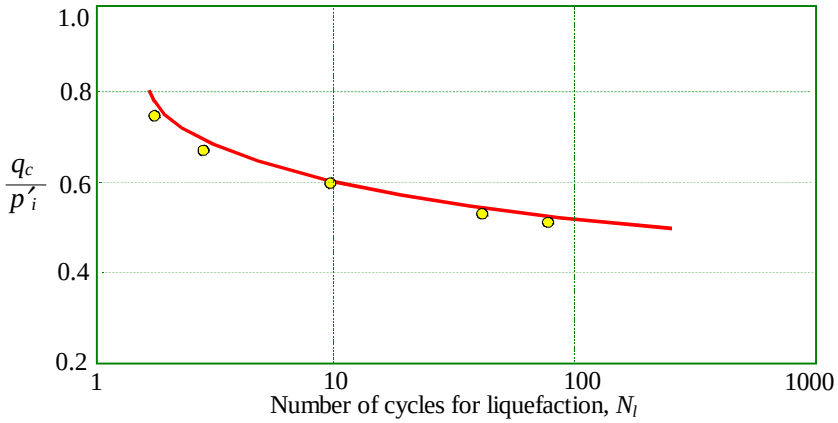

Fig. 2.12: Typical results from cyclic undrained triaxial tests on calcareous sand (Kaggwa, 1988)

The rate of pore pressure generation during the course of cyclic loading is also another important outcome of the laboratory tests. The rate of pore pressure generation is often expressed in terms of a mathematical function, such as the one suggested by Seed *et al.* (1975a):

$$\frac{u}{p'_i} = \frac{2}{\pi} Arc\sin\left(\left(\frac{N}{N_l}\right)^{\frac{1}{2\alpha}}\right) \qquad (2.1)$$

where u is the increase in pore pressure caused by application of N cycles of load, N_l is the number of cycles of load which causes liquefaction, p'_i is the initial mean effective stress, and α is a factor related to the pore pressure generation characteristics of the soil. Kaggwa (1988) showed that α depends on the initial deviatoric stress applied to the soil sample prior to the application of cyclic loads. For the calcareous sand studied by Kaggwa, α has been expressed as:

$$\alpha = 1.68.e^{6.79q/p'_i} \qquad (2.2)$$

where q is the initial deviatoric shear stress and p'_i is the initial consolidation pressure. A graphical representation of the pore pressure generation function of Equation (2.1), is shown in Fig. 2.13.

The results of cyclic laboratory tests on granular soils show that the change in volume or pore pressure occurs only if the amplitude of cyclic shear stress (or strain) exceeds a certain threshold value (Vucetic, 1994). In other words, when such a threshold is exceeded, the soil microstructure is irreversibly altered by cyclic shearing, which usually results in the

development of residual excess pore water pressures or volumetric strains. Below such a threshold, the soil microstructure and its engineering properties remain practically unchanged. The cyclic threshold shear stress can be extracted from test results, such as the data on Fig. 2.12, by extrapolation to a large number of cycles. The value of the cyclic threshold shear stress of a soil depends on the type and the relative density of the soil.

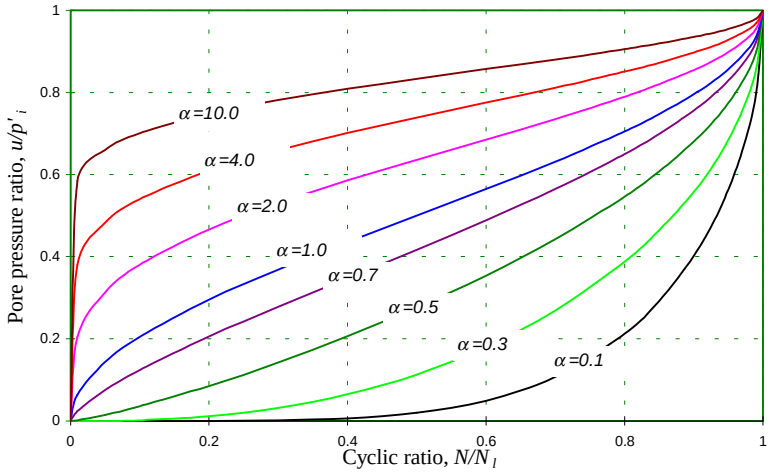

Fig. 2.13: Graphical representation of pore pressure generation function

2.4.3: Factors Affecting Liquefaction Potential of Granular Soils

The results of studies on the liquefaction potential of saturated granular soils under cyclic loading have generally confirmed that the resistance of samples of soil to liquefaction is influenced primarily by factors such as void ratio, initial confining stress, intensity of cyclic stress, previous strain history, method of sample preparation, etc. (Seed and Lee, 1966, Seed and Peacock, 1971, Kaggwa, 1988, Ishihara, 1993).

Effects of Relative Density

Relative density or void ratio has been recognised as a dominant factor influencing the cyclic strength of a particular soil. The resistance to liquefaction of a soil tends to increase with increasing the relative density at which the sample is prepared for the laboratory tests. If the cyclic strength is defined as the cyclic stress ratio which causes liquefaction in *20* cycles of uniform load application, then the influence of relative density, D_r, on cyclic strength may be shown as the curve plotted in Fig. 2.14 (Ishihara, 1996).

The undrained test condition inherently implies that the void ratio of a soil sample after liquefaction remains the same as the void ratio before liquefaction. However, the adequacy of this assumption has been questioned. Experimental liquefaction may in some cases be associated with redistribution of the void ratio within the sample during cyclic straining (Whitman, 1985), i.e. the development of a non-uniform sample.

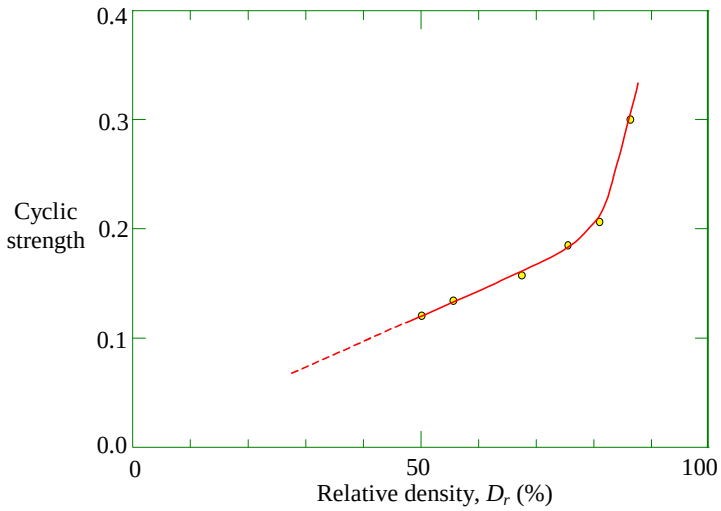

Fig. 2.14: Cyclic strength versus relative density (Ishihara, 1996)

Effects of Sample Preparation Method

Mulilis *et al.* (1977) showed that the cyclic strength of a sand may vary over a fairly wide range, depending on the nature of the fabric created by different methods of sample preparation. This implies that deposits of sands with similar density may exhibit varying resistance to cyclic load application. Yoshimi *et al.* (1984 and 1989) recovered high quality undisturbed samples by a freezing technique from in situ sand deposits in Niigata. Meanwhile, samples of sand from a man-made bin in which sand had been freshly deposited under water were recovered by the same technique. Results of cyclic triaxial tests show that the cyclic strength of undisturbed samples from the in situ deposit is about twice the cyclic strength of the sample from the newly deposited sand fill. The cyclic strength of the in situ deposits is therefore considered to vary greatly, depending on aging, inherent fabric of sand, etc. However, it was also shown that the degree of fabric dependence changes significantly with the level of shear strain to which the sand is deformed (Ishihara, 1993). The results of laboratory tests on reconstituted samples under application of low strain should be considered not to reflect the true behaviour of in situ sands, and high quality undisturbed samples are required in order to obtain reliable test results and to evaluate the cyclic performance of in situ deposits of sand. Obtaining such samples can be extremely difficult.

Effects of Strain History

The resistance of saturated sand samples to liquefaction also depends on the strain history of the sand prior to cyclic loading. Finn *et al.* (1970) postulated that the effect of any shear strain beyond a threshold value is to create a structure in the sand sample which is more sensitive to liquefaction than the structure created by consolidation. On the other hand, an increase in resistance to liquefaction has been observed even when the shear strain is below the threshold

value. This increase was considered to result from better interlocking of the particles in the original structure due to elimination of small local instabilities at the contact points without any general structural rearrangement taking place.

Effects of Initial Shear Stresses

Soil elements under a foundation are usually subjected to initial shear stresses prior to cyclic loading. Lee and Seed (1967) found that the existence of initial shear stresses on sands results in a higher liquefaction resistance when compared to sands without initial shear stresses. Vaid and Finn (1979) and then Vaid and Chern (1983) found that the resistance to liquefaction of sand could be either increased or decreased in the presence of initial shear stresses, depending on the relative density and level of the initial shear stresses. Ishibashi *et al.* (1985) investigated the effects of initial shear stresses on the cyclic behaviour of sand and concluded that pore water pressure generation was affected very little by the level of the initial shear stress. However, the level of initial shear stresses actually chosen for testing by Ishibashi *et al.* (1985) was believed by some researchers (e.g. Pillai, 1985) to be too low to show any effects. Marr and Christian (1981) and Figueroa (1993) found that the volumetric strains observed in drained cyclic tests are relatively insensitive to initial shear stresses. Kaggwa (1988) performed triaxial tests on sand with various initial shear stresses. Initial shear stress was found to affect the rate of pore pressure generation during cyclic loading, as expressed by Equation (2.2). The effects of initial shear stress were also considered in the definition of the maximum value of pore pressure which can ultimately be generated at the onset of liquefaction. Kaggwa used the term “limiting excess pore pressure” to explain liquefaction of sand. For cases of uniform cyclic loading, the limiting excess pore pressure, u_{max}, is the maximum excess pore pressure that a soil can sustain at a given deviator stress. u_{max} can be determined as the horizontal distance between the initial effective stress state and the failure envelope in p'-q stress space, as shown in Fig. 2.15.

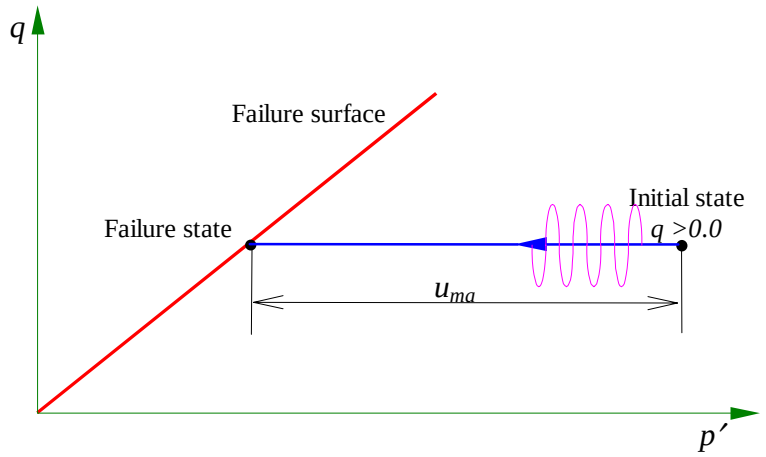

Fig. 2.15: Limiting excess pore pressure (Kaggwa, 1988)

2.5: CONSTITUTIVE MODELS FOR SOIL UNDER CYCLIC LOADING

In the analysis of soil under cyclic loading, it is very important to represent cyclic behaviour in the form of a mathematical model relating stresses and strains. Numerous constitutive models have been presented to duplicate the stress-strain relationships of granular soils under cyclic loading. However, most of the models can only be used to describe a pattern observed in one particular form of test (for example, triaxial compression tests, or constant volume simple shear tests). Even the most sophisticated models have failed to provide accurate predictions under generalised cyclic stress conditions. It is nonetheless possible to identify a number of models which can, in general, be classified into different categories, such as linear elastic models, linear viscoelastic models, damage models, etc. An extensive study of the models suitable for cyclic loading is presented by Poulos (1988).

Experimental observations show that the behaviour of soil under cyclic loading is controlled by the effective stresses, which in turn require knowledge of pore pressures that may be generated as a result of cyclic loading. Models which are successful in predicting the response of soils under monotonic loading may not be satisfactory for predicting the generation of pore pressures, but if some other route can be found for estimating the generated pore pressure, then the static model, with proper allowance made for the effective stress level, may be adequate for predicting the incremental response even under cyclic loading. The generation of pore pressure under undrained cyclic loading is then taken out of the stress-strain relationship and treated as a parameter whose variation has to be deduced independently from experimental tests.

The simplest soil model is the isotropic elastic model. When soil behaviour stays within the range of small strains, the use of an elastic model is appropriate. Elastic moduli are required in order to model soil behaviour properly. As the strain in the soil increases, soil behaviour becomes non-linear and the shear modulus tends to decrease, particularly as the shear strain increases. Therefore, often a modulus degradation function is used with the elastic models to duplicate the strain softening behaviour of the soil (See for example, Finn *et al.*, 1977, Dobry *et al.*, 1988). Deformation characteristics of the soil, obtained from laboratory tests, are used as key parameters to define the strain dependency of the shear modulus. An example of the degradation of the shear modulus during undrained cyclic loading applied to a calcareous sand is plotted in Fig. 2.16.

Isotropic elasto-plastic models, including elastic-perfectly-plastic models and isotropic hardening models, are widely used in geotechnics. The basic assumption in these models is that there is a limit to the region of elastic response, more often called the yield surface or yield locus, beyond which irrecoverable plastic deformations occur. The response of the soil is

entirely elastic and recoverable whenever the state of stress is inside the yield surface (Fig. 2.17). The location and the size of the yield surface and its dependency on stress history need to be defined. The elastic-perfectly-plastic Mohr-Coulomb model and the hardening Modified Cam-Clay model (Roscoe and Burland, 1968) are the most widely used models in this category. There exists a deficiency associated with these models in predicting soil response under cyclic loading. Development of pore pressure during cyclic loading causes the effective stress path not to come into contact with the yield locus. Therefore the elasto-plastic models have little role to play, since the state of stress remains in the elastic region. During cyclic loading, the work done on a soil sample is dissipated in rearranging the sand particles, thus creating irrecoverable strains. The energy dissipation for states of stress lying inside the yield locus has not been included in these models.

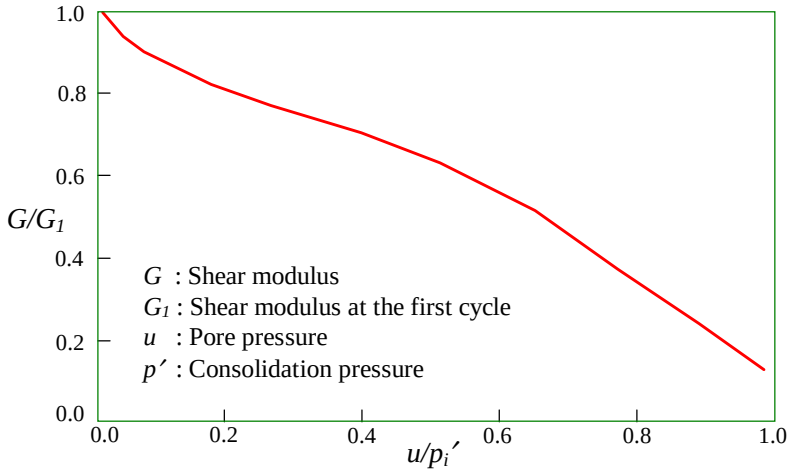

Fig. 2.16: Dependence of modulus degradation on pore pressure build-up, cyclic triaxial tests (Dobry *et al.*, 1988)

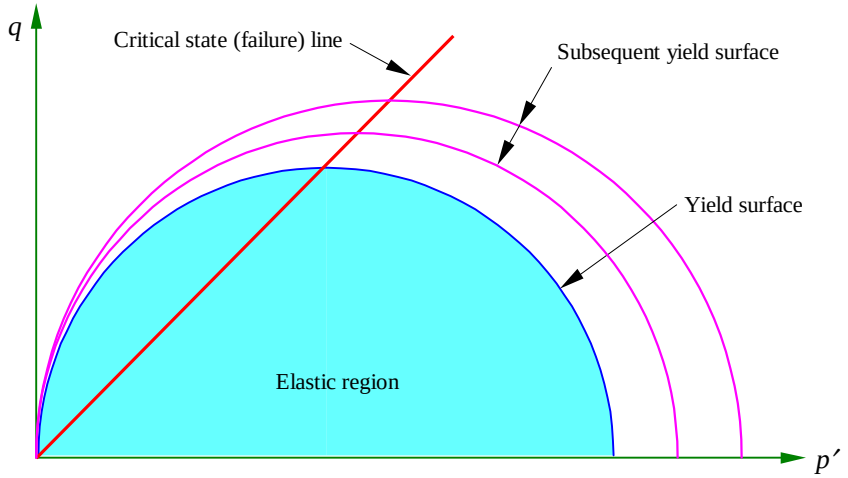

Fig. 2.17: Elastic region, yield surface and failure line in the Modified Cam-Clay model

Energy dissipation can be considered by introducing an extra plasticity factor into the linear-elastic model or the isotropic elasto-plastic models. For example, Carter *et al.* (1982)

introduced a model from the Cam-Clay family with an additional parameter which characterises cyclic behaviour. This parameter can be determined by experimental undrained cyclic tests. In this model the size of the yield surface was assumed to shrink back in such a way that, during at least a part of the cyclic loading, the stress state is in contact with the yield surface. Dafalias and Herrmann (1982) also presented a model, the bounding surface plasticity model, in which for any stress point inside the yield surface, a unique image point was defined on the surface. The value of the plastic modulus for the point depends on the distance between the stress point and its image. In this model, plastic deformations will occur for stress states inside the yield surface.

Energy dissipation in cyclic loading can also be included by introducing viscosity in an elastic or elasto-plastic model (Aubry *et al.*, 1985, Bhatia and Nanthikesan, 1987). Viscoelasticity models introduce a time-dependent contribution into the elastic response of the material. These models reproduce the effects of creep which is deformation under constant applied load, and relaxation which is change of load at constant deformation. Viscoelasticity models have been used in cyclic loading because there are many qualitative similarities between experimentally observed effects of cyclic loading and the effects of creep, and obviously the same model should be relevant in all situations. Viscoplasticity models place a limit on the region of elastic response and introduce a time dependent contribution into the plastic response of the soil. Key parameters in these models are the shear modulus and the damping ratio which can be determined as a function of shear strain. Generally, the key soil parameters are updated at each step of analysis, based on the level of strain attained. The viscosity models may predict the responses of soils which have constitutive characteristics with a truly viscous component, but they do not accurately predict the responses of many soils, particularly cohesionless soils, and for these soils the attempt to select quasi-viscoelastic or viscoplastic properties may lead to misleading predictions of prototype phenomena (Wood, 1991).

In damage models, the remaining strength of a material is lowered as a result of repeated application of a load, which would not lead to failure of the material under monotonic loading. The material is cumulatively damaged by the repeated loading. In soil mechanics, the most obviously damaging aspect of repeated loading may be build-up of pore pressure leading to reduction in effective stress and hence available shear strength. Such damage does not necessarily need to be permanent. Dissipation of pore pressure may leave the soil in a stronger condition than it was originally. Progressive build-up of volumetric strain under repeated loading might also be used as a damage parameter, but progressive densification of a soil is likely to be entirely beneficial to its subsequent response. Most of the models which use the results of laboratory tests involving cyclic loading fall into the damage model category. One of the latest models in this category was presented recently by Desai *et al.* (1998), as the “disturbed state concept”. In this model, the behaviour of sand under cyclic loading is

decomposed into the behaviour under monotonic loading and the disturbance caused by cyclic loading. As the load cycles increase, the effect of disturbance increases which causes degradation of the behaviour under monotonic loading.

Elasto-plastic, path dependent models are probably the most complex form of the constitutive models used in the analysis of cyclic loading. In these models, stress-strain relations are usually specified at each step of loading, unloading, and reloading conditions. These models must be used in the incremental numerical method, in which the stress path within each cycle of loading, unloading and reloading is followed completely. There is a large body of research on these types of constitutive models (see for example, Anandarajah, 1994, Matasovic and Vucetic, 1993, Zienkiewicz and Mroz, 1984). Both associated and non-associated plastic flow rules have been used in these models.

One dominant feature of complex mathematical models is that only a few of them can be applied to a boundary value problem with cyclic loading. The elasto-plastic path dependent models are the most complicated constitutive relationships and probably capable of accurate predictions of the response of soils in all imaginable changes of stress and strain. However, they are not usually practical for use in predicting the response of soils under a large number of cycles of loading. Excessive computational time, required to follow the stress-strain path of each soil element during each cycle, reduces the efficiency of these models in a boundary value problem. Furthermore, some of these models were developed particularly for triaxial stress-strain conditions and therefore cannot be used in three-dimensional stress conditions. Some models were developed only for one-dimensional problems.

Damage models are perhaps the most efficient models in terms of their applicability to a three-dimensional boundary value problem. They can be regarded as a pragmatic attempt to incorporate various features of the observed behaviour of soils rather than as a mathematically rigorous constitutive model. These models try to represent the experimentally observed responses of soils.

2.6: LIQUEFACTION ANALYSES OF FOUNDATIONS UNDER STORM LOADING

A chronological review of the literature dealing with the analyses of foundations under cyclic loading is presented here. The objective of this review is to investigate the methods that other researchers have used in the past for liquefaction analyses of foundations subjected to cyclic storm loading.

Bjerrum (1973) was the first to present a procedure for the calculation of excess pore water pressures which develop beneath a gravity-type offshore structure due to cyclic wave loads.

The offshore structure was a concrete oil tank resting on a sandy seabed on the Ekofisk field, North Sea, where the water is *70 m* deep. The tank, which was designed to be used as an oil storage as well as a production platform, has a diameter of *93 m* and a height of *90 m* (Fig. 2.18). The submerged weight of the Ekofisk tank is about *1900 MN* and it is designed to resist a horizontal force of *780 MN*, caused by a *23.8 m* high wave. A wave of this type has a period in the order of *14-18 sec*. The horizontal load increases from zero to its maximum value within less than *5 sec*. The permeability of the sand deposits encountered at this site is in the order of 10^{-5} *m/sec*. Given the low permeability combined with the length of the drainage path beneath the structure, it was considered that no significant drainage could be expected to occur during the passage of a single wave. A design storm with return period of *100* years was adopted for the analysis. Although the duration of the storm was predicted to be between 16 to *27 hrs*, only the worst *6 hrs* of such a *100* year storm were used in the analysis. Based on the results of undrained cyclic simple shear tests on saturated samples of the sand with relative density of D_r=*80%*, Bjerrum evaluated the excess pore pressure increment generated by every single wave during the storm. Assuming undrained conditions for the sand during the storm, the accumulated rise in pore pressure was calculated by summing up the pore pressure increments evaluated for single waves. Based on such a calculation, Bjerrum showed that excess pore pressure will rise to *31.1%* of the average vertical stress under the tank foundation, and therefore liquefaction would not occur.

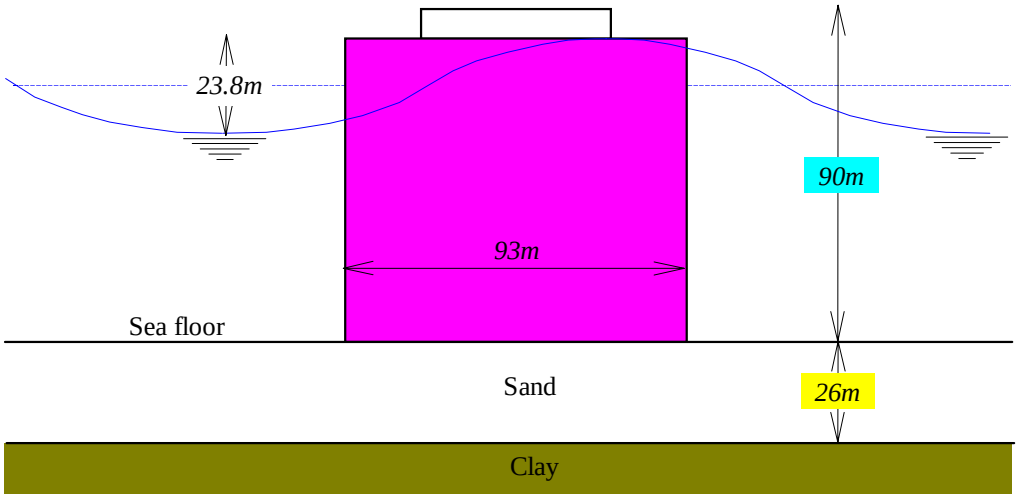

Fig. 2.18: Geometry of Ekofisk tank

The procedure adopted by Bjerrum (1973) considers only average conditions and ignores the actual distribution of stresses in the soil profile and the effect of pore pressure dissipation. It is obvious that this procedure is likely to overestimate the actual excess pore water pressures because completely undrained conditions are assumed. A more realistic approach in evaluating the stability of offshore foundations during an ocean storm should take into account the generation as well as the dissipation of pore pressures in the sand during the storm period.

Lee and Focht (1975) also evaluated the liquefaction potential of the Ekofisk tank considering all possible configuration of waves for the *100* year storm. A design curve for the *100* year storm, which represents the equivalent uniform cyclic stresses induced by the storm, was produced. The design curve was then compared with the cyclic strength curve of the soil, obtained from undrained cyclic triaxial tests on the Ekofisk sand with different relative densities of *100%*, *77%*, and *63%* (Fig. 2.19). For assured stability the cyclic strength of the soil must exceed the design curve for any number of cycles. By comparison of these two sets of curves, it was concluded that the sand with *100%* relative density would be safe against the *100* year storm whereas sands with either of the lower densities would not.

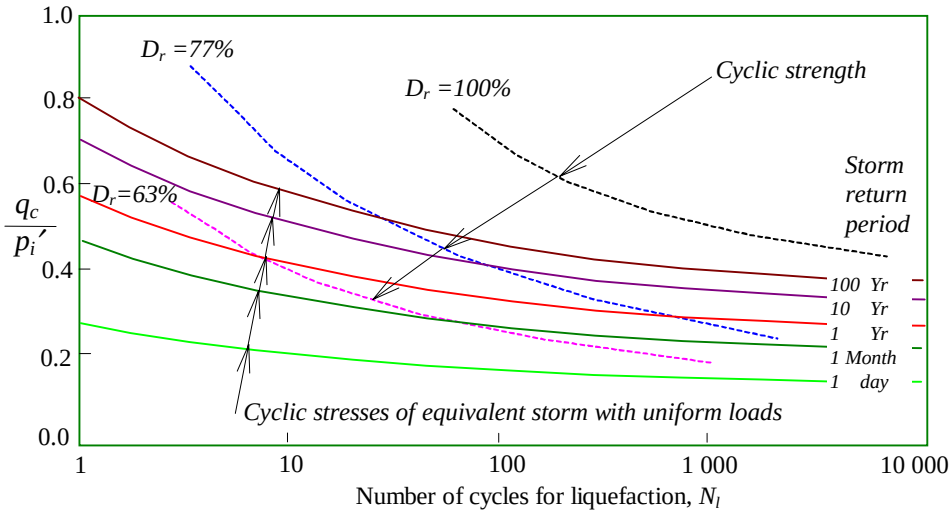

Fig. 2.19: Comparison of cyclic strength of the soil and cyclic stresses obtained from equivalent storms of uniform waves (Lee and Focht, 1975)

Lee and Focht (1975) then extended their studies to consider the effects of pore pressure dissipation during storm loading. Using knowledge of the coefficient of permeability and the modulus of compressibility of the sand, the time period for *10%* consolidation was estimated. Converting time into the number of waves (or load repetitions), a series of additional cyclic load tests was performed under partially drained conditions. After a certain number of cycles of undrained loading the tests were stopped and the amount of residual excess pore pressure was reduced by *10%*, allowing the samples to partially consolidate. This process was continued until the samples either failed by liquefaction or approached a stable condition. The beneficial effect of this partial drainage during cyclic loading resulted in an increase in cyclic strength, from zero increase at the first few cycles to almost double the strength for a large number of cycles (see also Jessberger and Jordan, 1981, Zen *et al.*, 1985). However, this effect alone was still not sufficient to assure adequate safety against the *100* year storm.

While the approach introduced by Lee and Focht (1975) provides an excellent example of a practical method of studying the development of pore water pressures beneath an offshore

tank, the method used to include the effect of pore pressure dissipation during a storm incorporates approximations that introduces additional uncertainty.

As explained previously, the increment in pore pressure for a given soil subjected to undrained cyclic loading depends on a number of factors, some of which were ignored in the previous analyses. These are: 1) the distribution of initial stresses, 2) the level of cyclic shear stress, 3) the existing pore pressure already built up by previous cyclic stress applications. A more rigorous solution to the problem was presented by Rahman *et al.* (1977), by considering the effects of stress distribution in the soil profile as well as pore pressure dissipation. It was assumed by Rahman *et al.* that waves are not strictly confined along a single direction and different waves may approach the structure randomly in any direction. The zone of directional randomness was assumed to be significantly wide, and therefore, every diameter of the structure becomes approximately identical with respect to the wave action. Thus the problem was approximated as an axi-symmetric system. The wave-induced forces were treated as static forces. It was assumed that only cyclic radial shear stresses cause progressive build-up of pore pressures and other cyclic stresses may cause a transient fluctuation of pore pressure about a certain mean value. Such fluctuations were assumed to be insignificant and thus they were ignored in the analysis. The shear stresses in the soil were evaluated by the theory of elasticity using the appropriate amplitudes for different wave forces. The resultant cyclic shear stress at any point was obtained by superposition of the effects of individual forces, taking their phase differences into account.

The basic equation governing the pore pressure response was obtained using Darcy's Law and continuity of pore fluid flow. The pore pressure generated due to cyclic loads was considered to be changing simultaneously because of diffusion within the soil and dissipation out of drainage boundaries. Results of undrained cyclic simple shear tests on saturated samples of sand were used to evaluate the cyclic strength of the soil. The cyclic strength of the soil is defined in terms of the number of cycles required to cause liquefaction for various levels of cyclic shear stress. A pore pressure generation function presented by Seed *et al.* (1975a), Equation (2.1), was also adopted to predict the rate of undrained pore pressure generation at any time, or at any given cyclic ratio, N/N_l. The cyclic strength data and the pore pressure generation function were used in conjunction with the cyclic shear stress ratio at any point in the soil to determine the pore pressure generated during any time interval. A finite element program, GADFLEA (Booker *et al.*, 1976), was developed to analyse the dissipation of pore pressure in the soil mass.

A storm with a *100* year return period was adopted. For the purposes of economy and convenience, the actual time history of the storm was replaced by that of an equivalent storm producing the same overall effects. This equivalent storm was determined using the weighting

procedure for wave effects described by Lee and Focht (1975) and Seed *et al.* (1975b). Two zones, one just beneath the centre of the tank and another beyond the edge of the tank, were considered to be the zones where significant pore pressure ratios are likely to develop. The analysis provided a complete time history of pore pressure response for selected points under the tank during the storm. The results were compared with the Bjerrum's undrained analysis, as shown in Fig. 2.20. For sand with a relative density of *85%*, the Bjerrum analysis shows liquefaction at the edge of the tank, while the method of Rahman *et al.* predicts that a pore pressure ratio of *22%* would develop at the peak of the storm, thereafter the pore pressure ratio would drop to a value of *6%* at the end of the storm. Even for sand with a relative density of *77%*, the finite element analysis predicts that the pore pressure ratio would not exceed *32%*. The finite element analyses showed that failure to include the effects of pore pressure dissipation during a storm could lead to a extremely conservative design.

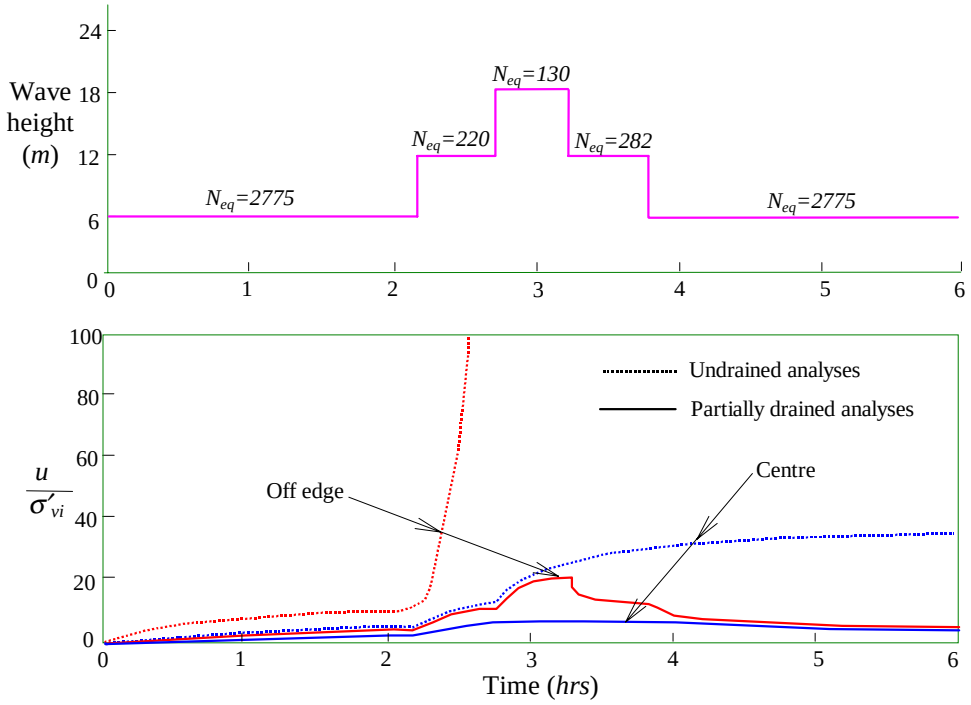

Fig. 2.20: Analysis of pore pressure generation for Ekofisk tank (Rahman *et al.*, 1977)

The method presented by Rahman *et al.* (1977) necessarily involves a number of approximations and thus the results should be used with caution and judgment in assessing their significance with regard to design. Besides the approximation made in using the axi-symmetric analysis of the loads and the pore fluid flow, the effects of soil non-linearity were not considered in the analysis. Nevertheless, this method has presented a solid base for the numerical analysis of liquefaction which has been used subsequently by a number of researchers.

Chugh and Thun (1985) used an uncoupled formulation to analyse the pore pressure response of a soil deposit under earthquake loading. By means of a dynamic response analysis of the soil deposit, the variation of shear stress caused by an earthquake at different depths in the soil was determined. The program GADFLEA (Booker *et al.*, 1976) was then used to calculate the generation and dissipation of pore pressure at any stage during the earthquake.

Lee and Poulos (1988) used the method suggested by Rahman *et al.* (1977) to analyse the influence of excess pore pressure on the axial response of an offshore pile. In their analysis, the pile was considered to be subjected to ambient and cyclic vertical loads. The stress distribution in the surrounding soil was estimated using an elastic finite element analysis. The pile was assumed to be subjected to a design storm, which could be represented by an equivalent number of waves of uniform height and period. These waves were assumed to induce only cyclic axial loading on the pile. The cyclic stresses developed along the pile-soil interface were computed by a boundary element method. Based on the cyclic stress ratio, the pore pressures generated due to a given number of load cycles were determined and the dissipation of pore pressures was calculated using the method described by Rahman *et al.* (1977). By relating pile skin friction to the over consolidation ratio or vertical effective stresses, skin friction was reduced during cyclic loading. The degradation of the elastic soil modulus was also considered in the same manner. Using this technique the reduction in the capacity of the pile due to cyclic load was studied. Lee and Poulos investigated the effects of various values of soil permeability and mean load level on pile capacity at a constant cyclic load, and the variation of pile head stiffness with cyclic load level.

Reese *et al.* (1988) also used an approach similar to the one presented by Rahman *et al.* (1977) to analyse an offshore pile subjected to cyclic lateral load induced by storm loading. The results of undrained strain-controlled cyclic triaxial tests on saturated sand were used to form a model for pore pressure prediction as a function of cyclic strain. The deflection of the pile was calculated using the *p-y* method. With a given deflection for the pile, the resulting strain field around the pile under lateral load was determined by a hybrid finite element formulation. A time period for the storm was selected and an average wave force was calculated over the time period. Knowing the distribution of strains in the soil continuum around the pile, the pore pressure generation model was used to predict the increase in pore water pressures during the time period. The distribution of stresses and strains around the pile is truly three-dimensional and so is the increase in pore water pressures. However, the analysis for the dissipation of excess pore water pressures was conducted using an axi-symmetric finite element method, assuming an axi-symmetric distribution of strains and excess pore water pressures around the pile. The gradient of excess pore water pressure in the circumferential direction and the associated flow were neglected in this method. The

distribution of pore water pressures around the pile was obtained at the storm peak and at the end of the storm.

Lee and Poulos (1990) simulated a pile subjected to axial storm loading in calcareous sediment. The soil was assumed to behave elastically and the pile-soil interface behaviour was simulated by a non-linear model. A degradation model was used to reduce the skin friction of the pile as well as the secant modulus of the soil due to cyclic loading.

Stamatopoulos *et al.* (1991) presented a numerical method for liquefaction analysis in which the results of drained cyclic tests were used. The volumetric and shear strains developed in drained triaxial tests, expressed by empirical relationships in terms of the effective stress, the cyclic strain, and the number of cycles, were used as the residual strains in the finite element formulation. In this method, the stiffness of the soil skeleton varies with the effective stresses based on an experimental relationship. The method was applied to analyse centrifuge tests simulating the earthquake response of a foundation resting on liquefiable sand. Analyses were carried out for different values of soil permeability, in order to back-calculate the in-situ permeability of the sand. This method has also been used by Bouckovalas (1991) to analyse the performance of the Ekofisk tank during the storm on 6 November 1973.

Verruijt and Song (1991) presented a method for liquefaction analysis of offshore foundations. The results of experimental tests were cast in a two-dimensional elastic stress-strain relationship. The maximum achievable pore pressure was also limited based on the values of the initial shear stresses and the amplitude of cyclic shear stress applied to the soil. The method was then used to analyse the Ekofisk tank in a plane strain finite element analysis. The foundation was modelled as a strip footing resting on a *16 m* deep layer of sand. The relative density of the sand was assumed as D_r*=100%*. Analysis of the problem with a *100* year storm predicted increases in pore pressures to *26.5 kPa* and *15 kPa* at the centre and under the edge of the tank, respectively. Variations of excess pore pressures at the edge and in the centre below the foundation during the storm are shown in Fig 2.21.

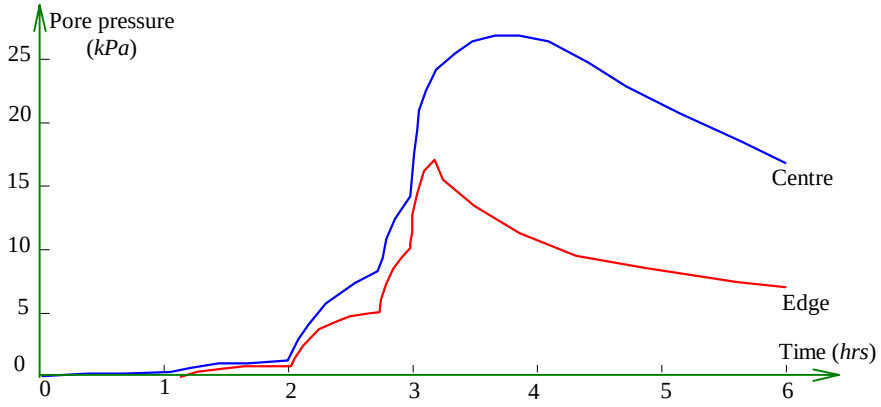

Fig. 2.21: Variations of pore pressures under the Ekofisk tank (Verruijt and Song, 1991)

Shahrour and Meimon (1992 and 1995) presented a method suitable for the analysis of marine foundations on cohesive soil subjected to periodic loads. The loadings are divided into two main categories; slow loads including submerged weight and cyclic loads induced by severe waves, fast loads which include a large number of cyclic loads of short periods. The problem of fast loading is first solved using an elastic soil model and the stress field is determined. The rate of viscoplastic strains and the hardening parameters can then be calculated from the elastic stress field. Based on these parameters and the stress field, the mean rate functions for slow loading can be calculated using an elasto-viscoplastic constitutive law. Finally, the problem under slow loading is solved for constant external forces using the classical incremental approach and a visco-plastic model with the mean rate parameters obtained previously. Shahrour and Meimon showed that this method is convenient for cyclic loads with low amplitudes and short periods. Comparison of the results of this method with those from the classical incremental method employing the same constitutive model showed that this method operates well for the calculation of settlements, but it gives poor predictions for the stress field and pore pressures, especially when the cyclic load amplitude increases. Furthermore, as mentioned previously, viscoplastic models are generally inappropriate for cohesionless soils, and therefore the use of this method for sand liquefaction must be viewed with caution.

2.7: OBSERVED BEHAVIOUR OF OFFSHORE FOUNDATIONS

In this section, a description is given of some experimental studies which potentially might be used for validation of the results of numerical analyses of liquefaction. Validation of any analytical method by means of experimental studies is clearly a very important step. One type of validation can be achieved by comparison of the analytical results with data obtained in the laboratory from cyclic tests on soil samples. Although this type of validation is an important first step, it is inadequate because laboratory tests generally involve “single element” behaviour, i.e. either the stress or strain field is prescribed and both are considered homogeneous. Therefore, emphasis here is placed on experimental tests on model foundations, i.e. boundary value problems, that allow a more stringent validation of proposed numerical analyses.

Many laboratory tests on foundations subjected to cyclic loads can be found in the literature. Most of the tests are either on cohesive soils or on sands under fully drained conditions which is not the main interest of the current study. Some of the tests have been performed on shaking tables for earthquake excitation and will not be elaborated here. Only a few laboratory tests on model foundations have been performed to study the liquefaction potential of foundations.

These experiments can be divided into two categories, tests with conventional apparatus at normal earth gravity of *1g*, and tests under centrifugal acceleration of *ng*, where *n* is a factor usually greater than *10*.

Most of the tests at normal earth gravity have been conducted under fully drained conditions and therefore are of only marginal interest here. There are difficulties in performing tests under partially drained conditions and this may account for the lack of such data. For example, the dimensions of model foundations are far less than the actual foundation in the field, but the permeability of the soil being simulated is approximately equal to the permeability of the soil in the field. It is not possible to use a soil with a lower permeability in a model, since the liquefaction characteristics of the soil in the model must be similar to those of the soil in the field. It is believed that this difficulty could be overcome if a pore fluid with higher viscosity is used in the model or if the model time is reduced by a factor equal to the physical scale of the test model. However, it would appear that no information on tests involving partial drainage conditions is currently available in the geotechnical literature. A series of tests on grouted piles subjected to axial cyclic loads at normal earth gravity conditions was performed by Lee and Poulos (1990) to study the accumulation of pile settlement under an irregular cyclic loading. The cyclic loads were assumed to be generated by a scaled storm profile with various intensities. Valuable information on the behaviour of piles subjected to cyclic loads under fully drained conditions was obtained.

In centrifuge tests at an acceleration of *ng*, all linear dimensions are divided by the factor *n*. If water is used as pore fluid, the model time scale would need to be reduced by n^2 to match the dissipation rate in the field. In practice, it is common to increase the pore fluid viscosity by *n* and reduce the time scale by a similar factor, in order to achieve correct scaling. Liu and Dobry (1997) conducted centrifuge tests on model footings to investigate the mechanism of liquefaction-induced settlement of a shallow foundation, as well as the effectiveness of sand densification. The base of each model was excited in-flight by horizontal shaking simulating an earthquake. Qualitative information was obtained on the effects of compaction and soil permeability on the settlement of the foundations.

While there seem to be no data from laboratory cyclic tests on foundations which are suitable to be compared with the predictions of numerical liquefaction models, data collected by Clausen *et al.* (1975) on the behaviour of the Ekofisk tank during some major storms can be used as a basis for validation of the liquefaction analysis of offshore foundations.

The Ekofisk tank was successfully installed on the seabed in the middle of the North sea in June 1973. The tank was instrumented to measure oceanographic data, pore pressures in the soil directly under the foundation, and the settlement and tilt of the tank. The tank was subjected to several major storms after installation. The most severe storm occurred shortly

after installation of the tank, on 19 November 1973. Unfortunately, the recording system was out of operation at that time. The most severe storm in which foundation performance was measured occurred on 6 November 1973. The maximum wave height was about *16 m* which caused the pore pressures in the upper sand layer to rise by *10-20 kPa*. The settlement of the tank increased by *0.02 m* during the storm. It was believed (Clausen *et al.*, 1975) that the maximum pore pressure at the base of the footing would probably have reached up to *40 kPa* during the storm on 19 November 1973. The generation of excess pore pressures during storms indicates that liquefaction of the sand deposit is a possibility that must be considered carefully in the design of offshore structures.

2.8: SUMMARY AND CONCLUSIONS

Offshore foundations are usually designed to operate under hostile environmental conditions. The environmental loads are usually cyclic in nature. The lateral load applied to offshore foundations is usually a substantial fraction of the vertical load, and the overturning moment is also very large compared with that of onshore structures. The stability of the foundations can be strongly affected if the seabed sediments have the potential to liquefy under cyclic loading.

Experimental tests on granular soils show that application of a large number of load cycles with moderate amplitude can produce a progressive degradation of soil resistance. Cyclic loading may result in densification of soils under drained conditions, or may build-up and maintain excess pore pressures in soils under undrained or partially drained conditions. Pore pressures generated during cyclic loading may bring the soil to a state of failure.

There are some quantitative experimental studies on liquefaction of footings in a centrifuge apparatus or in shaking table tests. Cyclic earthquake loads were usually simulated in the tests. Therefore, the results of these tests cannot be used either directly or indirectly to evaluate the predictions of liquefaction analysis of offshore foundations. However, there exist some observed data on the behaviour of an offshore foundation, the Ekofisk tank. The pore pressures in the soil under the tank and the settlement of the tank were measured during a severe storm. The data collected in the field can be used to verify any numerical method of liquefaction analysis.

There are numerous mathematical models which have been formulated to duplicate the “single element” behaviour of granular soils under cyclic loading. However, most of them lack practicability in boundary value problems. Some of the models can only be used to describe a pattern observed in one particular form of test. Even the most sophisticated incremental

elasto-plastic models have failed to provide accurate predictions under generalised cyclic stress conditions. In addition, application of an incremental elasto-plastic model in the analysis of a foundation subjected to cyclic loading is mostly not feasible since excessive computational time is required.

Various numerical methods for liquefaction analyses of offshore foundations have been presented in the past 25 years. The methods necessarily involve a number of approximations and assumptions related, in particular, to the behaviour of the soil under the foundations. The method presented by Rahman *et al.* (1977) has provided a solid base for the numerical analysis of liquefaction. The method can be used in a coupled finite element consolidation analysis to predict the generation of pore pressure in the soil under an offshore foundation subjected to cyclic loading. The results of experimental tests on saturated samples of sand under cyclic loading can be used in this type of analysis.

One of the major aspects of cyclic loading that has been ignored in almost all liquefaction analyses to date is the three-dimensional nature of storm loading. Combinations of vertical load, lateral load, and overturning moment on the foundations produce a three-dimensional distribution of stresses in the soil under the foundations. As a consequence, the distribution of pore pressure generated due to cyclic loading is also three-dimensional. A three-dimensional liquefaction analysis using the conventional finite element method is generally not feasible since it requires excessive computational time.

In the method presented by Rahman *et al.* (1977), the effects of non-linear behaviour of soil are ignored. Therefore, this method does not appear to be sufficient for a stability analysis. The effect of soil yield is considered to be significant in determining the overall response of foundations.

In this thesis, an efficient three-dimensional elasto-plastic finite element analysis will be developed to model the complicated behaviour of foundations under cyclic loading. The semi-analytical approach in the finite element formulation will be adopted using the discrete Fourier series. In this way the computational time required for a three-dimensional consolidation analysis is reduced to less than *5%* of the time required in the conventional three-dimensional finite element analysis. The discrete Fourier series representation of the field variables will reduce computational time by effectively reducing a three-dimensional problem into a series of two-dimensional problems of smaller size. Elasto-plastic models for soil will also be included in the analysis.

The method proposed by Rahman *et al.* (1977) will be modified and used in the liquefaction analysis. Attempts will be made to incorporate the effects of cyclic loading in the stress-strain relationship. A simple elasto-plastic formulation will be presented for liquefaction analysis.

An existing constitutive model, suitable for monotonic loading, with its well-tested structure, will be used as the basis of the elasto-plastic model. The effects of cyclic loading will be incorporated in the model by separate efforts. The elasto-plastic model will remove some of the existing disadvantages of elastic liquefaction analysis. In addition, it will enable stability analysis of foundations subjected to cyclic loading. Furthermore, it will show the importance of soil yield and plastic flow in a liquefaction analysis.

The literature review described in this chapter has revealed the need for high quality experimental data from liquefaction studies of offshore foundations. Centrifuge testing offers great promise in this regard. In the absence of any other data, the validation of the method for liquefaction analysis is still possible by analysing the Ekofisk tank and comparing the results of the analysis with the measured values of pore pressures and settlements of the tank. The development of the numerical model of liquefaction and its validation will be described in subsequent chapters.

Chapter 3

THREE-DIMENSIONAL ANALYSIS OF FOUNDATIONS IN CONSOLIDATING SOIL

3.1: INTRODUCTION

The equations of a nonlinear consolidating soil are very complex and in order to solve problems of any complexity it is usually necessary to resort to a numerical approach such as the finite element method. The conventional finite element method, which has proved to be an extremely powerful analytical tool for the solution of many engineering problems, is capable, at least in principle, of dealing with any two or three-dimensional problems. Potentially, a three-dimensional finite element analysis could be used to analyse most complicated soil problems. However, analysis of such problems usually involves the solution of very large sets of algebraic equations, which is extremely time consuming and expensive. This is particularly true when nonlinear and inelastic behaviour is included, when it is necessary to compute the complete load path from the initial elastic response, through yield, up to failure or when the analysis involves hundreds of steps in the time domain. It is therefore desirable to search for an alternative technique that can reduce the computational labour.

In many physical problems loading may be three-dimensional in nature but the geometry and material properties do not vary in one coordinate direction. Some practical situations where these conditions occur include problems involving a combination of axial and lateral forces on an axi-symmetric body, as well as some problems relating to long tunnels, buried structures, etc. In such cases it is possible to solve a set of algebraic equations arising from a substitute problem, not involving that particular coordinate, and to synthesize the true answer from a series of such simplified solutions. In general, this type of analysis has been termed the ‘semi-analytical method’ in finite element analysis.

In this study, the evolution of semi-analytical finite element methods relevant to the analysis of soil media is considered. A new method, which is the extension of previous works, is presented for the consolidation analysis of soil. Validation of the new method is carried out through comparison of the predictions made using this method with those predicted by analytic solutions or other available finite element programs. Finally, the behaviour of a pile subjected to lateral loading in a consolidating soil is studied.

3.2: SEMI-ANALYTICAL METHODS IN FINITE ELEMENT ANALYSIS

A combination of a two-dimensional finite element process and a continuous Fourier series in the third dimension has been shown to be an efficient way of analysing elastic and elasto-plastic behaviour. This method was first developed in the context of linear analysis by Wilson (1965) and applied to the determination of stresses and displacements within complex structures of revolution subjected to non-symmetric thermal and mechanical loads.

Extension of Wilson's work to an axi-symmetric elasto-plastic body was first investigated by Meissner (1976). In his method, the material stiffness matrix remains constant for all Fourier coefficients at any computational step. "After calculation and superposition of stresses in the 'circle line elements', the flow condition for the present stress state is approximated and nodal balance forces are determined. In the next step the continuum is subjected to these nodal loads which are expanded again in a Fourier series." (Meissner, 1976, p 1359)

Winnicki and Zienkiewicz (1979) used a visco-plastic formulation to tackle material non-linearity. In their method, it is assumed that in any time interval, the visco-plastic strain rate can be determined by the stress and strain conditions pertaining at the start of the interval. The increment of visco-plastic strain was then used to compute an 'initial strain force' for use in an elastic analysis based on the original elastic moduli. In a typical step of visco-plastic analysis, displacements, strains and stresses are evaluated at element integration points in the *r-z* plane and at several circumferential locations for which visco-plastic strains are calculated. The value of visco-plastic strain is then expanded into cosine and sine series, using a numerical integration rule, which allows new values of harmonic forces to be determined. Through numerical examples, it has been shown that the semi-analytical approach to nonlinear problems is *6-10* times cheaper than a fully three-dimensional approach. Lane and Griffiths (1988) used the same technique to compute the ultimate lateral resistance of circular piles.

The continuous Fourier series method has been successfully applied to the linear consolidation of 2-D layered soils by Booker and Small (1979). Carter and Booker (1983) used this

numerical technique to provide an efficient analysis of the consolidation of axi-symmetric elastic bodies subjected to non-symmetric loading. In their formulation, field quantities such as displacement, pore pressure, stress and boundary loading are expressed in the form of a Fourier series in the circumferential direction. An eight-node quadrilateral element which is isoparametric with respect to pore pressure and displacement, as well as an element which is isoparametric with respect to pore pressure but sub-parametric with respect to displacement were used.

Runesson and Booker (1983) employed a discrete Fourier series representation of nodal variables to reduce a two-dimensional problem to a succession of one-dimensional problems. It was assumed that the loading and hence the field variables are spatially periodic. The computational effort in this method has been shown to be reduced to *10%* of that required by the conventional solution technique for an elastic analysis of a two-dimensional mesh of *10* by *12* (isoparametric linear) elements. However, it was reported that very little is gained in total computer effort in a elasto-plastic analysis.

A double discrete Fourier series expansion of nodal displacement and pore pressures has been used by Runesson and Booker (1982) for a three-dimensional consolidation analysis. In this method, a prescribed traction which is periodic in two orthogonal directions is applied to the surface. In this way the three-dimensional problem is decomposed into a number of one-dimensional problems. For a mesh of *10* by *8* by *8* (linear) elements, the reduction in computer time was shown to be *1/270* of the time needed for a conventional three-dimensional finite element analysis.

Lai and Booker (1991) used the discrete Fourier approach to analyse the nonlinear behaviour of axi-symmetric solids under three-dimensional loading conditions. The computational advantage over a fully three-dimensional formulation was illustrated. It has been shown that for most practical problems, computation time reduces to less than *5%* of the time needed for conventional finite element analysis.

The continuous Fourier series approach is very useful for elastic analyses with relatively simple loading conditions. In such cases, only a few harmonics may be necessary to obtain an adequate representation of the field quantities. However, for analyses which incorporate elasto-plasticity, or in cases where loading conditions are relatively complicated, there are difficulties associated with the calculation of the values of harmonic forces as well as with summing the large number of Fourier terms, and the conformity of elements based upon such a representation combined with conventional elements.

The discrete Fourier series approach has several advantages over the continuous Fourier series approach. The discrete Fourier series terminates after a finite number of terms and it is always

possible to maintain conformity between elements. The integration of pseudo forces occurring in plasticity and visco-plasticity presents no extra difficulty in the discrete Fourier series method, which thus seems to be preferable for problems involving material non-linearity. Furthermore, in a liquefaction analysis, the calculation of pseudo initial strains, which takes into account the effects of irregular generation of pore water pressures, can be carried out without any special difficulty.

Application of the discrete Fourier series in an axi-symmetric space is superior to its application in an orthogonal space. In the method of Runesson and Booker (1982), in general, the load has a periodicity which does not truly represent a case commonly occurring in practice. Whereas, in an axi-symmetric body (Lai and Booker, 1991) the load is truly periodic and therefore can be simulated exactly.

The discrete Fourier series approach in finite element analysis has removed the need for a fully three-dimensional analysis in the study of the complicated problem of analysing axi-symmetric solids under general loading conditions. Hence, in the present study, the methods of Runesson and Booker (1983) and Lai and Booker (1991) are extended to a consolidation formulation. This allows for modelling of pore pressure generation under cyclic loading as well as the nonlinear behaviour of soil under varying loads.

3.3: FORMULATION OF A COUPLED FINITE ELEMENT METHOD BASED ON DISCRETE FOURIER SERIES

The semi-analytical approach adopted in this work is based on the assumption that field quantities, such as displacements and pore water pressures, can be approximated by a discrete Fourier representation. A semi-analytical finite element formulation for a three-dimensional consolidating soil is developed, based on the discrete Fourier representation of the field quantities.

In an axi-symmetric body, it is possible to divide the body into N identical wedges within a cylinder, provided that the geometry and material properties do not vary in the circumferential direction (Fig. 3.1). In this case the body exhibits a polar periodicity with period N. Therefore, any function g of the discrete variable j, defined in the N wedges satisfies:

$$g_j = g_{j \pm kN} \quad \text{for} \quad k=1,2,...$$

A periodic function like g_j of the discrete variable j can be represented in the discrete Fourier form as:

$$g_j = \frac{1}{\sqrt{N}} \sum_{k=0}^{N-1} G_k \, e^{ijk\alpha} \qquad (3.1)$$

where α is equal to $2\pi/N$ and G_k are the Fourier coefficients given by:

$$G_k = \frac{1}{\sqrt{N}} \sum_{j=0}^{N-1} g_j \, e^{-ijk\alpha} \qquad (3.2)$$

The field quantities for a consolidation problem in solid mechanics may be written in terms of their Fourier coefficients as:

$$(u_r, u_z, u_\theta, q, f)_j = \frac{1}{\sqrt{N}} \sum_{k=0}^{N-1} (U_r, U_z, U_\theta, Q, F)_k \, e^{ijk\alpha} \qquad (3.3)$$

where $(u_r, u_z, u_\theta)_j$ denote the nodal displacement components of wedge j, q_j are the excess pore pressures at nodes on wedge j, f_j are nodal forces applied to wedge j, and $(U_r, U_z, U_\theta, Q, F)_k$ are the k^{th} Fourier coefficients of nodal displacements, pore water pressures and external applied loads given by:

$$(U_r, U_z, U_\theta, Q, F)_k = \frac{1}{\sqrt{N}} \sum_{j=0}^{N-1} (u_r, u_z, u_\theta, q, f)_j \, e^{-ijk\alpha} \qquad (3.4)$$

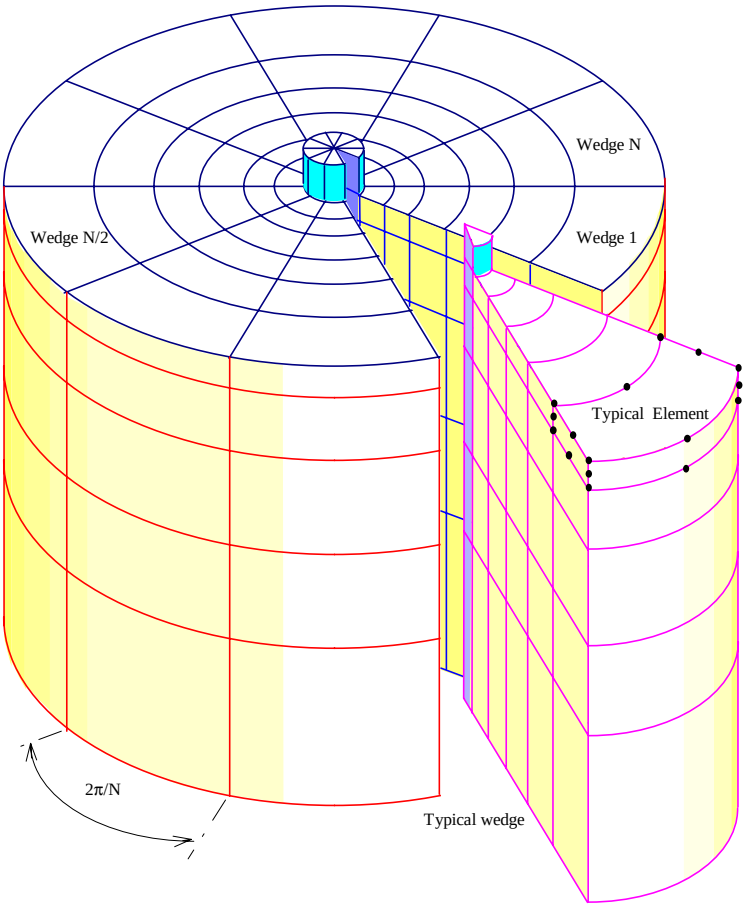

Fig. 3.1: Typical arrangement of wedges and elements in finite element idealization

A detailed formulation of the coupled finite element method for consolidation analysis is presented in Appendix 3.1. Equation (A3.1.13) shows that application of the principle of virtual work to a saturated soil leads to the following equation.

$$dn^T.\boldsymbol{S}.\Delta n = dn^T.\Delta r \qquad (3.5)$$

where $dn^T = (du^T , dq^T)^T$

$$\boldsymbol{S} = \begin{pmatrix} \boldsymbol{K} & -\boldsymbol{L}^T \\ -\boldsymbol{L} & -\Delta t.\beta.\boldsymbol{\Phi} \end{pmatrix}$$

$\Delta n = (\Delta u , \Delta q)^T$

$\Delta r = (f_R , f_p)^T$

In the above equations, u refers to nodal displacements, q represents nodal pore pressures, $\boldsymbol{K}$ is the stiffness matrix, $\boldsymbol{L}$ is the coupling matrix, t denotes time, β is an integration constant, $\boldsymbol{\Phi}$ is the flow matrix, f_R is the vectors of body forces and surface tractions, and f_p is the flow terms.

Since the body is divided into N identical wedges, the terms in the left hand side of Equation (3.5) can be expressed as the summation of the contributions from each of the wedges, i.e.

$$dn^T.\boldsymbol{S}.\Delta n = \sum_{j=1}^{N} da_j^T.\boldsymbol{S}_j.\Delta a_j \qquad (3.6)$$

where $\boldsymbol{S}_j$ is the stiffness matrix of a typical wedge and a_j is the vector of nodal displacements and pore water pressures of the wedge, consisting of nodal variables on the two vertical cutting planes, j and $j+1$, and variables at nodes within the wedge, viz.

$$a_j = (w_j , w'_j , w_{j+1})^T$$

where w_j, w_{j+1} and w'_j represent variables at nodes on the cutting planes j and $j+1$, and variables at nodes within the wedge, respectively.

The matrix $\boldsymbol{S}_j$ can be partitioned according to the above nodal subdivision, i.e.

$$\boldsymbol{S}_j = \begin{pmatrix} \boldsymbol{A}_S & \boldsymbol{B}_S & \boldsymbol{C}_S \\ \boldsymbol{B}_S^T & \boldsymbol{D}_S & \boldsymbol{E}_S \\ \boldsymbol{C}_S^T & \boldsymbol{E}_S^T & \boldsymbol{F}_S \end{pmatrix}$$

Thus Equation (3.6) may be written as:

$$\sum_{j=1}^{N} da_j^T.\boldsymbol{S}_j.\Delta a_j = \sum_{j=1}^{N} (dw_j^T , dw'^T_j , dw_{j+1}^T) \begin{pmatrix} \boldsymbol{A}_S & \boldsymbol{B}_S & \boldsymbol{C}_S \\ \boldsymbol{B}_S^T & \boldsymbol{D}_S & \boldsymbol{E}_S \\ \boldsymbol{C}_S^T & \boldsymbol{E}_S^T & \boldsymbol{F}_S \end{pmatrix} \begin{pmatrix} \Delta w_j \\ \Delta w'_j \\ \Delta w_{j+1} \end{pmatrix} \qquad (3.7)$$

Applying the discrete Fourier series representation to the nodal variables gives:

$$\begin{pmatrix} \Delta w_j \\ \Delta w'_j \\ \Delta w_{j+1} \end{pmatrix} = \begin{pmatrix} \frac{1}{\sqrt{N}} \sum_{l=0}^{N-1} \Delta W_l e^{ijl\alpha} \\ \frac{1}{\sqrt{N}} \sum_{l=0}^{N-1} \Delta W'_l e^{ijl\alpha} \\ \frac{1}{\sqrt{N}} \sum_{l=0}^{N-1} \Delta W_l e^{i(j+1)l\alpha} \end{pmatrix} \tag{3.8}$$

and

$$\begin{pmatrix} dw_j^T \\ dw'^T_j \\ dw_{j+1}^T \end{pmatrix} = \begin{pmatrix} \frac{1}{\sqrt{N}} \sum_{k=0}^{N-1} dW_k^T e^{ijk\alpha} \\ \frac{1}{\sqrt{N}} \sum_{k=0}^{N-1} dW'^T_k e^{ijk\alpha} \\ \frac{1}{\sqrt{N}} \sum_{k=0}^{N-1} dW_k^T e^{i(j+1)k\alpha} \end{pmatrix} = \begin{pmatrix} \frac{1}{\sqrt{N}} \sum_{k=0}^{N-1} dW_k^{T^*} e^{-ijk\alpha} \\ \frac{1}{\sqrt{N}} \sum_{k=0}^{N-1} dW'^{T^*}_k e^{-ijk\alpha} \\ \frac{1}{\sqrt{N}} \sum_{k=0}^{N-1} dW_k^{T^*} e^{-i(j+1)k\alpha} \end{pmatrix} \tag{3.9}$$

where ΔW and $\Delta W'$ are the k^{th} Fourier coefficients of Δw and $\Delta w'$, i.e.

$$\Delta W = (U_r \ , U_z \ , U_\theta \ , Q \ )$$

$$\Delta W' = (U'_r \ , U'_z \ , U'_\theta \ , Q' \ )$$

and $dW_k^{T^*}$ and $dW'^{T^*}_k$ are the k^{th} conjugate transposes of Fourier coefficients of dw and dw'. Substituting Equations (3.8) and (3.9) into Equation (3.7) results in:

$$\sum_{j=1}^{N} da_j^T . \boldsymbol{S}_j . \Delta a_j = \frac{1}{N} \sum_{j=1}^{N} \sum_{k=0}^{N-1} \sum_{l=0}^{N-1} e^{-ijk\alpha} \left(dW_k^{T^*}, dW'^{T^*}_k, dW_k^{T^*} e^{-ik\alpha} \right) \begin{pmatrix} \boldsymbol{A}_S & \boldsymbol{B}_S & \boldsymbol{C}_S \\ \boldsymbol{B}_S^T & \boldsymbol{D}_S & \boldsymbol{E}_S \\ \boldsymbol{C}_S^T & \boldsymbol{E}_S^T & \boldsymbol{F}_S \end{pmatrix} \begin{pmatrix} \Delta W_l \\ \Delta W'_l \\ \Delta W_l e^{il\alpha} \end{pmatrix} e^{ijl\alpha} \tag{3.10}$$

It can be shown that:

$$\frac{1}{N} \sum_{j=1}^{N} e^{ij(l-k)\alpha} = \begin{cases} 1 & if \ \ l = k \\ 0 & if \ \ l \neq k \end{cases}$$

Therefore, Equation (3.10) is simplified to:

$$\sum_{j=1}^{N} da_j^T . \mathbf{S}_j \Delta a_j = \sum_{k=0}^{N-1} (dW_k^{T^*} . \mathbf{S1}_k \Delta W_k + dW_k^{T^*} . \mathbf{S2}_k \Delta W'_k + dW'^{T^*}_k . \mathbf{S3}_k \Delta W_k + dW'^{T^*}_k . \mathbf{S4}_k . \Delta W'_k)$$

or

$$\sum_{j=1}^{N} da_j^T . \boldsymbol{S}_j . \Delta a_j = \sum_{k=0}^{N-1} \left(dW_k^{T^*}, dW'^{T^*}_k \right) \begin{pmatrix} \boldsymbol{S1}_k & \boldsymbol{S2}_k \\ \boldsymbol{S3}_k & \boldsymbol{S4}_k \end{pmatrix} \begin{pmatrix} \Delta W_k \\ \Delta W'_k \end{pmatrix} \tag{3.11}$$

or in a compact form:

$$dn^T . \boldsymbol{S} . \Delta n = \sum_{k=0}^{N-1} d\underline{N}_k^{T^*} . \underline{\boldsymbol{S}}_k . \Delta \underline{N}_k \tag{3.12}$$

In Equations (3.11) and (3.12), $\underline{\boldsymbol{S}}_k$ and $\underline{N}_k$ are the k^{th} Fourier coefficients of $\boldsymbol{S}$ and n, and $\boldsymbol{S1}_k$ to $\boldsymbol{S4}_k$ are the k^{th} Fourier coefficients of the partitioned $\boldsymbol{S}$, as defined below.

$$\boldsymbol{S1}_k = \boldsymbol{A}_S + \boldsymbol{C}_S . e^{ik\alpha} + \boldsymbol{C}_S^T . e^{-ik\alpha} + \boldsymbol{F}_S \qquad (3.13)$$

$$\boldsymbol{S2}_k = \boldsymbol{B}_S + \boldsymbol{E}_S^T . e^{-ik\alpha} \qquad (3.14)$$

$$\boldsymbol{S3}_k = \boldsymbol{B}_S^T + \boldsymbol{E}_S . e^{ik\alpha} \qquad (3.15)$$

$$\boldsymbol{S4}_k = \boldsymbol{D}_S \qquad (3.16)$$

The terms in the right hand side of Equation (3.5) can also be expressed as the summation of the contributions from each of the wedges;

$$dn^T . \Delta r = \sum_{j=1}^{N} da_j^T . \Delta r_j = \sum_{j=1}^{N} (dw_j^T , dw'^T_j) \begin{pmatrix} g_j \\ g'_j \end{pmatrix} \qquad (3.17)$$

where r_j represents nodal values of vector r on wedge j, g_j represents the nodal values for nodes in the cutting plane j and g'_j represents the nodal values for nodes within the wedge. g_{j+1} is absent because the imposed nodal values on interface boundaries must appear on only one interface boundary.

Utilizing the discreet Fourier series representation of dw^T, dw'^T, g_j and g'_j, and rearranging and simplifying Equation (3.17) results in:

$$dn^T . \Delta r = \sum_{k=0}^{N-1} (dW_k^{T^*} , dW'^{T^*}_k) \begin{pmatrix} G_k \\ G'_k \end{pmatrix} \qquad (3.18)$$

where G_k and G'_k are the k^{th} Fourier coefficients of vectors g_j and g'_j respectively. Equation (3.18) can be written in a compact form as:

$$dn^T . \Delta r = \sum_{k=0}^{N-1} d\underline{N}_k^{T^*} . \Delta \underline{R}_k \qquad (3.19)$$

Combining Equations (3.12) and (3.19) yields the equation of virtual work in a new form which contains Fourier coefficients of the equation components, i.e.

$$\sum_{k=0}^{N-1} d\underline{N}_k^{T^*} . \underline{\boldsymbol{S}}_k . \Delta \underline{N}_k = \sum_{k=0}^{N-1} d\underline{N}_k^{T^*} . \Delta \underline{R}_k \qquad (3.20)$$

Equation (3.20) is true for any arbitrary variations of virtual nodal values of $d\underline{N}_k^{T^*}$, thus:

$$\sum_{k=0}^{N-1} \underline{\boldsymbol{S}}_k . \Delta \underline{N}_k = \sum_{k=0}^{N-1} \Delta \underline{R}_k \qquad (3.21)$$

This equation defines N sets of equations relating the load-deformation behaviour of the consolidating body in discrete Fourier space, i.e.

$$\underline{\boldsymbol{S}}_k . \Delta \underline{N}_k = \Delta \underline{R}_k \quad \text{for } k=0 \text{ to } N-1 \qquad (3.22)$$

The modal stiffness matrices, $\underline{\boldsymbol{S}}_k$, given by Equation (3.22) are, in general, non-symmetric and complex. A simple redefinition of the degrees of freedom allows them to be converted to a real and symmetric matrix. In term of cylindrical polar coordinates, the nodal components consist of a radial displacement, u_r, a vertical displacement, u_z, a circumferential displacement, u_θ, and a pore pressure, q. The Fourier coefficients of the nodal variables at nodes on the cutting planes of a wedge are U_r, U_z, U_θ, Q, respectively, and the Fourier coefficients of nodal variables at nodes within the wedge are U'_r, U'_z, U'_θ, Q'. $\boldsymbol{A}_S$ to $\boldsymbol{F}_S$ can be decomposed into sub-matrices relating to each of these components, i.e.

$$\left(\mathbf{A}_S\right)\begin{pmatrix}\Delta u\\ \Delta q\end{pmatrix}=\begin{pmatrix}\mathbf{A}_{11} & \mathbf{A}_{12} & \mathbf{A}_{13}\\ \mathbf{A}_{21} & \mathbf{A}_{22} & \mathbf{A}_{23}\\ \mathbf{A}_{31} & \mathbf{A}_{32} & \mathbf{A}_{33}\end{pmatrix}\begin{Bmatrix}\Delta u_{r,z}\\ \Delta u_\theta\\ \Delta q\end{Bmatrix}$$

Because of the geometry of an axi-symmetric body, each wedge has reflective symmetry about its bisecting plane. Therefore,

$$\boldsymbol{C}_S^T = \boldsymbol{J}^T.\boldsymbol{C}_S.\boldsymbol{J} \qquad (3.23\text{-}a)$$

$$\boldsymbol{F}_S = \boldsymbol{J}^T.\boldsymbol{A}_S.\boldsymbol{J} \qquad (3.23\text{-}b)$$

$$\boldsymbol{E}_S = \boldsymbol{J}^T.\boldsymbol{B}_S^T.\boldsymbol{J} \qquad (3.23\text{-}c)$$

$$\boldsymbol{E}_S^T = \boldsymbol{J}^T.\boldsymbol{B}_S.\boldsymbol{J} \qquad (3.23\text{-}d)$$

and

$$\boldsymbol{D}_S=\begin{pmatrix}\boldsymbol{D}_{11} & 0 & \boldsymbol{D}_{13}\\ 0 & \boldsymbol{D}_{22} & 0\\ \boldsymbol{D}_{31} & 0 & \boldsymbol{D}_{33}\end{pmatrix} \qquad (3.23\text{-}e)$$

where

$$\boldsymbol{J}=\begin{pmatrix}\boldsymbol{I} & \boldsymbol{0} & \boldsymbol{0}\\ \boldsymbol{0} & -\boldsymbol{I} & \boldsymbol{0}\\ \boldsymbol{0} & \boldsymbol{0} & \boldsymbol{I}\end{pmatrix}$$

and $\boldsymbol{I}$ is identity matrix of the size of u_r or q.

Substitution of the relations (3.23) into Equation (3.13) gives:

$$\boldsymbol{S1}_k = \boldsymbol{A}_S + \boldsymbol{C}_S.e^{ik\alpha} + \boldsymbol{J}^T.\boldsymbol{C}_S.e^{-ik\alpha} + \boldsymbol{J}^T.A_S.\boldsymbol{J} \qquad (3.24)$$

It thus follows that

$$\boldsymbol{S1}_k = 2\begin{pmatrix}\boldsymbol{A}_{11}+\eta\,\boldsymbol{C}_{11} & i\mu\boldsymbol{C}_{12} & \boldsymbol{A}_{13}+\eta\boldsymbol{C}_{13}\\ i\mu\boldsymbol{C}_{21} & \boldsymbol{A}_{22}+\eta\boldsymbol{C}_{22} & i\mu\boldsymbol{C}_{23}\\ \boldsymbol{A}_{31}+\eta\boldsymbol{C}_{31} & i\mu\boldsymbol{C}_{32} & \boldsymbol{A}_{33}+\eta\boldsymbol{C}_{33}\end{pmatrix} \qquad (3.25)$$

in which $\eta=Cos(k\alpha)$ and $\mu=Sin(k\alpha)$. In the same way, the other components of matrix $\underline{\boldsymbol{S}}_k$ of Equation (3.12) can be expressed as:

$$\boldsymbol{S2}_k=\begin{pmatrix}\boldsymbol{B}_{11}(1+e^{-ik\alpha}) & \boldsymbol{B}_{12}(1-e^{-ik\alpha}) & \boldsymbol{B}_{13}(1+e^{-ik\alpha})\\ \boldsymbol{B}_{21}(1-e^{-ik\alpha}) & \boldsymbol{B}_{22}(1+e^{-ik\alpha}) & \boldsymbol{B}_{23}(1-e^{-ik\alpha})\\ \boldsymbol{B}_{31}(1+e^{-ik\alpha}) & \boldsymbol{B}_{32}(1-e^{-ik\alpha}) & \boldsymbol{B}_{33}(1+e^{-ik\alpha})\end{pmatrix} \tag{3.26}$$

$$\boldsymbol{S3}_k=\begin{pmatrix}\boldsymbol{B}_{11}^T(1+e^{ik\alpha}) & \boldsymbol{B}_{12}^T(1-e^{ik\alpha}) & \boldsymbol{B}_{13}^T(1+e^{ik\alpha})\\ \boldsymbol{B}_{21}^T(1-e^{ik\alpha}) & \boldsymbol{B}_{22}^T(1+e^{ik\alpha}) & \boldsymbol{B}_{23}^T(1-e^{ik\alpha})\\ \boldsymbol{B}_{31}^T(1+e^{ik\alpha}) & \boldsymbol{B}_{32}^T(1-e^{ik\alpha}) & \boldsymbol{B}_{33}^T(1+e^{ik\alpha})\end{pmatrix} \tag{3.27}$$

$$\boldsymbol{S4}_k=\begin{pmatrix}\boldsymbol{D}_{11} & \boldsymbol{0} & \boldsymbol{D}_{13}\\ \boldsymbol{0} & \boldsymbol{D}_{22} & \boldsymbol{0}\\ \boldsymbol{D}_{31} & \boldsymbol{0} & \boldsymbol{D}_{33}\end{pmatrix} \tag{3.28}$$

Substituting the above relationships into Equation (3.22) yields:

$$\begin{pmatrix}2(\mathbf{A}_{11}+\eta\mathbf{C}_{11}) & 2i\mu\mathbf{C}_{12} & 2(\mathbf{A}_{13}+\eta\mathbf{C}_{13}) & \mathbf{B}_{11}(1+e^{-ik\alpha}) & \mathbf{B}_{12}(1-e^{-ik\alpha}) & \mathbf{B}_{13}(1+e^{-ik\alpha})\\ 2i\mu\mathbf{C}_{21} & 2(A_{22}+\eta\mathbf{C}_{22}) & 2i\mu\mathbf{C}_{23} & \mathbf{B}_{21}(1-e^{-ik\alpha}) & \mathbf{B}_{22}(1+e^{-ik\alpha}) & \mathbf{B}_{23}(1-e^{-ik\alpha})\\ 2(\mathbf{A}_{31}+\eta\mathbf{C}_{31}) & 2i\mu\mathbf{C}_{32} & 2(\mathbf{A}_{33}+\eta\mathbf{C}_{33}) & \mathbf{B}_{31}(1+e^{-ik\alpha}) & \mathbf{B}_{32}(1-e^{-ik\alpha}) & \mathbf{B}_{33}(1+e^{-ik\alpha})\\ \mathbf{B}_{11}^T(1+e^{ik\alpha}) & \mathbf{B}_{12}^T(1-e^{ik\alpha}) & \mathbf{B}_{13}^T(1+e^{ik\alpha}) & \mathbf{D}_{11} & \mathbf{0} & \mathbf{D}_{13}\\ \mathbf{B}_{21}^T(1-e^{ik\alpha}) & \mathbf{B}_{22}^T(1+e^{ik\alpha}) & \mathbf{B}_{23}^T(1-e^{ik\alpha}) & \mathbf{0} & \mathbf{D}_{22} & \mathbf{0}\\ \mathbf{B}_{31}^T(1+e^{ik\alpha}) & \mathbf{B}_{32}^T(1-e^{ik\alpha}) & \mathbf{B}_{33}^T(1+e^{ik\alpha}) & \mathbf{D}_{31} & \mathbf{0} & \mathbf{D}_{33}\end{pmatrix}\begin{Bmatrix}(\Delta U_{r,z})_k\\ (\Delta U_\theta)_k\\ (\Delta Q)_k\\ (\Delta U'_{r,z})_k\\ (\Delta U'_\theta)_k\\ (\Delta Q')_k\end{Bmatrix}=\begin{pmatrix}(G_{r,z})_k\\ (G_\theta)_k\\ (G_p)_k\\ (G'_{r,z})_k\\ (G'_\theta)_k\\ (G'_p)_k\end{pmatrix} \tag{3.29}$$

where $(G_{r,z,\theta})_k$ and $(G_p)_k$ are the Fourier coefficients of f_R and f_p corresponding to the nodes on the cutting plane of the wedge, $(G'_{r,z,\theta})_k$ and $(G'_p)_k$ are the Fourier coefficients of f_R and f_p corresponding to the nodes within the wedge, respectively.

A real and symmetric form of Equation (3.29) can finally be obtained by multiplying the fourth, fifth and sixth rows by $e^{-ik\alpha/2}$, and multiplying the second and fifth rows by i, i.e.

$$\begin{pmatrix}2(\boldsymbol{A}_{11}+\eta\boldsymbol{C}_{11}) & 2\mu\,\boldsymbol{C}_{12} & 2(\boldsymbol{A}_{13}+\eta\boldsymbol{C}_{13}) & 2\eta'\boldsymbol{B}_{11} & 2\mu'\boldsymbol{B}_{12} & 2\eta'\boldsymbol{B}_{13}\\ -2\mu\,\boldsymbol{C}_{21} & 2(\boldsymbol{A}_{22}+\eta\boldsymbol{C}_{22}) & -2\mu\,\boldsymbol{C}_{23} & -2\mu'\boldsymbol{B}_{21} & 2\eta'\boldsymbol{B}_{22} & -2\mu'\boldsymbol{B}_{23}\\ 2(\boldsymbol{A}_{31}+\eta\boldsymbol{C}_{31}) & 2\mu\,\boldsymbol{C}_{32} & 2(\boldsymbol{A}_{33}+\eta\boldsymbol{C}_{33}) & 2\eta'\boldsymbol{B}_{31} & 2\mu'\boldsymbol{B}_{32} & 2\eta'\boldsymbol{B}_{33}\\ 2\eta'\boldsymbol{B}_{11}^T & -2\mu'\boldsymbol{B}_{12}^T & 2\eta'\boldsymbol{B}_{13}^T & \boldsymbol{D}_{11} & \boldsymbol{0} & \boldsymbol{D}_{13}\\ 2\mu'\boldsymbol{B}_{21}^T & 2\eta'\boldsymbol{B}_{22}^T & 2\mu'\boldsymbol{B}_{23}^T & \boldsymbol{0} & \boldsymbol{D}_{22} & \boldsymbol{0}\\ 2\eta'\boldsymbol{B}_{31}^T & -2\mu'\boldsymbol{B}_{32}^T & 2\eta'\boldsymbol{B}_{33}^T & \boldsymbol{D}_{31} & \boldsymbol{0} & \boldsymbol{D}_{33}\end{pmatrix}\begin{Bmatrix}(\Delta U_{r,z})_k\\ i(\Delta U_\theta)_k\\ (\Delta Q)_k\\ e^{-ik\alpha/2}(\Delta U'_{r,z})_k\\ ie^{-ik\alpha/2}(\Delta U'_\theta)_k\\ e^{-ik\alpha/2}(\Delta Q')_k\end{Bmatrix}=\begin{pmatrix}(G_{r,z})_k\\ i(G_\theta)_k\\ (G_p)_k\\ e^{-ik\alpha/2}(G'_{r,z})_k\\ ie^{-ik\alpha/2}(G'_\theta)_k\\ e^{-ik\alpha/2}(G'_p)_k\end{pmatrix} \tag{3.30}$$

In Equation (3.30), $\eta'=Cos(k\alpha/2)$ and $\mu'=Sin(k\alpha/2)$. This equation represents a general form of a semi-analytical finite element formulation suitable for a quadratic element with four degrees of freedom per node. By removing rows and columns related to mid-side nodes, the modal stiffness equation for linear elements can be obtained, i.e.

$$\begin{pmatrix} 2(\boldsymbol{A}_{11}+\eta\boldsymbol{C}_{11}) & 2\mu\,\boldsymbol{C}_{12} & 2(\boldsymbol{A}_{13}+\eta\boldsymbol{C}_{13}) \\ -2\mu\,\boldsymbol{C}_{21} & 2(\boldsymbol{A}_{22}+\eta\boldsymbol{C}_{22}) & -2\mu\,\boldsymbol{C}_{23} \\ 2(\boldsymbol{A}_{31}+\eta\boldsymbol{C}_{31}) & 2\mu\,\boldsymbol{C}_{32} & 2(\boldsymbol{A}_{33}+\eta\boldsymbol{C}_{33}) \end{pmatrix} \begin{Bmatrix} (\Delta U_{r,z})_k \\ i(\Delta U_{\theta})_k \\ (\Delta Q)_k \end{Bmatrix} = \begin{Bmatrix} (G_{r,z})_k \\ i(G_{\theta})_k \\ (G_p)_k \end{Bmatrix} \qquad (3.31)$$

A solution to Equation (3.30) or (3.31) can be obtained by separating the real and imaginary parts of the right hand side vector and solving for the real and imaginary parts of the Fourier coefficient of the nodal variables. Since the modal stiffness matrix is identical for both real and imaginary parts of the equation, it can be set up and factorized once. Then the real and imaginary components of the displacement coefficients can be calculated by a back-substitution process for real and imaginary parts of the load vector. Finally, the nodal variables can be calculated from their Fourier coefficients using Equation (3.3).

In practice, it is only necessary to solve Equation (3.30) or (3.31) for the first half of the discrete Fourier coefficients by taking advantage of the symmetry about one vertical plane. In a purely elastic material, the solution to the problem reduces to the solution of Equation (3.30) or (3.31) for only the first two modes of the discrete Fourier coefficients, since the body forces and surface traction, which are expressed in term of η and μ, have zero values for all but the first two modes of the discrete Fourier coefficients.

3.4: STRESS-STRAIN MODELS

Simulation of soil behaviour in a plastic state is very complex. A significant idealization of soil behaviour is usually essential in order to make the mathematical formulation of any model tractable. Depending on the level of sophistication of treatment, a whole class of soil models has been proposed. Since any explicit descriptions in phenomenological or mathematical terms are bound to be an idealization of the actual behaviour of soils, it cannot be expected that any model will be valid over a wide range of conditions. Most of the models are formulated to simulate a certain behaviour of a particular soil and may require a large number of parameters. The most popular models are generally defined by a few material parameters which ideally have a clear physical meaning and can usually be determined from standard tests.

In this work, two of the plasticity models commonly used in geotechnical engineering, namely the Mohr-Coulomb model and the Modified Cam-Clay model, are adopted. It is believed that these models are capable of simulating a wide range of soil behaviour for many practical problems in soil mechanics.

For soil, perfect plasticity is a useful design simplification. The Mohr-Coulomb model is certainly the best known perfect plasticity model in soil mechanics. In this model the effect of

hydrostatic pressure on the strength of granular materials is taken into consideration. The Mohr-Coulomb model reduces to the Tresca model if the material friction angle is set to zero.

A more complex stress-strain behaviour of soil is approximated by a more sophisticated hardening plasticity theory. The Modified Cam-Clay model is an isotropic, nonlinear elastic strain-hardening plastic model. In this model, elastic volumetric strain is non-linearly dependent on hydrostatic pressure and independent of deviatoric stresses. Volumetric strain is assumed to be partially recoverable.

The basic formulation of elasto-plastic models has been extensively described in many standard texts and will not be elaborated on here. In brief, the incremental theory of plasticity is based on three fundamental assumptions: the shape of an initial yield surface, f, the evolution of subsequent loading surfaces, and the formulation of an appropriate flow rule, g. An explicit expression for an elasto-plastic constitutive model is usually in the form of:

$$d\sigma_{ij} = \boldsymbol{D}^{ep}_{ijkl} d\varepsilon_{kl}$$

in which $\boldsymbol{D}^{ep}$ is the elasto-plastic stiffness matrix defined as:

$$\boldsymbol{D}^{ep}_{ijkl} = \boldsymbol{D}^{e}_{ijkl} - \frac{\boldsymbol{D}^{e}_{irsl} \dfrac{\partial g}{\partial \sigma_{rs}} \dfrac{\partial f}{\partial \sigma_{mn}} \boldsymbol{D}^{e}_{mnkl}}{A + \dfrac{\partial g}{\partial \sigma_{ab}} \boldsymbol{D}^{e}_{abcd} \dfrac{\partial g}{\partial \sigma_{cd}}} \qquad (3.32)$$

Equation (3.32) is a general form of the elasto-plastic stiffness matrix for perfectly-plastic, isotropic-hardening, and anisotropic-hardening materials. The hardening modulus, A, plays an important role in describing the behaviour of the material, and it has different forms for various types of materials. For a perfectly plastic model, the hardening modulus vanishes. In Equation (3.32), $\boldsymbol{D}^{e}$ is the elastic stiffness matrix, g is a plastic potential function and f is a failure criterion. Different definitions for A, g and f result in a different form of the constitutive model.

3.5: CHOICE OF ELEMENT TYPES

The type of element used in a three-dimensional finite element analysis affects the accuracy of the solution and the computation time. Further, in a consolidation analysis, the interpolation functions used in the element formulation affect the stability as well as the accuracy of the solution. The use of complex elements with many degrees of freedom usually satisfies both the accuracy and efficiency of the solution in three-dimensional finite element analysis.

The use of simple constant and linear strain tetrahedra in three-dimensional finite element analysis is not customary, since the number of elements which has to be used to achieve a given degree of accuracy is often very large. This results in very large numbers of simultaneous equations and a large band width, and consequently, increases the computational effort.

The introduction of isoparametric elements was one of the most significant developments in finite element theory. As a result, many elements with a high degree of accuracy have been developed. The standard linear 8-noded and quadratic 20-noded isoparametric hexahedron finite elements are the most widely used elements in three-dimensional analysis. However, the linear strain elements exhibit some deficiencies associated with their inability to represent certain simple stress gradients (Zienkiewicz *et al.*, 1971; Wilson *et al.*, 1973; Herrmann, 1973; Taylor *et al.*, 1976; Cook, 1974 and 1975). Therefore, in order to obtain accurate results, particularly in problems where bending behaviour is important, the use of the standard linear 8-noded hexahedral element should be avoided.

Finite element solutions of consolidation problems may exhibit oscillating pore pressures, which tend to increase when the time steps are reduced (Sandhu *et al.*, 1977; Nishizaki *et al.*, 1982; Reed, 1984). One remedy for this deficiency is to use finite elements which are isoparametric with respect to displacements but sub-parametric with respect to pore pressure. However, if the deformation behaviour of the body is of greater interest, the isoparametric elements give the most satisfactory results. Furthermore, it can be shown that the results obtained using three-dimensional isoparametric quadratic elements are as good as the results from mixed elements, i.e. those that are isoparametric with respect to displacements and sub-parametric with respect to pore pressures (see section 3.7.2).

All elements are usually integrated numerically by Gauss quadrature rules. The full integration rule is the only sure way to avoid mesh instability (hourglass modes). However, a reduced integration scheme is often used for numerical integration of some elements. In reduced integration, certain higher order polynomial terms happen to vanish at Gauss points, so that these terms make no contribution to strain energy. This is in fact often a positive advantage in that a low order rule tends to soften an element, thus countering the over stiff behaviour associated with an assumed displacement field (Cook *et al.*, 1989; Zienkiewicz and Taylor, 1989). Furthermore, since the expense of generating the stiffness matrix by numerical integration is proportional to the number of sampling points, using fewer sampling points means lower cost.

In this study, unless otherwise stated, all the analyses are performed using standard 20-noded isoparametric hexahedron finite elements together with a reduced integration scheme (Cook *et al.*, 1989). In the modal analysis described previously, the standard 20-noded

element changes to its equivalent 12-noded half element (Fig. 3.2), which results in further reduction in computer storage and computation time.

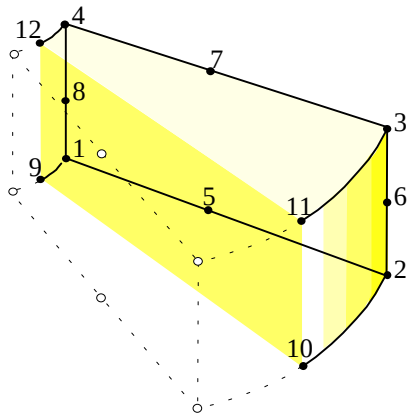

Fig. 3.2: Typical 12-noded element used in modal analysis

3.6: COMPUTATION PROCESS AND CONVERGENCE

A numerical solution to the problems of elasto-plasticity cannot be approached directly and some form of iterative technique will usually be required. Depending upon the forms of the constitutive relations used in material modelling, many variations of the solution process exist. The most commonly used techniques are the 'Newton-Raphson method' and the 'Modified Newton-Raphson methods'.

The 'Newton-Raphson method' is probably the most rapidly convergent process for solution of non-linear problems. In this method, the solution is obtained through a linearization process in which the material constants are continuously adjusted through successive iterations. At each iteration, the material parameters, updated at the end of the previous iteration, are used in the calculation of the stiffness matrix. This method, apart from its rapid convergence, is quite expensive and therefore inconvenient. A new stiffness matrix, which becomes non-symmetric for non-associated elasto-plasticity, has to be formed and factorized for each iteration.

In the 'Modified Newton-Raphson method', the solution is arrived at by some trial and error process in which, at the final stage, the material constants are so adjusted that the appropriate constitutive law is satisfied. Arbitrary and constant material parameters can be used in the calculation of the stiffness matrix, however, the initial material parameters are normally used. The material parameters can be updated at some stage in the solution process. Although the procedure will converge at a slower rate, the overall computer time used in the process is sometimes less than that of the 'Newton-Raphson method'.

The 'Newton-Raphson method' is not applicable to the numerical scheme developed in this work, since the fundamental assumption of superposition, expressed in Equation (3.6), will be violated. The 'Modified Newton-Raphson method' is also not suitable for consolidation analysis with a coupled formulation and a time marching process, because the rate of pore pressure dissipation at each time interval depends on the intensity of pore pressure and its spatial gradient, which in turn depend on the rate of volumetric strain, and this is not evaluated in an accurate way by using the initial stiffness. Therefore, a new method based on the 'Modified Newton-Raphson method' together with the residual force method is adopted in the solution procedure. The new method, which incorporates a pseudo force in the load vector, has been used previously by Lai (1989) in an iterative process. It has been shown (Appendix 3.2) that the new method does not have any particular advantage over the 'Modified Newton-Raphson method' in an iterative solution, whereas in an incremental load path approach or a time-marching scheme, as used in consolidation analyses, some significant advantages can be achieved by the new method.

The general incremental load-displacement equation has been found (Equation 3.5 or 3.22) to be:

$$\Psi = \boldsymbol{S}.n - r = 0 \qquad (3.33)$$

In the problem of elasto-plasticity, the matrix $\boldsymbol{S}$ is a function of the unknown vector n, and therefore a direct solution to Equation (3.33) by any numerical method will result in an incorrect value of n. Consequently, the value of Ψ will not be precisely equal to zero. Iterative techniques are usually needed to determine n. In the iteration process, Equation (3.33) can be approximated, to the first order, by:

$$\Psi_{(n_{i+1})} \approx \Psi_{(n_i)} + \left(\frac{\partial \Psi}{\partial n}\right)_i \Delta n_i = 0 \qquad (3.34)$$

where i is the iteration counter, $n_{i+1} = n_I + \Delta n_i$ and $(\partial\Psi/\partial n)_i = \boldsymbol{S}_i$ is the stiffness matrix. Equation (3.34) immediately gives the iterative correction as:

$$\Delta n_i = -S_i^{-1} \Psi_i \qquad (3.35)$$

With n_0 as an initial value for nodal variables, a series of successive approximations gives the final nodal variables as:

$$n_{i+1} = n_0 + \sum_{j=1}^{i} \Delta n_j \qquad (3.36)$$

In an incremental finite element formulation, where each load increment is denoted by Δr_i, Equation (3.34) can be written as:

$$\boldsymbol{S}\, \Delta n_i = r_i + \Delta r_i - \int \boldsymbol{B}^T \sigma_i \, dV \qquad (3.37)$$

The integral expression in Equation (3.37) represents the internal forces due to application of previous load increments. In the 'Newton-Raphson method' the tangential stiffness, $\boldsymbol{S}_T$, will be used whereas in the 'Modified Newton-Raphson method' usually the initial elastic stiffness, $\boldsymbol{S}_I$, will be used. These processes are illustrated schematically in Fig. 3.3 and Fig. 3.4 respectively.

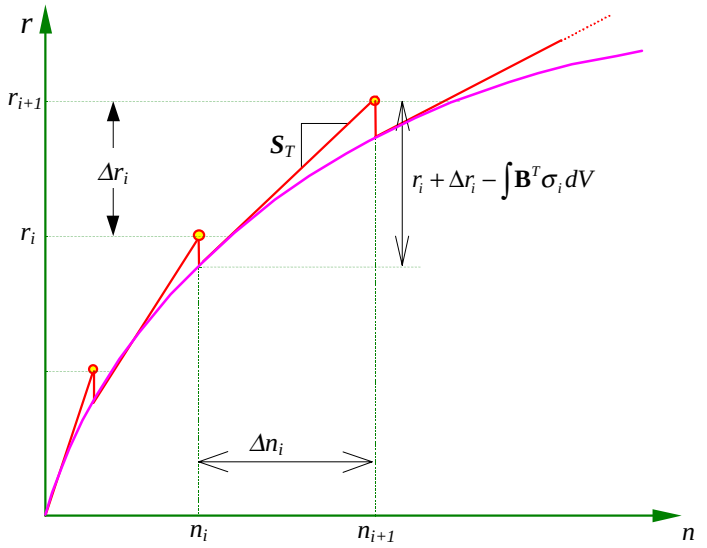

Fig. 3.3: Tangent stiffness method in a load increment process

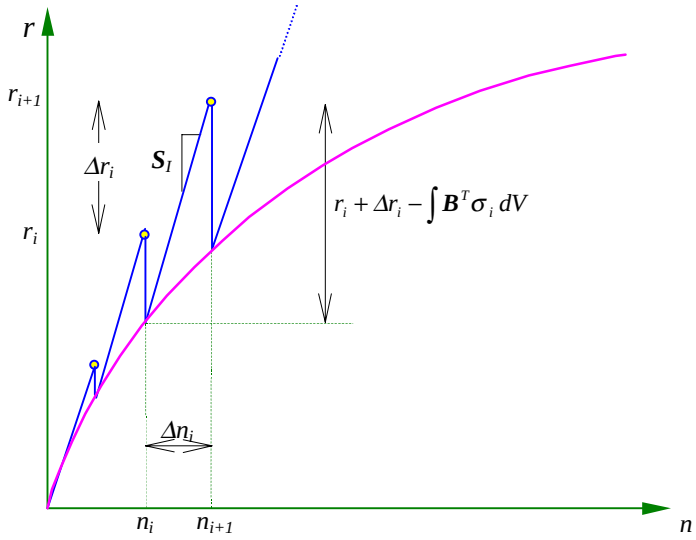

Fig. 3.4: Initial stiffness method in a load increment process

The tangent stiffness matrix $\boldsymbol{S}_T$ consists of an initial or elastic stiffness matrix $\boldsymbol{S}_I$ and a dyadic component $\boldsymbol{S}_D$ which arises from any elasto-plastic yielding within the body and is dependent on the current state of stress and strain (Equation 3.32), i.e.

$$\boldsymbol{S}_T = \boldsymbol{S}_I - \boldsymbol{S}_D \qquad (3.38)$$

Combining Equation (3.37) and (3.38) results in another form of the 'Newton-Raphson method' (Fig. 3.5):

$$\boldsymbol{S}_I\,\Delta n_i = r_i + \Delta r_i - \int \boldsymbol{B}^T \sigma_i\, dV + \boldsymbol{S}_D\,\Delta n_i \qquad (3.39)$$

The term $S_D\,\Delta n_i$ in Equation (3.39) can be approximated with only a little extra effort. Referring to the elasto-plastic stiffness matrix of Equation (3.32) and approximating Δn_{i-1} by Δn_i, the vector $[S_D\,\Delta n_i]$ can be obtained at the beginning of each increment as:

$$\boldsymbol{S}_D\,\Delta n_i = \int \boldsymbol{B}^T \left(\boldsymbol{D}^e - \boldsymbol{D}_i^{ep} \right) \boldsymbol{B}\,\Delta n_{i-1}\, dV \qquad (3.40)$$

In Equation (3.40), $\boldsymbol{D}_i^{ep}$ is the elasto-plastic constitutive matrix which is updated according to the current state of stress and strain, $\boldsymbol{D}^e$ is either the elastic constitutive matrix or the matrix used in calculation of the stiffness matrix $\boldsymbol{S}_I$. In practice, $\boldsymbol{D}^e$ can be evaluated at each Gauss point by averaging the values of the updated material parameters over all the wedges in the finite element model.

The solution of the equation governing the behaviour of an elasto-plastic material may therefore be obtained by application of the following solution algorithm:

$$\boldsymbol{S}_I\,\Delta n_i = r_i + \Delta r_i - \int \boldsymbol{B}^T \left(\sigma_i + \left(\boldsymbol{D}_i^{ep} - \boldsymbol{D}^e \right) \boldsymbol{B}\,\Delta n_{i-1} \right) dV \qquad (3.41)$$

This method is illustrated schematically in Fig. 3.5.

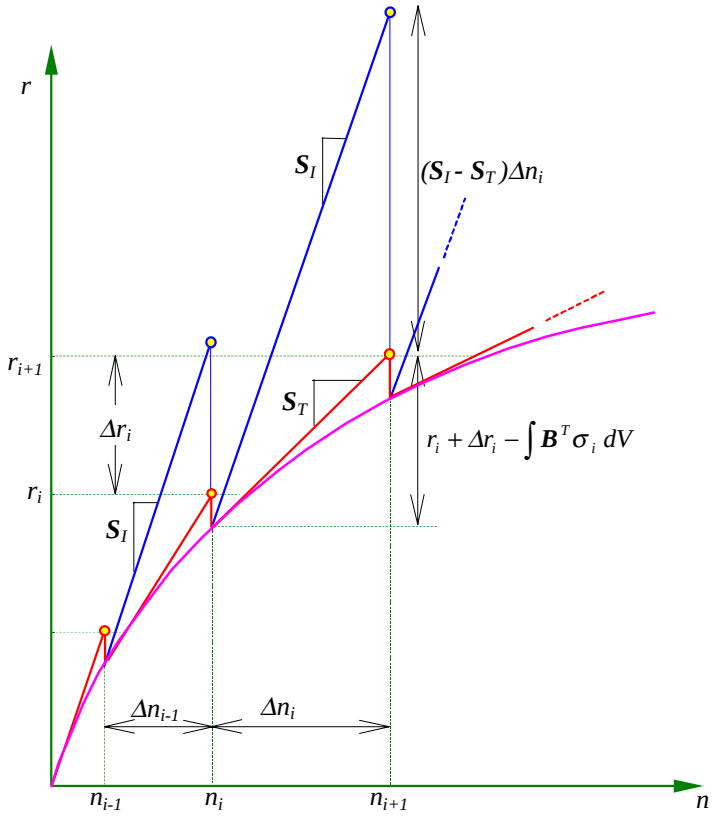

Fig. 3.5: New method in a load increment process

The limitations of the new solution scheme presented here and its advantages over the 'Modified Newton-Raphson method' are discussed in Appendix 3.2.

3.7: NUMERICAL VERIFICATION AND ILLUSTRATIVE EXAMPLES

The new method developed in this work was employed to analyse some problems with known analytic solutions. By comparing the results, it is possible to evaluate the accuracy of the formulation and also identify any possible weaknesses associated with the proposed method.

Three problems will be considered in this section. In the first example the failure loads for a cylinder of soil under internal pressure deforming under drained and partially drained conditions will be evaluated. The second example is a plane strain problem in which an infinitely long and rigid pile translates horizontally through an elastic-perfectly-plastic infinite medium. The third example is a problem of a laterally loaded pile in consolidating soil in which the time-dependent lateral response of the pile will be examined.

3.7.1. Consolidation of a Cylinder Under Internal Pressure

In this example, the problem of a long cylinder of saturated soil subjected to uniform internal pressure is studied. The results obtained from the numerical method developed here are compared with analytical and independent numerical solutions.

A thick-walled cylinder of weightless saturated soil is subjected to an internal pressure p and zero external pressure (Fig. 3.6). The external diameter of the cylinder is twice its internal diameter. It is assumed that the soil obeys the Mohr-Coulomb failure criterion with a non-associated flow rule. Under fully drained conditions, it has a cohesion c', a friction angle $\phi' = 30^o$, a zero dilation angle, ψ, a zero Poisson's ratio, ν', and an elastic shear modulus of $G = 100\ c'$. Because of the assumed initial conditions (zero stress), the undrained shear strength of the soil can be calculated as $s_u = c' . Cos\phi = 0.866\ c'$ (see Fig. 3.7).

A numerical study of this problem was presented previously by Small *et al.* (1976). The theoretical failure pressures for the cylinder can be found as $1.21\ c'$ for undrained conditions (Prager and Hodge, 1951) and $1.02\ c'$ for fully drained conditions (Small *et al.*, 1976).

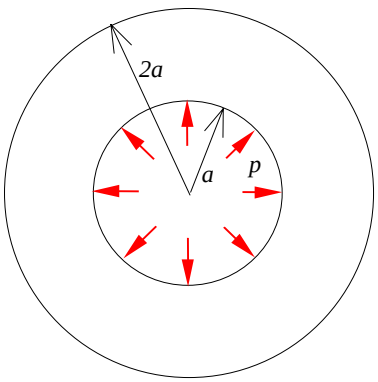

Fig. 3.6 : Cylinder under uniform internal pressure

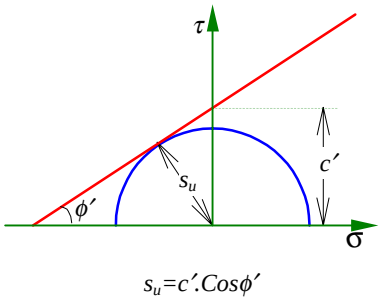

Fig. 3.7 : Undrained shear strength of weightless soil

To examine the consolidation behaviour of soil, it is convenient to introduce a non-dimensional time factor T_v, defined as:

$$T_v = \frac{2G.t.k(1-\nu'_s)}{\gamma_w(1-2\nu'_s)a^2}$$

where k is the coefficient of soil permeability, γ_w is the unit weight of the pore fluid, a is the inner radius of the cylinder and t represents time. It is also convenient to define a load rate parameter:

$$\omega = \frac{d(p/s_u)}{dT_v}$$

The larger is the value of ω, the faster the load is applied.

The problem was analysed for three different loading rates, i.e. $\omega = 10^7$ for fast loading, $\omega = 10.4$ for an intermediate rate, as used by Small *et al.* (1976), and $\omega = 10^{-7}$ for slow loading conditions. The number of wedges used in this analysis is not important, since it is only necessary to solve the problem for the first mode of the discrete Fourier coefficient because of the symmetric loading. The non-dimensional load-deformation curves predicted by the analyses are presented in Fig. 3.8. The failure pressures predicted for drained and undrained conditions using the discrete Fourier approach are in very good agreement with the corresponding theoretical values. The results of numerical studies by Small *et al.* (1976) for the intermediate loading rate of $\omega = 10.4$ are also plotted in Fig. 3.8. Good agreement with the results of the current studies is shown.

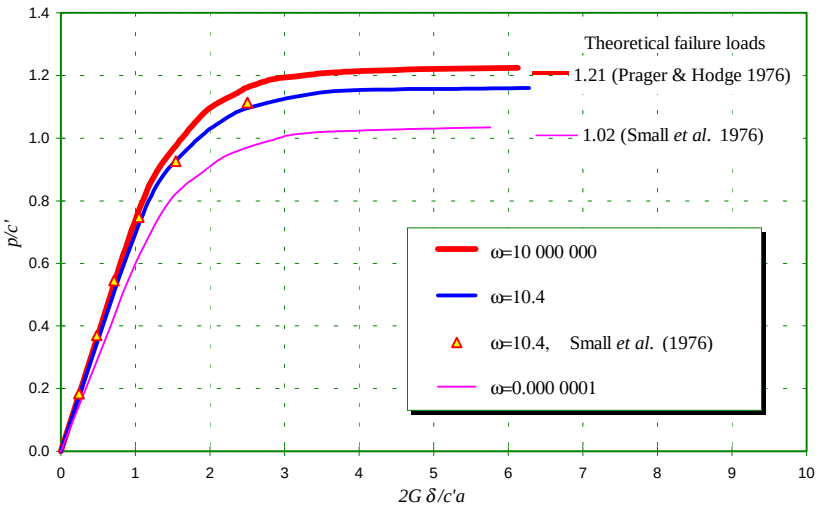

Fig. 3.8 : Load-Deformation response of cylinder under internal pressure
(δ is the radial movement of the inner surface)

3.7.2. Horizontally Loaded Rigid Circular Pile

The problem of a laterally loaded rigid pile embedded in a saturated soil under drained, undrained and partially drained conditions is described in this section, and the results of numerical analyses are compared with corresponding analytical solutions.

There does not seem to be a rigorous solution published to date in the literature for the problem of a laterally loaded pile in a consolidating cohesive-frictional soil. However, the ultimate lateral pressure p_u, required to cause failure in a purely cohesive soil, has been estimated by a number of researchers. In particular, the case of a pile segment translated laterally through soil, with no component of axial (vertical) movement (i.e. plane strain) has been studied in detail. Broms (1964) approximated the ultimate lateral pressure which develops along a laterally loaded pile using the theory of plasticity. It was assumed that slip or rupture of the soil takes place along two families of failure or rupture surfaces which are inclined at angle of 90^o degrees to each other. He showed that the ultimate lateral resistance of various pile sections with smooth or rough surfaces varies between $8.28\ s_u$ and $12.56\ s_u$, where s_u is the undrained shear strength of the soil. Based on his calculation, the ultimate lateral resistance is $9.14\ s_u$ for a smooth circular pile, $8.28\ s_u$ for a smooth square pile, and $11.42\ s_u$ for a rough square pile. Poulos and Davis (1980) studied this problem for piles with rectangular cross sections with different aspect ratios using the classical theory of plasticity and limit analysis. The ultimate lateral resistance for a square smooth pile was found to be $8.28\ s_u$, while for a square rough pile the value was quoted as $11.14\ s_u$. Randolph and Houlsby (1984) used the classical theory of plasticity and developed exact solutions for the limiting lateral resistance of a circular pile in cohesive soil. For a perfectly rough pile, the ultimate lateral pressure was shown to be $(4\sqrt{2}+2\pi)\,s_u \approx 11.94\,s_u$. No allowance was made for the possible influence of elastic deformation of the soil on the limiting resistance. It should be noted that elastic deformation of soil can influence the collapse load when the plastic region is fully confined by unyielding material, as in the problem being considered here.

Analytical solutions for both stress and displacements for the lateral loading of a rigid circular pile section embedded in an elasto-plastic medium have been presented by Baguelin *et al.* (1977). Various investigators have also studied this problem using finite element techniques, e.g. Kooijman and Vermeer (1988), Lane and Griffiths (1988), Lai (1989), Chen and Poulos (1993).

In the numerical example considered here, a rigid pile section of diameter D_p, pushed laterally by an average horizontal pressure p into a saturated weightless soil, is analysed. The soil has a uniform undrained shear strength s_u, taken to be unity for convenience. For fully drained conditions, the soil has a Young's modulus given by $E'_s=300\ s_u$ and a Poisson's ratio $\nu'_s = 0.30$. It is assumed that the soil obeys the Mohr-Coulomb failure criterion and a

non-associated flow rule. The friction angle and the dilation angle of the soil were taken to be $\phi' = 30^o$ and $\psi = 0$. Because of the assumed initial zero stresses, the drained cohesion of the soil can be calculated as $c' = s_u / Cos\phi' = 1.155\ s_u$ (see Fig. 3.7)

The diameter of the outer boundary of the soil region is D_s, with the ratio of D_s/D_p taken to be *20*, sufficient to minimize boundary effects. The outer boundary of the soil is free to drain.

In this study attention is firstly restricted to the undrained behaviour of the soil. Analyses were conducted for various numbers of wedges N in the circumferential direction (i.e. the number of modes of the discrete Fourier series). N was varied from *5* to *12*, in order to examine its effect on the numerical solution. Subsequently, the effect of drainage was studied by applying the load on the pile at different (finite) rates.

The dimensionless load deformation response of the soil is shown in Fig. 3.9 for analyses with various numbers of wedges. Although the collapse loads for models with *8*, *10* and *12* wedges are very close to each other, generally the collapse load predicted using a mesh with a small number of wedges is higher than that for a mesh with a larger number of wedges. All of the numerical solutions overestimate the failure load predicted by Randolph and Houlsby (1984). For the case of $N = 12$, the collapse load of the pile tends to approach a limiting value of about $12.9\ s_u$, which is *8%* above the theoretical solution for a rigid plastic material of $11.94\ s_u$. The collapse load was taken as the point where the slope of the load deformation curve first reaches a steady low value. A value closer to the theoretical failure load can be achieved using a finer mesh for the soil in the radial direction. By increasing the number of soil elements from *10* to *30*, the difference between the theoretical and the numerical solution reduces to *6.3%*.

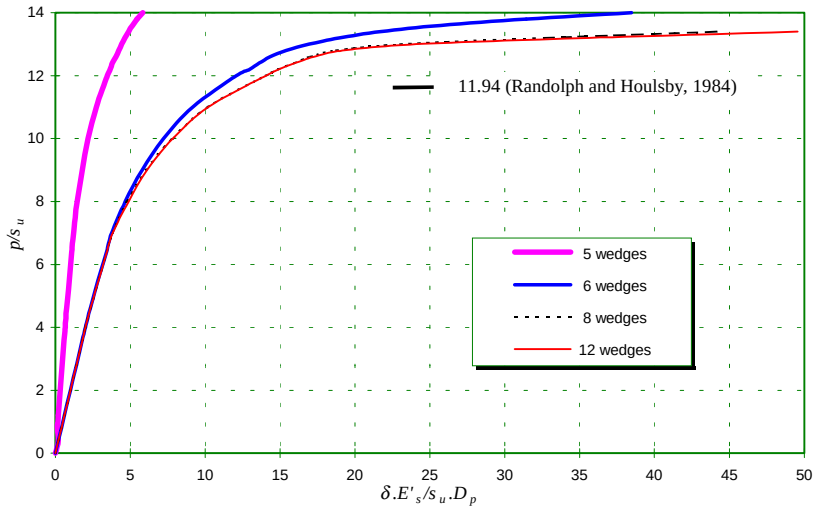

Fig. 3.9 : Load-deformation response of rigid pile, undrained condition
(δ is lateral movement of the pile)

The elasto-plastic consolidation behaviour of the soil was studied using non-dimensional load rates of $\omega=10^{7}$, *10*, *1* and 10^{-7}. For this problem the number of wedges was taken as *N=12*. The non-dimensional time factor is defined as:

$$T_v = \frac{k(1-\nu'_s)E'_s\, t}{\gamma_w(1-2\nu'_s)(1+\nu'_s)D_p^2}$$

The results of the elasto-plastic consolidation analyses with different load rates are compared in Fig. 3.10. The initial stiffness of the soil increases with an increase in the load rate, ω. Decreasing the load rate increases the ultimate lateral resistance of the pile. To approximate drained conditions, the loading rate was set to $\omega = 10^{-7}$. For this case, the ultimate resistance increases to a value of about *17.5* s_u, about *35%* above that for undrained conditions. There is no published analytical solution for a laterally loaded pile under either fully drained or partially drained conditions.

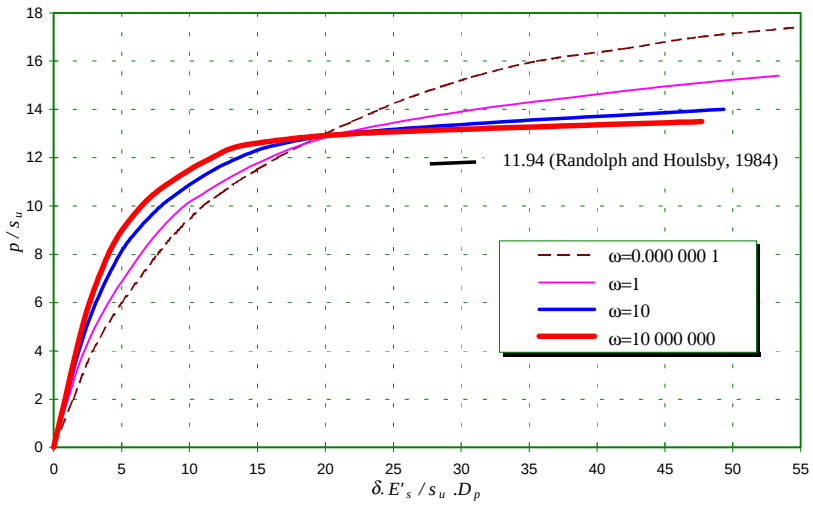

Fig. 3.10 : Load-deformation response of rigid pile, partially drained condition
(δ is lateral movement of the pile)

3.7.3. Laterally Loaded Pile in Consolidating Soil

To illustrate the accuracy of the newly developed algorithm and to demonstrate the power of the technique in a consolidation analysis, the time dependent behaviour of a vertical pile embedded in a saturated elasto-plastic soil and subjected to a lateral load applied at the mudline, is examined here. This problem was also studied by Carter and Booker (1983) for a consolidating soil with a perfectly elastic skeleton.

A pile with diameter D_p is embedded in a layer of saturated cohesionless soil which obeys the Mohr-Coulomb failure criterion. For this hypothetical problem, both associated flow rule and non-associated flow rule plasticity were considered for a purely frictional soil. The friction

angle of the soil is $\phi' = 30^o$, and the dilation angle is $\psi = 30^o$ for the associated flow rule and $\psi = 0$ for the non-associated flow rule. The soil has a saturated unit weight of $\gamma_{sat} = 1.7\gamma_w$, where γ_w is the unit weight of pore water, a Young's modulus for fully drained conditions given by $E'_s = 3000\ \gamma_w$ and a Poisson's ratio $\nu'_s = 0.30$. The initial effective stress state in the soil was assumed to be given by:

$$\sigma'_{vo} = (\gamma_{sat} - \gamma_w)\, z$$

$$\sigma'_{ro} = K_o\, \sigma'_v$$

where σ'_{vo} is the initial vertical stress, σ'_{ro} is the initial radial stress, z is the depth below the surface, and K_o is the coefficient of the lateral soil pressure, taken to be $K_o = 0.5$. The Young's modulus of the pile material is $E_p = 1000\ E'_s$. The problem was analysed assuming elastic as well as elasto-plastic models for the soil. Both associated and non-associated flow rules were assumed for the elasto-plastic models.

The dimensions of the problem are defined in Fig. 3.11, which also indicates a vertical cross-section of the finite element mesh used in the computations.

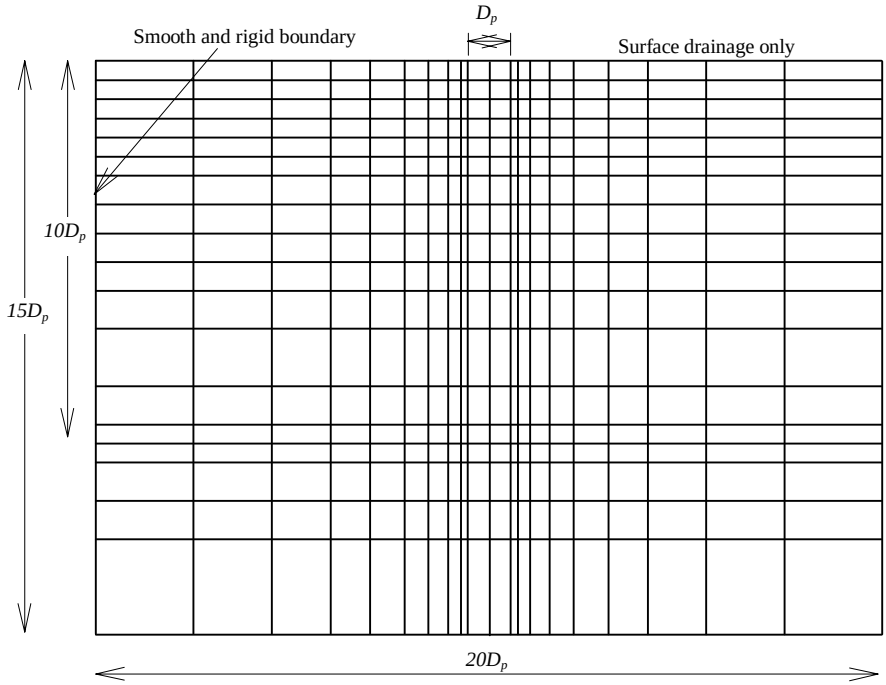

Fig. 3.11: Finite element mesh

The non-dimensional time factor and the load rate are defined here as:

$$T_v = \frac{k(1-\nu'_s)E'_s\, t}{\gamma_w(1-2\nu'_s)(1+\nu'_s)D_p^2}$$

$$\omega = \frac{d(H/\gamma_w D_p^3)}{d\,T_v}$$

An elastic analysis of the problem was conducted to evaluate the accuracy of the newly developed algorithm. Results of an analysis using the continuous Fourier series method suggested by Carter and Booker (1983) have also been obtained with both isoparametric elements and mixed elements. The mixed elements are isoparametric with respect to displacements and sub-parametric with respect to pore pressure. Mixed elements are used sometimes in consolidation analysis in order to overcome the deficiency associated with the use of small time steps at the early stage of consolidation, as explained in Appendix 3.1.

In the elastic analysis, a horizontal load, H, was applied rapidly to the pile head. Thereafter the load was held constant with time. The number of wedges used in the elastic analysis does no have any effect on the predicted responses of the pile. The predicted lateral displacements of the pile head in the direction of the applied load are plotted against dimensionless time, T_v, in Fig. 3.12. The results of the analysis using the continuous Fourier method with isoparametric elements show discrepancies of about % at the early stage of consolidation. The results of the new method of analysis using the discrete Fourier approach are in close agreement with the results of the analysis using the continuous Fourier method and the mixed type of elements, obtained independently by Carter and Booker (1983).

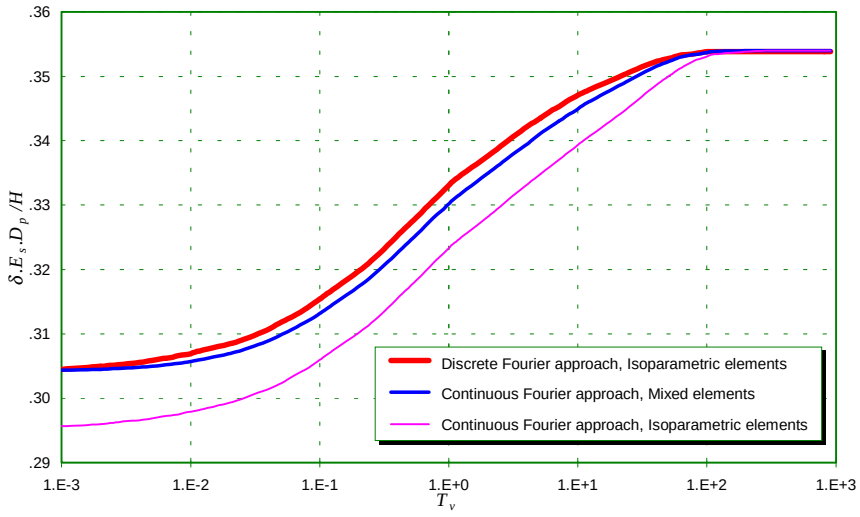

Fig. 3.12: Comparison of the lateral displacements of the pile head in elastic soil

In a series of elasto-plastic analyses, the total lateral load was varied from $H=5\gamma_w D_p^3$ to $55\gamma_w D_p^3$. In each case the total load was applied during a total time of $T_v=0.00001$, with a loading rate of $\omega=100000$. This loading rate was sufficiently high to approximate an initial undrained loading. Thereafter, the load was maintained constant with time and the analyses were continued, allowing excess pore pressures to dissipate, and thus for the soil to consolidate. All elasto-plastic analyses have been carried out using $N=12$.

The time-dependent lateral displacements of the pile head predicted by the elasto-plastic analyses with both associated and non-associated flow rules are plotted in Fig. 3.13 for the case where the horizontal load is $H = 15\gamma_w D_p^3$. Also presented in Fig. 3.13 is the response of the pile in the elastic soil. A significant dependence of the response of the pile on the assumed soil model can be observed in Fig. 3.13. The largest displacement for the pile head is predicted by the elasto-plastic soil model with a non-associated flow rule. At the end of loading, the displacement of the pile head predicted using a non-associated flow rule with $\psi = 0$ is about twice that predicted using an associated flow rule. The stiffer behaviour of a pile in soil with an associated flow rule can be attributed to the dilative characteristic of the soil after failure. Expansion of the soil increases confining pressures which in turn increase soil resistance, causing stiffer behaviour in comparison to the behaviour of soil with a non-associated flow rule and a dilation angle of $\psi = 0$.

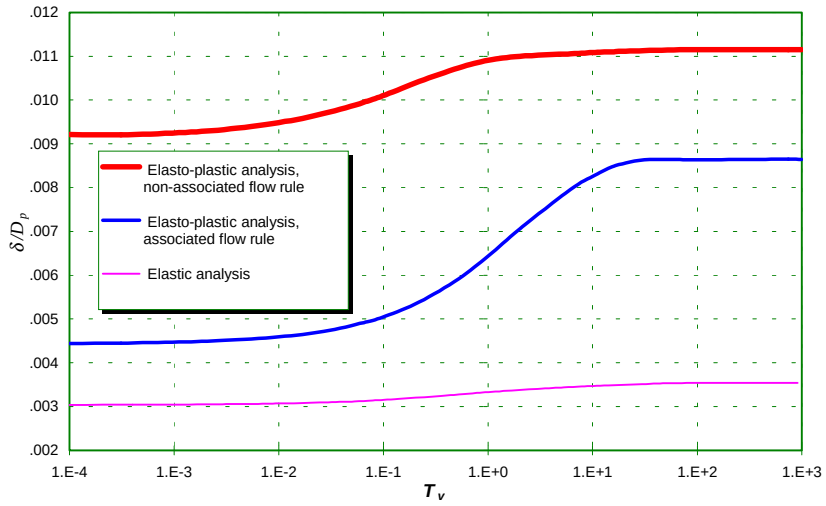

Fig. 3.13: Comparison of the lateral displacements of the pile head in elastic and elasto-plastic soils

The predicted lateral load-displacement curves for the pile head, for cases where the pile deforms under fully drained conditions, are presented in Fig. 3.14. Cases are plotted for the elasto-plastic soil model with both associated and non-associated flow rules as well as for the elastic soil model. As explained previously, the soil with an associated flow rule and dilation angle of $\psi = 30^o$ is stiffer than the soil with a non-associated flow rule and a dilation angle of $\psi = 0$.

The predicted responses of the pile in an elasto-plastic soil obeying an associated flow rule ($\phi = \psi = 30^o$) are plotted in Fig. 3.15. Lateral displacements of the pile deforming under both fully drained and rapid loading conditions followed by consolidation are presented for various horizontal load levels. The response of the pile during rapid loading is almost linear and close to the elastic responses of the piles. During consolidation under a maintained load level, the

lateral displacements of the piles increase, so that the displacements at the end of consolidation become approximately equal to the displacements predicted by the elasto-plastic analysis assuming fully drained conditions.

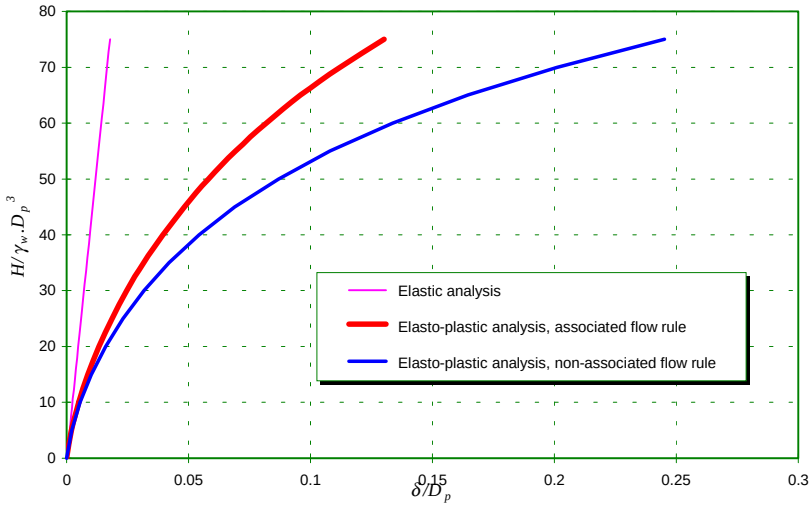

Fig. 3.14: Comparison of the pile response with different soil models, each deforming under fully drained conditions

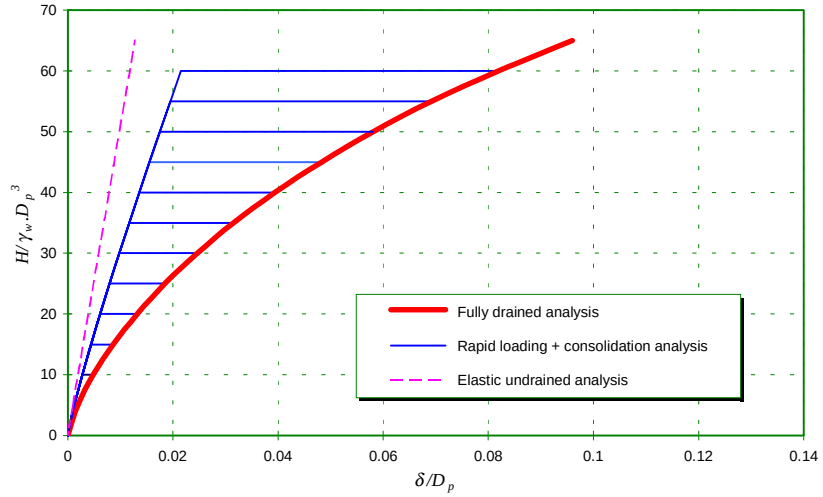

Fig. 3.15: Lateral displacement relationships for laterally loaded piles, Mohr-Coulomb soil model with associated flow rule, $\phi = \psi = 30^o$

Responses of piles in elasto-plastic soil obeying a non-associated flow rule, $\phi = 30^o$ and $\psi = 0$, deforming under both fully drained conditions and rapid loading conditions followed by consolidation are presented in Fig. 3.16. With this soil model, the responses of the piles during rapid loading are not linear. Responses of the piles during loading are very close to those corresponding to the fully drained conditions. For cases where the load is applied rapidly and then maintained, the displacements at the end of consolidation are greater than the

displacements predicted by separate analyses assuming fully drained conditions. This behaviour indicates that for a soil that obeys the Mohr-Coulomb failure criterion and a non-associated flow rule, the load path has an important influence on the final displacement of the soil, as might have been expected.

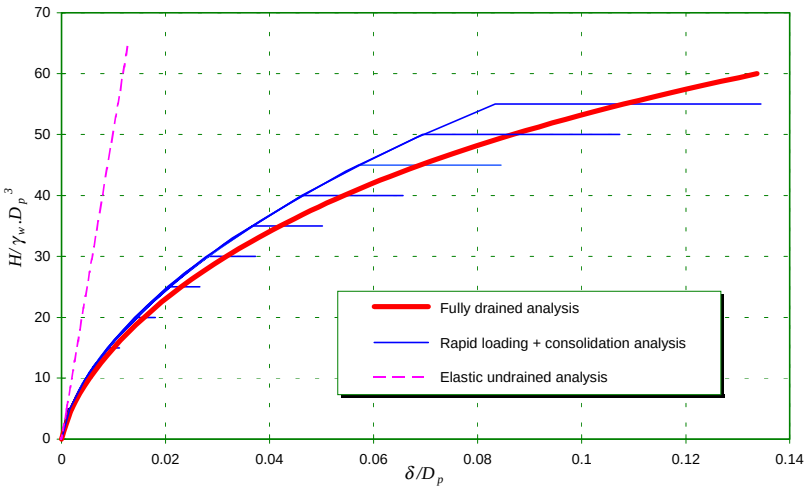

Fig. 3.16: Lateral displacement relationships for laterally loaded piles, Mohr-Coulomb soil model with non-associated flow rule, $\phi = 30^o$, $\psi = 0$

Figs 3.17 to 3.20 show the expansion of the yield zones around the piles in the plane of the applied load, for different cases of fully drained conditions, rapid loading conditions, associated flow rule plasticity and non-associated flow rule plasticity. Comparison of Fig. 3.17 and Fig. 3.18 shows that at the end of rapid loading, there is a clear difference between the plastic zones resulting from analyses using associated and non-associated flow rule plasticity models. In the case of using an associated flow rule, the plastic zones for all load levels are concentrated around the pile head and close to the soil surface. However, in the case of using a non-associated flow rule with $\psi = 0$, the plastic zone starts to expand around the pile tip at a horizontal load of approximately $H = 25\gamma_w D_p^3$, and finally it surrounds the entire pile. The results of analyses of fully drained conditions, Fig. 3.19 and Fig. 3.20, also show that the plastic zones resulting from the use of a non-associated flow rule are larger than those that resulting from the use of an associated flow rule.

Differences in the plastic zones predicted by the analyses for rapid loading conditions and for fully drained conditions can be observed by comparing Fig. 3.17 with Fig. 3.19 and Fig. 3.18 with Fig. 3.20, for an associated flow rule and a non-associated flow rule, respectively. The plastic zones are generally deeper for drained conditions. At the back of the pile, opposite to the direction of the applied horizontal load, the plastic zones are larger under undrained conditions, whereas on the other side of the pile they are slightly larger for fully drained conditions.

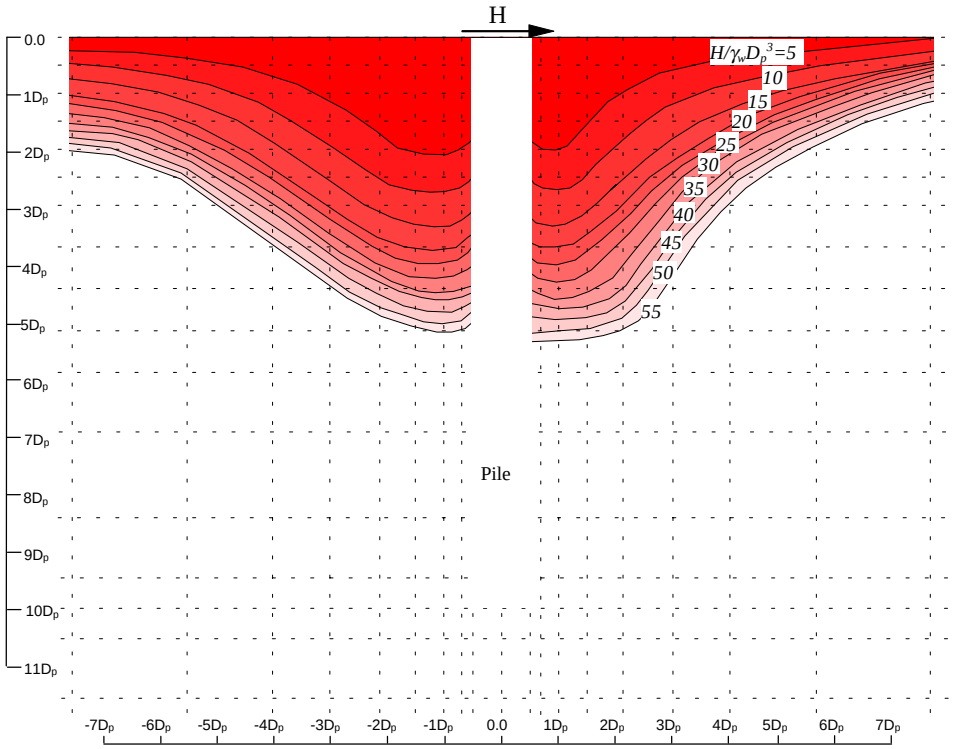

Fig. 3.17: Expansion of the plastic zone under various load levels at the end of rapid loading. Mohr-Coulomb soil model with associated flow rule, $\phi = \psi = 30^o$

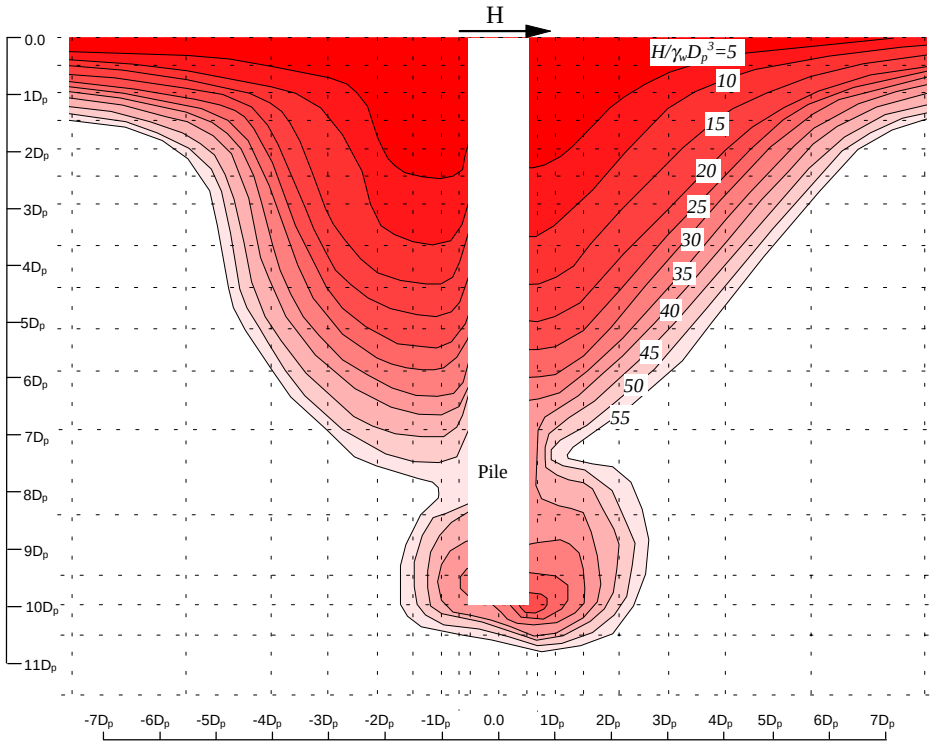

Fig. 3.18: Expansion of the plastic zone under various load levels at the end of rapid loading. Mohr-Coulomb soil model with non-associated flow rule, $\phi = 30^o$, $\psi = 0$

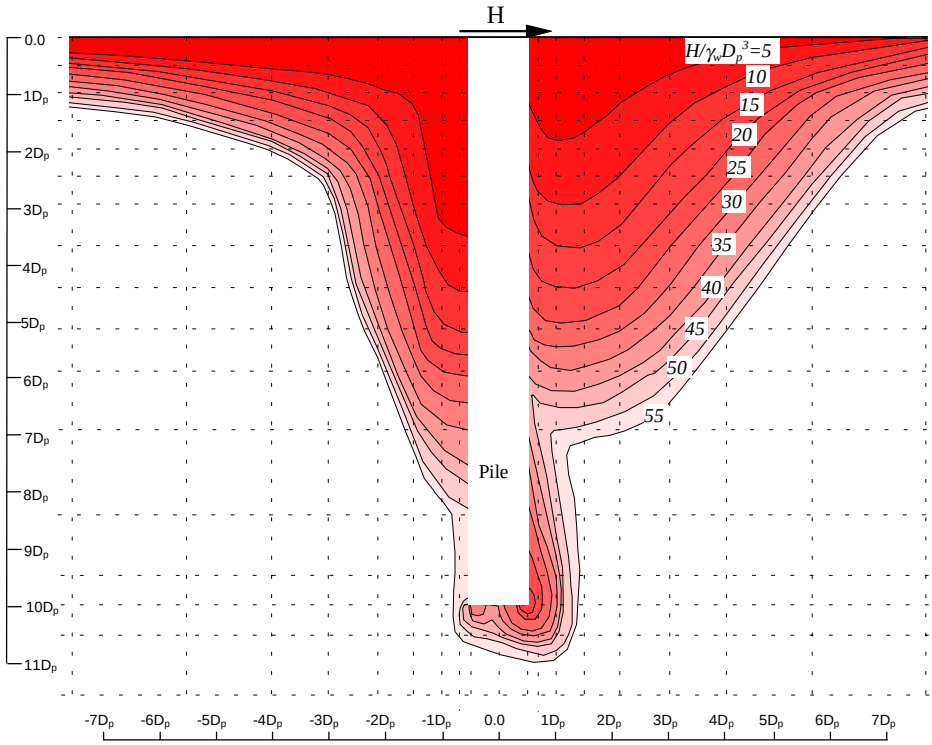

Fig. 3.19: Expansion of the plastic zone under various load levels in a fully drained analysis. Mohr-Coulomb soil model with associated flow rule, $\phi = \psi = 30^o$

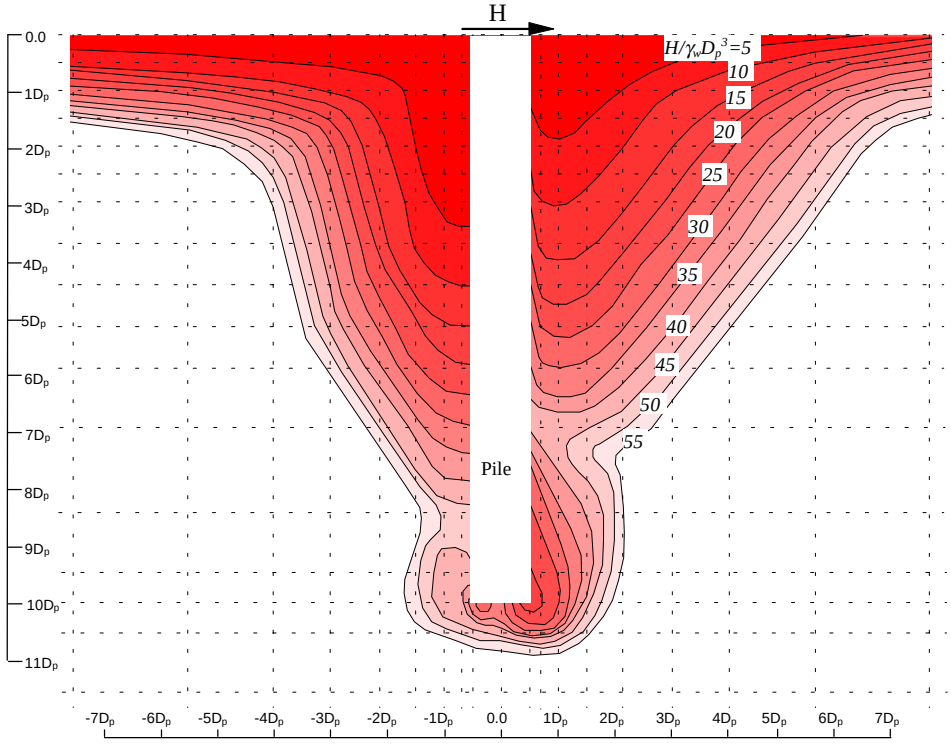

Fig. 3.20: Expansion of the plastic zone under various load levels in a fully drained analysis. Mohr-Coulomb soil model with non-associated flow rule, $\phi = 30^o$, $\psi = 0$

The difference in pile response for different plasticity models can be attributed to the differences in the stress distributions predicted for the various soil models. This is illustrated by the distributions of radial effective stresses, σ'_r, and excess pore water pressures, p, predicted by the analyses for a horizontal load of $H = 15\gamma_w D_p^3$. These distributions are illustrated in Figs 3.21 to 3.26. Both associated and non-associated flow rule plasticity models were used in the analyses for both rapid loading conditions and fully drained conditions. The plots are in the vertical plane of the applied horizontal load. The differences between the distribution of radial effective stresses at the end of rapid loading are clear. Relatively high radial effective stresses can be detected close to the pile head and at the surface of the soil when an associated flow rule is adopted.

Differences between radial stresses at the end of loading are mainly due to differences between excess pore water pressures predicted by different soil models. The highly dilative behaviour of the soil with an associated flow rule, $\psi = 30^o$, causes the plastic soil, which is close to the pile head, to expand. As a consequence, negative pore water pressures develop close to the soil surface during the period of loading. In general, the zone of negative pore water pressure predicted using an associated flow rule is greater than that predicted using a non-associated flow rule. As a result, at most times the effective stresses at any point in soil with an associated flow rule are generally greater than those predicted for a non-associated flow rule. This results in a stronger and stiffer response of the pile in the soil with the associated flow rule.

In contrast to the undrained responses described above, the final distribution of radial stresses in the drained analyses are less dependent on the choices of the flow rule (see Fig. 3.25 and Fig. 3.26).

3.8: CONCLUSIONS

An efficient formulation based on a semi-analytical finite element method was described for the analysis of consolidation of an axi-symmetric soil body subjected to three-dimensional loading. Expressing the field quantities in the form of discrete Fourier series results in a set of modal equations which can be solved separately. This has the effect of considerably reducing the necessary storage and the cost of solving three-dimensional problems. Introduction of the discrete Fourier series into finite element consolidation analysis removes the need for a fully three-dimensional finite element analysis to study time-dependent, non-linear, elasto-plastic, axi-symmetric problems.

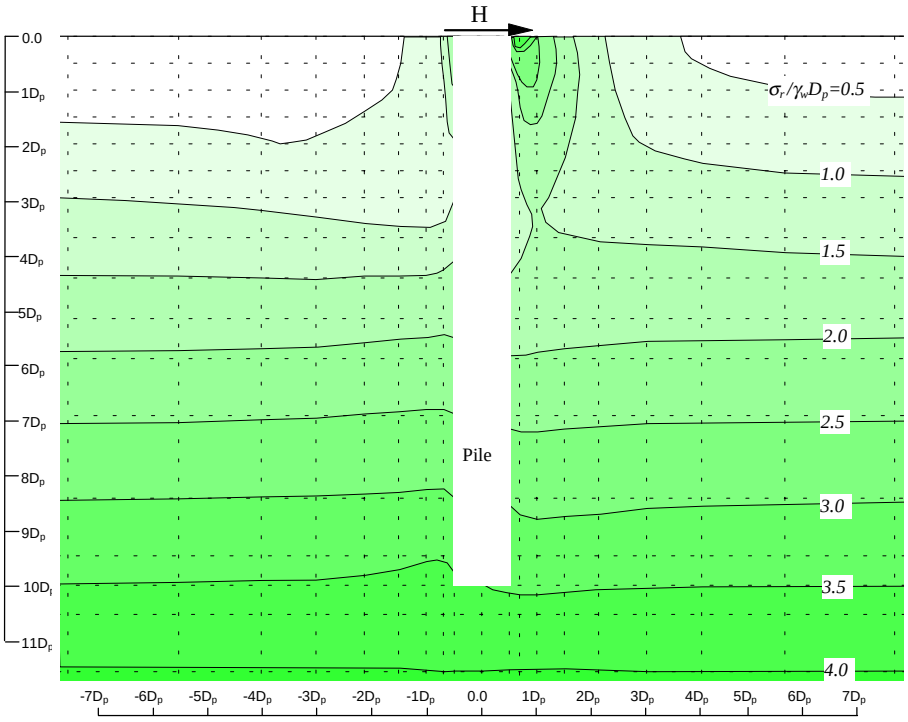

Fig. 3.21: Distribution of the radial stresses at the end of rapid loading, $H=15\gamma_w D_p^3$. Mohr-Coulomb soil model with associated flow rule, $\phi = \psi = 30^o$

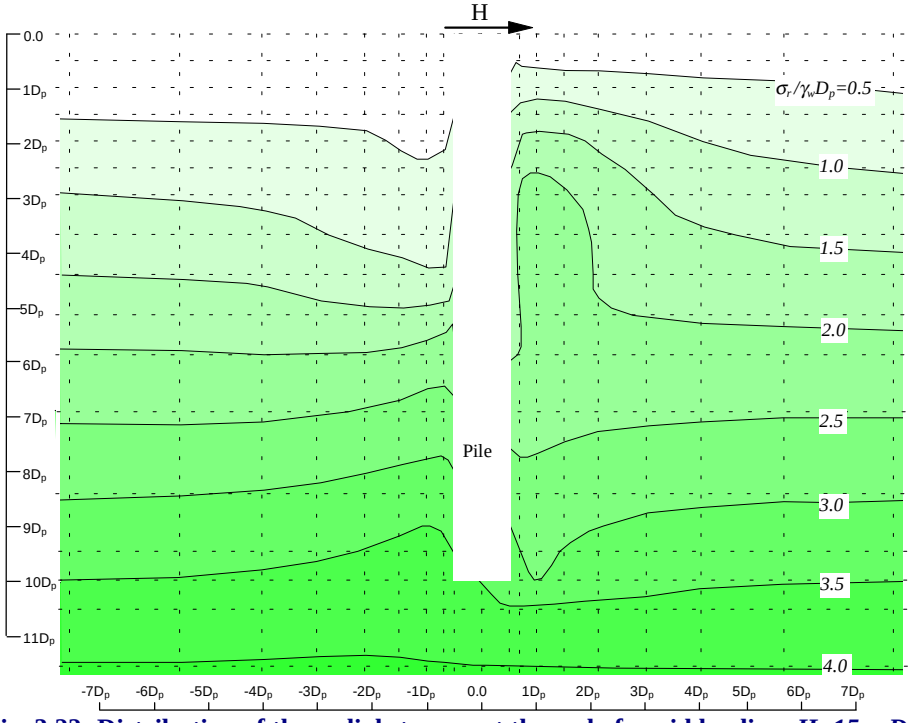

Fig. 3.22: Distribution of the radial stresses at the end of rapid loading, $H=15\gamma_w D_p^3$. Mohr-Coulomb soil model with non-associated flow rule, $\phi = 30^o$, $\psi = 0$

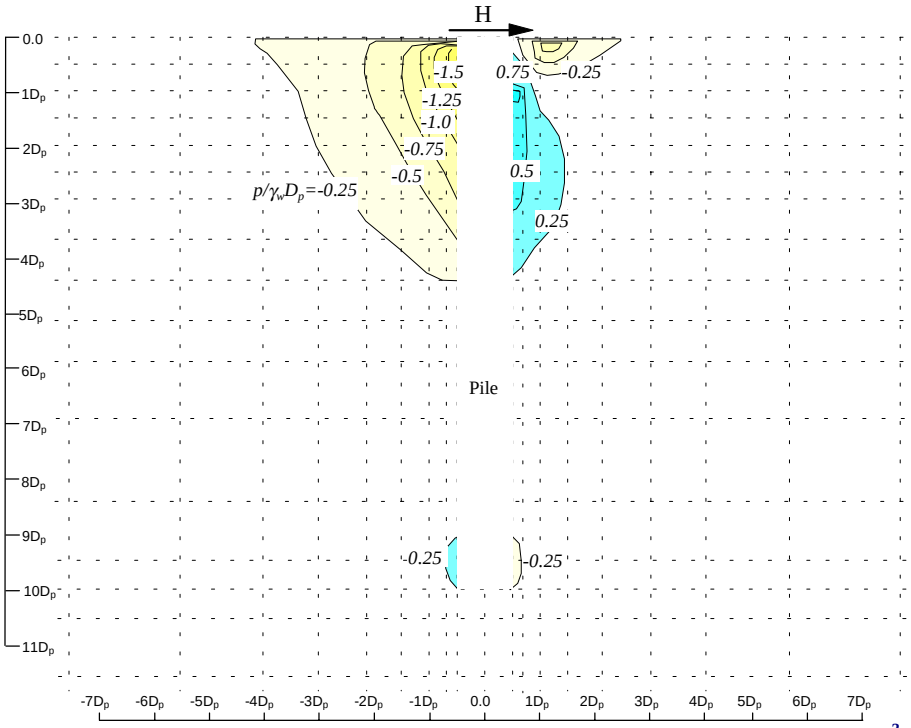

Fig. 3.23: Excess pore water pressures at the end of rapid loading, $H=15\gamma_w D_p^3$. Mohr-Coulomb soil model with associated flow rule, $\phi = \psi = 30^o$

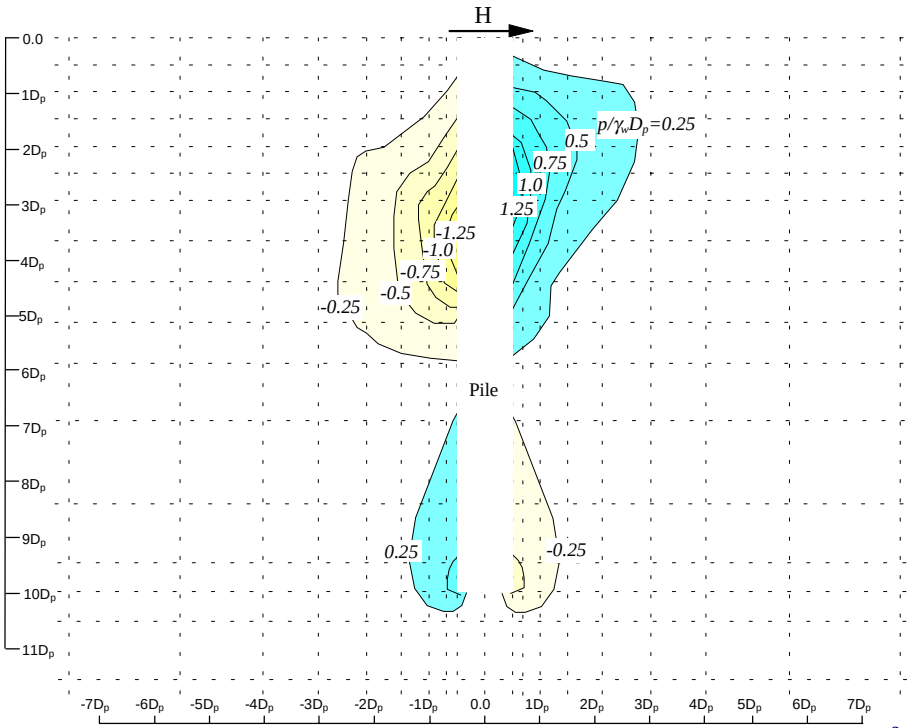

Fig. 3.24: Excess pore water pressures at the end of rapid loading, $H=15\gamma_w D_p^3$. Mohr-Coulomb soil model with non-associated flow rule, $\phi = 30^o$, $\psi = 0$

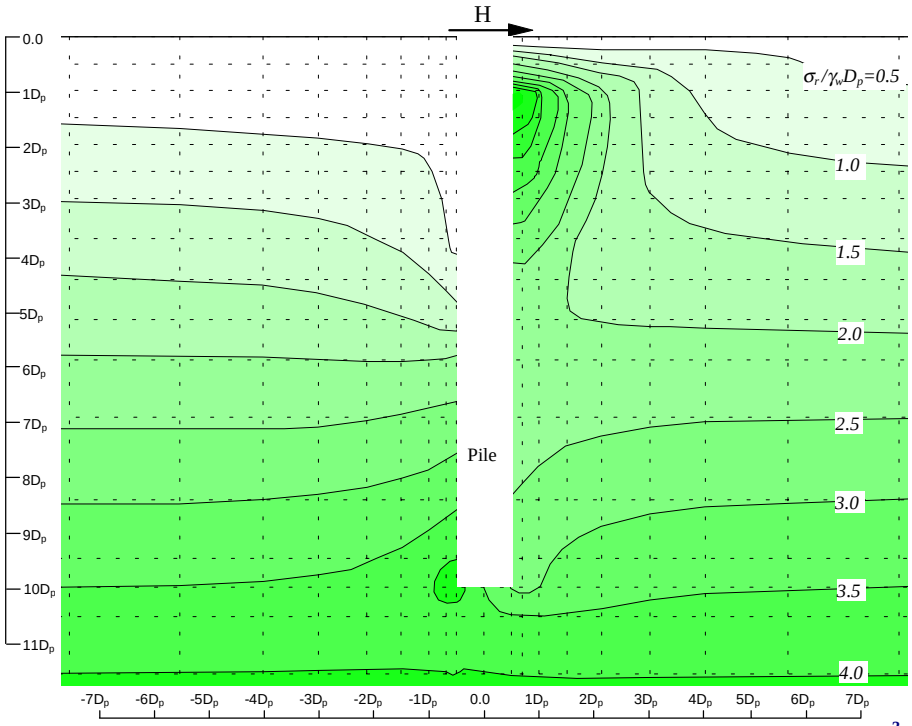

Fig. 3.25: Distribution of the radial stresses in drained conditions, $H=15\gamma_w D_p^3$. Mohr-Coulomb soil model with associated flow rule, $\phi = \psi = 30^o$

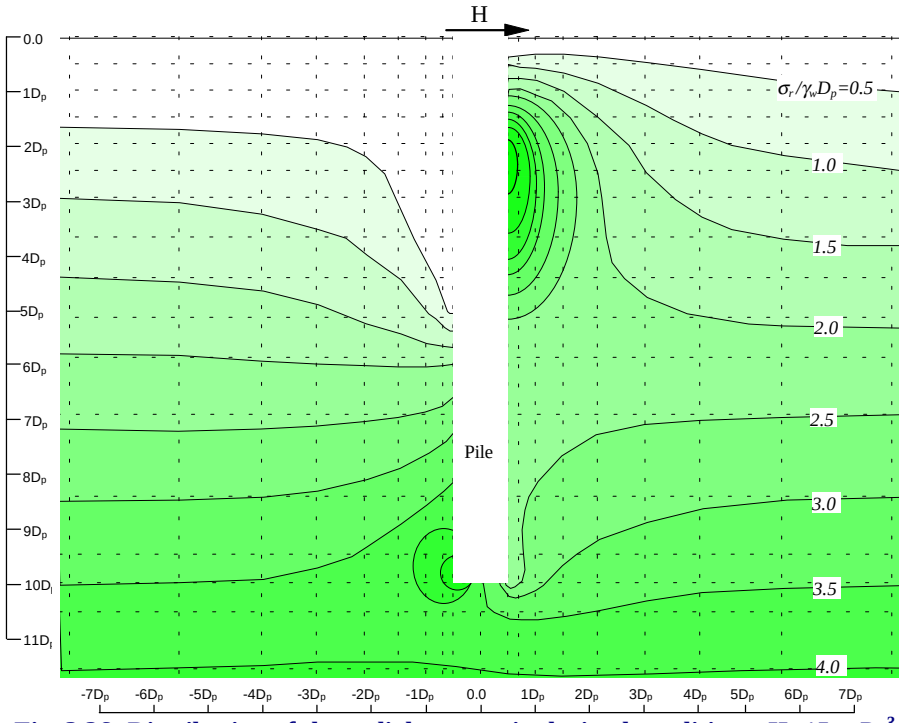

Fig. 3.26: Distribution of the radial stresses in drained conditions, $H=15\gamma_w D_p^3$. Mohr-Coulomb soil model with non-associated flow rule, $\phi = 30^o$, $\psi = 0$

The efficiency of the semi-analytical method can be demonstrated by comparing the corresponding computational time required for the direct formulation of the finite element method and that for application of the discrete Fourier series. Using the usual solution techniques with solvers which take into account the equation bandwidth, the computational time required for any formulation is approximately proportional to the number of equations times the square of the bandwidth. Therefore, the ratio of the computational time required for the two formulations can be expressed as:

$$\frac{T_{semi-analytical}}{T_{direct\ \ formulation}} \cong \frac{144 N_r^3 N_z N_d^3 (2+N)}{32 N_r^3 N_z^3 N_d^3 M} \cong \frac{9(2+N)}{2 N_z^2 N} \qquad (3.42)$$

where N_r and N_z are the number of columns and rows of the finite element mesh and N_d is the number of degree of freedom. For the mesh presented in Fig. 3.11, for example, with $N_z=18$ and $N=12$, Equation (42) shows that the computational time for the semi-analytical method reduces to about *1.6%* of the time required for the direct formulation. A solution to the elasto-plastic problem of laterally loaded pile presented in this chapter, using the semi-analytical method and a computer with Pentium-*166MHz* processor, takes less than *2* minutes for each time increment.

The capability and accuracy of the method have been demonstrated through analysis of three problems. Independent solutions are available for two of these problems and good agreement with these solutions was demonstrated. There appears to be no published solutions for laterally loaded pile foundations in consolidating elasto-plastic soil. However, application of this method to the problem of a laterally loaded pile indicates promising results.

The discrete Fourier approach in a semi-analytical finite element analysis provides an efficient and convenient tool which can be used in the analysis of some complex elasto-plastic three-dimensional problems. An important problem in soil mechanics is the bearing capacity of foundations under combined three-dimensional loading. This problem will be considered in the next chapter where the interaction of lateral load, vertical load and moment on circular foundations resting on a purely cohesive soil will be investigated. Liquefaction analysis of offshore foundations under storm loading can also be performed with this semi-analytical method of consolidation analysis. A liquefaction analysis usually needs a fine temporal discretization in which dissipation of the pore pressure generated due to wave loads is allowed. The semi-analytical method of consolidation analysis is a practical tool to tackle liquefaction problems in a three-dimensional continuum. Application of this method to the liquefaction analysis of offshore foundations will be demonstrated in Chapters 5 to 7.

Appendix **3.1**

FORMULATION OF A COUPLED FINITE ELEMENT METHOD FOR CONSOLIDATION ANALYSIS

The finite element equations of a consolidating soil can be obtained in a variety of ways, all relying on some integral statement corresponding to the equilibrium condition and the continuity of pore water. The well known general theory of three dimensional consolidation of Biot (1941) is usually applied in deriving the equations. This theory considers the elastic deformation of a porous medium and the interaction of the solid and fluid phases. Several investigators have developed methods of solving Biot's equations of consolidation by application of the finite element technique (e.g. Sandhu and Wilson, 1969, Christian and Boehmer, 1970, Small, Booker and Davis, 1976, Small and Booker, 1977 and 1982, Runesson and Booker, 1982, Carter and Booker, 1983, Hsi and Small, 1992) based on spatial as well as temporal discretization.

Coupled finite element equations for consolidation analysis can be obtained by using the principle of virtual work. For any virtual displacement, $d\delta$, the equilibrium equations and the stress boundary conditions are satisfied if :

$$\int d\varepsilon^T . \sigma . dV - \int d\delta^T . R . dV = 0 \qquad (A3.1.1)$$

Similarly, for any virtual pore pressure, dp, the assumption of continuity of pore fluid is satisfied if:

$$\int \nabla dp . v . dV - \int dp . \frac{\partial \varepsilon_v}{\partial t} . dV = 0 \qquad (A3.1.2)$$

In the above equations, ε and σ refer to strain and stress, V indicates the volume, the vector R contains the components of body forces and surface tractions, p refers to excess pore water pressures in the soil, δ refers to displacements, v are the components of superficial velocity of pore fluid flow, ε_v is volumetric strain, and t denotes time.

Introducing N_p as the shape functions for pore pressure and N_d as the shape functions for displacements, the variation of field variables can be approximated from nodal variables, i.e.

$$\delta = N_d \,.\, u$$

$$p = N_p \,.\, q$$

where u and q are the nodal displacements and nodal pore pressures, respectively.

In order to be consistent with the traditional sign convention adopted in soil mechanics, it will be assumed that both compressive stress and strain are positive. Therefore, the strains are defined by:

$$\varepsilon = - \boldsymbol{B} \,.\, u \qquad (A3.1.3)$$

$$\varepsilon_v = \varepsilon_r + \varepsilon_z + \varepsilon_{\theta\in} = -e^T.\boldsymbol{B}.u \qquad (A3.1.4)$$

and the gradients of the pore pressure by:

$$\nabla p = \left(\frac{\partial p}{\partial r}, \frac{\partial p}{\partial z}, \frac{\partial p}{\partial \theta}\right)^T = E.q \qquad (A3.1.5)$$

Darcy's law for the flow of pore fluid may be written as:

$$v = -\frac{k}{\gamma_w}\left(\frac{\partial p}{\partial r}, \frac{\partial p}{\partial z}, \frac{\partial p}{\partial \theta}\right)^T = -\frac{k}{\gamma_w}.E.q \qquad (A3.1.6)$$

In the above equations $\boldsymbol{B}$ is the matrix of strain-displacement transformations, $e=(1,1,1,0,0,0)^T$, k is the matrix of permeability coefficients, γ_w is the unit weight of pore water, and $E=(\partial N_p/\partial r, \partial N_p/\partial z, \partial N_p/\partial \theta)^T$.

Considering $\boldsymbol{D}$ as the constitutive matrix of the solid skeleton, the stress-strain relation can be written in the form

$$\sigma = \boldsymbol{D}\varepsilon + ep \qquad (A3.1.7)$$

Insertion of Equations (A3.1.3) and (A3.1.7) into the internal virtual work Equation (A3.1.1) results in:

$$d\varepsilon^T.\sigma = -du^T.\boldsymbol{B}^T.\sigma = -du^T.\boldsymbol{B}^T(\boldsymbol{D}\varepsilon + e.p) = du^T.\boldsymbol{B}^T.\boldsymbol{D}.\boldsymbol{B}^T.u - du^T.\boldsymbol{B}^T.e.N_p.q \qquad (A3.1.8)$$

Substituting Equation (A3.1.8) into (A3.1.1) gives:

$$du^T\left(\boldsymbol{K}.u - \boldsymbol{L}^T.q\right) = du^T \int N_d.R.dV \qquad (A3.1.9)$$

where $\boldsymbol{K} = \int \boldsymbol{B}^T.\boldsymbol{D}.\boldsymbol{B}.dV$

$\boldsymbol{L}^T = \int \boldsymbol{B}^T.e.N_p.dV$

Equation (A3.1.9) can be written in incremental form as:

$$du^T\left(\boldsymbol{K}.\Delta u - \boldsymbol{L}^T.\Delta q\right) = du^T \int N_d.\Delta R.dV \qquad (A3.1.10)$$

The components of Equation (A3.1.2) can also be written in the following forms:

$$\nabla dp.v = dq^T.E^T.v = -\frac{1}{\gamma_w} dq^T.E^T.k.E.q$$

$$dp.(\partial \varepsilon_v / \partial t) = dq.N_p.e^T.\boldsymbol{B}.(\partial u / \partial t)$$

As a result, Equation (A3.1.2) becomes

$$\int \nabla dp.v.dV - \int dp.\frac{\partial \varepsilon_v}{\partial t}.dV = -dq^T\left(\boldsymbol{\Phi}.q + L.\frac{\partial u}{\partial t}\right) = 0 \qquad (A3.1.11)$$

where $\boldsymbol{\Phi} = \frac{1}{\gamma_w}\int E^T.k.E.dV$

Equation (A3.1.11) can be integrated with respect to time by using an approximate single step integration rule, i.e.

$$\int_t^{t+\Delta t} q.dt = \Delta t\left[(1-\beta).q_t + \beta.q_{t+\Delta t}\right] = \Delta t\left(q_t + \beta.\Delta q\right)$$

where Δt is the increment of time over which the integration is performed, q_t is the value of pore pressure at the beginning of the current increment, and β is a parameter which corresponds to the particular interpolation, with $\beta = 0$ forward interpolation, $\beta = 0.5$ linear interpolation, $\beta = 1$ backward interpolation, $\beta = 2/3$ parabolic interpolation, etc.

By application of this integration rule, Equation (A3.1.11) becomes:

$$dq^T(-L.\Delta u - \Delta t.\beta.\boldsymbol{\Phi}.\Delta q) = dq^T(\Delta t.\boldsymbol{\Phi}.q_t) \qquad (A3.1.12)$$

A combination of Equations (A3.1.10) and (A3.1.12) results in a coupled set of equations of virtual work for consolidation analysis, i.e.

$$\begin{pmatrix} du^T & , & dq^T \end{pmatrix}\begin{pmatrix} \boldsymbol{K} & -\boldsymbol{L}^T \\ -\boldsymbol{L} & -\Delta t.\beta.\boldsymbol{\Phi} \end{pmatrix}\begin{pmatrix} \Delta u \\ \Delta q \end{pmatrix} = \begin{pmatrix} du^T & , & dq^T \end{pmatrix}\begin{pmatrix} f_R \\ f_p \end{pmatrix} \qquad (A3.1.13)$$

where $f_R = \int N_d.\Delta R.dV$

$f_p = \Delta t.\boldsymbol{\Phi}.q_t$

Equation (A3.1.13) is true for any arbitrary variations of virtual nodal values of displacements and pore pressures, thus:

$$\begin{pmatrix} \boldsymbol{K} & -\boldsymbol{L}^T \\ -\boldsymbol{L} & -\Delta t.\beta.\boldsymbol{\Phi} \end{pmatrix}\begin{pmatrix} \Delta u \\ \Delta q \end{pmatrix} = \begin{pmatrix} f_R \\ f_p \end{pmatrix} \qquad (A3.1.14)$$

A solution to Equation (A3.1.14) gives the increments in the nodal variables over any time increment Δt. If the nodal variables are known at time t_1, they can be found at time $t_2 = t_1 + \Delta t$ and so the solution can be marched forward in time in the usual way.

The conditions of stability and accuracy of the consolidation algorithm have been examined by many researchers, among them Booker and Small (1975), Sandhu *et al.* (1977), Vermeer and Verruijt (1981) and Reed (1984). Booker and Small (1975) have examined the algorithm for a time integration involving the parameter β, and concluded that the process is unconditionally stable for $\beta \geq 0.5$. Sandhu *et al.* (1977) examined several integration algorithms in the time domain. They have shown that in temporal meshes involving drastic changes in the size of the time step, the error in pore pressure estimation is associated with the use of $\beta = 0.5$. In the current study a temporal integration with $\beta = 1$ (implicit Euler backward interpolation method) is used for all analyses.

It is generally understood that the accuracy of the consolidation algorithms increases as the time steps decrease in magnitude. However, the consolidation analysis often exhibits oscillation of pore pressures, which tend to increase when the time steps are reduced. Sandhu *et al.* (1977) noted that the elements which are isoparametric with respect to both displacements and pore pressure, can have this type of deficiency. This deficiency was also verified by Nishizaki *et al.* (1982), who made comparative studies of the numerical performance of various element types. They also found that the accuracy in pore pressures at the early stage of consolidation will improve if elements which are isoparametric with respect to displacements but sub-parametric with respect to pore pressure are used. However, the isoparametric elements gave the most satisfactory results regarding settlement. Reed (1984) developed a smoothing technique to remove the oscillatory errors in initial pore pressures, associated with the use of isoparametric elements. Vermeer and Verruijt (1981) showed that there is a lower limit for the time steps, below which spatial oscillations will occur. For a uniform mesh of elements of length Δh, the lower bound for the time step in terms of the coefficient of one dimensional consolidation c_v was presented as:

$$\Delta t \geq \frac{(\Delta h)^2}{6\beta c_v}$$

Thus a solution for very small time steps will require a fine mesh to be used.

In the current study, the quadratic isoparametric element is used in modelling consolidating soil. Attention will be focused on the use of suitable mesh when the values of pore pressures are required at the early stages of consolidation.

Appendix 3.2

VALIDATION OF THE PSEUDO RESIDUAL FORCE METHOD IN ANALYSIS OF AN ELASTO-PLASTIC MEDIUM

In the formulation of the new algorithm for the solution of non-linear problems, an approximation has been made in Equation (3.39), when the vector of unknown incremental displacements, Δn_i, is replaced by the previous incremental displacements, Δn_{i-1}. This approximation may affect the result of the analysis in cases where the difference between values of a nodal variable for two consecutive increments becomes large. This condition arises when, for instance, the load steps or time steps of consecutive increments vary from a large value to a small value. In this appendix, the effects of the approximation on the numerical results will be examined in more detail.

The validation of the new solution algorithm is demonstrated by the analysis of a simple axi-symmetric problem. The results obtained from the new solution scheme are compared with the results from a conventional finite element program. The effect of variable time steps on the results is also evaluated. The advantages of the new method over the initial stiffness method are demonstrated. Finally, the shortcomings of the new method in iterative solution schemes are described.

The problem considered is a circular footing resting on a layer of over-consolidated clay (AFENA Users' Manual, Carter and Balaam, 1995 and also Britto and Gunn, 1987, p. 406). The soil skeleton was idealised using the Modified Cam-Clay constitutive model. The following parameters were used to represent the mechanical behaviour of the soil material in this problem.

Strength parameter	$M = 0.888$
Plastic consolidation parameter	$\lambda = 0.161$
Elastic consolidation parameter	$\kappa = 0.062$
Critical void ratio at $p'=1$ kPa	$e_{cs} = 1.789$
Poisson's ratio	$\nu' = 0.25$
Permeability (isotropic)	$k = 0.05$ m/sec

It was assumed that the upper *1 m* of the clay layer is heavily over-consolidated while the underlying material is more lightly over-consolidated. The variation of initial horizontal effective stress, σ'_{ro}, was related to the initial vertical effective stress, σ'_{vo}, as follows:

$\sigma'_{ro}=1.99\ \sigma'_{vo}$ for depth up to *1 m*

$\sigma'_{ro}=13.89+0.601\ \sigma'_{vo}$ for depth below *1 m*

The unit weight of pore water was assumed to be $\gamma_w = 10\ kN/m^3$ and the saturated unit weight of the soil to be $\gamma_{sat} = 20\ kN/m^3$. It was also assumed that the maximum value of effective overburden pressure was *50 kPa* higher in the past at all horizons in the current soil layer. Thus, the initial size of the elliptical yield locus was defined with a mean effective stress as $p'_c = 50\ kPa + (\gamma_{sat} - \gamma_w) \times z$, where z is the depth below the soil surface. A uniform normal pressure of *100 kPa* was applied over a circle of radius *4 m* on the surface of the clay layer. The mesh used for this problem is illustrated in Fig. A3.2.1.

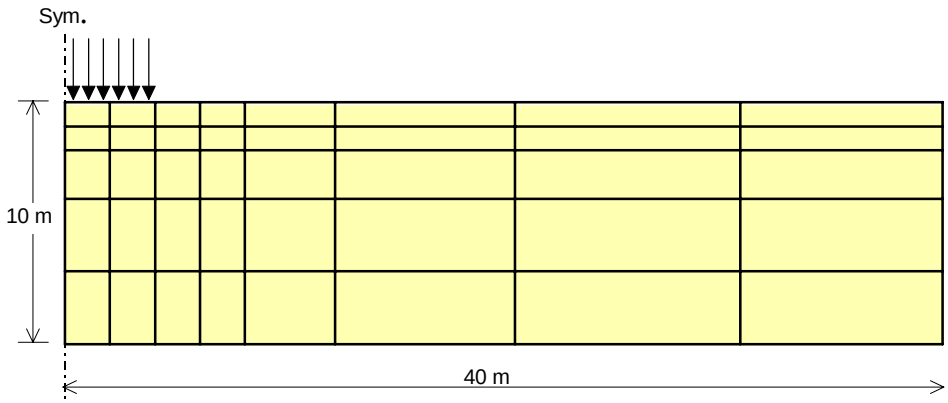

Fig. A3.2.1: Axi-symmetric mesh for circular footing on Modified Cam-Clay

A time marching scheme was used in the analysis of the consolidation problem, with a time interval of Δt. In the case of the analysis of fully drained conditions, a load increment process was adopted, with a load increment Δp. Load step Δp and time step Δt were varied for the different analyses.

A3.2.1: Comparison of Results

In this section the results of the analysis using the new method are compared with the result of a tangent stiffness method, obtained from the finite element code 'AFENA' (Carter and Balaam, 1995), employing conventional axi-symmetric consolidation elements.

The intensity of the uniform loading was assumed to increase linearly with time so that a maximum load of *100 kPa* was applied in *40* equal increments during a total period of one second. The analysis was continued beyond this time with longer time steps to allow any excess pore pressures generated by loading to dissipate, and thus for the soil to consolidate.

The predicted load-displacement curves for this problem are plotted in Fig. A3.2.2. The results of the new method are in good agreement with the results obtained from 'AFENA'. At higher load levels the displacements predicted by the new method are slightly less than those predicted by 'AFENA'. However, the final settlement of both analyses is very close, with only *3%* difference.

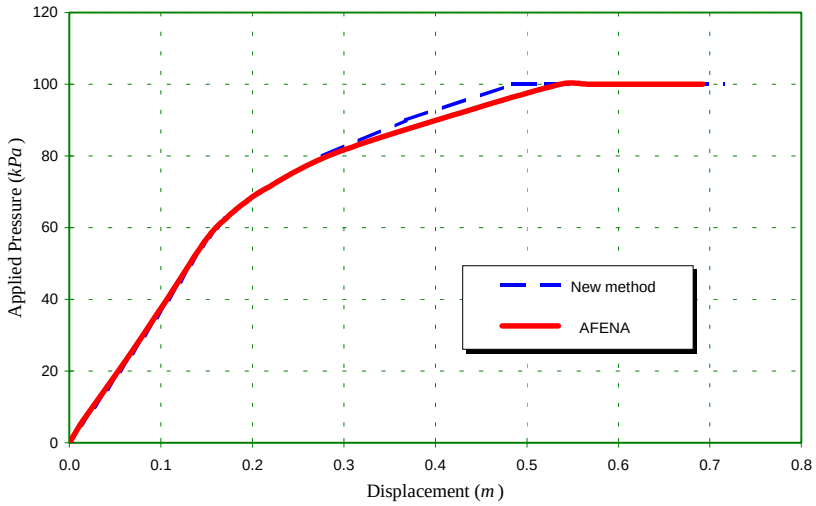

Fig. A3.2.2: Comparison of the results obtained from the new method and the results obtained from AFENA.

A3.2.2: Effects of Variable Time Steps or Load Steps

In this section, the problem of A3.2.1 was re-analysed using a variety of time steps. In one analysis the time steps were changed repeatedly in consecutive time steps from $\Delta t=0.025\ sec$ to $\Delta t=0.10\ sec$. Two separate analyses were also performed using constant time steps of $\Delta t=0.025\ sec$ and $\Delta t=0.10\ sec$. The load was applied to the surface of the soil layer at a rate of $100\times t$. The results of the analysis with varying time steps are compared with those of analyses with constant time steps in Fig. A3.2.3.

The same problem was also analysed for fully drained conditions using a load increment process. In one analysis the load steps were changed repeatedly in consecutive load steps from $\Delta p=2.5\ kPa$ to $\Delta p=10\ kPa$. Two other analyses were performed using constant load steps of $\Delta p=2.5\ kPa$ and $\Delta p=10\ kPa$. The results are compared in Fig. A3.2.4.

The analyses with the smaller constant time or load steps give more accurate results, since during the analysis the non-linear material parameters are updated more frequently, and therefore drift from the yield surface is less than in cases with larger time or load steps. The analysis with varying time or load steps results in a fluctuating load-deflection curve. This behaviour is as a result of the approximation made in Equation (3.39). However, from Figs A3.2.3 and A3.2.4, it is clear that the results are in a range between the two extreme

cases obtained using constant time or load steps. This indicates that the results of the new algorithm can be regarded as reliable even in cases where variable time steps and load steps are used.

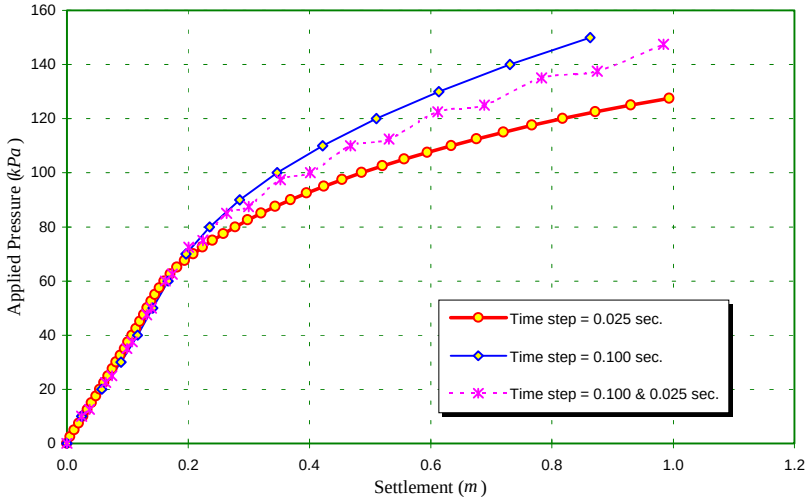

Fig. A3.2.3: The effect of varying time steps on the results of a consolidation analysis.

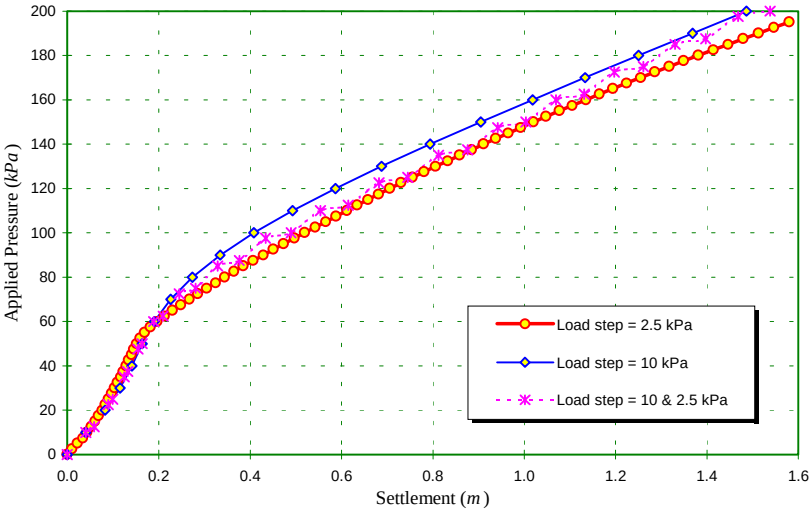

Fig. A3.2.4: The effect of varying time steps on the results of a drained analysis.

It is perhaps worthwhile to mention that there should be a unique curve for the drained cases with constant load steps. The fact that there are small differences can be attributed to finite step size (see Fig. 3.3 to 3.5). However, in consolidation analyses, the curves are not necessarily the same because the loading rate is varied.

A3.2.3: Advantages of the New Method Over the Initial Stiffness Method

In order to show the advantages of the new method over the initial stiffness method, the previous example was analysed using different solution algorithms, viz. the new method, the initial stiffness method, and the tangent stiffness method. Equal time steps and load steps were

used in all of the analyses. To magnify the differences obtainable with the different algorithms, the time step and load step were deliberately chosen to be very large, i.e. $\Delta p=2.5\ kPa$ and $\Delta t=0.025\ sec$. In the consolidation analyses, the load was applied to the surface of the soil layer at a rate of $100\times t$. The results of the analyses are compared in Figs A3.2.5 and A3.2.6, for the consolidation and fully drained analyses, respectively.

The tangent stiffness method obviously gives a more accurate result compared to the initial stiffness method, because in the tangent stiffness method the material parameters, and therefore the stiffness matrix, are updated at each time step or load step. It can be seen that the results of analyses with the new method are very close to the more accurate solution of the tangent stiffness method. For the same step sizes, the results of analysis with the initial stiffness method are less accurate than the results of the new method.

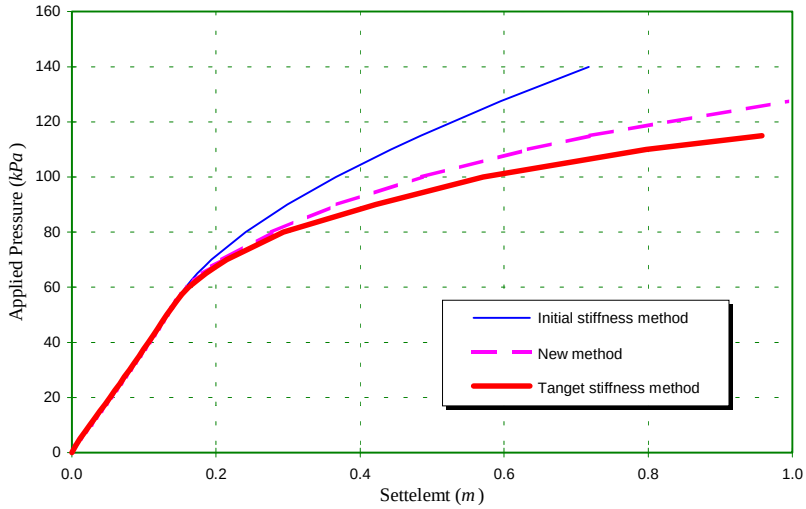

Fig. A3.2.5: Comparison of the results of different solution schemes in a consolidation analysis.

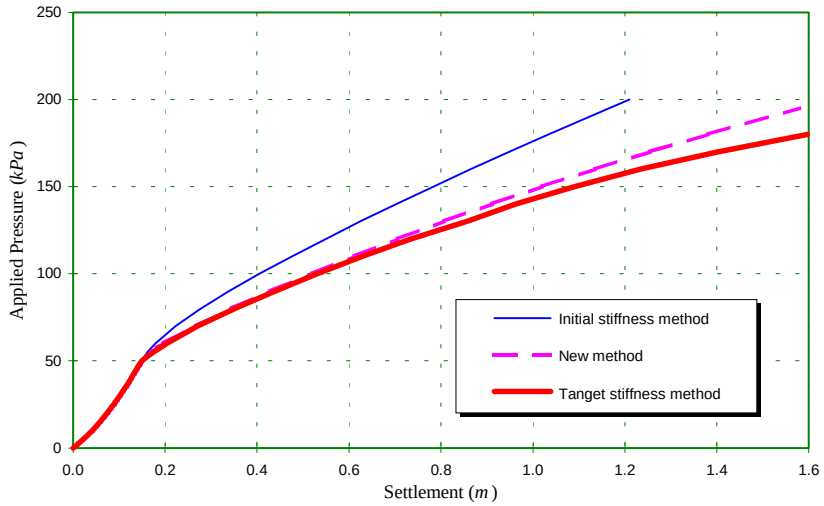

Fig. A3.2.6: Comparison of the results of different solution schemes in a drained analysis.

A3.2.4: Deficiency of the New Method in an Iterative Solution Procedure

The new method has no particular advantage over other methods of analysis if iterative techniques are used to solve the non-linear equations. To illustrate a particular deficiency of the new method in an iterative solution algorithm, the previous example problem was analysed for fully drained conditions with a single load increment of *50 kPa*. The load was then increased to *100 kPa* in one step. The displacements at the centre of loading at any iteration are compared in Fig. A3.2.7 with the displacements of the same point obtained using the initial stiffness method. It can be seen that for the new method the number of increments required for convergence is not less than the number required for the initial stiffness method. The reason for this deficiency can be explained as follows. In Equation (3.39) an approximation has been made where the unknown incremental displacements, Δn_i, are replaced by the previous incremental displacements, Δn_{i-1}. A solution to the problem after the application of any load increment results in a relatively large displacement, Δn_1, compared to the incremental displacements from subsequent iterations at constant load, i.e. $\Delta n_{2, 3, ..}$. In the second iteration after the application of the load increment, Δn_1 will be used instead of Δn_2 in Equation (3.39) to evaluate the pseudo residual force. Using Δn_1, which is much greater than Δn_2, adds a relatively large pseudo residual force to the unbalanced force vector and therefore, the solution algorithm results in another large incremental displacement which is, of course, not correct. This deficiency vanishes after a few iterations.

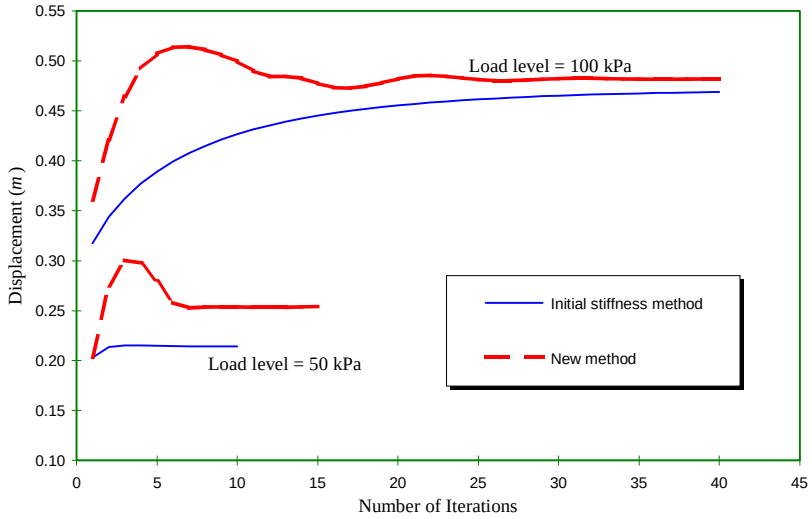

Fig. A3.2.7: Rate of convergence for different methods of non-linear analysis in an iterative process.

Chapter 4

BEARING CAPACITY OF OFFSHORE SHALLOW FOUNDATIONS ON COHESIVE SOILS

4.1: INTRODUCTION

Many offshore structures are founded on shallow foundations. Examples range from mobile drilling rigs, such as jackups with spudcan foundations and submersible platforms with bearing pads, to production structures, such as steel piled jackets with temporary 'mudmat' support and gravity structures with multiple footings. These structures are typically subjected to large vertical loads of self weight, equipment, etc., and large lateral loads and overturning moments due to waves, winds, currents, earthquakes, etc. The loads are transferred to the seabed by shallow foundations of circular or polygonal shape. One especially important aspect of the behaviour of these structures is the ultimate bearing capacity of their foundation.

Numerical analysis of circular foundations subjected to combinations of moment, vertical and lateral forces is considered in this chapter. Only the simple case of foundations on homogeneous soil and undrained conditions is studied. It is also assumed that the soil-foundation interface provides uplift resistance due to the suctions developed during undrained uplift loading. Emphasis is on the effects of lateral force and moment on the vertical bearing capacity of foundations. The results of the numerical analysis are presented in the form of interaction diagrams in moment, horizontal load and vertical load space as well as a simple mathematical expression for the failure locus. This study also provides an insight into the modes of failure of circular foundations under various combinations of loads. Except where otherwise stated, all of the theoretical and experimental relationships given here are simplified for homogeneous purely cohesive soil.

It should be mentioned that the aims of this study are not only to determine equations for bearing capacity, but also to demonstrate the accuracy, the efficiency and the power of the analytical tool described in Chapter 3.

4.2: AVAILABLE BEARING CAPACITY EQUATIONS

The bearing capacity of foundations is one of the main subjects in soil mechanics and foundation engineering. There is extensive literature dealing with the bearing capacity of foundations, both theoretically and experimentally. A list of principal contributions to this subject can be found in Vesic (1973), Chen and McCarron (1991), and Tani and Craig (1995). Most of the design methods for estimating bearing capacity are based on the original studies of a strip punch by Prandtl (1921) and Reissner (1924), modified to accommodate the conditions not included in the Prandtl-Reissner solution, such as load inclination, footing shape, etc. The modifications are usually based on either limit equilibrium analyses or empirical approaches. These conventional design methods provide simple and effective tools for estimation of the bearing capacity of foundations of regular shape and relatively simple modes of loading. However, for more complex foundations under substantial moment and lateral load, or foundations on non-homogeneous soil, the conventional equations may not provide theoretically or practically reliable solutions. In these cases, more reliable solutions may be obtained by defining failure loci and interaction equations for foundations. A failure locus defines the load conditions under which failure of a foundation will occur.

4.2.1: Conventional Bearing Capacity Equations

The conventional bearing capacity equations (e.g., Vesic, 1975; Bowles, 1982; Chen and McCarron, 1991) are generally used to evaluate the stability of foundations against static bearing failure, provided that the underlying soil profile can be suitably characterized as a homogeneous material. For the short term stability problem of saturated clay, the undrained condition can reasonably be assumed for carrying out a total stress analysis. Hence, a cohesion equivalent to the undrained shear strength of the soil, $c = s_u$, together with a zero internal friction angle, $\phi = 0^o$, can be used in the evaluation. For these conditions, the bearing capacity of a rigid surface foundation subjected to a vertical loading may be expressed (approximately) as (Vesic, 1975):

$$V_u = s_u \, N_c \, \zeta_s \, \zeta_e \, \zeta_i \, A \qquad (4.1)$$

Where V_u is the ultimate vertical load on the foundation, N_c is the dimensionless bearing capacity factor for cohesion, ζ_s is the factor which considers the effects of foundation shape and ζ_e and ζ_i are factors which consider the effects of load eccentricity and load inclination, and A is the contact area of the foundation.

The bearing capacity factor N_c for a long rectangular foundation has been determined by Prandtl (1921) and Reissner (1924) (quoted by Vesic, 1973) using the theory of plasticity. A value of $N_c = 2 + \pi$ is now generally accepted in foundation engineering practice for a long strip footing.

The values of shape factor, ζ_s, for a circular footing vary from *1.1* (e.g. Meyerhof, 1980) to *1.3* (e.g., Terzaghi and Peck, 1948). A widely used expression for the shape factor (Vesic, 1975) suggests a value of *1.2* for a circular footing. Therefore, the ultimate bearing capacity of circular foundations on clay under a central-vertical load, V_u, is conventionally calculated as:

$$\frac{V_u}{A} = 1.2(2+\pi)s_u \approx 6.17 s_u \qquad (4.2)$$

For foundations subjected to eccentric inclined load, the common practice is to resolve this load into two parts, an eccentric vertical load and a central inclined load. The bearing capacity of the footing is then obtained by analysing the problem in two separate parts. Eccentricity is treated using reduced dimensions for the foundation by introducing a fictitious effective area of the foundation on which the eccentric vertical load is assumed to act centrally. Based on this assumption, the interaction diagram for vertical load and moment is a simple parabolic curve. Vesic (1975) has presented an approximate expression for the inclination factor ζ_i for square and rectangular foundations subjected to vertical and horizontal loads. Considering the shape factor, the inclination factor and the effect of eccentricity, the vertical bearing capacity, *V*, of a rectangular foundation subjected to horizontal load, *H*, can be obtained as:

$$\frac{V_u}{B'L'} = \left(1+\frac{B'/L'}{2+\pi}\right)\left(1-\frac{\frac{2+B'/L'}{1+B'/L'}H}{(2+\pi)s_u B'L'}\right)(2+\pi)s_u \qquad (4.3)$$

where B' and L' are the dimensions of the fictitious effective area of the foundation. There is no explicit expression to evaluate the effects of an eccentric-inclined load for a circular foundation. Use of an equivalent dimension for a circular footing in the above equation will increase the degree of uncertainty of the bearing capacity equation which already suffers from the approximations due to eccentricity, shape factor and inclination factor.

Bolton (1979) presented a theoretical expression for the vertical capacity of a strip footing subjected to inclined load as follows.

$$\frac{V}{A} = s_u\left(1+\pi - Arc\sin\frac{H}{As_u} + \sqrt{1-\frac{H}{As_u}}\right) \qquad (4.4)$$

Theoretical analysis of foundations subjected to both eccentric and inclined load was first presented by Saran and Agrawal (1991). Their studies on shallow strip foundations with a rough base resulted in a series of charts expressing the bearing capacity factor, N_c, in terms of load eccentricity and the load inclination angle. However, there is no mention of the possible application of their results for circular footings.

4.2.2: Interaction Equations and Failure Locus

For any foundation, there is a three-dimensional surface, independent of load path, containing all combinations of loads, *V*, *H*, and *M*, that represents a failure envelope for the foundation. The failure envelope also represents the bearing capacity equation and can be written in the form of:

$$f(V, H, M)=0 \qquad (4.5)$$

where *V*, *H* and *M* are vertical load, horizontal load and overturning moment on the foundation at failure. Any combination of loads inside the failure locus can be regarded as a safe load combination for the foundation. This hypothesis has been supported at model scale by a large number of experiments on shallow footings on sand by Butterfield and Gottardi (1994). They have also shown that a simple three-dimensional envelope in *V*, *H*, and *M* space exists that locates the end points of all conceivable load paths to the failure of a footing. The failure locus for strip footings was presented in the form of:

$$f(V,H,M)=\left(\frac{H}{\alpha_1 V_u}\right)^2+\left(\frac{M}{\alpha_2 B V_u}\right)^2-\frac{\alpha_3 H.M}{\alpha_1\alpha_2 B V_u^2}-\left(\frac{V}{V_u}\left(1-\frac{V}{V_u}\right)\right)^2=0 \qquad (4.6)$$

where V_u is the ultimate bearing capacity of foundation under central vertical load, *B* is the breadth of the footing and α_1 to α_3 are constants, obtained from the experimental results as $\alpha_1 = 0.52$, $\alpha_2 = 0.35$, and $\alpha_3 = 0.44$. The failure locus in the *V*-*H* plane or the *V*-*M* plane is a parabolic curve whereas on the *H*-*M* plane, at $V/V_u = 0.5$, the failure locus is an ellipse rotated through an angle of 13^o from the *H* axis toward the negative direction of the *M* axis.

Martin (1994) presented a failure locus for spudcan footings on cohesive soil as:

$$f(V,H,M)=\left(\frac{H}{H_0}\right)^2+\left(\frac{M}{M_0}\right)^2-\left(\alpha_1+\alpha_2\frac{V}{V_u}\left(\frac{V}{V_u}-1\right)\right)\left(\frac{HM}{H_0 M_0}\right)-\alpha_3\left(\frac{V}{V_u}\right)^{\alpha_4}\left(1-\frac{V}{V_u}\right)^{\alpha_5}=0 \qquad (4.7)$$

where H_0 is the maximum horizontal load in the absence of moment, M_0 is the maximum moment in the absence of horizontal load, α_1 to α_5 are constants, obtainable from four independent parameters. In his study, no tensile resistance of the footing was considered. The shape of the failure locus in *M*-*H* space is an eccentric ellipse rotated through an angle from the *H* axis toward the *M* axis, in the opposite direction to that suggested by Butterfield and Gottardi (1994).

Osborne *et al.* (1991) also presented a three-dimensional failure locus for circular foundations based on centrifuge test data on sand. Inspired by this idea, Murff (1994) suggested a more general form of three-dimensional failure locus, admitting some tension capacity, which might be possible due to suction under foundations on the seabed, as:

$$f(V,H,M)=\sqrt{\left(\frac{M}{D}\right)^2+\alpha_1 H^2}+\alpha_2\left(\frac{V^2}{V_c}-V\left(1+\frac{V_t}{V_c}\right)+V_t\right)=0 \qquad (4.8)$$

where α_1 and α_2 are constants, V_c is the compression capacity under pure vertical load, and V_t is the tension capacity of the footing. For the special case of $V_t = 0$, Equation (4.8) is similar to the one presented by Osborne *et al.* (1991).

A simple form of Equation (4.8) which might be suitable for foundations on saturated clay under undrained conditions (e.g. fast loading) assuming $V_t = -V_c = -V_u$, is as follows;

$$f(V,H,M) = \sqrt{\left(\frac{M}{\alpha_3 V_u D}\right)^2 + \left(\frac{H}{\alpha_4 V_u}\right)^2} + \left(\frac{V}{V_u}\right)^2 - 1 = 0 \qquad (4.9)$$

$\alpha_3 V_u D$ and $\alpha_4 V_u$ can be seen as the capacity of the foundation under pure moment, M_u, and pure horizontal load, H_u, respectively. Therefore the above equation can be reduced to:

$$f(V,H,M) = \sqrt{\left(\frac{M}{M_u}\right)^2 + \left(\frac{H}{H_u}\right)^2} + \left(\frac{V}{V_u}\right)^2 - 1 = 0 \qquad (4.10)$$

A finite element study of the failure locus for strip foundations on non-homogeneous clay under combined loading was presented by Bransby and Randolph (1997a, 1997b). To model the non-homogeneity of the soil, it was assumed that the undrained shear strength of the soil is proportional to depth, increasing at a rate k. The results of the numerical analyses were supported by upper bound plasticity analyses. A failure locus similar to the one presented by Murff (1994) was presented by Bransby and Randolph as follows:

$$f(V,H,M) = \sqrt[\alpha_3]{\left(\frac{M^*}{M_u}\right)^{\alpha_1} + \left(\frac{H}{H_u}\right)^{\alpha_2}} + \left(\frac{V}{V_u}\right)^2 - 1 = 0 \qquad (4.11)$$

in which

$$\frac{M^*}{ABs_{uo}} = \frac{M}{ABs_{uo}} - \frac{z}{B} \times \frac{H}{As_{uo}}$$

where M^* is the moment calculated about a reference point above the base of the footing at a height z, α_1 to α_3 are factors depending on the degree of non-homogeneity of the soil, kB/s_{uo}. s_{uo} is the soil shear strength at the level of the foundation base. For the special case of $k\,B/s_{uo} = 6$, it was shown that the best fit of Equation (4.11) to the results can be achieved using $\alpha_1 = 2.5$, $\alpha_2 = 5$, $\alpha_3 = 2$, $z/B = 0.545$ and $M_u = 1.426\,ABs_{uo}$. An alternative expression for the failure locus resulting from a separate curve fitting in the *(V-H)*, *(V-M)* and *(H-M)* planes was also suggested by Bransby and Randolph (1997a, 1997b) as:

$$f(V,H,M) = \left(\frac{V}{V_u}\right)^{2.5} - \left(1 - \frac{M^*}{M_u}\right)\left(1 - \frac{H}{H_u}\right)^{0.33} + 0.5\left(\frac{M^*}{M_u}\right)\left(\frac{H}{H_u}\right)^5 = 0 \qquad (4.12)$$

The shapes of failure loci in three orthogonal planes were presented; among them there is a non-symmetric failure envelope in *M-H* space. The shape of the failure envelope in *M-H* space was confirmed using upper bound plasticity mechanisms.

4.3: FINITE ELEMENT MODEL

Finite element analyses of a circular foundation resting on the surface of homogeneous soil deforming under undrained conditions were performed to investigate the shape of the failure envelope in the *V-H-M* space for the foundations. The shape of the failure locus, the expansion of plastic zones during loading, and the movement of soil at failure are presented. A simple mathematical equation describing the failure locus in terms of all three components of the load is also presented.

The finite element formulation presented in Chapter 3 has been used to find the bearing capacity of a circular footing under combined loading. The footing was assumed to be rigid and rough and it has a diameter D. The soil is assumed to obey the Tresca failure criterion with a uniform undrained shear strength of s_u. The Young's modulus of the soil in an undrained condition is assumed to be $E_u = 300\, s_u$. The Poisson's ratio of the soil is taken as $\nu \approx 0.5$ ($=0.49$ to avoid numerical difficulties) to model the constant volume of the soil under undrained conditions. Therefore, the rigidity index of the soil is $G/s_u \approx 100$, where G is the elastic shear modulus of the soil. No attempt has been made to model the soil-foundation separation on the tension side of the footing under large moment.

The finite element mesh used in the analyses is shown in Fig. 4.1, which also defines the overall geometry of the problem. The number of wedges in the circumferential direction was taken to be *12*. The foundation was modelled as a solid cylinder of elastic elements. A thin layer of continuum elements was used in the region of the soil-foundation interface, which considerably improved the predictions of the lateral response of the foundation. A better soil-foundation interface model may have been achieved using interface elements beneath the foundation, but the degree of accuracy achieved with the thin layer of elements was considered acceptable.

A series of finite element analyses was carried out to investigate the failure points for a range of combinations of compressive vertical load, horizontal load and moment. Fig. 4.2 shows the actual load on the footing and its vertical and horizontal components and the moment resulting from the load eccentricity. Also shown in Fig. 4.2 is the sign convention for loads and moment used in this study. In the finite element analyses the vertical and horizontal loads were applied on the foundation by means of uniform tractions at the soil-footing interface.

Overturning moment was also modelled as a couple composed of uniform horizontal tractions at the top and the bottom surface of the footing. Various combinations of loads and moment were used in a series of analyses with the incremental load method in order to obtain the failure envelope for the foundation.

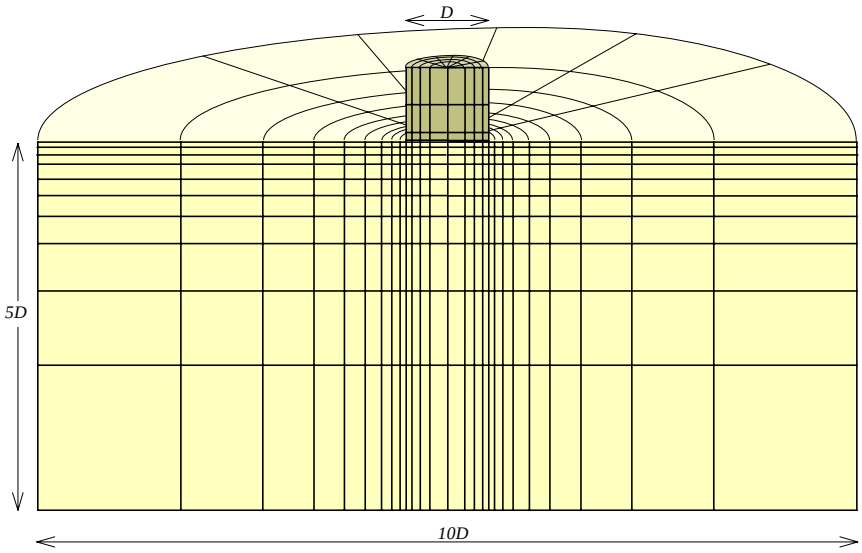

Fig. 4.1: Finite element mesh and geometry of the problem

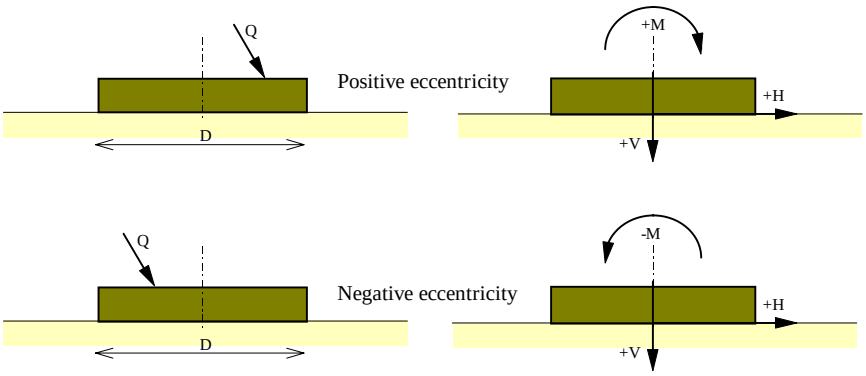

Fig. 4.2: Load and direction of its components on the foundation

4.4: FAILURE POINT

In all the finite element analyses reported here the loading was specified by increasing the total nodal force applied to the rigid footing, i.e., it was load-defined rather than displacement defined. This posses special problems for the determination of the ultimate capacity, as explained below.

The ultimate bearing capacity of the foundation under combined loads and moment was obtained by introducing a consistent method for definition of the failure points. A very

versatile ultimate load criterion, which is recommended for general use, defines the ultimate load as the point where the slope of the load settlement curve first reaches zero or, more usually, a steady low value. This criterion requires that the analysis be carried to very large displacements.

In load-defined elasto-plastic finite element analyses of foundations subjected to vertical load and/or moment, it is very difficult to find a point at which overall failure can be deemed to occur. This difficulty arises because there may not be a distinct change in the numerical prediction of the system stiffness, due to the fact that there is a continuous and steady rate of local failure in the soil (see, for example, Fig. 4.3). Theoretically, collapse of the system corresponds to a singular global stiffness matrix. However, round-off error in the numerical solution scheme ensures that the singular condition is never precisely satisfied. For a foundation subjected to horizontal loading, however, the errors due to round-off may be less significant. Under horizontal load, the total failure is usually sudden and therefore quite distinct. It coincides with the failure of the last Gauss point of the soil elements on the soil-foundation interface. Therefore with any combination of horizontal load, vertical load and moment, an indication of the failure point can be best determined from the horizontal load-displacement curve. The failure of foundations under pure vertical load or pure moment is also best determined using a combination of a very low value of horizontal load with applied vertical load or moment (see Fig. 4.4 and Fig. 4.9).

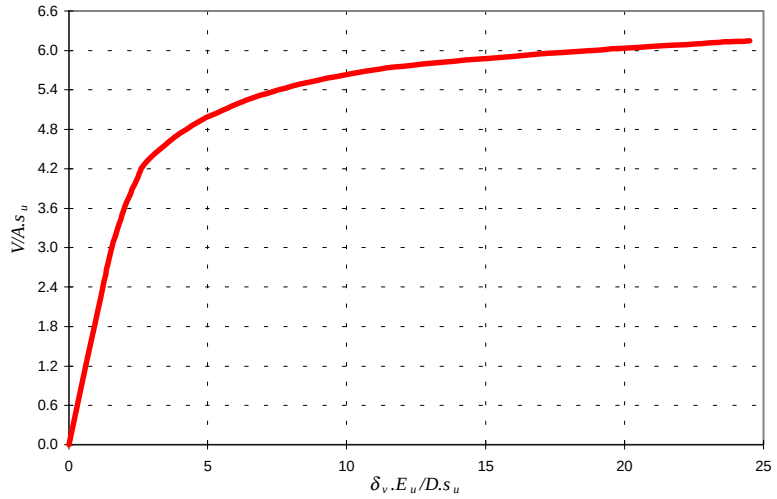

Fig. 4.3: Load-displacement response of the foundation under pure vertical loading

A typical dimensionless load-displacement curve for footing under a combination of loads and moment is shown in Fig. 4.5. δ_v, δ_h and θ are the horizontal and vertical displacement of the centre of the foundation, and the rotation of the foundation, respectively. As an example, the horizontal load, vertical load and overturning moment at failure can be extracted from Fig. 4.5 as $H=-0.375A.s_u$, $V=4.5A.s_u$, and $M=0.375A.D.s_u$.

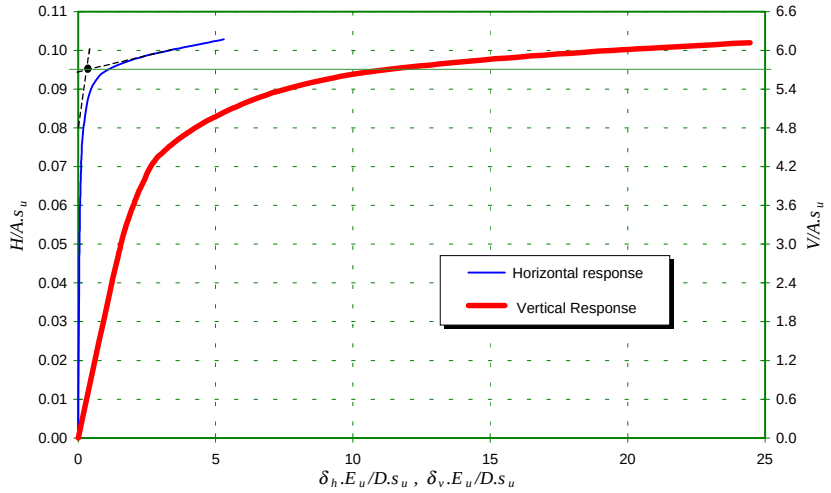

Fig. 4.4: Load-displacement response of the foundation under vertical and horizontal loading

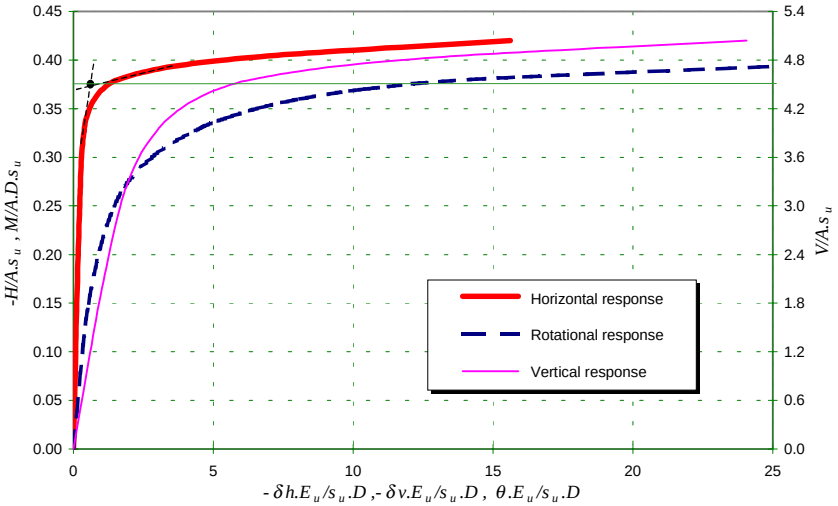

Fig. 4.5: Typical load displacement curves for a foundation under combined loading

4.5: TWO DIMENSIONAL FAILURE ENVELOPES

4.5.1: Vertical-Horizontal (*V-H*) Loading Plane

The ultimate vertical load capacity of the foundation, V_u, was obtained from the results of finite element analysis with $V/H=60$ and $M=0$. The small horizontal component of load was used to define better the ultimate load point, as described in the previous section. A value of $V_u = 5.7A.s_u$ can be deduced from the load displacement curve corresponding to this case, presented in Fig. 4.4. This value is about *10%* less than the ultimate bearing capacity predicted by the conventional bearing capacity formulae (Equation 4.2). This implies that in the conventional method of bearing capacity calculation, a shape factor of *1.1* for circular

foundations, as suggested by Meyerhof (1980), may be more suitable. It is worth noting that the ultimate load of $V_u = 5.7A.s_u$ predicted by the finite element procedure described here is very close to the solution of $V_u = 5.69A.s_u$, obtained independently by Cox (1961) for the problem of a smooth rigid cylindrical punch loading the surface of a rigid plastic half-space.

To evaluate any possible effect of the horizontal load of $H=V/60$ on the vertical bearing capacity, another analysis with a lower value of horizontal load, $H=V/600$, was carried out. The same value for the ultimate vertical bearing capacity was obtained, indicating the negligible influence of these relatively small horizontal loads on the vertical capacity of the footing.

The capacity of the foundation under pure horizontal load was predicted by the finite element method to be $H_u/As_u = 1.02$ (Fig. 4.6) which compares well with the exact solution of $H_u/As_u = 1.0$.

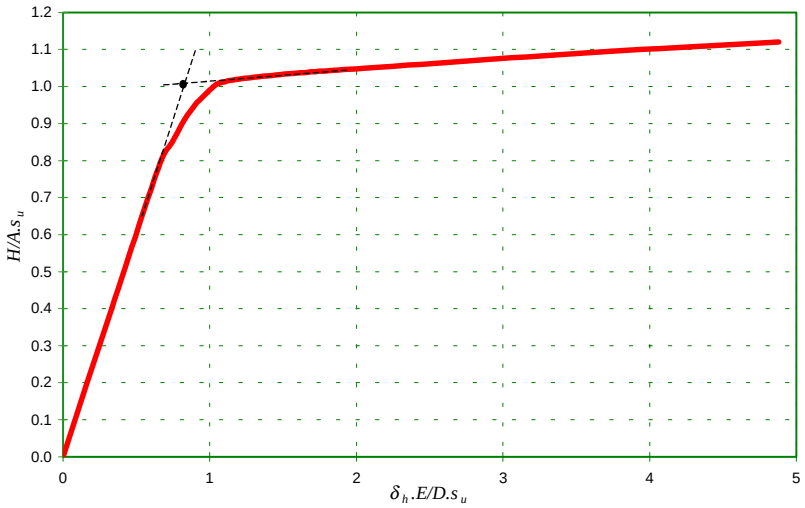

Fig. 4.6: Load-displacement response of the foundation under pure horizontal load

The numerically predicted failure envelope in the *V-H* plane is presented on Fig. 4.7, together with the conventional and theoretical representations of the failure locus. The conventional failure locus was obtained from Equation (4.3) for the special case of $B' = L'$ as:

$$\frac{V_u}{A.s_u} = 1.2\left((2+\pi) - \frac{3H}{2A.s_u}\right) \qquad (4.13)$$

Applying the shape factor of $\zeta_s = 1.2$ to the Equation (4.4), presented by Bolton (1979) for a strip footing, gives another interaction equation for horizontal and vertical loads on circular foundations as follows.

$$\frac{V}{A.s_u} = 1.2\left(1 + \pi - Arc\sin\frac{H}{As_u} + \sqrt{1 - \frac{H}{As_u}}\right) \qquad (4.14)$$

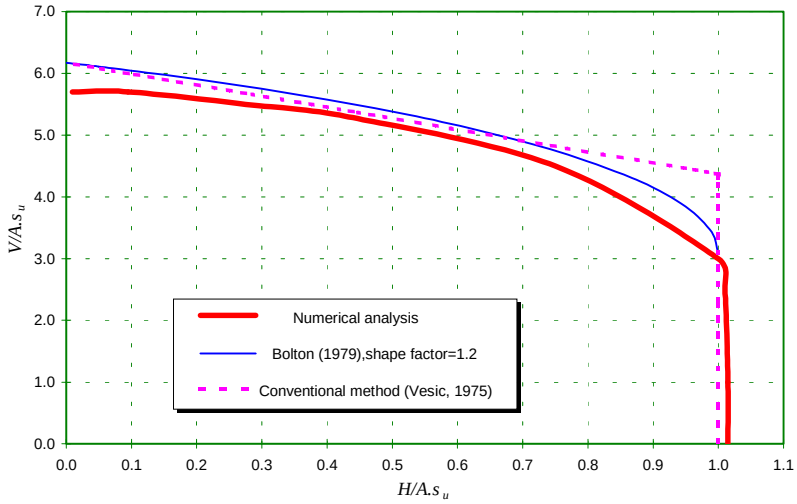

Fig. 4.7: Failure loci for foundations under inclined loading (*M=0*)

Comparison of the curves in Fig. 4.7 shows that the numerical analyses generally give a more conservative bearing capacity for foundations subjected to inclined load. The results of the numerical analyses are very close to the results of the theoretical expression of Bolton (1979). Admitting the limitations on the accuracy of the theoretical values calculated for strip footings, the difference between analytical and numerical analyses indicates that the widely used shape factor of $\zeta_s=1.2$ for circular footings may be slightly high.

All three methods indicate that there is a critical angle of inclination, measured from the vertical direction, above which the ultimate horizontal resistance of the foundation dictates the failure of the foundation. Where the inclination angle is more than the critical value, the vertical force does not have any influence on the horizontal capacity of the foundation. The critical angle is predicted to be 19^o by the numerical studies and from Bolton's expression (1979), compared to 13^o predicted by the conventional method of Vesic (1975).

A non-dimensional form of the conventional Equation (4.13) can be obtained as:

$$\frac{V}{V_u} = 1 - \frac{3H}{2(2+\pi)H_u} \qquad (4.15)$$

where V_u is the ultimate vertical bearing capacity of the foundation under pure vertical load and H_u is the ultimate horizontal capacity of the foundation under pure horizontal load.

The theoretical expression for the interaction of horizontal and vertical loads, Equation (4.4), presented by Bolton (1979), can also be written in a non-dimensional form as:

$$\frac{V}{V_u} = 0.5 + \frac{1}{2+\pi}\left(Arc\cos\frac{H}{H_u} + \sqrt{1-\left(\frac{H}{H_u}\right)^2} \right) \qquad (4.16)$$

The failure Equation (4.10) presented by Murff (1994) for the special case of $V_t = -V_c$ and $M=0$ also results in:

$$\left(\frac{V}{V_u}\right)^2 = 1 - \frac{H}{H_u} \tag{4.17}$$

The failure functions (4.11) and (4.12), suggested by Bransby and Randolph (1997a) for strip footings on non-homogeneous soil, with $kB/s_{uo} = 6$ and $M^* = 0$ result in:

$$\left(\frac{V}{V_u}\right)^2 = 1 - \left(\frac{H}{H_u}\right)^{2.5} \tag{4.18}$$

$$\left(\frac{V}{V_u}\right)^{2.5} = \left(1 - \frac{H}{H_u}\right)^{0.33} \tag{4.19}$$

The non-dimensional failure envelope predicted by the present numerical analyses is compared with those of Vesic, Murff, Bolton, and Bransby and Randolph in Fig. 4.8. The shape of the failure locus predicted by the numerical analyses is closest to the one obtained by Bolton (1979). It is also evident from Fig. 4.8 that the failure locus predicted by the numerical analyses is very close to the failure functions suggested by Bransby and Randolph (1997a) for low values of horizontal loads.

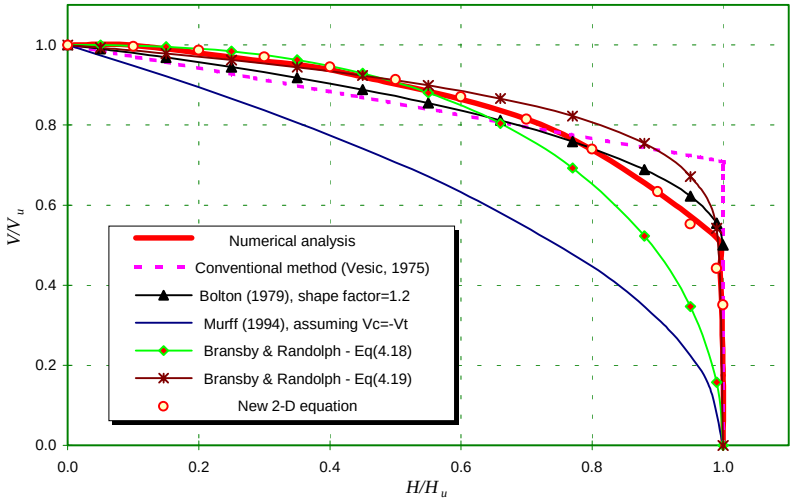

Fig. 4.8: Failure loci in the non-dimensional loading plane of *V-H* for foundations under inclined loading (*M=0*)

It can be seen that the conventional method, compared with the numerical results, gives a good approximation of the failure locus except for high values of horizontal loads. The failure locus presented by Murff (1994) gives a very conservative approximation of the numerical and conventional failure loci.

From the results of the numerical analyses, a simple new approximate equation for the failure locus can be found as follows;

$$\frac{V}{V_u} = 0.35 + 0.65\sqrt{1-\left(\frac{H}{H_u}\right)^2} \qquad (4.20)$$

The failure locus corresponding to the new equation is also shown in Fig. 4.8.

4.5.2: Vertical-Moment (*V-M*) Loading Plane

For the foundation under pure moment, an ultimate capacity of $M_u = 0.8A.D.s_u$ is obtained from the results of finite element analysis, assuming $M/H=100$ and $V=0$. Fig. 4.9 shows the load displacement curves under this combination of load and moment. No independent data are available to check the validity of this result. A more accurate value for the capacity of the foundation under pure moment may have been achieved using a finer mesh for the foundation and the soil underneath the foundation. However, the degree of accuracy achieved was considered acceptable.

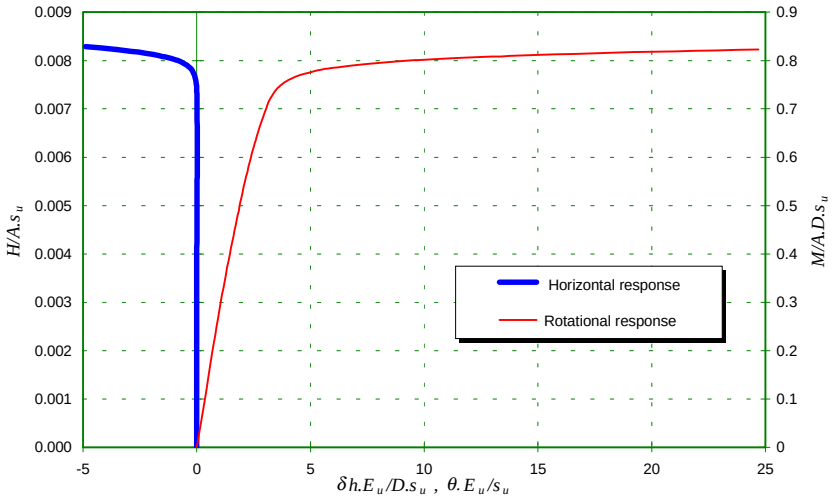

Fig. 4.9: Moment-rotation response of the foundation under vertical and horizontal loading

The conventional method does not provide an explicit equation to approximate the bearing capacity of circular foundations under eccentric load. However, the general recommendation is to calculate the vertical bearing capacity of a foundation with a fictitious effective area on which the load is centrally applied, so that its geometric centre coincides with the load centre. The effective area of a circular foundation, A', under a load applied with an eccentricity of $e=M/V$ can be calculated as (see Fig. 4.10):

$$A' = \frac{D^2}{2}\left(Arc\cos\frac{2e}{D} - \frac{2e}{D}\sqrt{1-\left(\frac{2e}{D}\right)^2}\right)$$

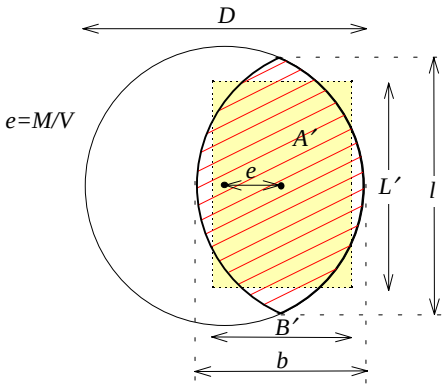

Fig. 4.10: Effective area of circular footings subjected to eccentric load

The aspect ratio of the effective area can also be approximated as the ratio of the line lengths *b* to *l*, as shown in Fig. 4.10.

$$\frac{B'}{L'} = \frac{b}{l} = \sqrt{\frac{D-2e}{D+2e}}$$

Hence, the interaction equation for circular foundations subjected to eccentric loading can be obtained from the conventional method as:

$$(2+\pi)\frac{D^2}{2}\left(1+0.2\sqrt{\frac{D.V-2M}{D.V+2M}}\right)\left(Arc\cos\frac{2M}{D.V}-\frac{2M}{D.V}\sqrt{1-\left(\frac{2M}{D.V}\right)^2}\right)s_u - V = 0 \qquad (4.21)$$

The failure envelope predicted by the numerical analyses and Equation (4.21) are plotted together in Fig. 4.11. The conventional method ignores the tensile capacity of the soil and produces a simple parabola. The conventional method is conservative over almost the whole range of vertical load and moment, and it shows a maximum moment of $M=0.59A.D.s_u$ where the vertical load is $V=0.3A.s_u$.

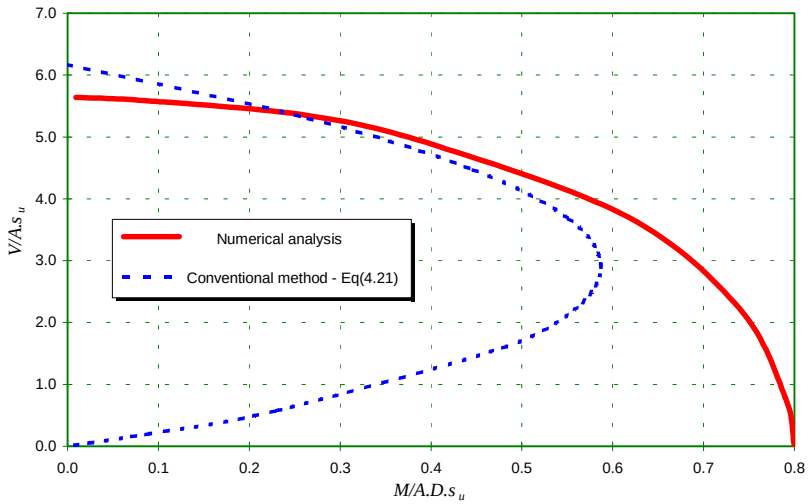

Fig. 4.11: Failure loci for foundations under eccentric loading (*H=0*)

The failure Equation (4.10) presented by Murff (1994) for the special case of $V_t = -V_c$ and $H=0$ results in:

$$\left(\frac{V}{V_u}\right)^2 = 1 - \frac{M}{M_u} \tag{4.22}$$

The failure functions (4.11) and (4.12), suggested by Bransby and Randolph (1997a) for strip footings on non-homogeneous soil, with $kB/s_{uo} = 6$ and $H=0$ result in:

$$\left(\frac{V}{V_u}\right)^2 = 1 - \sqrt{\left(\frac{M}{M_u}\right)^{2.5}} \tag{4.23}$$

$$\left(\frac{V}{V_u}\right)^{2.5} = 1 - \frac{M}{M_u} \tag{4.24}$$

The failure envelope predicted by the present numerical studies is compared with those of the conventional method (Equation 4.21), Murff (Equation 4.22) and Bransby and Randolph (Equations 4.23 and 4.24) in Fig. 4.12. In deriving the non-dimensional conventional failure envelope, the ultimate moment capacity is taken to be $M_u = 0.8A.D.s_u$, as obtained from the numerical analyses. The failure envelopes approximated by the conventional method, Murff (1994) and Bransby and Randolph (1997a) are all conservative with respect to the failure envelope predicted by the numerical analyses. It is noted that the failure equations presented by Bransby and Randolph were suggested for strip footings, rather than the circular footing considered here.

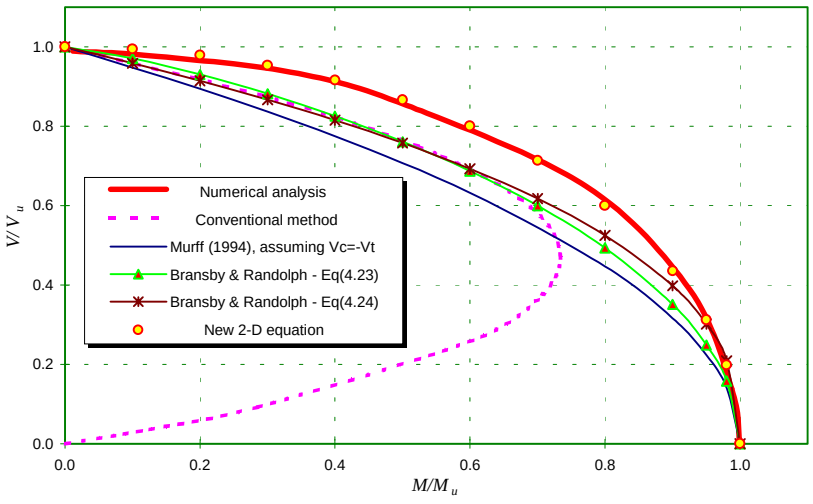

Fig. 4.12: Failure loci in the non-dimensional loading plane of *V-M* for foundations under eccentric loading (*H=0*)

A new simple equation for the interaction of moment and vertical force can be deduced from the results of the numerical analysis, i.e.

$$\frac{V}{V_u} = \sqrt{1 - \left(\frac{M}{M_u}\right)^2} \qquad (4.25)$$

The failure envelope predicted by the new equation is also plotted in Fig. 4.12. The new equation matches well the failure envelope predicted by numerical analysis.

4.5.3: Horizontal-Moment (*H-M*) Loading Plane

A series of numerical analyses in the *H-M* plane (with zero vertical load) was performed. The failure locus obtained from the analyses for horizontal load and moment is plotted in Fig. 4.13. A maximum moment capacity of $M=0.89A.D.s_u$ is obtained from these analyses, which is *11%* greater than the predicted capacity of the foundation under pure moment. The maximum moment coincides with a horizontal load of $H=0.71A.s_u$. Application of this value of horizontal load with moment mobilises the shear strength of more soil under the foundation during failure and therefore increases the moment capacity of the foundation. Bransby and Randolph (1997a, 1997b) identified two different upper bound plasticity mechanisms for strip footing under moment and horizontal load, a scoop mechanism and a scoop-wedge mechanism. The later mechanism results in a greater ultimate moment capacity for strip footings.

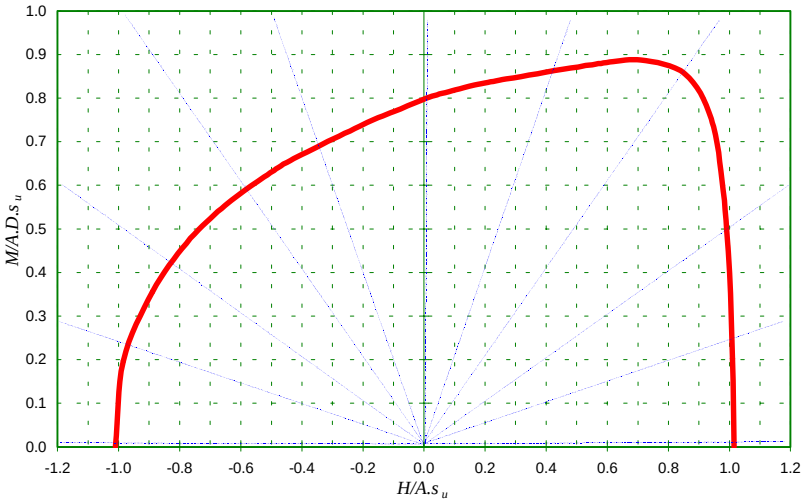

Fig. 4.13: Failure locus for foundations under moment and horizontal load (*V=0*)

The non-symmetric failure locus is very similar to the failure locus obtained by Bransby and Randolph (1997a, 1997b) for strip footings using finite element analysis and upper bound plasticity analysis. If the failure locus is to be approximated as an eccentric ellipse, to resemble the failure envelope presented by Martin (1994) or Butterfield and Gottardi (1994), then the direction of its rotation is from the *M* axis toward the *H* axis, in the same direction as found by Martin (1994) but in the opposite direction of the failure locus suggested by Butterfield and Gottardi (1994).

The failure envelope presented by Murff (1994) for the special case of $V_t = -V_c$ and $V=0$ results in:

$$\left(\frac{M}{M_u}\right)^2 + \left(\frac{H}{H_u}\right)^2 = 1 \qquad (4.26)$$

A non-dimensional form of the numerically predicted failure locus and the suggestion by Murff, Equation (4.26), are plotted in Fig. 4.14. It can be seen that the failure locus presented by Murff (1994) is symmetric and the maximum moment coincides with zero horizontal loading, whereas the numerical analyses show that the maximum moment is sustained with a positive horizontal load. The failure locus obtained from Murff's equation becomes non-conservative when $M \times H \leq 0$.

Bransby and Randolph (1997b) redefined the position of the moment reference point to a point above the footing so that the true moment, M^*, on the foundation would have two components; the applied moment, M, and $H \times L$, where L is the distance of the moment reference point from the foundation surface. The shape of the failure locus in the M^*-H plane was shown to be almost symmetric. For a strip footing on soil with a non-homogeneity index of $kB/s_{uo} = 6$, values of $L/B = 0.545$ and $M_u = 1.426ABs_{uo}$ have been suggested for substitution into Equations (4.11) and (4.12). These equations can then be simplified to:

$$\frac{M}{M_u} = \left(1 - \left(\frac{H}{H_u}\right)^5\right)^{0.4} + \frac{0.545H}{1.426H_u} \qquad (4.27)$$

$$\frac{M}{M_u} = \frac{\left(1 - \frac{H}{H_u}\right)^{0.33}}{0.5\left(\frac{H}{H_u}\right)^5 + \left(1 - \frac{H}{H_u}\right)^{0.33}} + \frac{0.545H}{1.426H_u} \qquad (4.28)$$

A graphical representation of Equations (4.27) and (4.28) is also shown in Fig. 4.14.

A new approximate equation has been obtained from the numerical results, which is suitable to be used in H-M space, i.e.

$$\frac{M}{M_u} = 0.6\sqrt{1 - \left(\frac{H}{H_u}\right)^2} + \frac{0.4\cos\left(\frac{H}{H_u}\right)}{1 - 0.8\sin\left(\frac{H}{H_u}\right)} \qquad (4.29)$$

The new equation, plotted in Fig. 4.14, is in good agreement with the numerical failure envelope. A small divergence exists around the position of the maximum moment, where the new equation gives conservative values for moment and lateral load.

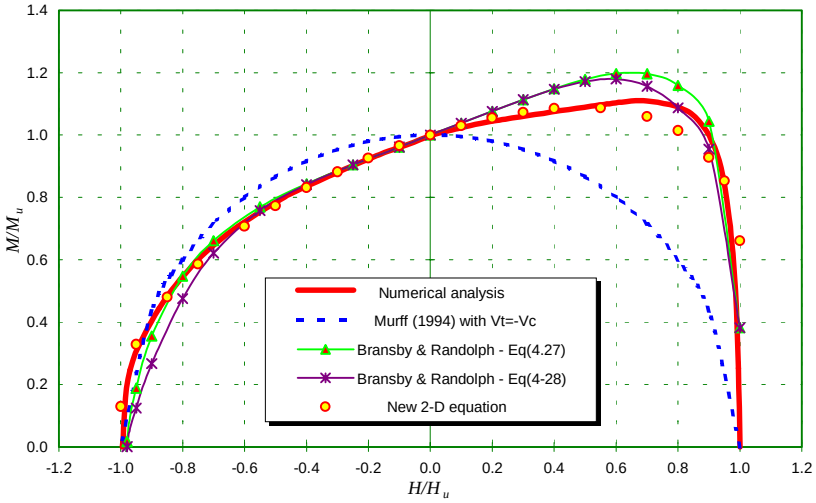

Fig. 4.14: Failure loci in the non-dimensional loading plane of *M-H* for foundations under moment and horizontal load (*V=0*)

4.6: THREE-DIMENSIONAL FAILURE ENVELOPE

Various combinations of loads and moment were used in a series of finite element analyses to evaluate the failure envelope in *V-H-M* space. Any combination of loads with a constant ratio of horizontal load to moment, *H/M*, and varying values of vertical load, *V*, represents a line in the *H-M* loading plane. Lines with a constant *H/M* have been drawn with the dashed lines on the *H-M* plane in Fig. 4.13. Between *7* to *10* analyses with different values of vertical load were conducted for every selected ratio of *H/M*.

A three-dimensional image of the failure envelope for foundations under combined compressive vertical load, horizontal load and moment is presented in Fig. 4.15. Representations of the failure envelope in the *M-H* space, the *V-M* space and the *V-H* space are also presented as contour plots in Fig. 4.16, Fig. 4.17 and Fig. 4.18, respectively.

The equi-vertical load diagram of Fig. 4.16 offers a very convenient design tool for offshore foundations on uniform clays, since the vertical loading on the foundations remains almost constant after construction and during environmental loading periods. The environmental conditions usually apply horizontal loading on the superstructure above the foundation which results in horizontal and moment loadings on the foundation in a plane of fixed (or almost fixed) V/V_u.

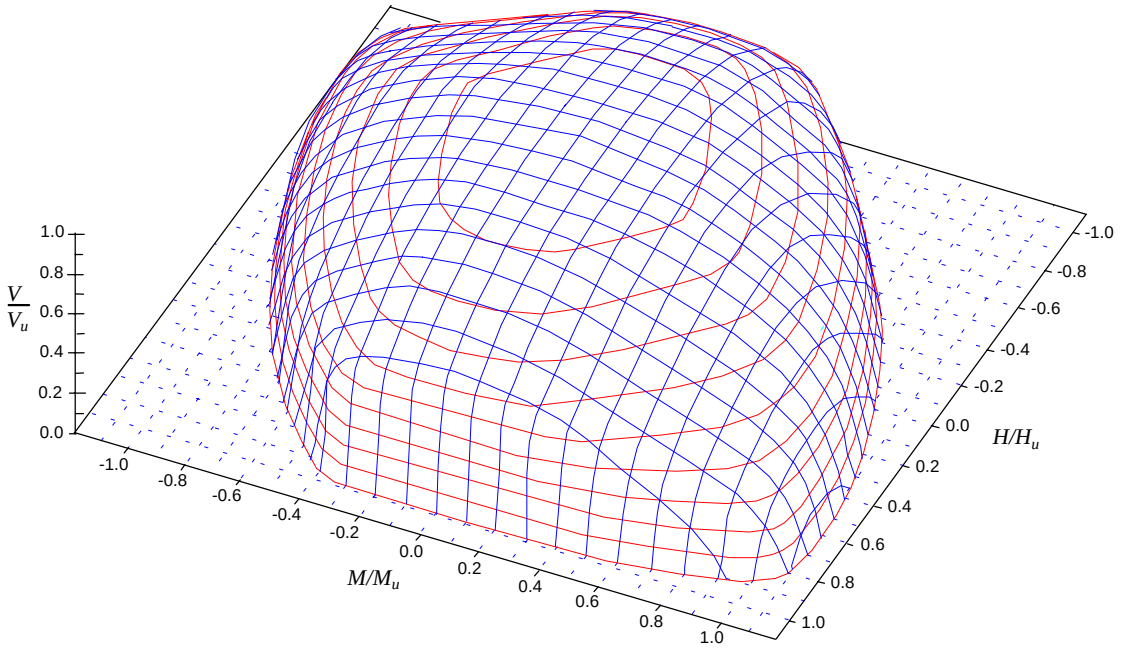

Fig. 4.15: Three-dimensional failure envelope in the non-dimensional space for foundations under combined loads and moment

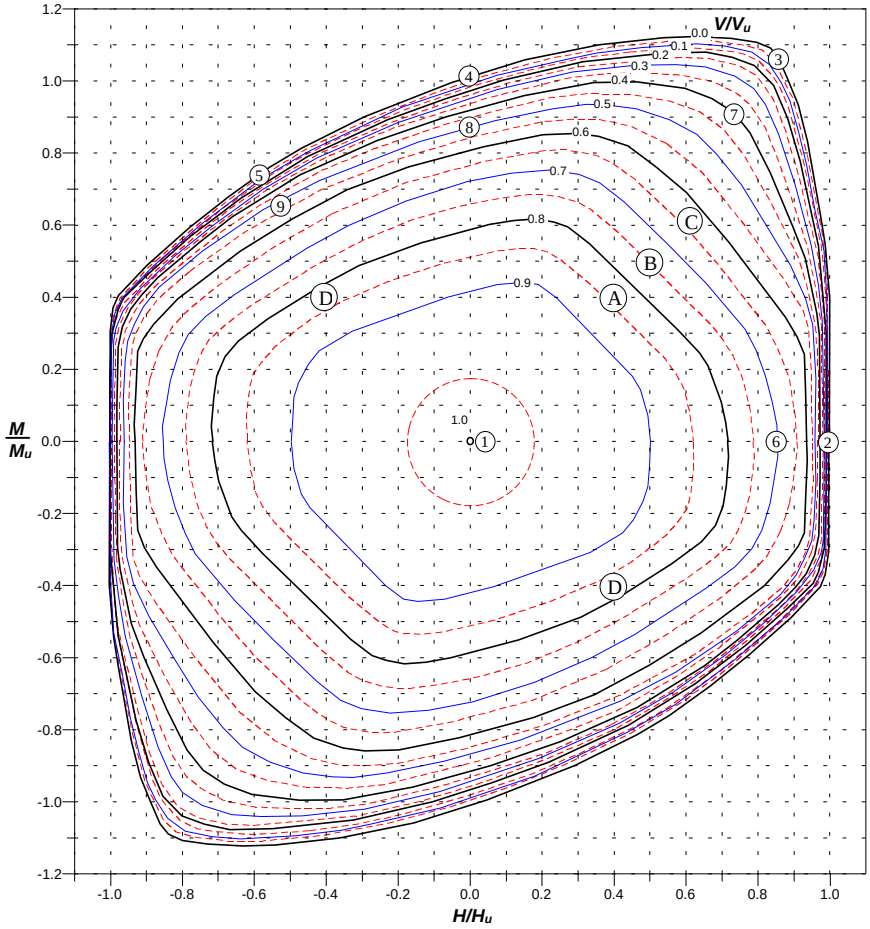

Fig. 4.16: Failure loci in the non-dimensional *H-M* space

Fig. 4.16 shows that the maximum moment is sustained when $M \times H > 0$. The maximum moment occurs at $H/H_u = 0.71$ when $V = 0$. With increasing vertical load, the position of the maximum moment shifts toward the moment axis.

Fig. 4.17 shows that the vertical bearing capacity of a foundation subjected to a specific horizontal load is larger if the moment is applied in the same direction as that of the horizontal load. This fact is also evident from Fig. 4.18, which shows that the vertical bearing capacity of a foundation subjected to a specific moment is greater if the horizontal load is applied in the same direction as the moment.

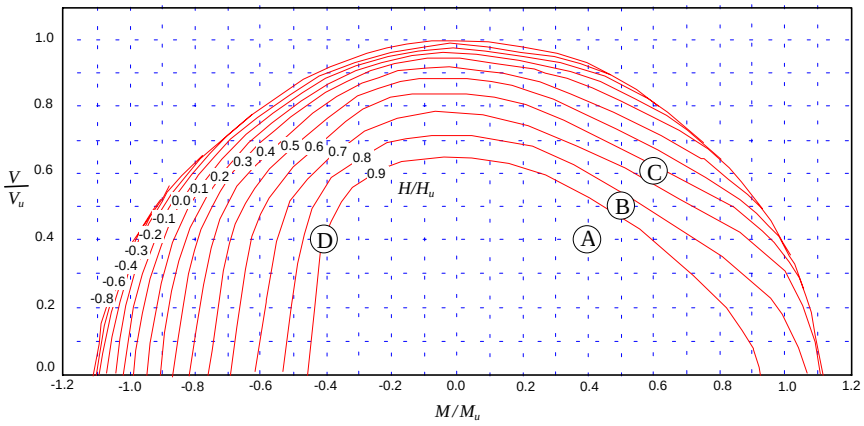

Fig. 4.17: Failure loci in the non-dimensional *V*-*M* space

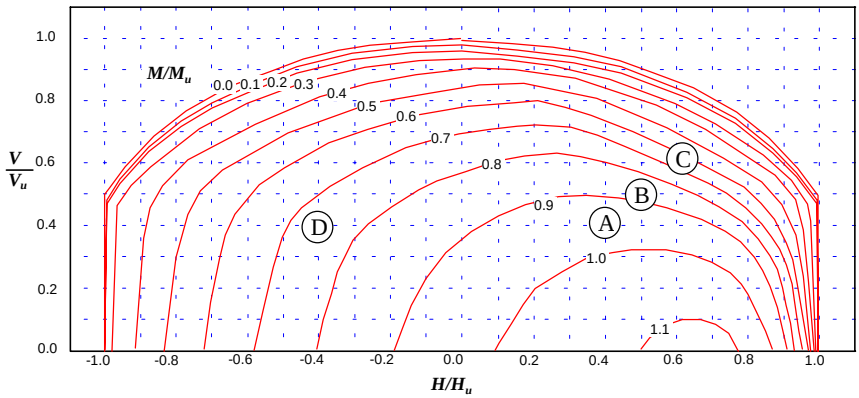

Fig. 4.18: Failure loci in the non-dimensional *V*-*H* space

The three-dimensional representation of the failure envelope provides a convenient way to explore the safety of any specific combination of loads and moment, and the consequences of any change in the loading. Clearly the loading path has an important influence of the margin of safety. For example, consider an initial load combination of $V/V_u = H/H_u = M/M_u = 0.4$ which is represented by point A on Figs 4.16 to 4.18. For a foundation under maintained values of this horizontal load and moment, the maximum tolerable vertical load can be found from Fig. 4.16 as $V_{max}/V_u = 0.84$. In the same way the maximum tolerable horizontal load and moment can also be found from Figs 4.17 and 4.18 as $H_{max}/H_u = 0.92$ and $M_{max}/M_u = 0.95$.

The minimum safety factor for the foundation under these loads is therefore *S.F.=0.84/0.4=2.1 (=0.84/0.4)*. If the loads and moment all increase by *25%*, i.e. $V/V_u = H/H_u = M/M_u = 0.5$, to point *B* on Figs 4.16 to 4.18, the safety factor reduces to *1.5*. Proportional increases of *56%* to the loads and moment bring the foundation to its failure point (point *C*). If the initial load combination of point *A* is applied to the foundation and then the direction of horizontal load or moment is changed (point *D*), then the safety factor reduces from *2.1* to *1.8*.

A three-dimensional failure equation should not only incorporate the basic characteristics of the conventional bearing capacity equations but also it should have the distinct advantages of mathematical simplicity. An accurate three-dimensional equation for the failure envelope in its complete form, which accounts for the load inclination and eccentricity, is likely to be a complex algebraic expression. Some degree of simplification is essential in order to obtain a convenient form of the failure envelope that reflects the essential nature of the classical equations. Depending on the level of the simplification, different classes of failure equations may be obtained.

In the previous section, the failure envelopes suggested by different sources were compared in two-dimensional loading planes. It was demonstrated that the failure equation presented by Murff (1994) has simplicity in its mathematical expression, but does not fit the failure envelopes produced by the conventional and numerical analyses. The failure equation presented by Bransby and Randolph (1997a) for strip footings matches the data for circular footing in two planes, but does not give a suitable answer in three-dimensional space. The expression suggested from the experimental data by Martin (1994) and Butterfield and Gottardi (1994), are for special cases where the tensile strength between the soil and foundation is zero. The new equations suggested in the previous section give very good approximations to the numerical failure loci in the two dimensional planes, though casting them in one single equation to be used in three-dimensional load space does not yield a simple mathematical expression.

A new equation describing the failure locus in terms of all three components of the load is proposed here. It is demonstrated that it provides a good approximation to the bearing capacity of shallow foundations subjected to combined loading. In the formulation of this equation, advantage was taken of the fact that the moment capacity of the foundation is related to the horizontal force acting simultaneously on the foundation. The proposed approximate failure equation is expressed as:

$$f(V,H,M)=\left(\frac{V}{V_u}\right)^2+\left(\frac{M}{M_u}\left(1-\alpha_1\frac{H.M}{H_u|M|}\right)\right)^2+\left|\left(\frac{H}{H_u}\right)^3\right|-1=0 \qquad (4.30)$$

where α_1 is a factor that depends on the soil profile. For the homogeneous soil studied here the value of $\alpha_1 = 0.3$ provides a good fit to the bearing capacity predictions from the numerical analysis.

Perhaps inevitably, the three-dimensional failure locus described by Equation (4.30) will not match the numerical data over the whole range, especially around the abrupt changes in the failure locus which occur when horizontal load is high. However, the overall approximation to the numerical predictions is considered satisfactory, and sufficient for many practical applications. In particular, the representations of Equation (4.30) in the *V*-*H* plane, *V*-*M* plane, and *M*-*H* plane are presented in Figs 4.19 to 4.21, together with the results of the numerical analyses. It can be seen that the proposed equation provides a very good approximation to the failure condition on these three loading planes.

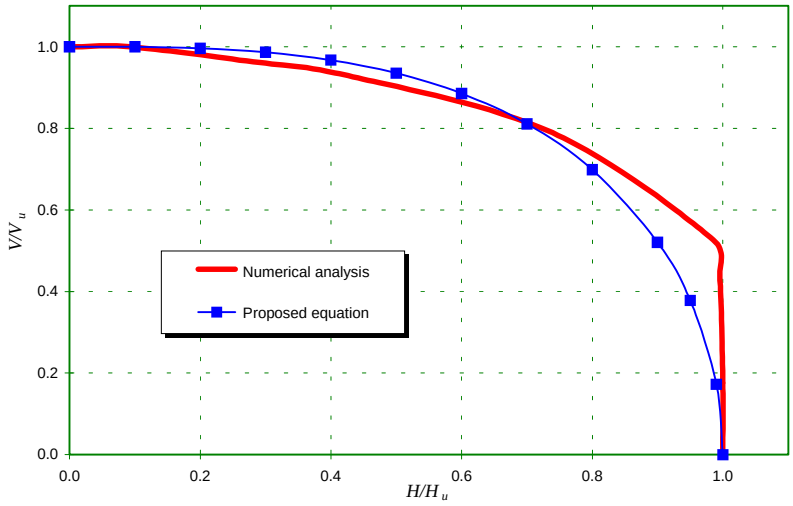

Fig. 4.19: Representation of the proposed failure equation in the non-dimensional *V*-*H* plane

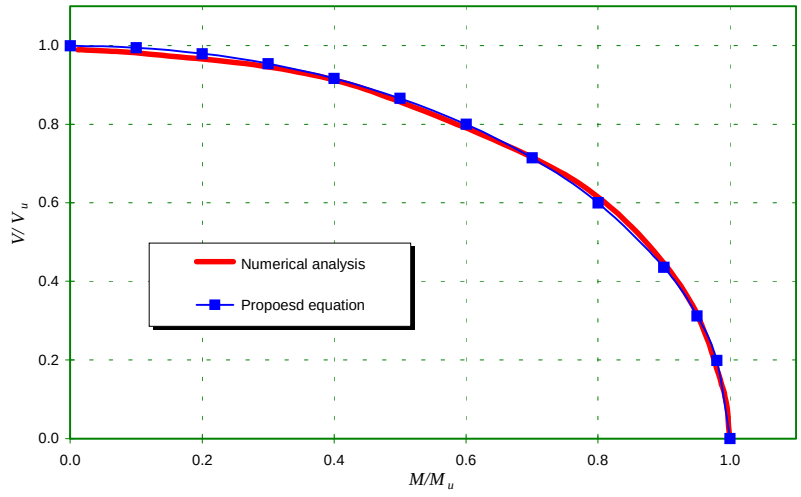

Fig. 4.20: Representation of the proposed failure equation in the non-dimensional *V*-*M* plane

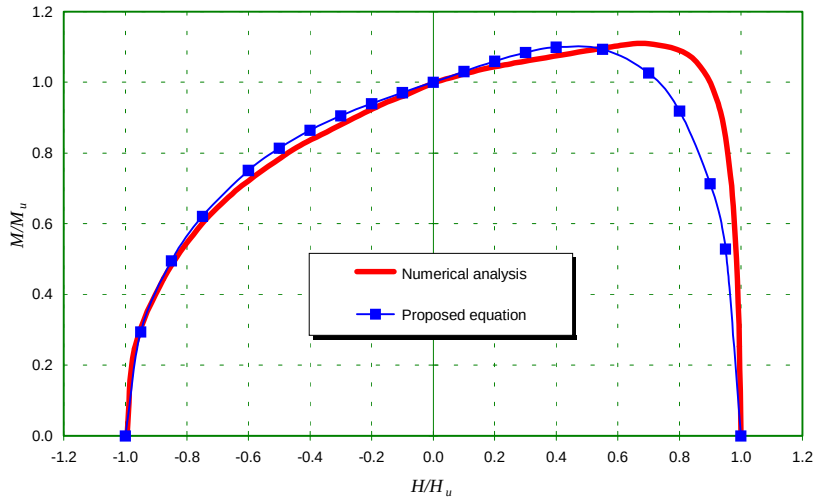

Fig. 4.21: Representation of the proposed failure equation in the non-dimensional *M-H* plane

A representation of the proposed approximate equation for the failure locus is shown in Figs 4.22, 4.23 and 4.24, in the non-dimensional *M-H* space, *V-M* space and *V-H* space, respectively. Fig. 4.22 is comparable with the results of the numerical analyses presented in Fig. 4.16. Fig. 4.23 and Fig 4.24 are also comparable with the results of the numerical analyses in *V-M* space and *V-H* space, presented in Fig. 4.17 and Fig. 4.18, respectively.

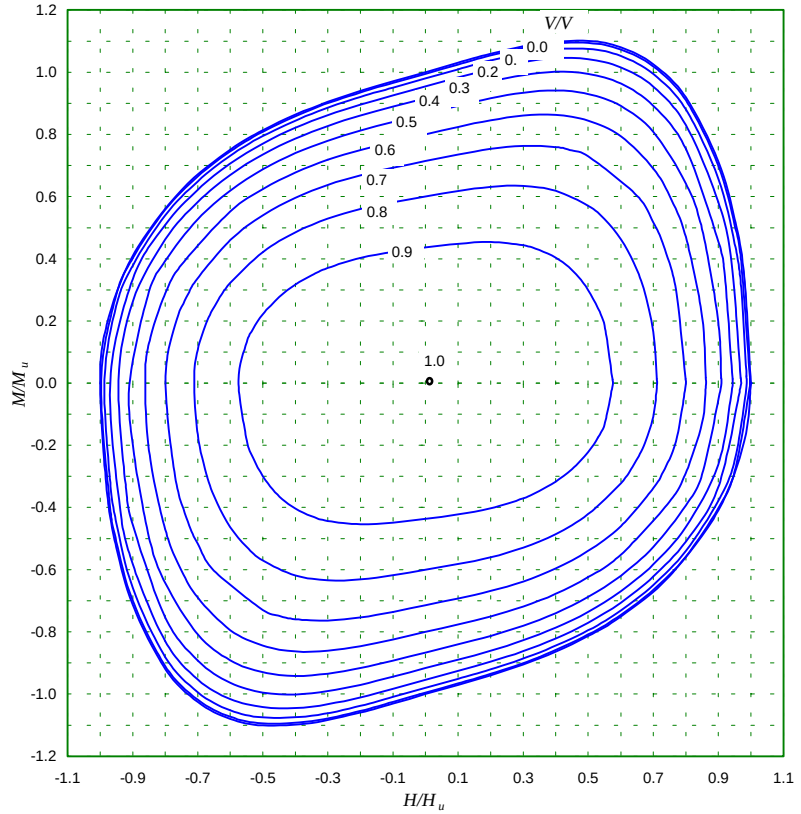

Fig. 4.22: Representation of the proposed failure equation in the non-dimensional *M-H* space

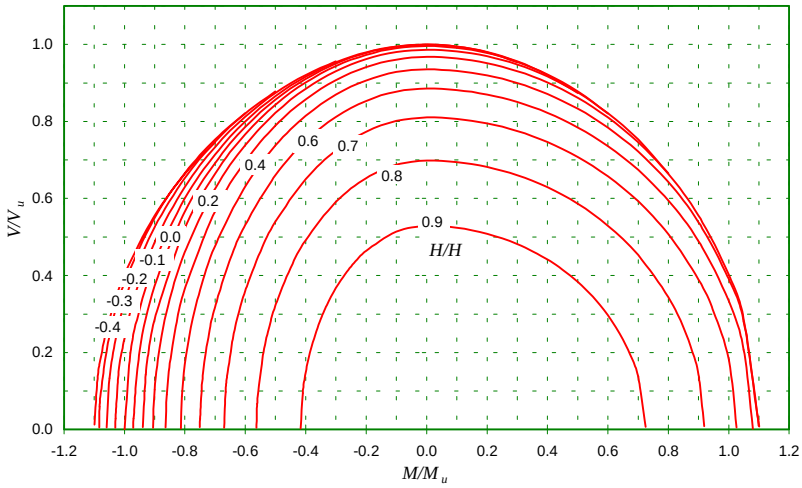

Fig. 4.23: Representation of the proposed failure equation in the non-dimensional *V-M* space

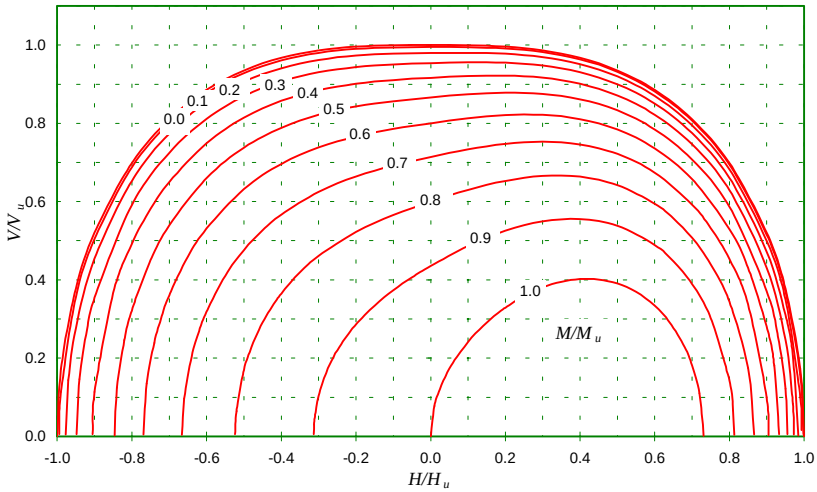

Fig. 4.24: Representation of the proposed failure equation in the non-dimensional *V-H* space

4.7: PLASTIC ZONE AND SOIL MOVEMENT

The patterns of soil movement at failure and the development of plastic zones and failure mechanisms in the soil under a footing are also of some interest. The expansion of plastic zones with increasing load and the movements of soil are studied for *9* cases of different combinations of loads and moment. The various combinations of failure loads are identified in Fig. 4.16 as circles, which are numbered from *1* to *9*. In all cases, the loading was applied proportionally to the foundation using an incremental load path up to the failure point.

The results of the predictions of these analyses in the plane of the applied loads are presented in Figs 4.25 to 4.33. The plastic zones for different ratios of the applied load to the maximum

tolerable load, V/V_{max}, H/H_{max}, or M/M_{max}, were obtained. The general directions of the movement of the soil particles at failure were also recorded. The patterns of movement are illustrated by curves superimposed on the cross-sections of Figs 4.25 to 4.33.

Plastic zones expand differently under various combinations of loads and moment. For instance, under central vertical load, plastic zones expand to a distance of approximately *1.0D* from the centre of the footing and to a depth of *1.5D* under the foundation at failure (Fig. 4.25), whereas for the foundation under pure horizontal loading, plastic zones are concentrated under the foundation with a maximum plan size of just slightly greater than the dimension of the foundation (Fig. 4.26). For a foundation subjected to moment, increase in the horizontal load will cause the plastic zones to expand more (Fig. 4.27 to 4.29). In all cases, the soil beneath the edge of the rigid footing yields first, as might be expected. As the loads are increased, the small "bubbles" of yielded soil beneath the edge of the footing expand. Eventually the plastic zone spreads over the whole area under the foundation, ultimately providing a collapse mechanism.

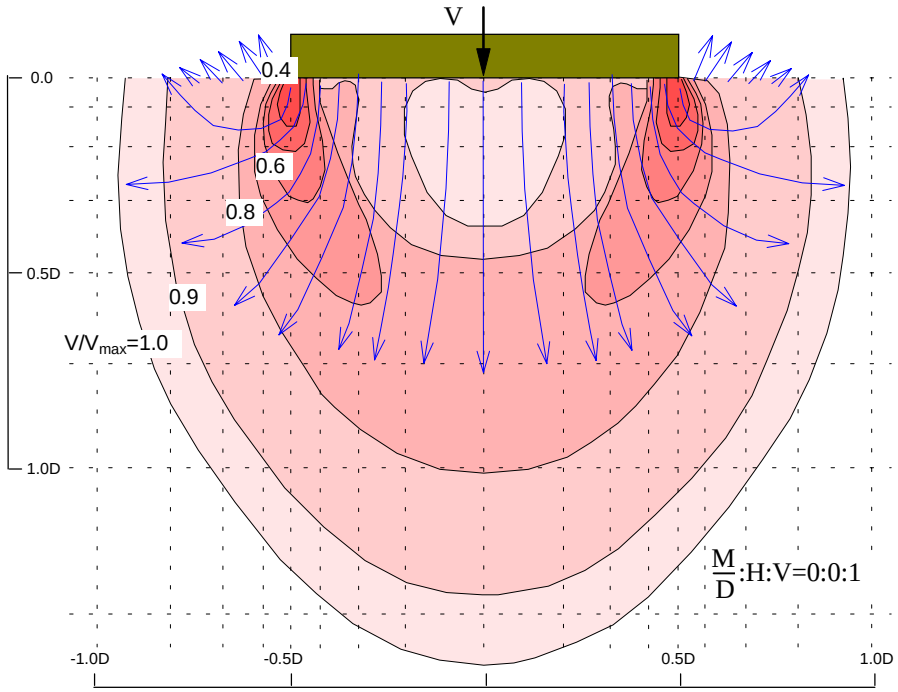

Fig. 4.25: Expansion of plastic zone and direction of soil movement, Case (1)

For foundations under moment and lateral load, there exists a point around which the foundation and soil tend to rotate. The position of this rotation point depends on the relative intensity of applied moment and horizontal load. Under pure horizontal load, the rotation point is in the soil far below the foundation, Fig. 4.26. Application of moment brings the rotation point up, closer to the foundation, Fig. 4.27. At a certain ratio of the applied moment to the horizontal load, the rotation point reaches the interface of the soil and foundation. This ratio effectively determines the extent of the plastic zone and therefore, the maximum

moment capacity for the foundation. Reducing the horizontal force and increasing the moment brings the rotation point above the foundation base. For instance, under pure moment (see Fig. 4.28), or when the direction of applied moment and applied horizontal force are opposite (see Fig. 4.29), the rotation point moves above the foundation base, the moment capacity reduces, and the plastic zone becomes smaller than the one corresponding to the maximum moment capacity.

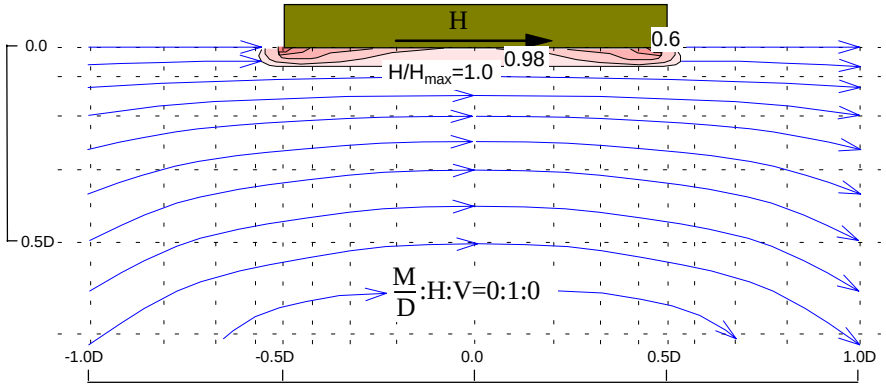

Fig. 4.26: Expansion of plastic zone and direction of soil movement, Case (2)

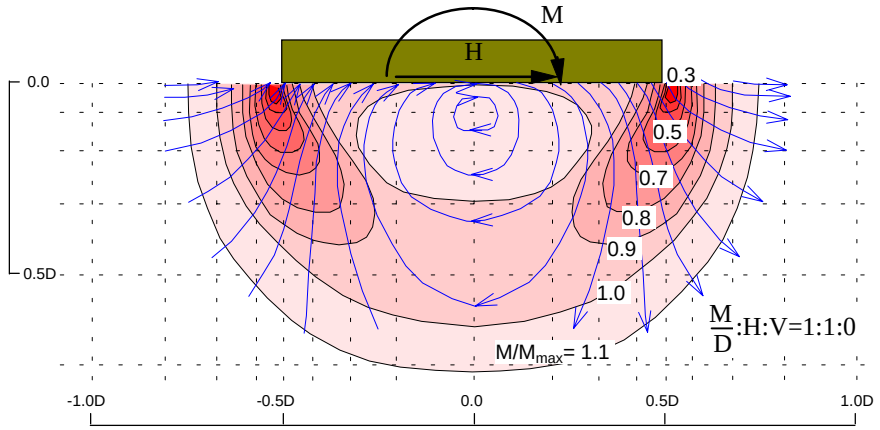

Fig. 4.27: Expansion of plastic zone and direction of soil movement, Case (3)

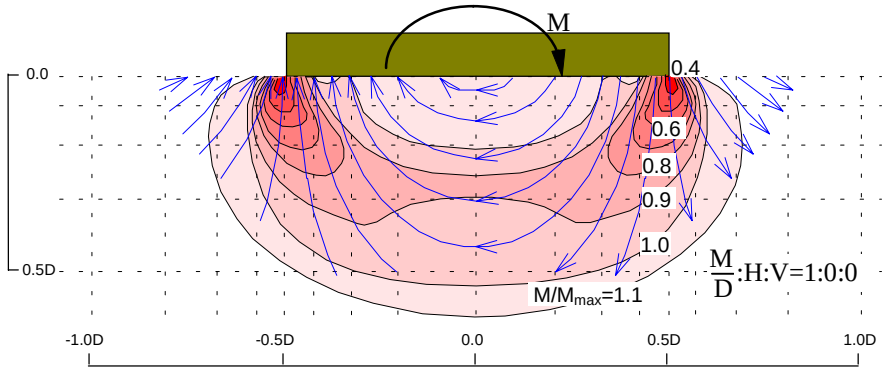

Fig. 4.28: Expansion of plastic zone and direction of soil movement, Case (4)

The plastic zone and the movement of soil are not symmetric when a combination of vertical load, horizontal load and moment is applied on the foundation (Fig. 4.30 to 4.33).

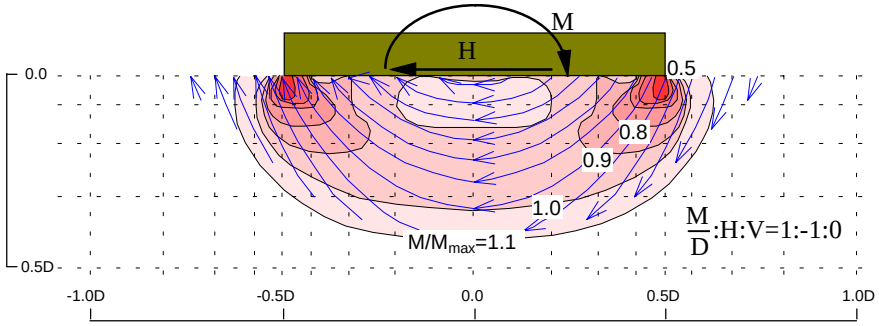

Fig. 4.29: Expansion of plastic zone and direction of soil movement, Case (5)

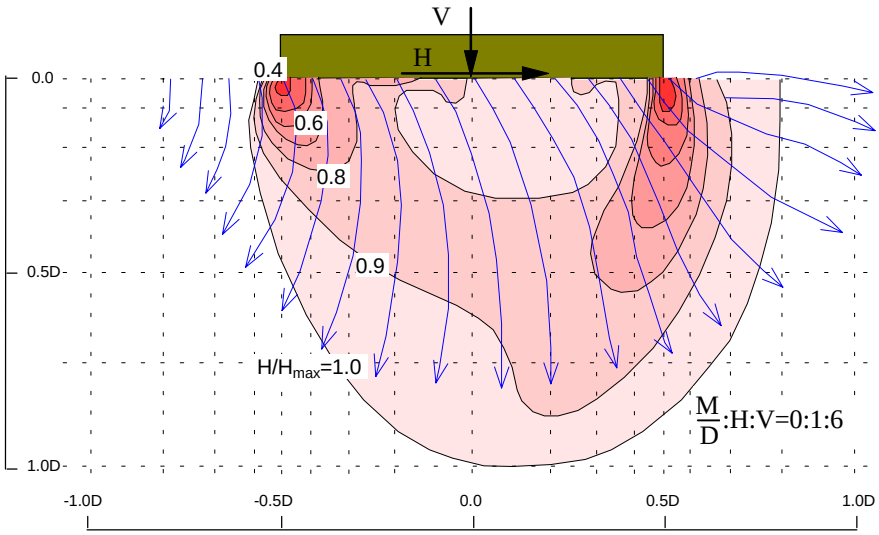

Fig. 4.30: Expansion of plastic zone and direction of soil movement, Case (6)

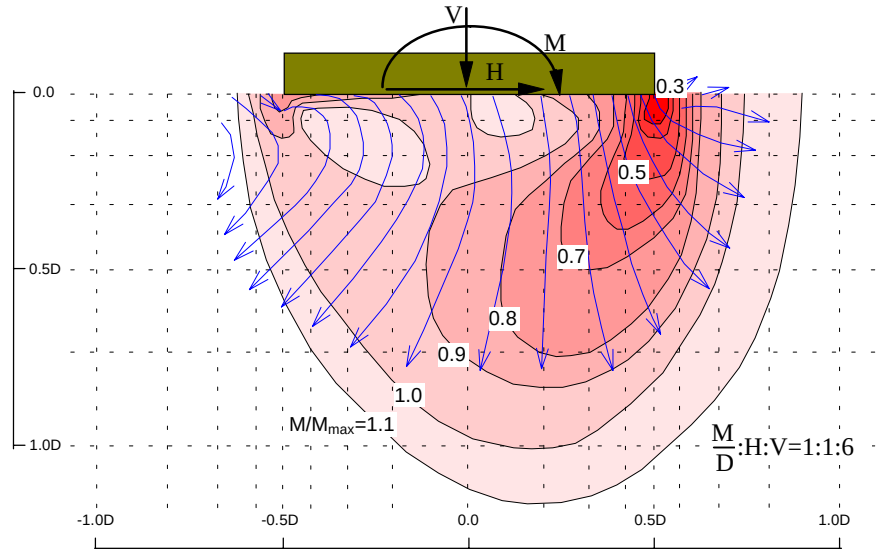

Fig. 4.31: Expansion of plastic zone and direction of soil movement, Case (7)

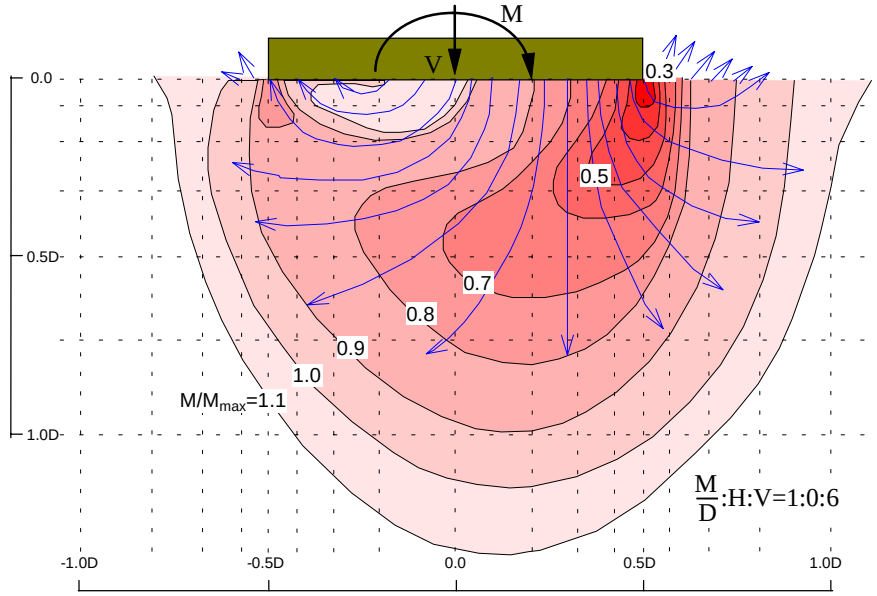

Fig. 4.32: Expansion of plastic zone and direction of soil movement, Case (8)

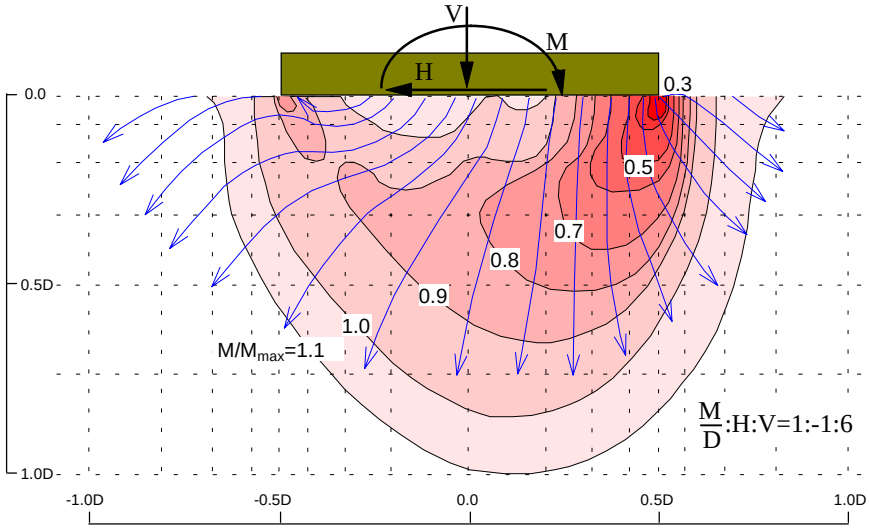

Fig. 4.33: Expansion of plastic zone and direction of soil movement, Case (9)

4.8: CONCLUSIONS

The semi-analytical finite element method presented in Chapter 3 was used in this study to investigate the bearing capacity of circular foundations on uniform deposits of undrained clay and also to demonstrate the power and accuracy of the numerical method.

An important outcome of the numerical studies is that the conventional method of bearing capacity calculation does not always give a conservative prediction. The approximate numerical results indicate that the widely accepted value of the shape factor, $\zeta_s = 1.2$, used in

the conventional method may be slightly high for circular footings. The finite element calculations indicate that a better value for the shape factor may be the one suggested by Meyerhof (1980) as $\zeta_s = 1.1$. The conventional method also gives a non-conservative bearing capacity for foundations under large horizontal loads.

The finite element results suggest that horizontal loads much smaller than the ultimate capacity H_u have very little effect on vertical capacity. It was also shown that shallow foundations are most vulnerable to horizontal load and moment if the vertical load is higher than about $0.5V_u$. This has important consequences in relation to the safety of shallow offshore foundations subjected to lateral loads.

The failure loci, presented either in two dimensional load space or three-dimensional load space, do indeed provide a convenient way to investigate the bearing capacity of a foundation under combined loading. The graphical displays present a clear image of the safety of a foundation under any specific combination of loads and moment, and the consequences of any change in the loading.

The failure loci in non-dimensional load space predicted by the finite element analysis are broadly similar to those obtained by Bransby and Randolph (1997a) in their theoretical studies on shallow strip foundations on non-homogeneous soil. Results of experimental studies by Martin (1994) and Butterfield and Gottardi (1994) also show similar trends in behaviour for shallow foundations of different shapes on different soil profiles. This indicates that the definition of a single general bearing capacity equation, or the failure function, for all types of shallow foundations may be feasible.

The approximate failure equation proposed in this study includes all three components of the load in a simple mathematical expression. It has been shown that the proposed equation approximates very well the numerically predicted three-dimensional failure envelope. The failure equation offers a very convenient way to calculate the bearing capacity and to explore the safety of circular foundations under combined loading.

The accuracy of the numerical method was demonstrated through comparison of its results with analytical and classical solutions to the problem of the bearing capacity of shallow foundations. This should provide confidence in the use of the method (and the computer program) to tackle problems of unknown solution. The behaviour of offshore foundations under cyclic wave loads is among those problems, and will form the subject of subsequent chapters.

Chapter 5

FINITE ELEMENT ANALYSIS OF LIQUEFACTION

5.1: INTRODUCTION

Developing a method of analysis to predict the behaviour of granular soil under the foundations of offshore structures subjected to cyclic loading is the main subject of this chapter.

Foundations of marine structures are generally subjected to two major types of loading; ambient loads due to the submerged weight of the structure and cyclic loads due to wave forces applied during a storm. Cyclic loads usually include a large number of cycles of short to medium periods (*5* to *15 sec*) with variable amplitude. Laboratory tests on samples of granular soils show that application of a large number of cyclic loads with moderate amplitude can produce a progressive degradation of the soil resistance which can alter the stability of marine structures founded on them. It is therefore essential to consider these kinds of loads in the design of marine foundations.

Liquefaction analysis of offshore foundations under cyclic loads can be performed by means of analytical or numerical methods provided that an appropriate constitutive law for the behaviour of saturated granular soils subjected to cyclic loads is adopted. However, the behaviour of granular soils even under static monotonic loading is a subject of some complexity which has attracted a lot of research effort in the past and is still continuing to do so. Part of the difficulty is associated with the two-phase nature of the material. The derivation of governing equations which takes into account all features of the problem is a demanding task, if indeed it is possible at all. Various approximations have to be introduced in order to derive a practical solution to the problem. The validity of any numerical solution is, of course, related directly to the soil model and the level of approximations used in deriving the governing equations of the model. Cyclic loading, such as that experienced by marine and offshore structures subjected to wave loading, increases the complexity of the relevant formulations and constitutive laws. Phenomena such as permanent volumetric strains (densification) and permanent shear strains, which occur after each cycle of load, should be

included in the governing equations. The plasticity models described in Chapter 3, the Mohr-Coulomb model and the Modified Cam Clay model, are not suitable for cyclic load histories, because within a constant or isotropically hardening yield surface, no amount of stress cycling can produce any permanent strains. To produce the essential features of cyclic load response, the constitutive models discussed in Chapter 3 need to be modified or replaced.

Residual stresses and strains resulting from cyclic loading can be predicted by at least two numerical approaches. The first approach is to use a constitutive equation capable of accommodating the additional effects of cyclic loading. Many sophisticated models have been developed for this purpose, but they mostly require the use of numerous model parameters. In this approach the classical incremental method is required for repeated solution of the non-linear governing equations using a large number of steps for each cycle of loading. Application of this method for liquefaction analysis of an offshore foundation is not currently feasible because it requires excessive computational effort. In the second approach, a simpler methodology can be adopted which makes liquefaction analysis feasible. The conventional constitutive models, suitable for monotonic loading, with their well-tested structure are retained and the effects of cyclic loading are incorporated independently. This method is based on an experimental determination of soil behaviour under a large number of cycles, including measurements of the evolution of strain and pore pressure generation with cyclic loading. Such an approach has the advantage of simplicity and the most direct use of the experimental evidence, and for these reasons it is adopted in the present study.

A single ocean wave loading is usually applied to the soil within a relatively short time interval. As the time interval becomes shorter, the dynamic response may become important. However, in a relatively heavy storm, the higher wave components of the storm have large periods of the order of *10 sec* or more. Zienkiewicz and Bettess (1982) and Ishihara (1996) showed that the amplification effects of such cyclic loads, associated with dynamic response, may often be insignificant and thus can be ignored. Accordingly, in this study the wave induced forces are treated as static forces for the purpose of stress evaluation, and the amplitude of the cyclic shear stress is assumed to be directly proportional to the corresponding amplitude of the different wave forces.

Generalized governing equations for the behaviour of saturated sands under cyclic loading are given here. The formulations presented establish the basic model into which detailed constitutive relationships for any material type can be inserted. The equations are then simplified in the framework of the isotropic elastic stress-strain relationship. A practical procedure is developed to analyse the pore pressure response under offshore foundations. All elements of the analysis are illustrated in an example using the Ekofisk tank (Clausen

et al., 1975) as a case study. The validity and the limitations of the method are evaluated by comparing the results of the analysis with the observed behaviour of the tank.

5.2: DERIVATION OF GENERAL EQUATIONS

Liquefaction of granular soil is directly related to the deformation pattern of the soil mass. Therefore, the constitutive equations of the soil material are clearly of the highest importance in a liquefaction analysis. Nevertheless, the nature of the problem, irrespective of the detail of constitutive relations, requires a proper description of the interaction of the fluid and solid phases. With incorrect modelling of this interaction, the basic features of the physics governing the problem can be missed.

The most important feature of cyclic strain response is the tendency for cumulative densification which is responsible for such phenomena as liquefaction and loss of strength, particularly when the loading is undrained. All efforts will be concentrated on including this aspect in the stress-strain relationship. In this study, a method presented by Zienkiewicz *et al.* (1982) and also Booker (1996) will be used to include the additional accumulation of strains in the formulation of governing equations.

Cyclic loading on saturated granular soils can be viewed as an agency that causes a reorientation and repositioning of soil particles, which leads to a reduction in void spaces. As a consequence, in an undrained cyclic loading, water pressure in the voids rises and in a drained cyclic loading, displacement increases (Fig. 5.1). For the drained case, the change in the void spaces due to cyclic loading can be considered as a change in strain, $d\varepsilon^c$, within the soil.

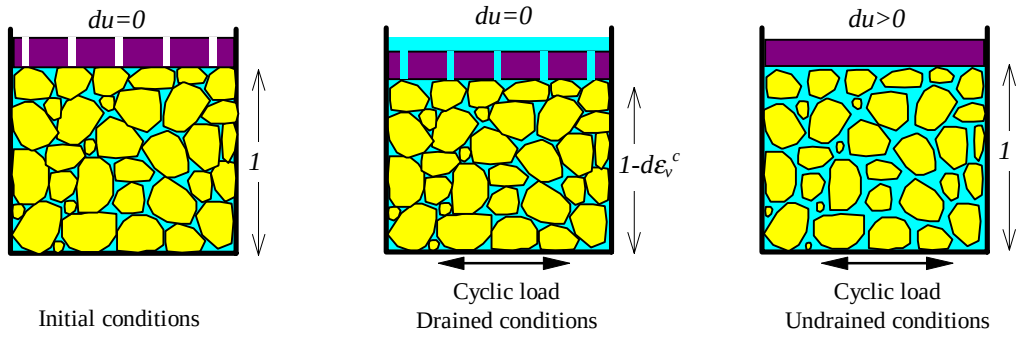

Fig. 5.1: Mechanism of change in pore water pressure or volume due to cyclic load under constant total stress

A reasonable approximation to the cyclic strain generated by cyclic load is to consider it to be isotropic, so that the cyclic strain vector, $d\varepsilon^c$, may be written as:

$$d\varepsilon^{c} = \frac{1}{3} e.d\varepsilon_v^{c} \qquad (5.1)$$

where $d\varepsilon_v^c$ is the change in the volumetric strain due to the change in the void volume and $e=(1,1,1,0,0,0)^T$.

The total strain increment, $d\varepsilon^t$, can be regarded as the sum of the changes of that part of the strain which is related directly to the ambient stress change, $d\varepsilon^s$, and that part of the strain which is generated by the cyclic loads, $d\varepsilon^c$, i.e.

$$d\varepsilon^t = d\varepsilon^s + d\varepsilon^c \qquad (5.2)$$

Retaining the basic elasto-plastic constitutive relationship (Equation 3.32), the general stress-strain relationship is given as:

$$d\sigma' = \boldsymbol{D}(d\varepsilon^t - d\varepsilon^c) \qquad (5.3)$$

in which $\boldsymbol{D}$ is the stiffness matrix of the solid skeleton.

Definition of effective and total stresses and their link with pore pressure gives:

$$d\sigma = d\sigma' + e.du \qquad (5.4)$$

where $d\sigma$ denotes change in total stress in the soil, and u is excess pore water pressure.

Substituting Equations (5.1) and (5.4) into Equation (5.3) yields:

$$d\varepsilon^t = e.d\varepsilon_v^c/3 + \boldsymbol{D}^{-1}(d\sigma - e.du) \qquad (5.5)$$

provided the matrix $\boldsymbol{D}^{-1}$ exists, a matter that is discussed below.

For a drained test, $du=0$, where the average stress level is held constant, i.e. $d\sigma=0$, Equation (5.5) shows that the strain produced by cyclic loading in the soil is an isotropic strain equal to $e.d\varepsilon_v^c/3$. For an undrained test, $e^T.d\varepsilon^t=0$, with a constant average stress level, $d\sigma=0$, the pore water pressure will rise to du_c due to cyclic loading. Therefore Equation (5.5) gives:

$$e^T.e.d\varepsilon_v^c/3 + e^T.\boldsymbol{D}^{-1}(-e.du_c)=0 \qquad (5.6)$$

Since $e^T.e=3$, it follows that

$$d\varepsilon_v^c = e^T.\boldsymbol{D}^{-1}.e.du_c \qquad (5.7)$$

where du_c represents the pore pressure generated by cyclic loading alone.

Equation (5.7) relates the pore pressure generated in an undrained cyclic test to the volumetric strain that will occur in a drained cyclic test under the same cyclic stresses. By this expression the volumetric strain and the pore water pressure induced by cyclic loading can be used interchangeably in all computations, provided that the inverse of the elasto-plastic stiffness matrix, $\boldsymbol{D}^{-1}$, exists. In most elasto-plastic models, $\boldsymbol{D}^{-1}$ can be evaluated before the ultimate

failure state, i.e. if the soil behaves elastically or hardens plastically. When the stress state reaches the ultimate failure condition $\boldsymbol{D}^{-1}$ may no longer exist. In this case no additional pore pressure is generated by cyclic loading. The use of pore pressure data obtained from undrained laboratory tests in Equation (5.7) is usually more convenient, as it represents the most direct connection between the results of experimental tests and subsequent calculations.

Substituting Equation (5.7) in (5.5) results in a general stress-strain relationship that can be used in the formulation of the finite element method for cyclic loading, i.e.

$$d\varepsilon^t = e.e^T.\boldsymbol{D}^{-1}.e.du_c/3+\boldsymbol{D}^{-1}(d\sigma-e.du) \qquad (5.8)$$

or in a more general form:

$$d\sigma - e.du = \boldsymbol{D}.d\varepsilon^t - \boldsymbol{D}.\, d\varepsilon^c \qquad (5.9)$$

in which:

$$d\varepsilon^c = e.e^T.\boldsymbol{D}^{-1}.e.du_c/3 \qquad (5.10)$$

Computationally, the term $d\varepsilon^c$ (or $\boldsymbol{D}\, d\varepsilon^c$) in Equation (5.9) can be regarded as an initial strain (or initial stress) in the standard finite element formulation. The effects of this extra term in the right-hand-side vector of the finite element equation are similar to the effects of application of extra forces to the soil mass. These extra forces would produce excess pore pressures under undrained conditions or settlements under drained conditions or a combination of excess pore pressures and settlements under partially drained conditions, such as the conditions frequently encountered for soils under offshore foundations.

Equation (5.9) presents a general form of stress-strain relationship that can be used to model the behaviour of saturated granular soils subjected to cyclic loading. The detailed constitutive relationships for any material type can be used in this equation provided $\boldsymbol{D}^{-1}$ can be found. In this chapter, the equation will be modified for an elastic material. Under certain conditions the same modification can also be applied to the elastic-perfectly- plastic material of the Mohr-Coulomb model, which is the subject of the studies in Chapter 6.

5.3: PROCEDURE FOR LIQUEFACTION ANALYSIS OF OFFSHORE FOUNDATIONS

The analysis of the potential for liquefaction in the soil near a foundation includes several important steps: the definition of a storm, the computation of initial stresses in the soil, the computation of cyclic shear strains or stresses within the soil continuum, the prediction of the generation of excess pore water pressure, and the computation of the dissipation of pore water pressure.

The following steps outline a procedure in a typical ocean wave-induced liquefaction analysis.

1): Establish the oceanographic parameters: This includes a study of historical ocean storm data to select the design storm. The deep ocean waves generated by the design storm and the distribution of waves of different heights should then be determined. Wave characteristics such as height, length and period should also be estimated.

2): Establish the design soil profile for the analysis: A number of offshore borings should be drilled to assess the sub-bottom soil profile and to define the characteristics of the different layers, i.e. the permeability, compressibility, and some other parameters required in defining the soil stress-strain relationship. Representative undisturbed samples should be taken for cyclic testing in the laboratory.

3): Estimate the cyclic shear strength of different soil layers: This is generally accomplished directly by performing cyclic tests on undisturbed samples obtained from potentially liquefiable layers.

4): Estimate the static ambient forces and moment applied to the foundation from the superstructure. This usually needs a static equilibrium analysis.

5): Estimate the wave induced cyclic forces on the structure and its foundation: This needs a knowledge of wave drag forces applied to different parts of the superstructure. The foundation forces and moment are generally estimated using a static equilibrium analysis. However, an approximate dynamic analysis of the superstructure might give more reliable cyclic loads for the foundation.

6): Estimate the distribution of stresses developed below the sea floor as a result of static ambient loads: This usually needs a finite element equilibrium analysis.

7): Divide the design storm into a number of parcels of waves of equal height. Each parcel may contain many waves. The storm is usually modelled in time by a sequence of parcels of waves of progressively larger height until the peak storm wave height is reached. After the peak, the height of the waves gradually decreases. The direction of each individual wave passage is assumed to lie in one direction, usually in the direction of ambient current and wind.

8): For each wave parcel, estimate the distribution of cyclic stresses developed below the sea floor as a result of the cyclic wave loads. This usually needs a separate finite element equilibrium analysis. The cyclic stresses are used only for estimation of pore pressures generated by the wave parcels.

9): For each wave parcel, perform a finite element consolidation analysis, incorporating the effects of the generation and dissipation of pore water pressures in the soil below the foundation. This usually requires a number of stages:

9-1): Calculate the excess pore pressures generated due to the application of the current parcel of waves. This stage will be explained in detail later.

9-2): Include the generated excess pore pressures in the finite element equations of consolidation.

9-3): Solve the equations of consolidation for dissipation of the pore pressures and calculation of any changes in displacements and stresses.

10): Continue the analysis for all parcels of waves by following all processes from Step *8* until all parcels of waves are finished and the end of the storm is reached.

5.4: CALCULATION OF PORE PRESSURE

The model proposed here for liquefaction analysis is based on the direct use of the results of undrained cyclic tests on saturated samples of soil in the finite element consolidation analysis. The pore pressure generated during the application of each parcel of waves should be calculated from the test data and used in the analysis.

The results of laboratory tests usually reveal two main characteristics of liquefiable soil; the cyclic strength of the soil and the rate of pore pressure generation. The cyclic strength is usually presented as the number of cycles of load which is required for liquefaction of the soil, N_l. As an example, the number of cycles required for liquefaction of a sand under various cyclic load levels, obtained from triaxial tests, is shown in Fig. 5.2. The cyclic strength of the soil depends upon many factors. The most important factors are the initial effective stress (i.e. initial vertical effective stress in simple shear tests, σ'_{vi}, or initial mean effective stress in triaxial tests, p'_i), the cyclic stress level (i.e. cyclic shear stress in simple shear tests, τ_c, or cyclic deviatoric stress in triaxial tests, q_c), and relative density, D_r.

The rate of generation of pore pressure during cyclic loading can be expressed in terms of normalized pore pressure and normalized number of load cycles. A pore pressure generation function has been defined by Seed *et al.* (1975a) as:

$$\frac{u_c}{u_{\max}} = \frac{2}{\pi} Arc\sin\left(\left(\frac{N}{N_l}\right)^{\frac{1}{2\alpha}}\right) \qquad (5.11)$$

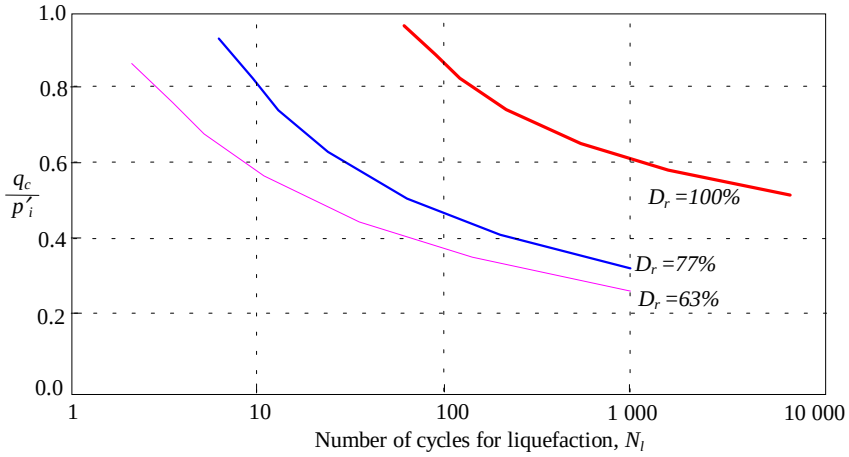

Fig. 5.2: Triaxial cyclic strength of the Ekofisk sand (Lee and Focht, 1975)

where u_c is the pore pressure generated after N cycles of load, N_l is the number of cycles which would cause liquefaction, u_{max} is the maximum achievable pore pressure at the onset of liquefaction, i.e. after the application of N_l cycles of load, and α is a parameter related to the pore pressure generation characteristics of the soil. The maximum pore pressure is usually defined based on the type of cyclic test and the definition of liquefaction. For example, in a simple shear test, liquefaction is characterised by a rise in pore water pressure to a value equal to the initial vertical effective stress, σ'_{vi}. Accordingly, the maximum pore pressure in this case is taken as σ'_{vi}. In a cyclic triaxial test on isotropically normally consolidated soil the maximum pore pressure is traditionally taken as the initial mean effective stress, p'_i, i.e. the consolidation cell pressure.

Equation (5.11) can be used in a liquefaction analysis to calculate the increment in pore pressure generated as a result of an increment in the number of load cycles, ΔN, applied under undrained conditions, provided that the amplitude of cyclic load does not vary during the analysis. However, in a real situation, the amplitude of cyclic load may change during a storm. The excess pore pressure may also be partially dissipated. Therefore, it is convenient that an equivalent number of cycles, N_{eq}, which represents the effects of previous cycles of loads of different amplitudes and dissipation of pore water pressure, is evaluated based upon the current value of excess pore pressure, i.e.

$$N_{eq} = N_l \left(Sin\left(\frac{\pi u}{2u_{\max}} \right) \right)^{2\alpha} \qquad (5.12)$$

where u is the current value of excess pore pressure and u_{max} is the maximum achievable pore pressure in the soil.

In deriving Equation (5.12), it was assumed that at any stage during cyclic loading the existing pore pressure, u, represents the effects of all cycles of load (including change in amplitude) that have been applied to the system in the past, and the effects of drainage.

The increment in excess pore pressure due to the further application of ΔN cycles of load of given amplitude under undrained conditions can now be calculated by the following equation.

$$\Delta u_c = \frac{2u_{\max}}{\pi} Arc\sin\left(\left(\frac{N_{eq}+\Delta N}{N_l}\right)^{\frac{1}{2\alpha}}\right) - u \qquad (5.13)$$

where u is the existing pore pressure in the soil.

The generated pore pressures will then be used in the finite element equations of consolidation using Equation (5.9). The equations of consolidation will be solved for dissipation of pore pressures over the period of the wave parcel, and therefore, any changes in pore pressures will be calculated. This process should be followed for all parcels of load cycles, ΔN_i, until all of the load cycles are finished. The process of liquefaction analysis is described schematically in Fig. 5.3.

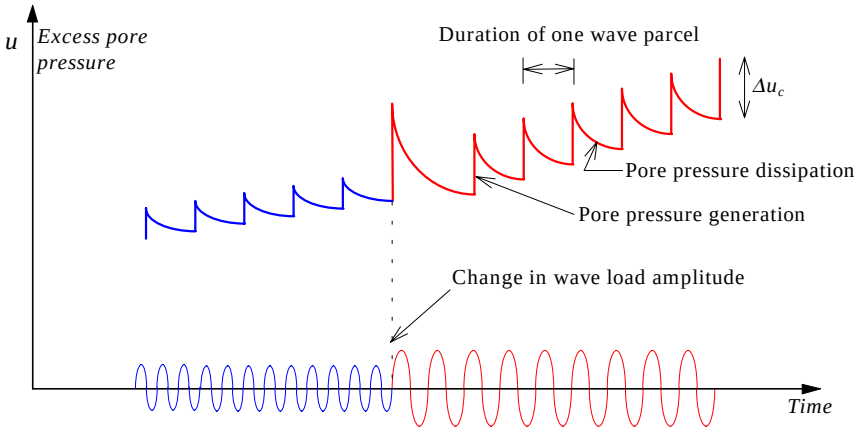

Fig. 5.3: Schematical representation of generation and dissipation of pore pressure in a liquefaction analysis

5.5: SIMPLIFICATION OF THE GENERAL EQUATIONS FOR AN ELASTIC CONSTITUTIVE MODEL

The general stress-strain relationship for the behaviour of saturated sands subjected to cyclic loading, Equation (5.9), can be simplified for use in a liquefaction analysis assuming an essentially elastic soil skeleton but allowing pore pressure accumulation under undrained cyclic loading.

The effects of cyclic loading have been considered in the general equation by including an additional term, $\boldsymbol{D}.d\boldsymbol{\varepsilon}^c$, in the finite element equation of consolidation. For an elastic soil skeleton, the additional term can be calculated from Equation (5.10) as:

$$\boldsymbol{D}^{e}.d\varepsilon^{c} = \boldsymbol{D}^{e}.e.e^{T}.\boldsymbol{D}^{e\,-1}.e.du_{c}/3 \qquad (5.14)$$

where $\boldsymbol{D}^{e}$ is the elastic stress-strain matrix. For any isotropic elastic stiffness matrix, it can be shown that:

$$\boldsymbol{D}^{e}.e.e^{T}.\boldsymbol{D}^{e\,-1}=3 \qquad (5.15)$$

Substituting Equation (5.15) into Equation (5.14) results in:

$$\boldsymbol{D}^{e}.d\varepsilon^{c} = e.du_{c} \qquad (5.16)$$

Therefore, Equation (5.9) is simplified for use in a modified elastic analysis as:

$$d\sigma - e.du = \boldsymbol{D}^{e}.d\varepsilon^{t} - e.du_{c} \qquad (5.17)$$

5.6: LIQUEFACTION ANALYSIS OF AN OFFSHORE FOUNDATION

Application of the modified elastic method in a liquefaction analysis of an offshore foundation is presented in this section. The offshore structure adopted in the analysis is the Ekofisk tank (Clausen *et al.*, 1975) which was constructed in the North Sea in 1973. The modified elastic stress-strain relationship of Equation (5.17) is used in the finite element analysis of consolidation. The results of the analysis will be compared with an existing approximate analytical solution as well as with data collected from the soil under the tank during storms.

5.6.1: Historical Background

The Ekofisk tank is a concrete structure which was installed in *70 m* of water in the North Sea on June 1973. The tank was constructed for oil storage to maintain production in bad weather. It has also been used as a production platform. The tank has a horizontal cross section shaped like a square with rounded corners. The oil is stored in nine interconnected compartments in the centre of the tank, surrounded by a perforated breakwater wall which reduces the wave forces on the structure.

The seabed beneath the tank consists of a fine sand to a depth of *26 m*. Interbedded in this sand layer at a depth of about *16-18 m* is a layer of stiff clay with low plasticity. Below *26 m*, hard clays are interbedded with sand layers to a great depth. In-situ cone penetration tests before installation of the tank indicated that the sand was very dense with a relative density of about *100%* in the upper few metres (Andersen, 1991).

The Ekofisk tank was instrumented to measure oceanographic data, pore pressures in the soil directly under the foundation, and the settlement and tilt of the tank (Clausen *et al.*, 1975). The instrumentation included strain gauges, uplift pressure gauges, piezometers, inclinometers, etc. The piezometers were placed at depths up to *23 m* below the foundation.

As mentioned previously, the tank was subjected to several major storms after installation. The most severe storm occurred shortly after installation of the tank, on 19 November 1973, with an estimated maximum wave height of about *21 m*. Unfortunately the recording system was out of operation at that time. The most severe storm in which foundation performance was measured occurred on 6 November 1973. The maximum wave height was about *16 m* which caused the pore pressure in the upper sand layer to rise by *10-20 kPa* (Clausen *et al.*, 1975). The settlement of the tank increased by *0.02 m* during the storm. During the period of severe storms, on 15-20 November, the tank settled an additional *0.03-0.05 m*. It was believed that the maximum pore pressure at the base of the footing reached up to *40 kPa* during the storm on 19 November 1973 (Clausen *et al.*, 1975). The generation of excess pore pressures during storms indicates that liquefaction of even very dense sand deposits is a possibility that must be considered carefully in the design of offshore structures.

Liquefaction analysis of the Ekofisk tank was the subject of many studies before and after the installation of the tank. The first and simplest form of study was performed by Bjerrum (1973), in which the effects of drainage and stress distributions in the soil under the foundation were completely ignored. Lee and Focht (1975) extended the method presented by Bjerrum and considered the effects of pore pressure dissipation during storm loading using results from experimental studies. In their work, the results of a series of cyclic load tests on samples of sand, obtained under partially drained conditions, were used. This method also ignores the distribution of stresses in the soil. The same test results were used for all elements of the soil regardless of the drainage conditions and position of the elements beneath the tank. Rahman *et al.* (1977) presented a numerical solution to the problem by considering the effects of stress distribution in the soil profile as well as pore pressure dissipation. Results of a standard type of cyclic simple shear test were used to evaluate the generation of pore pressure during cyclic loading. The distribution of stresses was evaluated using the theory of elasticity. The problem of pore pressure dissipation was then approximated in an axi-symmetric finite element system. Verruijt and Song (1991) also employed a two dimensional plain strain coupled finite element analysis to examine the problem. A function was used to model the volumetric strain due to cyclic loading. In their analysis, the maximum achievable pore pressure, generated at each point in the soil, was limited to a value less than the initial mean effective stress.

The main problem in the method presented by Rahman *et al.* (1977) is the approximation made in using the axi-symmetric analysis of pore water flow. The distribution of cyclic stresses is three-dimensional, and thus, the pore water pressure generated during cyclic loading will not be axi-symmetric. The method has been used widely by other researchers, though to date none has presented a better solution to tackle the three-dimensional nature of

the problem. Although this method is also applicable in a standard three-dimensional finite element analysis, the computational time required in such an analysis is excessive because in a liquefaction analysis usually the whole process of generation and dissipation of pore pressure must be followed hundreds of times for all waves during a storm. The semi-analytical approach in the finite element method, presented in Chapter 3, is an efficient alternative to the standard three-dimensional finite element analysis. This method can be used for generation and dissipation of pore water pressure in three-dimensional space. Application of Equation (5.17) in the stress-strain relationship can provide an insight into the stress paths that elements of soil may follow during storm loading.

5.6.2: Definition of the Problem

The Ekofisk tank has a diameter of *93 m* and a height of *90 m*. It rests on a *26 m* layer of sandy seabed which overlays a stiff clay stratum. The mean water depth is *70 m* (Fig. 5.4).

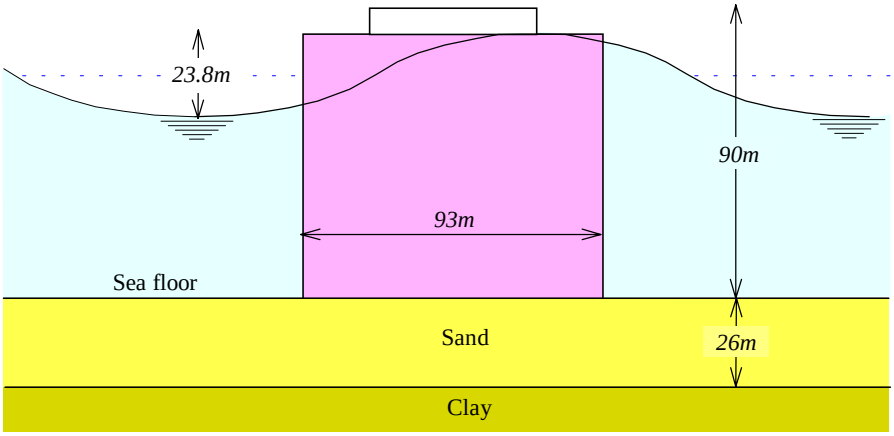

Fig. 5.4: Geometry of the Ekofisk tank

The permeability of the sand in the Ekofisk field is of the order of 10^{-5} *m/sec* (Bjerrum, 1973). The coefficient of volume compressibility is $m_v=1.73\times10^{-5}\ m^2/kN$ (Rahman *et al.*, 1977). Assuming a Poisson's ratio of $\nu=0.25$, the drained Young's modulus of the sand can be calculated from the value of m_v, as $E'=48000\ kN/m^2$. The saturated unit weight of the sand varies between *13.4* to *17.6* kN/m^3. However, a value of $\gamma_{sat}=17.3\ kN/m^3$, which was used by Rahman and his co-workers, is also adopted in this study. The initial value of the coefficient of lateral earth pressure is assumed to be $K_o=0.5$.

The design storm has a return period of *100* years. The characteristics of waves assumed in the design storm, presented by Rahman *et al.* (1977), are shown in Table 5.1. For purposes of economy and convenience, Rahman *et al.* replaced, in their analysis, the time history of the design storm by that of an equivalent storm producing approximately the same effects. Both the design storm and the equivalent storm are shown in Fig. 5.5. In the present study the effects of both time histories on the response of the foundation will be demonstrated.

Table 5.1: Characteristics of waves in the design storm

Wave group	Wave height (*m*)	Wave period (*sec*)	Number of waves	Duration (*sec*)	Elapse time (*sec / hrs*)
1	0.6	5.0	236	1180	1180 / 0.33
2	2.0	7.2	235	1692	2872 / 0.80
3	6.0	10.0	243	2430	5302 / 1.47
4	10.0	11.5	235	2702	8004 / 2.22
5	14.0	12.5	141	1762	9766 / 2.71
6	18.0	13.2	61	800	10566 / 2.94
7	22.0	13.4	16	214	10780 / 2.99
8	25.0	13.5	3	40	10820 / 3.01
9	22.0	13.4	16	214	11034 / 3.07
10	18.0	13.2	61	800	11834 / 3.29
11	14.0	12.5	141	1762	13596 / 3.78
12	10.0	11.5	235	2702	16298 / 4.53
13	6.0	10.0	243	2430	18728 / 5.20
14	2.0	7.2	235	1692	20420 / 5.67
15	0.6	5.0	236	1180	21600 / 6.00

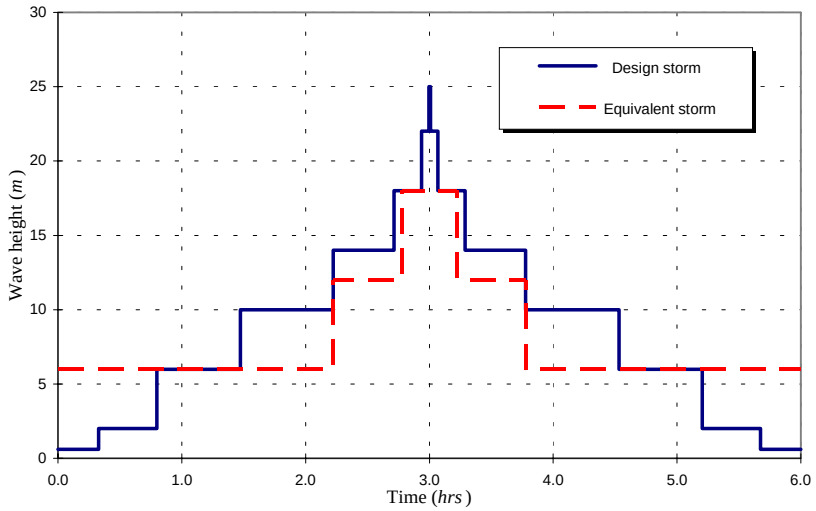

Fig. 5.5: Histogram of the *100 yr* design storm and the equivalent storm

The results of triaxial tests on saturated samples of sands from the Ekofisk field have been presented in Fig. 5.2. Data obtained from simple shear tests on saturated samples of the sand are shown in Fig. 5.6. Although the relative density of the sand was found to be close to $D_r=100\%$, some of the analyses will also be conducted for a relative density of *77%*, in order to compare the results of this study with those obtained by Rahman *et al.* (1977). The rate of pore pressure generation during cyclic loading was defined by the mathematical expression of Equation (5.11), with a pore pressure generation parameter of $\alpha=0.7$ (Rahman

et al., 1977). The effects of initial shear stresses on the cyclic strength of the sand were evaluated by Rahman in an approximate manner. However, these effects are ignored in this study, since no relevant experimental data are available for the Ekofisk sand.

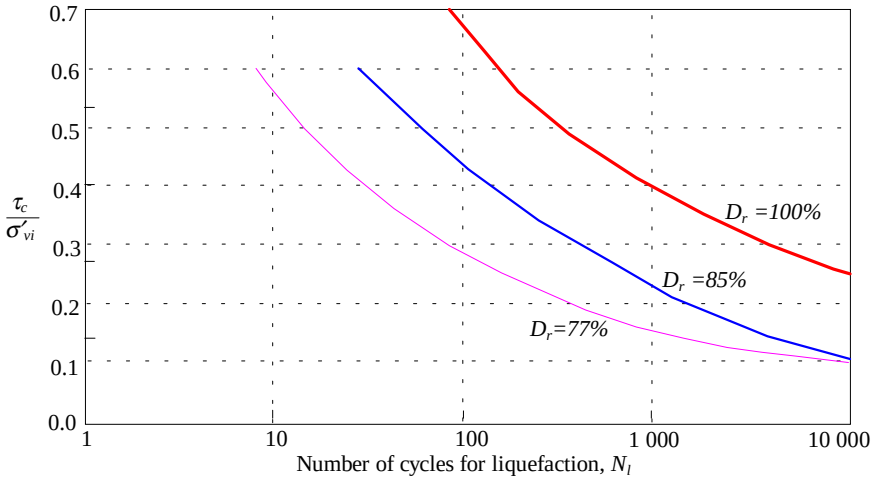

Fig. 5.6: Cyclic strength of Ekofisk sand in simple shear test (used by Rahman *et al.*, 1975)

The submerged weight of the Ekofisk tank is about *1900 MN*. The forces that are generated by the storm waves may be evaluated from the MacCamy and Fochs (1954) formula derived from diffraction theory (as reported by Rahman *et al.*, 1977). Variations of the lateral force and moment on the base of the footing are shown in Fig. 5.7. Rahman *et al.* (1977) compared these values with those obtained from laboratory model tests. They concluded that due to the effects of breakwater baffles surrounding the tank, only *80%* of the lateral force and moment computed from diffraction theory would actually be applied to the foundation. The reduced values for the lateral load, H_c, and the moment, M_c, will be used in the present analyses. For simplicity, the moment is considered as $M_c=36\times H_c$. Fig. 5.7 indicates that this linear approximation is reasonable. The effects of cyclic vertical force were found to be very small and this force is therefore ignored in the analyses.

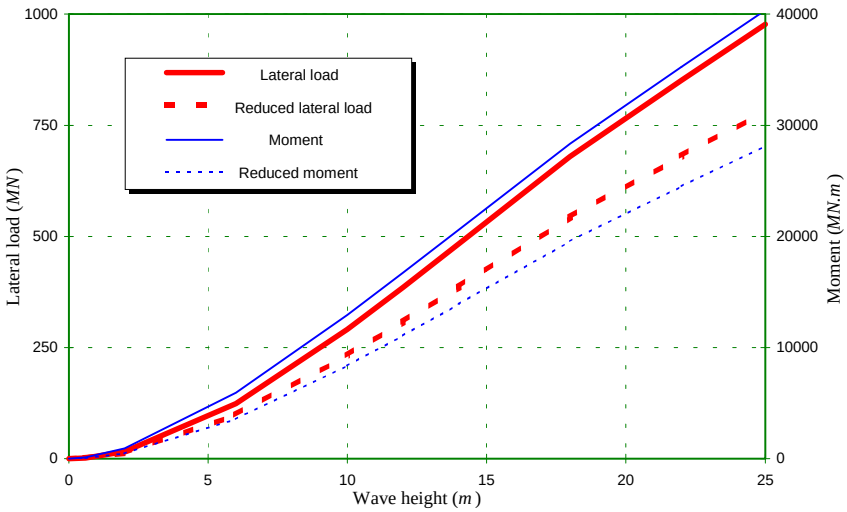

Fig. 5.7: Variation of cyclic lateral load and moment with wave height

5.6.3: Finite Element Analysis

The finite element mesh used in the analysis is presented in diametral cross-section in Fig. 5.8. In order to reduce the effects of rigid boundaries on stress distribution within the sand layer, a layer of clay with a thickness of *24 m*, with the same elastic properties as the sand, is included under the sand layer. The clay layer and the interface between the foundation and the sand are assumed to be impermeable. Perfect drainage was assumed on the remaining parts of the boundary.

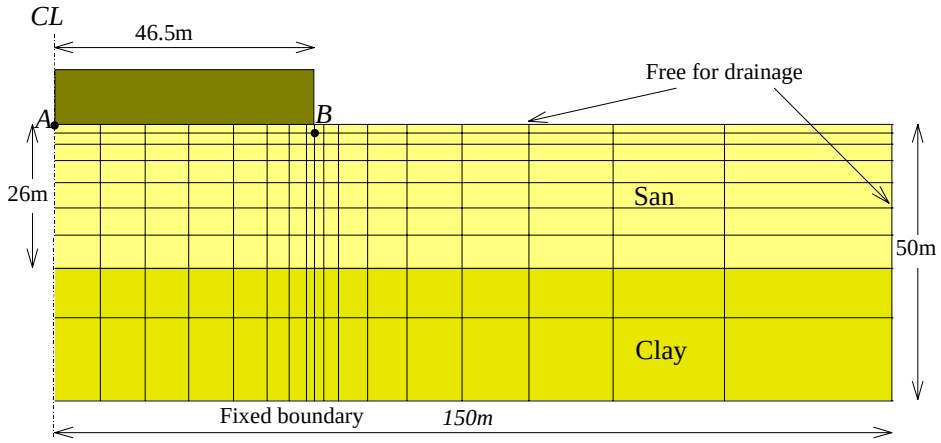

Fig. 5.8: Finite element mesh

The problem will be analysed with various assumptions related to liquefaction criteria, flexibility of the foundation, and cyclic shear stress. Table 5.2 sets out the assumptions that will be made in each analysis. The method of analysis is, in principle, very close to the method presented by Rahman *et al.* (1977). Therefore, the results of the analysis should be comparable with the existing solution presented by Rahman *et al.* (1977). The liquefaction criterion used by Rahman will be used in the first analysis. The results will be compared and the effects of the other factors will be considered in the subsequent analyses.

Table 5.2: Assumptions made for different analyses

Analysis Number	Type of Foundation	Cyclic stress	Maximum pore pressure	Relative Density	Storm Histogram	Experimental data
1st analysis	Flexible	Radial shear stress	Initial vertical effective stress	*77%*	Equivalent Storm	Rahman *et al.* (1977)
2nd analysis	Rigid	Radial shear stress	Initial vertical effective stress	*77%*	Equivalent Storm	Rahman *et al.* (1977)
3rd analysis	Rigid	Total shear stress	Initial vertical effective stress	*77%*	Equivalent Storm	Rahman *et al.* (1977)
4th analysis	Rigid	Total shear stress	Initial vertical effective stress	*100%*	Equivalent Storm	Rahman *et al.* (1977)
5th analysis	Rigid	Deviatoric shear stress	Initial mean effective stress	*100%*	Equivalent Storm	Rahman *et al.* (1977)
6th analysis	Rigid	Deviatoric shear stress	Initial mean effective stress	*100%*	Design storm	Rahman *et al.* (1977)
7th analysis	Rigid	Deviatoric shear stress	Initial mean effective stress	*100%*	Design storm	Lee & Focht (1975)

First analysis

Rahman *et al.* (1977) defined the onset of liquefaction of a soil as a condition when the excess pore water pressure in the soil increases to a value equal to the initial vertical stress, σ'_{vi}. Based on this assumption, the maximum achievable pore pressure is $u_{max} = \sigma'_{vi}$. A distribution of stresses was obtained based on the solutions for a flexible square footing on an elastic half space. The horizontal cyclic shear stresses were used for generation of pore pressure.

In this analysis, the liquefaction data for the soil with a relative density of $D_r = 0.77\%$, presented by Rahman *et al.*, are used. In order to make the results of this analysis comparable with the solution obtained by Rahman *et al.*, the foundation of the tank is considered to be flexible. The histogram of the equivalent storm is used in this analysis. The onset of liquefaction is assumed to be the same as that defined by Rahman and his co-workers. Radial cyclic shear stresses (Fig. 5.9) are used in this analysis to define the intensity of cyclic loads used to generate excess pore pressure.

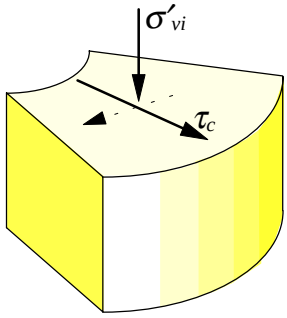

Fig. 5.9: Definition of stresses in the first analysis

The variation of the pore pressure ratio, u/σ'_{vi}, predicted from this analysis is compared with the solution presented by Rahman *et al.* (1977) in Fig. 5.10. The pore pressure ratio at the edge of the footing is obtained from a point *1.5 m* below the edge of the foundation in the plane of the lateral cyclic load, i.e. point (*B*) in Fig. 5.8. The predictions obtained from the finite element analysis are generally greater than those presented by Rahman *et al.* (1977). The pore pressure ratio predicted at the centre of the foundation is about double the ratio presented by Rahman *et al.* (1977). The pore pressure ratio predicted at the point below the edge of the foundation is greater than the ratio calculated by Rahman *et al.* for most of the time during the storm. However, the stress ratio at this point falls below the ratio presented by Rahman *et al.* during the last *2 hrs* of the storm. The differences in the variations of pore pressures can be attributed to the different stress distributions in the soil.

The distribution of the pore pressure ratio predicted at the storm peak, i.e. *3.22 hrs* after the beginning of the storm, in the vertical plane of the applied lateral cyclic load, is presented in

Fig. 5.11. The pore pressure ratio reaches $u/\sigma'_{vi} = 1.0$ at a zone close to the surface adjacent to the foundation, indicating liquefaction. In the solution presented by Rahman *et al.*, no part of the soil "liquefied", according to the adopted definition of liquefaction.

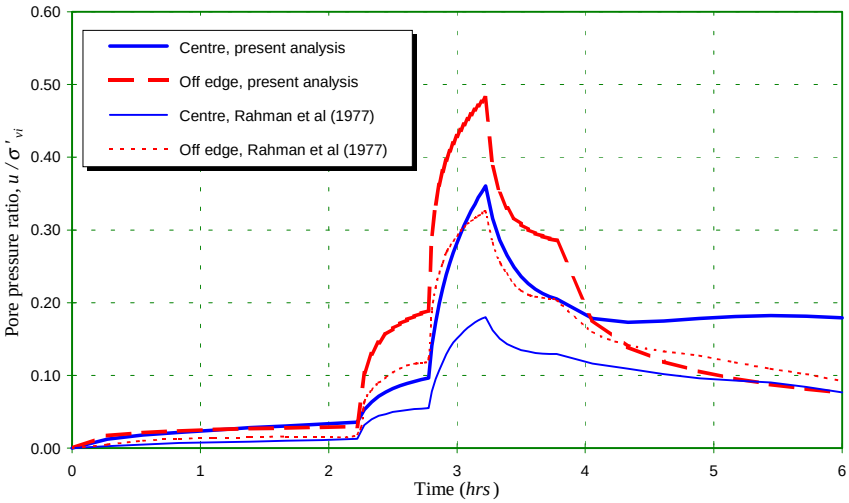

Fig. 5.10: Comparison of the pore pressure ratio predicted from the first analysis with those obtained by Rahman *et al.* (1977)

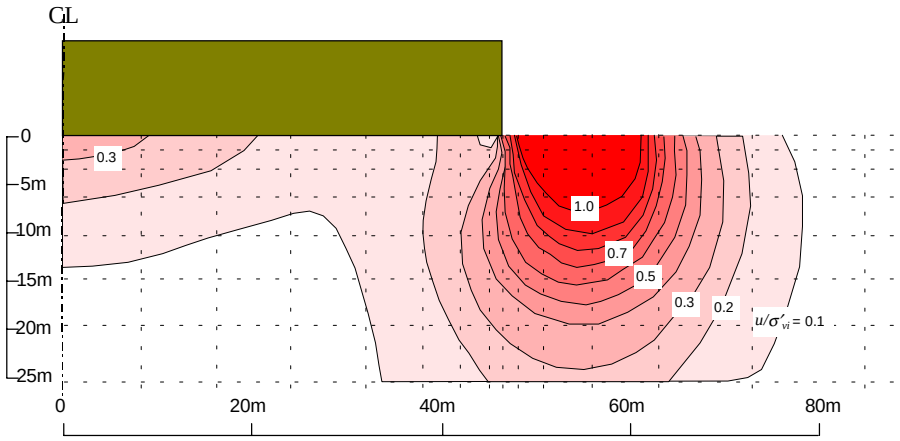

Fig. 5.11: Distribution of pore pressure ratio at the storm peak, flexible footing, 1st analysis

The distribution of pore pressure in the soil at the storm peak is shown in Fig. 5.12. The pore pressure at the centre of the footing reaches *88 kPa*. The maximum pore pressure is generated at a depth of about *9 m* below the edge, with a value of *128 kPa*. The variation of pore pressure with time is illustrated in Fig. 5.13. The pore pressure at point (*B*), *1.5 m* below the edge, is less than the pore pressure at the centre of the foundation for most of the time during the storm.

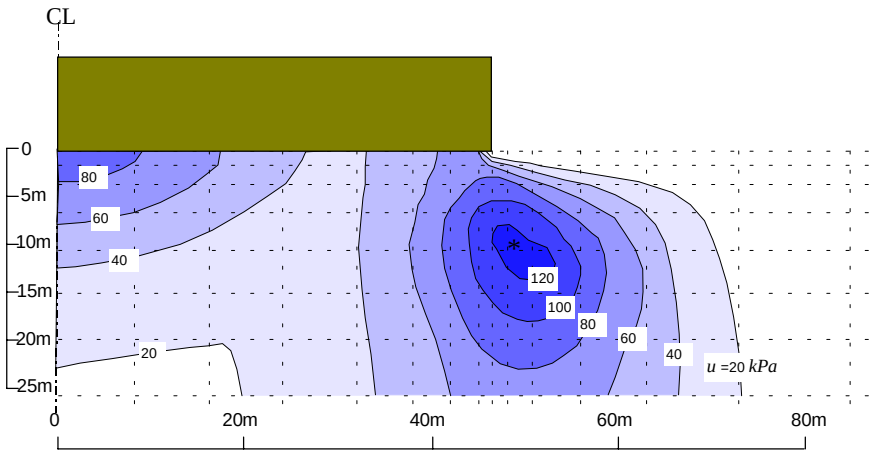

Fig. 5.12: Distribution of pore pressure at the storm peak, flexible footing, 1st analysis

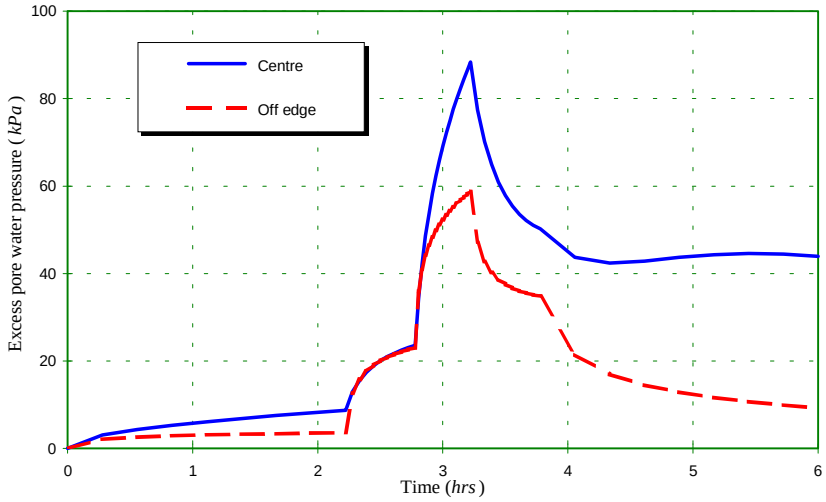

Fig. 5.13: Variation of excess pore pressures with time, flexible footing, 1st analysis

Second analysis

In this analysis, all of the assumptions made in the first analysis are retained except that the foundation is considered to be rigid. Under this assumption the distribution of stresses in the soil under the tank is changed. As a consequence, the pore pressures generated due to the storm loading beneath the foundation increase. The variations of pore pressures with time at the centre and the edge of the footing (Points *A* and *B* in Fig. 5.8) are shown in Fig. 5.14. The variations of pore pressures predicted in the first analysis with the flexible footing are also presented. The pore pressures at the edge of the footing in both analyses are very similar, while a significant difference between the pore pressures predicted at the centre of the rigid footing and the flexible footing can be observed. The value of the pore pressure at the centre of the rigid footing is less than that predicted at the centre of the flexible footing at the storm peak, i.e. *3.22 hrs.* after the beginning of the storm. However, the pore pressure under the

rigid footing continues rising after the peak and reaches a value of about *95 kPa* at a time of *4.3 hrs*, while the pore pressure under the flexible footing reduces after the storm peak.

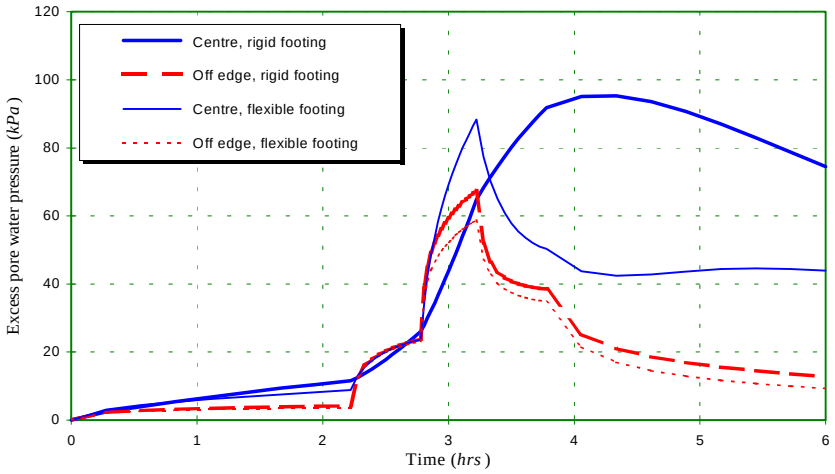

Fig. 5.14: Comparison of pore pressures predicted for flexible and rigid foundations

The pore pressure ratio in the soil at the storm peak, predicted from the second analysis, is shown in Fig. 5.15. A liquefaction zone can be observed adjacent to the footing close to the surface. The distribution of pore pressure at the storm peak is also presented in Fig. 5.16, which is significantly different from the pore pressure distribution under the flexible footing. At most locations, pore pressures beneath the rigid foundation are generally larger than those predicted from the previous analysis. The maximum pore pressure at the storm peak reaches *123 kPa* at a point about *9 m* below the edge of the foundation.

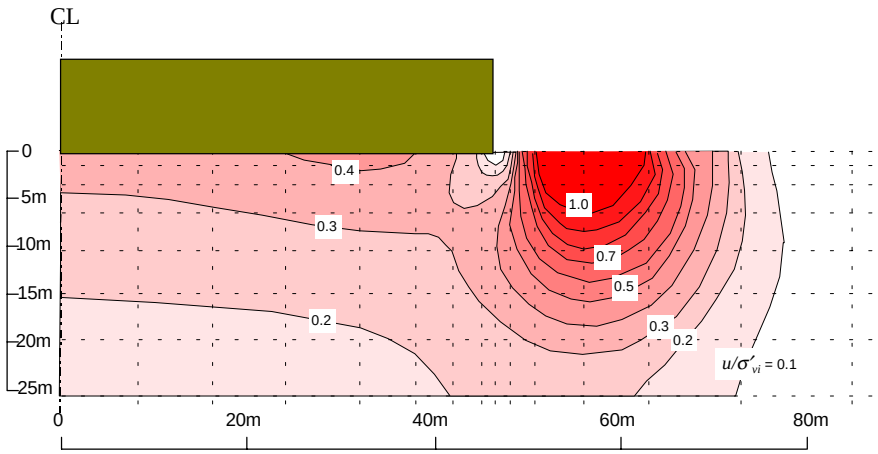

Fig. 5.15: Distribution of pore pressure ratio at the storm peak, rigid footing, 2nd analysis

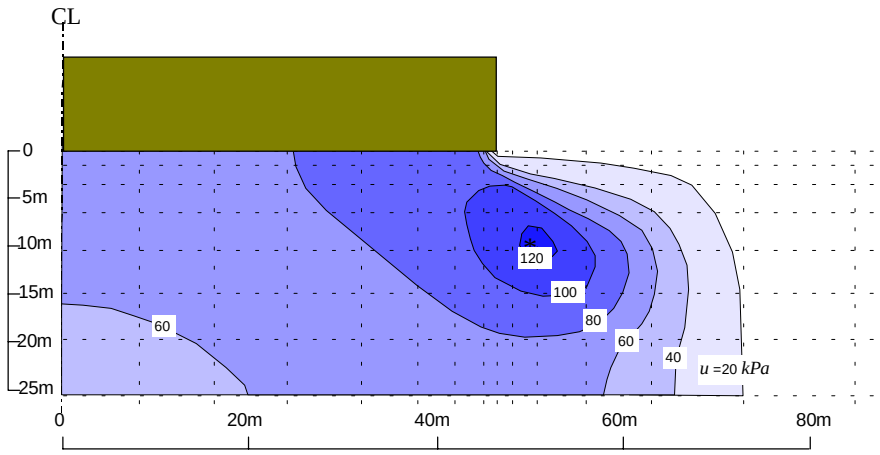

Fig. 5.16: Distribution of pore pressure at the storm peak, rigid footing, 2nd analysis

Third analysis

This analysis is the same as the second analysis, with a rigid footing, except that the definition of cyclic shear stress is changed. Cyclic shear stress is taken as the resultant of the two components of cyclic shear stresses in the horizontal plane (termed the total shear stress), as shown in Fig. 5.17.

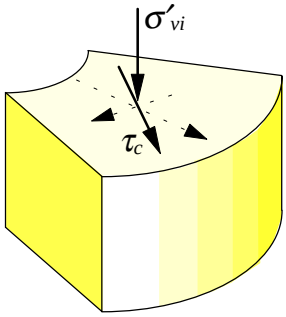

Fig. 5.17: Definition of stresses in the third analysis

The variations of pore pressures predicted from the second and the third analyses are compared in Fig. 5.18. With the new assumption, an increase of about *10%* in pore pressures can be observed for much of the storm duration. However, the general trends of the pore pressure variations are similar in both analyses. The maximum pore pressure at the centre of the foundation is about *109 kPa*, which is predicted at time *4.3 hrs*. The distributions of the pore pressure ratio and excess pore pressure, presented in Figs. 5.19 and 5.20, are very similar to those predicted in the second analysis. Pore pressure at the storm peak reaches *128 kPa* under the edge of the foundation at a depth of about *9 m*.

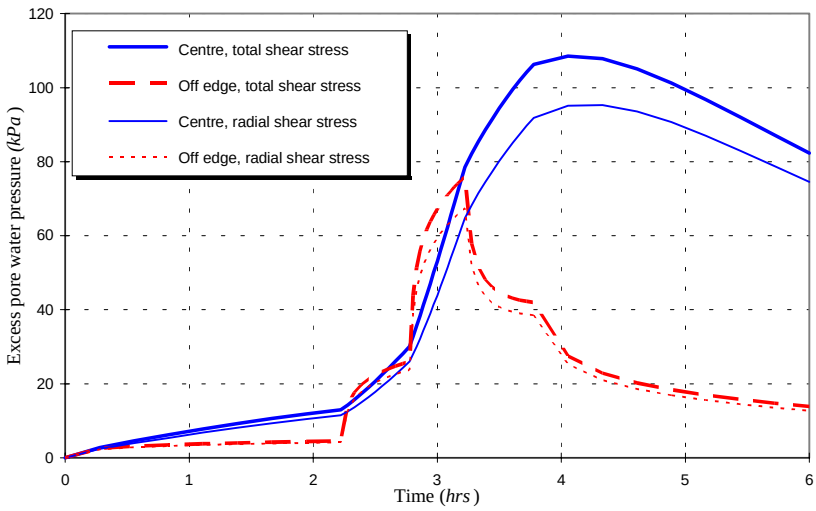

Fig. 5.18: Effects of application of total shear stress instead of radial shear stress on variation of pore pressures

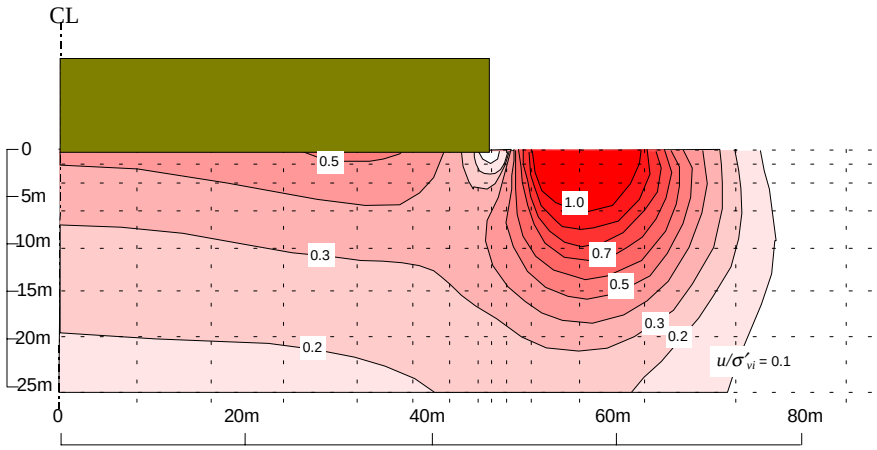

Fig. 5.19: Distribution of pore pressure ratio at the storm peak, rigid footing, total shear stress

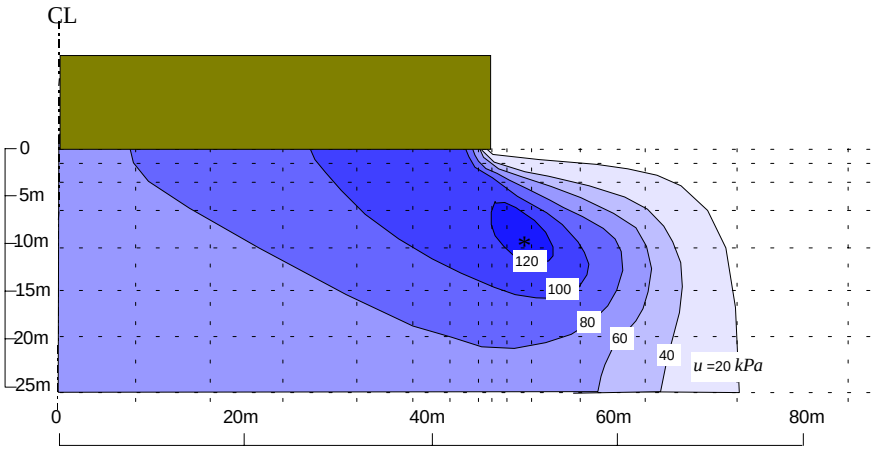

Fig. 5.20: Distribution of pore pressure at the storm peak, rigid footing, total shear stress

Fourth analysis

The relative density of the sand under the foundation has been found to be close to D_r=*100%*. As reported by Clausen *et al.* (1975), the in-situ penetration resistance was compared to the penetration resistance for the cone in a laboratory calibration chamber filled with Ekofisk sand and compacted to different known densities. This comparison indicated that the relative density of the sand was greater than *100%*. Therefore, for consistency the liquefaction data corresponding to the sand with a relative density of D_r =*100%* should be used in the liquefaction analysis of the tank.

Keeping all the assumptions made in the third analysis, the liquefaction data for the sand with a relative density of *100%* are used in the fourth analysis.

The variations of pore pressures with time predicted in the third and fourth analyses are compared in Fig. 5.21. The pore pressures predicted from the analysis with D_r =*100%* are significantly less than those predicted by the previous analyses. Clearly, relative density has a very important influence on the generation of pore water pressure during storm loading. The maximum pore pressure reaches only *13 kPa* while the average pore pressure under the foundation is about *10 kPa*. This prediction is also less than the observed pore pressure under the tank.

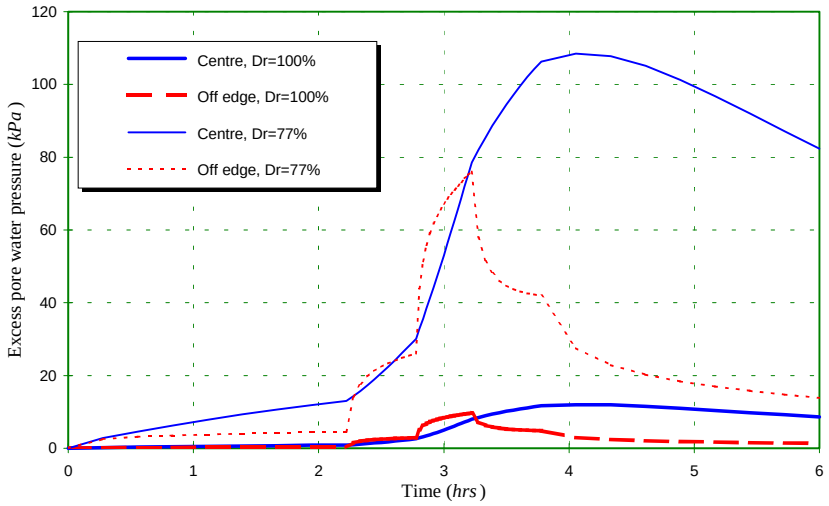

Fig. 5.21: Comparison of pore pressures predicted for sands with relative densities of 77% and 100%

The pore pressures measured at several points under the tank on 6 December 1973 were *10-20 kPa*. It was also believed that due to the most severe storm on 19 November 1973, which had a probable maximum wave height of *21 m*, corresponding to *90%* of the *24 m* high design wave, the pore pressure would have increased up to approximately *40 kPa*, as estimated by Clausen *et al.* (1975). Taking into account the severity of the *100 yr* design storm

and the loading sequence used in the analyses, the pore pressures predicted by the finite element analysis are expected to be greater than *40 kPa*.

5.6.4: Alternative Liquefaction Criterion

An alternative criterion for liquefaction can be defined as a condition where excess pore pressure increases to a value equal to the initial mean effective stress in the soil. In this case generation of pore pressure is assumed to be a function of the cyclic stress ratio, q_c/p'_i, where p'_i is the initial mean effective stress produced in the soil after the application of the ambient load, and q_c is the cyclic deviatoric shear stress. The cyclic deviator stress is obtained by calculating the difference between the initial deviator stress resulting from the ambient loads, q_i, and the deviator stress resulting from the application of the ambient and the maximum cyclic loads together, q_{i+c}. In some cases, the cyclic deviatoric stress obtained by application of cyclic loads in the positive direction (increasing q) may be different from the cyclic deviatoric stress obtained by application of cyclic loads in the negative direction. Therefore, the average value of cyclic deviatoric stresses, resulting from the application of cyclic loads in both directions, is used in the analyses (Fig. 5.22), i.e.

$$q_c = \frac{(q_{i+c} - q_i) + (q_i - q_{i-c})}{2} \qquad (5.18)$$

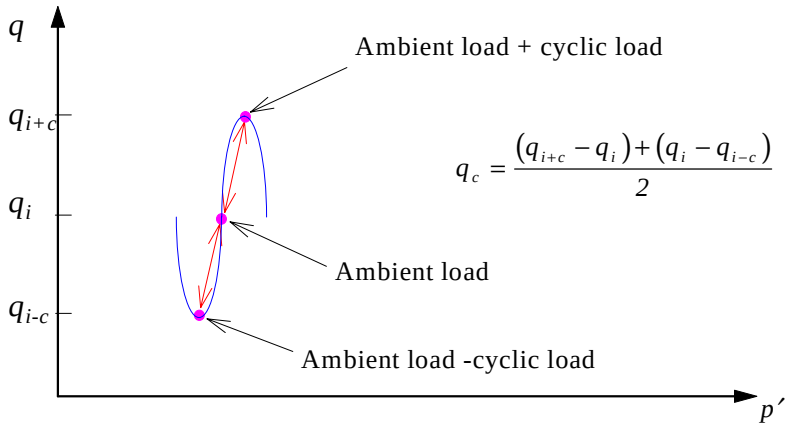

Fig. 5.22: Definition of cyclic deviatoric stress

The liquefaction data obtained from triaxial tests by Lee and Focht (1975), Fig. 5.2, are suitable to be used directly with the alternative liquefaction criterion. However, in order to obtain a valid comparison of the results of the analysis using the new criterion with those obtained previously, the simple shear test data presented by Rahman *et al.* (1977) are converted to triaxial stress conditions and will be used in the liquefaction analysis. Seed and Peacock (1971) introduced several conversion factors which depend on various liquefaction criteria. For the liquefaction criterion defined in this section, they suggested that the

liquefaction data obtained from simple shear tests can be converted to triaxial stress conditions according to the following equation.

$$\frac{\tau_c}{\sigma'_{vi}} = \frac{1+2K}{3}\left(\frac{q_c}{2p'_i}\right) \qquad (5.19)$$

where K is the coefficient of lateral pressure in the simple shear test. Assuming isotropic consolidation conditions for soil samples, i.e. $K=1.0$, the cyclic stress ratio obtained from the simple shear tests should be multiplied by 2 to be converted to the cyclic ratio in triaxial stress conditions, i.e.

$$\left(\frac{q_c}{p'_i}\right)_{triaxial} = 2\times\left(\frac{\tau_c}{\sigma'_{vi}}\right)_{simpleshear} \qquad (5.20)$$

The converted simple shear data for various values of K are compared with the data obtained by Lee and Focht (1975) from triaxial tests in Fig. 5.23.

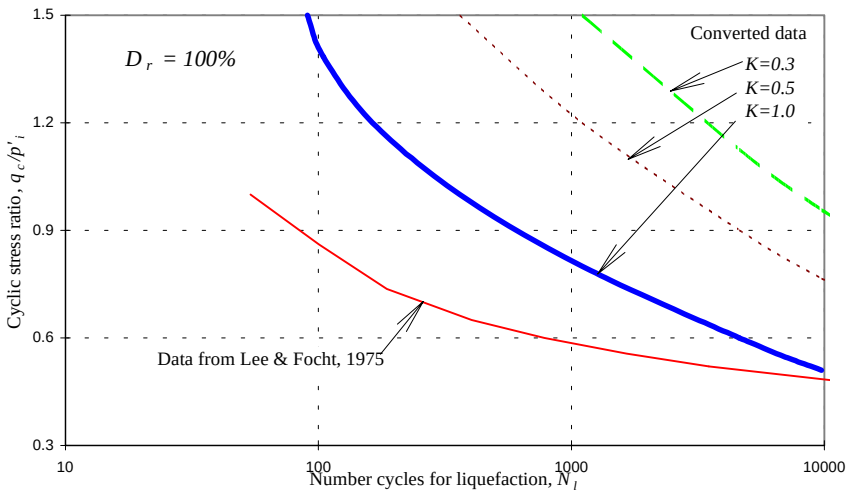

Fig. 5.23: Comparison of the data obtained indirectly from Rahman *et al.* (1977) and the test data presented by Lee and Focht (1975)

Fifth analysis

The converted data from simple shear tests, assuming $K=1.0$, are used in this analysis. It is assumed that liquefaction occurs if the generated excess pore pressure reaches the value of the initial mean effective stress.

The variation of pore pressure with time, predicted from this analysis, is presented in Fig. 5.24. Also shown in Fig. 5.24 are the results obtained from the previous analysis with the simple shear test data for the sand with a relative density of *100%*. The pore pressures predicted from this analysis are slightly greater than those predicted in the previous analysis. However, the maximum value of pore pressure is still less than that observed by Clausen *et al.* (1975).

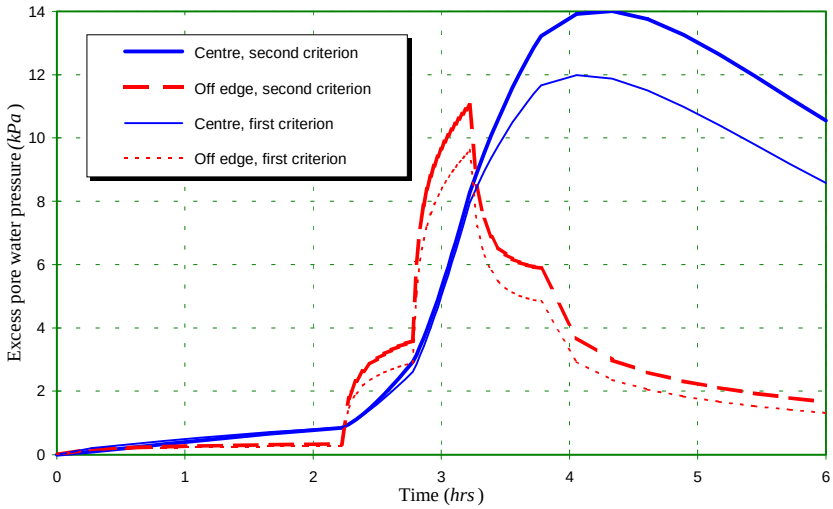

Fig. 5.24: Comparison of the results of analyses obtained from two liquefaction criteria:
1- using the vertical effective stress and cyclic shear stress in the horizontal plane
2- using the mean effective stress and cyclic deviatoric stress

Sixth analysis

The effects of the time history of the storm on the pore pressures generated under the foundation are evaluated in this analysis. The time history of the equivalent storm, used in the previous analyses, is replaced by that of the design storm (see Fig. 5.5 for a comparison of the equivalent and design storms). All other assumptions made in the fifth analysis are retained. The predicted pore pressure at the centre of the footing reaches *18.7 kPa* (Fig. 5.25) which shows an increase of about *33%* compared to the pore pressure predicted using the time history of the equivalent storm. However, the maximum pore pressure is still less than that observed by Clausen *et al.* (1975).

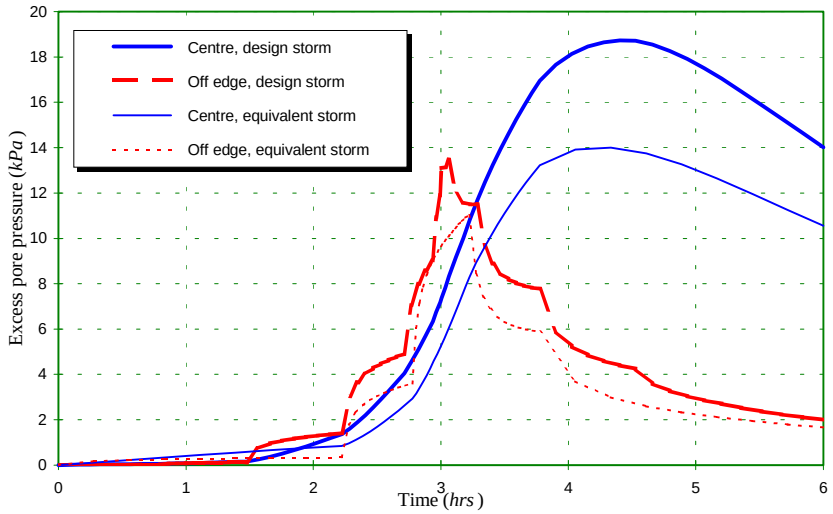

Fig. 5.25: Effects of different time histories of the storm on the pore pressure response of the soil under the foundation

There exists some degree of uncertainty in the liquefaction data converted from the simple shear test results. The actual coefficient of lateral pressure in the simple shear test is unknown, and as the results in Fig. 5.23 reveal, the conversion is quite sensitive to the assumed value of *K*. Besides, it is quite unlikely that the sand could withstand a cyclic deviator stress in the order of $q_c \geq 1.5p'_i$, as indicated by the converted data shown in Fig. 5.23. It is more logical to use the data obtained directly from triaxial tests. This option is examined in the following section.

Seventh analysis

The liquefaction data obtained from triaxial tests by Lee and Focht (1975) are used in this analysis. All other assumptions are the same as those made in the previous analysis. The histogram of the design storm is used in this analysis. The variation of pore pressure with time, predicted in this analysis, is presented in Fig. 5.26. Pore pressure at the edge of the foundation reaches a maximum value of *24 kPa* at the storm peak, while the maximum pore pressure at the centre of the foundation is generated *4.5 hrs* after the storm began, with a value of *44 kPa*. Shown also in Fig. 5.26 are the pore pressures predicted in the sixth analysis, with the liquefaction data converted from simple shear tests presented by Rahman *et al.* (1977). An increase of about *130%* in pore pressures is predicted when the liquefaction data obtained by Lee and Focht (1975) are used in the analysis.

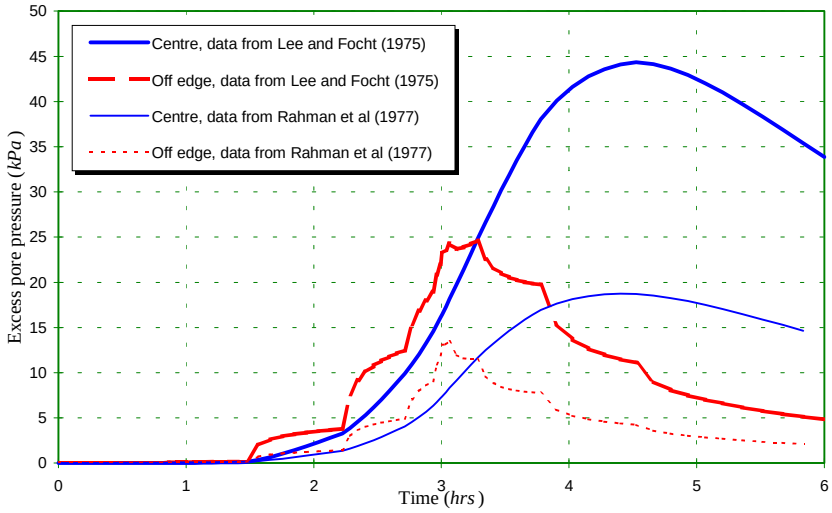

Fig. 5.26: Comparison of pore pressures predicted using two different sets of liquefaction data

The distribution of pore pressure predicted at the storm peak, i.e. at time *3.01 hrs*, is presented in Fig. 5.27. The maximum pore pressure at this time is about *46 kPa* which is generated at a depth of about *9 m* below the edge of the footing.

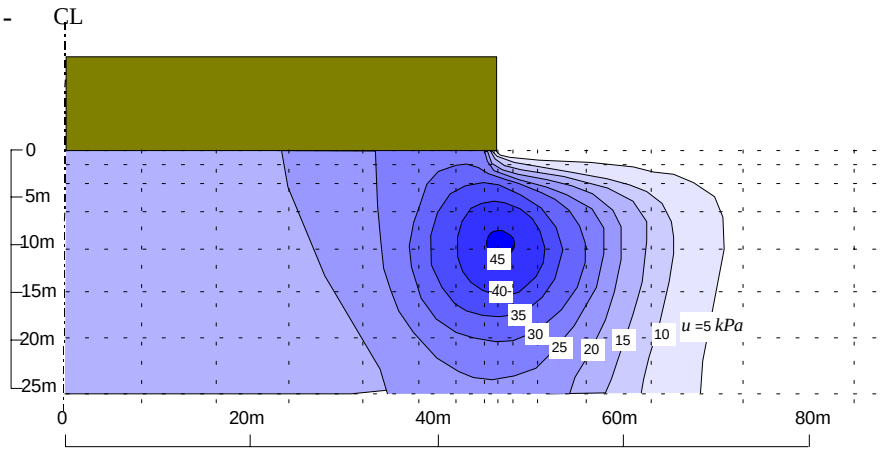

Fig. 5.27: Distribution of pore pressure at the storm peak at time=*3.01 hrs*

The distribution of pore pressure at time *4.5 hrs* is shown in Fig. 5.28. The maximum pore pressure at this stage is about *44 kPa* which is generated under the foundation base. The average pore pressure under the foundation is about *37 kPa*. The distribution of the pore pressure ratio is presented in Fig. 5.29. It shows that a zone of liquefied soil develops close to the free surface and over a distance of *15-35 m* from the edge of the foundation.

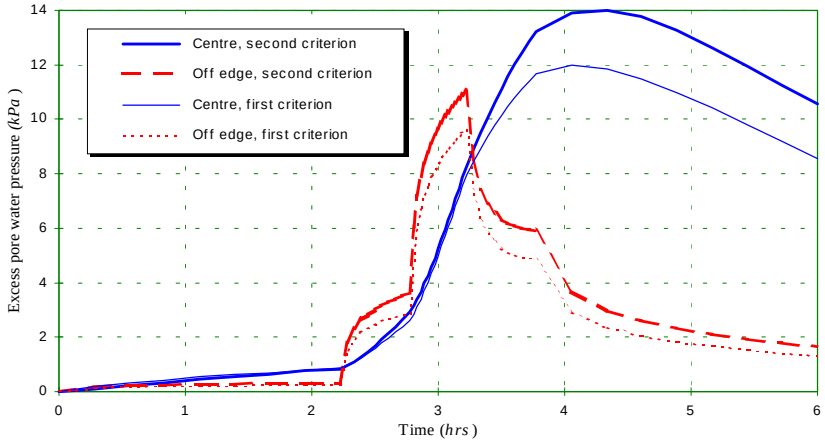

Fig. 5.28: Distribution of pore pressure at time=*4.5 hrs*

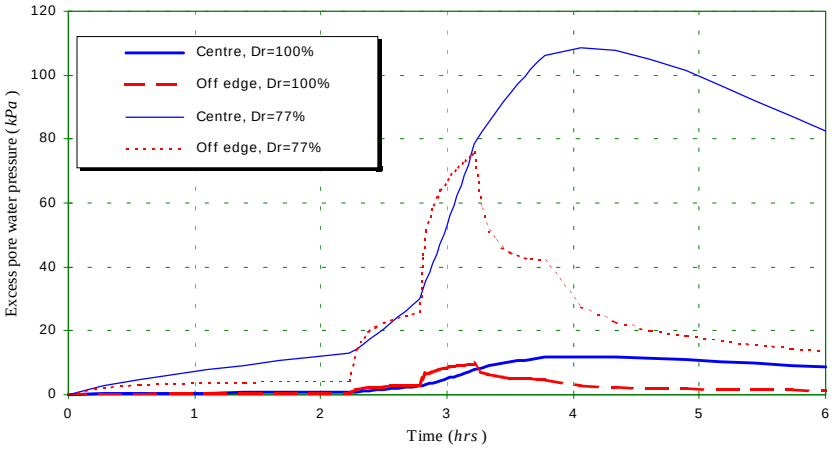

Fig. 5.29: Liquefied zone and distribution of pore pressure ratio, u/p'_i, at time=*4.5 hrs*

The settlement of the foundation is predicted to increase by about *0.03 m* as a result of the storm. The predicted settlement is, of course, related directly to the soil stiffness properties assumed in the analysis. The settlement predicted by this analysis is less than the average value of the observed settlements during severe storms in November 1973. The settlement following the storm on 19 November was about *0.03-0.05 m* (Clausen *et al.*, 1975). The storm on 19 November had a probable maximum wave height of about *21 m*, corresponding to *90%* of the *24 m* high in the storm design wave. Taking the severity of the design storm into account, the settlement predicted by the analysis is expected to be greater than the observed value. The variation of predicted settlement with time is presented in Fig. 5.30. The foundation continues to settle for about *10 hrs* after the storm finishes.

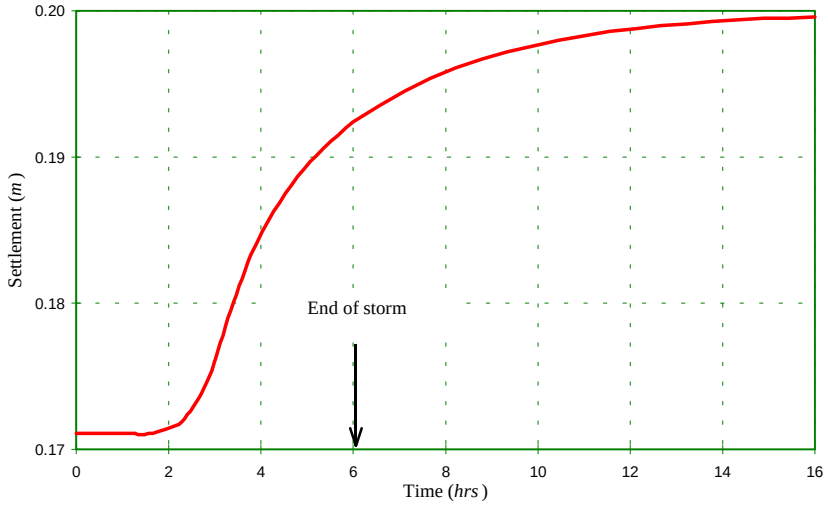

Fig. 5.30: Variation of settlement during the storm

5.7: EVALUATION OF THE RESULTS

The maximum values of pore pressures predicted by different analyses are presented in Table 5.3 together with the assumptions and criteria used in each analysis. The basic assumptions used in the first analysis and the change in the assumptions made for the subsequent analyses are also presented in this table.

In the first analysis, the results of the current method of liquefaction were compared with those obtained by Rahman *et al.* (1977). The assumptions related to the liquefaction criterion, flexibility of foundation, and density of the soil were similar to those used by Rahman *et al.* (1977). It was shown that the two sets of results are in good agreement, although some discrepancies existed which can be related to the different stress distributions assumed in the soil under the foundation. Through the second and third analyses, the effects of the rigidity of

the foundation and the replacement of the radial cyclic shear stress with the resultant cyclic shear stress on the horizontal plane and its influence on pore pressure generation were examined. Both changes resulted in higher pore pressures being predicted in the soil. By employing liquefaction data related to the true density of the sand in the fourth analysis, a significant reduction in pore pressures was predicted. The predicted pore pressures in the fourth analysis were less than those observed under the tank when it was subjected to a more moderate storm.

Table 5.3: Predictions from different analyses

Analysis Number	**Assumptions**	**u_{max}** (storm peak)	**u_{max}** (centre)	**U_{max}** (off edge)
1st analysis	Flexible footing, Radial cyclic shear stress, First liquefaction criterion, D_r=*77%*, Equivalent design storm, Data from Rahman *et al.* (1977)	*128 kPa*	*88 kPa*	*59 kPa*
2nd analysis	~~Flexible footing~~ Rigid footing	*123 kPa*	*95 kPa*	*67 kPa*
3rd analysis	~~Radial cyclic shear stress~~ Total cyclic shear stress	*128 kPa*	*109 kPa*	*76 kPa*
4th analysis	~~D_r=77%~~ D_r=*100%*	*13 kPa*	*12 kPa*	*10 kPa*
5th analysis	~~First liquefaction criterion~~ Alternative liquefaction criterion	*15 kPa*	*14 kPa*	*11 kPa*
6th analysis	~~Equivalent storm~~ Design storm	*22 kPa*	*19 kPa*	*13 kPa*
7th analysis	~~Data from Rahman *et al.* (1977)~~ Data from Lee and Focht (1975)	*46 kPa*	*44 kPa*	*24 kPa*

The liquefaction criterion was changed in the fifth analysis. In the new criterion, cyclic strength data for triaxial stress conditions are required. Therefore, the simple shear test data were converted to the triaxial stress conditions and used in the fifth analysis. However, the predicted pore pressures were still lower than expected. The pore pressures predicted in the fourth and fifth analyses, with different liquefaction criteria, were virtually the same. The effects of the time history of the storm on pore pressure generation were examined in the sixth analysis. Pore pressures under the foundations increased by *33%* when the time history of the equivalent storm was replaced by that of the design storm. However, the predicted pore pressures were still lower than those observed. It was suspected that the liquefaction data used by Rahman *et al.* (1977) may not represent the true behaviour of the sand. Therefore, the liquefaction data obtained originally by Lee and Focht (1975) were used in the seventh analysis with the new liquefaction criterion. Relatively high values of pore pressure under the tank were predicted. The average pore pressure under the tank was predicted to be around *39 kPa* with a maximum value of *46 kPa*. The maximum pore pressure is in very good agreement with the pore pressure estimated by Clausen *et al.* (1975). Assuming that the pore pressures generated under the tank are proportional to the settlements, Clausen *et al.* (1975) estimated that the maximum pore pressure under the tank would reach about *40 kPa* during

the storm on 19 November 1973. The settlement of the tank, predicted in the seventh analysis, is less than the minimum value of the observed settlement following the storm on 19 November 1973.

It should be remembered that the modified elastic stress-strain relationship, adopted in the analyses here for sand, does not represent the true behaviour of sand under high pore pressures. The pore pressures in the sand were allowed to increase up to the initial mean effective stresses (or initial vertical effective stresses). This is a suitable assumption for isotropically consolidated sands where there are no initial shear stresses. However, in the presence of initial shear stresses in the soil, this assumption overestimates pore pressures and leads to stress conditions which are not always physically reasonable for sand. A study of the stress paths in the soil during the storm loading reveals some shortcomings related directly to the elastic representation of the stress-strain behaviour of the sand.

5.8: STRESS PATHS IN ELASTIC LIQUEFACTION ANALYSES

Variations of stresses in the soil during storm loading are studied in this section. Several representative points in the soil are considered. The positions of these points are shown in Fig. 5.31. Variations of the deviatoric shear stress versus the mean effective stress for representative points, predicted by the seventh analysis, are presented in Fig. 5.32 to Fig. 5.34.

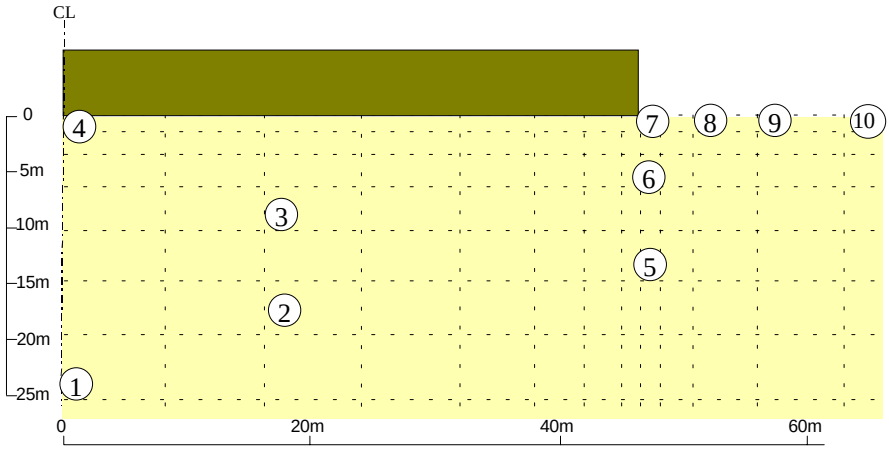

Fig. 5.31: Positions of the representative points in the soil for which stress paths are studied

In the soil elements situated under the middle part of the foundation, i.e. points (1) to (4), the mean effective stresses generally reduce while the intensities of waves are greatest. During the last parcel of waves when the intensities of waves are low, the deviatoric shear stresses and the mean effective stresses increase rapidly. The decrease and increase in the mean effective stresses coincide with the increase and decrease in pore pressures at the middle of the foundation. At the end of the storm, when the soil is consolidating, the pore water transfers

some of its pressures to the soil skeleton and the mean effective stresses increase. The effective stresses at the middle of the foundation are always positive, i.e. compressive (Fig. 5.32).

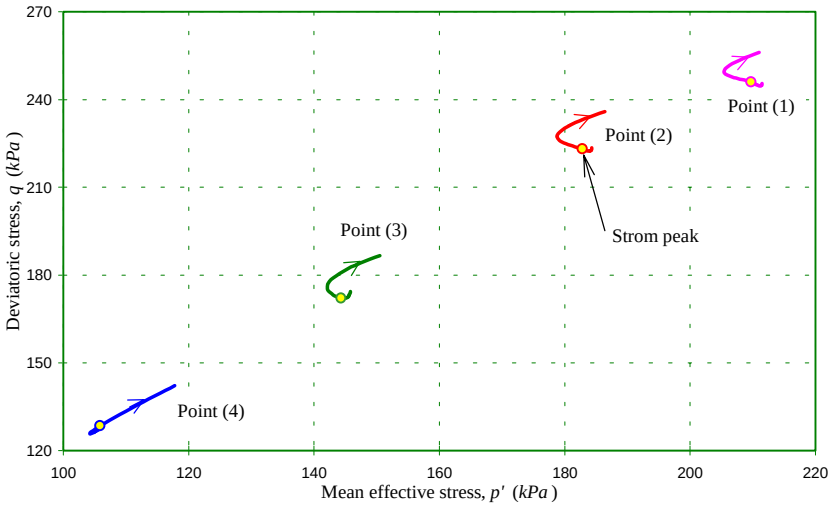

Fig. 5.32: Stress paths for points (1) to (4)

The points under the edge of the footing, points (5) to (7), show unusual and unrealistic stress paths (Fig. 5.33). Overall, the mean effective stresses change from positive values to negative values i.e. tension, a situation that is unlikely to be sustained in the ground. The stress paths of these points clearly show the unrealistic behaviour predicted for some points by the modified elastic model in liquefaction analysis. The large values of the negative mean effective stresses show that the diffusion of pore water from the middle of the footing toward the free drainage boundaries increases pore pressures at the elements under the edge.

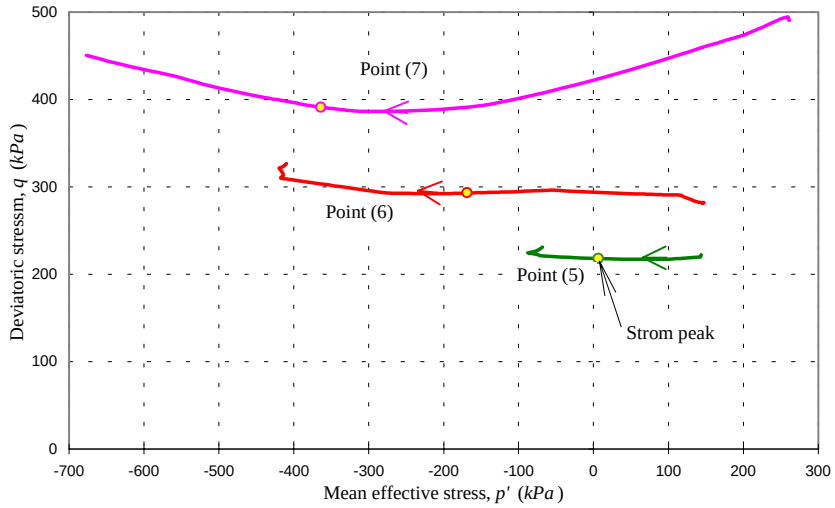

Fig. 5.33: Stress paths for points (5) to (7)

The stress paths of the points close to the surface near the foundation, points (8) to (10), also show that the mean effective stresses are predicted to become negative during the storm (Fig. 5.34) while the deviatoric stresses increase.

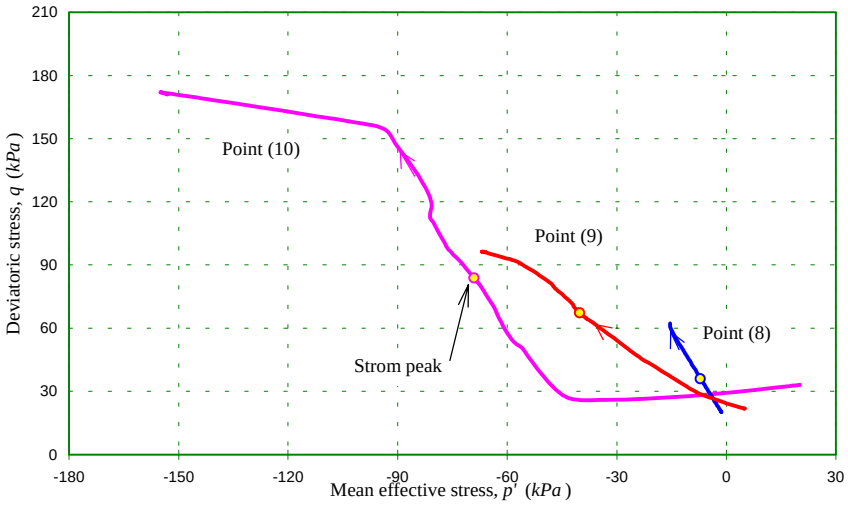

Fig. 5.34: Stress paths for points (8), (9) and (10)

5.9: CONCLUSIONS

A general form of the governing equations for liquefaction analysis was presented in this chapter. The equations were then simplified to a form suitable for the modified elastic soil model and an elastic liquefaction analysis. A general procedure for liquefaction analysis was also presented. The method was used to predict the behaviour of a foundation system. The foundation of the Ekofisk tank has been used as a case study, since there exist measurements of the foundation response during storms. To be able to compare the results of the method presented in this chapter with other published results, the studies of the Ekofisk tank started with some simple but unrealistic assumptions related to the flexibility of the foundation, the relative density of the soil, the cyclic stresses, and the liquefaction criterion. The effects of each assumption on the predicted liquefaction behaviour of the foundation were then studied. Application of the liquefaction data obtained from triaxial tests in the analysis gave promising pore pressure predictions. However, the predicted settlement of the tank during the storm is less than the observed settlement.

The stress paths predicted for some representative points in the soil were also investigated. These highlighted some problems with the prediction of the behaviour of some elements of the soil, specially under the edge of the foundation and at the surface close to the foundation. The mean effective stresses under the edge of the foundation were predicted to change from

positive values to negative values. This behaviour is not realistic for sands, and the false prediction is attributed partially to the diffusion of pore water from zones with high pressures toward zones with low pressures and the inability of the modified elastic constitutive model to deal with unrealistic stress conditions. Lack of any limitation on the values of generated pore pressures is one reason for this type of difficulty. There is also no limitation on the stress ratio in the soil to prevent negative mean effective stresses. It is believed that an appropriate elasto-plastic constitutive model may eliminate these problems from the liquefaction analysis.

Attempts will be made in the next chapter to eliminate the problems present in the modified elastic liquefaction analysis. The elasto-plastic Mohr-Coulomb model will be used for the soil skeleton and a limit will be applied on the pore pressures generated during cyclic loading.

Chapter 6

ELASTO-PLASTIC ANALYSIS OF LIQUEFACTION

6.1: INTRODUCTION

A liquefaction study of foundations using an elasto-plastic model for the constitutive behaviour of soil is the main subject of this chapter. The results of experimental tests are interpreted in the context of an elasto-plastic model and a new model for liquefaction analysis is presented.

The application of an elasto-plastic model in a liquefaction analysis has several advantages. One of the major advantages is that the stability of the soil-foundation system can be monitored during cyclic loading. The elasto-plastic model limits the stresses in the soil to a range of possible states. Furthermore, valuable information about the displacement of the foundation, the stress paths in the soil, the pore pressure generated in the soil during cyclic loading, and the zone of failure for the soil can also be obtained.

In this chapter, a new elasto-plastic model for liquefaction analysis is presented, but first brief consideration is given to some constitutive models which can describe soil response under cyclic loading. Some of the difficulties associated with the models are given. A relatively simple practical model, based on an elastic-perfectly-plastic soil response is presented. Application of the model in liquefaction analysis of an offshore foundation is demonstrated. Finally, the performance of the model is discussed by comparing the analysis results with the observed behaviour of a foundation subjected to cyclic loading.

6.2: ELASTO-PLASTIC SOIL MODEL

Numerous constitutive models have been proposed to predict the behaviour of granular soils under cyclic loading. A brief review of the existing models has been given in Chapter 2. An extensive study of the models suitable for cyclic loading is presented by Poulos (1988). Most of the existing models are based on the concepts of strain softening or modulus degradation

(e.g. Finn *et al.*, 1977 or Dobry *et al.*, 1988), the critical state models (e.g. Carter *et al.*, 1982), bounding surface models (e.g. Dafalias and Herrmann, 1982), elastic viscoplastic models (e.g. Aubry *et al.*, 1985, Bhatia and Nanthikesan, 1987) and so on. Almost all of these models fall into the elasto-plastic category. Depending on the degree of simplification and the number of assumptions made in deriving the governing equations, a wide variety of models for soil under cyclic loading has been proposed. However, not all of the models are capable of predicting the detailed characteristics of cyclic responses. Most of the models have a limited practical significance, since they show a good prediction for soil behaviour only under special stress conditions. Some of the most successful models reproduce only some of the observed responses of soils (Poulos, 1988). These models need a relatively large number of parameters, many of which are usually difficult to determine. Besides, application of these models in a numerical finite element analysis usually needs excessive computational time and therefore, is not feasible. Accordingly, it is necessary to adopt a simple approximate approach for estimating the cyclic behaviour of soils in most practical problems.

A model is presented here which can be used in an elasto-plastic liquefaction analysis of offshore foundations on granular soil. In this model the elastic-perfectly-plastic formulation of the Mohr-Coulomb model defines the stress-strain relationship, the yield surface, and the direction of plastic flow for the soil. The effects of cyclic loading are included by modifying the stress-strain relationship in the Mohr-Coulomb model.

In the Mohr-Coulomb model the yield surface coincides with the failure surface. Under monotonic loading the yield surface defines the stress conditions under which plastic deformation occurs for the soil. It also separates zones of elastic behaviour from those of plastic behaviour. Stress paths within the yield surface result in purely recoverable (elastic) deformations, while paths which intersect the yield surface produce both recoverable and permanent (plastic) deformations.

The Mohr-Coulomb yield surface is constant in the stress space. Therefore, this model, in its standard form, is not suitable for cyclic loading, since within a constant yield surface no amount of stress cycling can produce any permanent strains. The effects of cyclic loading can be considered in the model by including some plastic deformations in the system when the state of stress is inside the yield locus. Therefore, the response of the soil under cyclic loading does not remain elastic while the state of stress is inside the yield locus. The governing equations for cyclic loading for a general soil model have been presented in Chapter 5. In particular, the effects of cyclic loading can be included in the Mohr-Coulomb model using Equation (5.9). When the state of stress reaches the yield surface, under either monotonic or cyclic loading, soil behaviour is defined by the Mohr-Coulomb model and the cyclic load is considered to have no further effects on soil behaviour, i.e. the element of soil is at failure.

Within the framework of the deformation theory of plasticity, the total strain increment, $d\varepsilon$, is decomposed into the elastic strain increment, $d\varepsilon^e$, and the plastic strain increment, $d\varepsilon^p$, by a simple superposition, i.e.

$$d\varepsilon = d\varepsilon^e + d\varepsilon^p \qquad (6.1)$$

Under monotonic loading, the elastic strain increment is assumed to be completely described by the Hooke's law where, for an isotropic material, two material parameters, such as Young's modulus and Poisson's ratio, are constant. The relative magnitudes of the plastic strains are obtained from the flow rule. The flow rule specifies the relationship between the increment of the plastic strain and the present state of stress for a yielded soil subjected to further loading.

Under cyclic loading, another component of plastic strain increment, which is the result of cyclic loading only, $d\varepsilon_v^c$, is added to Equation (6.1), i.e.

$$d\varepsilon = d\varepsilon^e + d\varepsilon^p + d\varepsilon_v^c \qquad (6.2)$$

The additional plastic strain produced during cyclic loading can be obtained from experimental tests on samples of soil. The results of drained tests can be used directly in finite element formulation. However, experimental tests are usually carried out on saturated samples of soil under undrained conditions and the generated excess pore pressures are recorded during the tests. The excess pore pressure can be related to the volumetric plastic strain, as shown in Chapter 5, by the following equation

$$d\varepsilon_v^c = e^T.\boldsymbol{D}^{-1}.e.du_c \qquad (6.3)$$

where ε_v^c is the additional volumetric plastic strain due to cyclic loading under drained conditions, $\boldsymbol{D}$ is the stiffness matrix of the soil skeleton, u_c is the pore pressure generated due to cyclic loading under undrained conditions, and $e=(1,1,1,0,0,0)^T$. Having one of the effects of cyclic loading, either the volumetric strain or the excess pore pressure, the other effect can be calculated by Equation (6.3). The accuracy of the volumetric strain, calculated from excess pore pressure, depends, of course, on the stiffness matrix, $\boldsymbol{D}$, assumed for the soil. In Equation (6.3), $\boldsymbol{D}$ is the elastic stiffness matrix, since it is assumed that cyclic loading has no further effect on the behaviour of the soil when the state of stress reaches the yield surface.

No attempt has been made to verify the accuracy of Equation (6.3) for an elastic-perfectly-plastic soil model, since there are no quantitative data from cyclic tests under both drained and undrained conditions for any sand with a known stress-strain relationship. However, where the results of undrained cyclic tests are expressed in term of excess pore pressure, the rate of generation of pore pressure should include the effects of any possible non-linearity in soil behaviour. In other words, the results of undrained cyclic tests with pore pressure measurement capture the non-linearity of the behaviour of the soil skeleton before the onset of liquefaction or failure. Therefore, the elastic-perfectly- plastic model together with the

experimental data on samples of saturated soil should provide a reasonable representation of soil behaviour under cyclic loading.

Although the proposed elasto-plastic model is very simple and clear in its definition, application of the model in a finite element analysis needs some further idealizations regarding the concept of liquefaction. The definition of liquefaction should be revised in the framework of the elasto-plastic soil model. Some approximations and assumptions are also required to generalize the data, obtained under triaxial stress conditions, to the complete three-dimensional stress state which exists in the field. In an attempt to cast the liquefaction phenomenon within the elasto-plastic model, the effects of cyclic loading on soil are expressed in terms of the damage done to the structure of the soil. By this means the generation of excess pore pressure under cyclic loading is related to the amount of damage done to the soil.

6.2.1: Experimental Findings on the Liquefaction of Granular Soils

In laboratory cyclic tests on undrained saturated samples of granular soils using a stress controlled method, the average values of the mean total stress and the deviatoric shear stress are usually kept constant. In perhaps the simplest case of a cyclic triaxial test, the sample is isotropically consolidated and then subjected to two-way cyclic loading. The change in the average values of stress can be shown in the Cambridge p'-q space, where p' is the mean effective stress and q is the deviatoric shear stress (Fig. 6.1). During the application of cyclic stress under undrained conditions, pore pressure generally increases and effective stress decreases by the same value, since the mean total stress is kept constant. Therefore the state of stress moves from the initial state (point A in Fig. 6.1) along the p' axis toward the origin. When the stress path reaches the origin, the excess pore pressure would be equal to the value of the initial mean effective stress, p'_i. At this state, the effective stresses, and therefore the shearing resistance of the soil grains are eliminated, the soil flows like a viscous liquid, and liquefaction is said to have occurred.

In the more general case of cyclic triaxial tests, an initial shear stress is applied to the soil together with an initial mean effective stress (point B in Fig. 6.1), prior to the application of the cyclic stresses. Pore pressure build-up usually reduces the mean effective stress while the mean value of the shear stress is maintained constant by the test apparatus. Therefore, the stress path moves toward the deviator axis and eventually reaches the failure envelope (Fig. 6.1). For stress controlled tests, the soil would fail at this stage and show excessive deformation. In strain controlled tests, when the stress path reaches the failure surface, continuous deformation together with low resistance may result in reduction of the deviatoric stress, and the stress path moves downward along the failure surface.

A unified definition of liquefaction can be adopted as the condition where the stress path reaches the failure surface as a result of the reduction in mean effective stress during cyclic loading. Pore pressure at the onset of liquefaction reaches its maximum value, u_{max}, which is equal to the horizontal distance between the initial state of stress and the failure envelope. This more general definition includes the traditional definition of liquefaction which is suitable for soils under initial isotropic pressure.

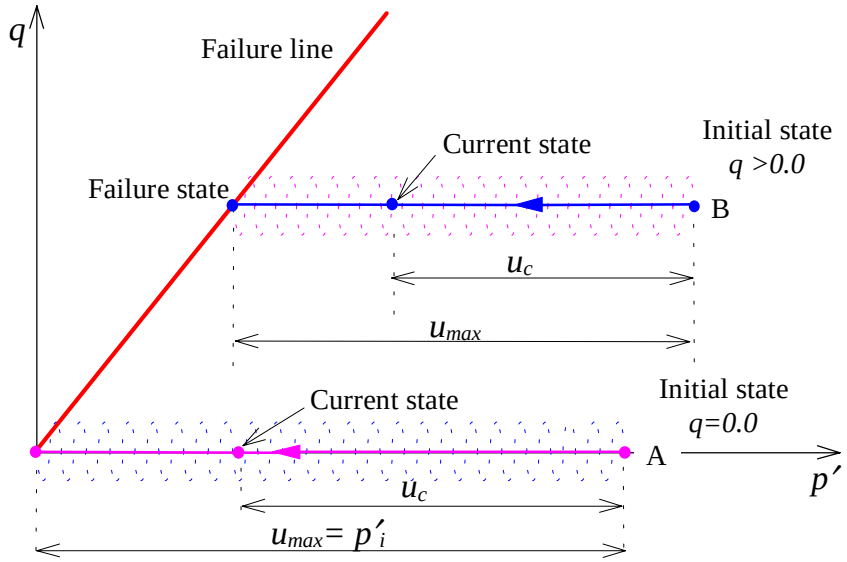

Fig. 6.1: Stress paths in undrained triaxial tests on saturated sands

6.2.2: Liquefaction of Soil-Foundation Systems

The application of cyclic loads on a foundation may cause liquefaction in some elements of the soil under the foundation. However, the foundation may continue to transfer the ambient loads to other parts of the soil where there still exists some shearing resistance. During cyclic loading, there is a continuous generation of pore pressures, a continuous reduction in the overall factor of safety, and a continuous increase in the settlement of the foundation. At some stage the whole soil system may lose its resistance against external loads. In this case, the foundation experiences excessive displacement and collapses. If the foundation can sustain the external load during cyclic loading, it will regain most if not all of its original shear strength when the pore pressures are dissipated from the soil.

The definition of liquefaction for an element of soil under a foundation is not as simple as that for a sample of soil in a “single element” laboratory test, because the stress paths that elements of soil follow in the field are generally more complex than the relatively simple stress paths applied in laboratory tests.

6.2.3: Laboratory and Field Stress Conditions

The stress conditions applied in the laboratory are usually the simple triaxial stress conditions where two out of the three principal stresses acting on a "single element" of soil are equal (or assumed equal). The cyclic stresses are also applied in the direction of the principal stresses. The average initial total stresses are often maintained constant during the application of cyclic load. Therefore, the stress paths are constrained to follow certain directions toward the failure envelope. For such cases the stress states on the failure envelope at the onset of liquefaction can be pre-determined.

Generally stress conditions in the field are truly three-dimensional. Cyclic stresses are usually applied in a direction completely different from the direction of the initial principal stresses. More importantly, the values of the mean total stress and the deviatoric shear stress, transferred to the soil by the external ambient loads, vary during the application of cyclic loads. Change in the average mean stress or deviatoric stress is primarily due to stress redistribution inside the "multi-element" soil body. The distribution of total stresses due to ambient loads may be changing continuously, because of the change in the stiffness of the soil. When the pore pressures inside the soil increase, stresses in some elements of the soil reach the yield surface which results in a reduction of soil stiffness. The consequent change in the stiffness of the soil results in a redistribution of stresses. The effective stress paths do not necessarily move horizontally toward the failure envelope (as shown in Fig. 6.1), and therefore, the stress states for the onset of failure (or liquefaction) cannot be determined at the beginning of a phase of cyclic loading.

While some valuable laboratory data on liquefaction behaviour of sands are currently available, none of them completely covers the complex stress conditions that exist in the field. Therefore, some idealizations and assumptions are necessary to make possible the numerical analysis of liquefaction under general stress conditions.

6.2.4: General Definition of Liquefaction

A new liquefaction criterion is presented that may be used to define liquefaction in the case of a "single element" laboratory test as well as in field stress conditions.

The generation of pore pressure during cyclic loading can be seen as "damage" done to the shearing resistance of the soil skeleton. As the pore pressure increases, the shearing capacity of the soil reduces. Eventually, the shearing resistance of the soil may reduce to a value equal to the shear stress applied to the soil by the ambient loads. At this stage, the state of stress would be on the failure locus where further reduction in the effective stress or further increase in the loads would cause unlimited plastic shearing. This stage can be regarded as the onset of liquefaction.

The reduction in the shearing resistance for an element of soil during cyclic loading is illustrated in the Cambridge p'-q space in Fig. 6.2, where the projections of the Mohr-Coulomb failure surface for selected Lode angles are presented. Overall, the soil has an initial shearing resistance of q_{fi} at a mean effective stress, p'_i. The initial shear stress is q_i. Therefore, the extra shearing capacity of the soil at the initial conditions can be regarded as $S_i = q_{fi} - q_i$. After the application of cyclic load, the mean effective stress reduces to p'_s as pore pressure is generated and the applied shear stress changes to q_s. The shearing resistance of the soil at this point reduces to q_{fs}. As a consequence, the extra shearing capacity of the soil reduces to $S_s = q_{fs} - q_s$. In this case the "damage" done to the soil structure can be considered as the reduction in the shearing resistance of the soil. A damage index, *DI*, can be introduced to represent the amount of damage done to the sand structure by cyclic loading.

$$DI=A/B=(S_i-S_s)/S_i \qquad (6.4)$$

where A is the difference between the initial and current mean effective stresses, i.e. $A=p'_i-p'_s$, and B is the difference between the initial effective stress and the effective stress at the failure state, i.e. $B=p'_i-p'_f$. Equation (6.4) can be verified from the properties of the similar triangles in Fig. 6.2. The damage index, *DI*, ranges from zero to one. While $DI = 0$ indicates that no damage has been done to the soil by cyclic loading, $DI = 1$ represents full damage to the soil structure. When $DI = 1$, the soil does not have any further resistance to shear loading, and if unrestrained under the current load, it would show an infinite shearing displacement.

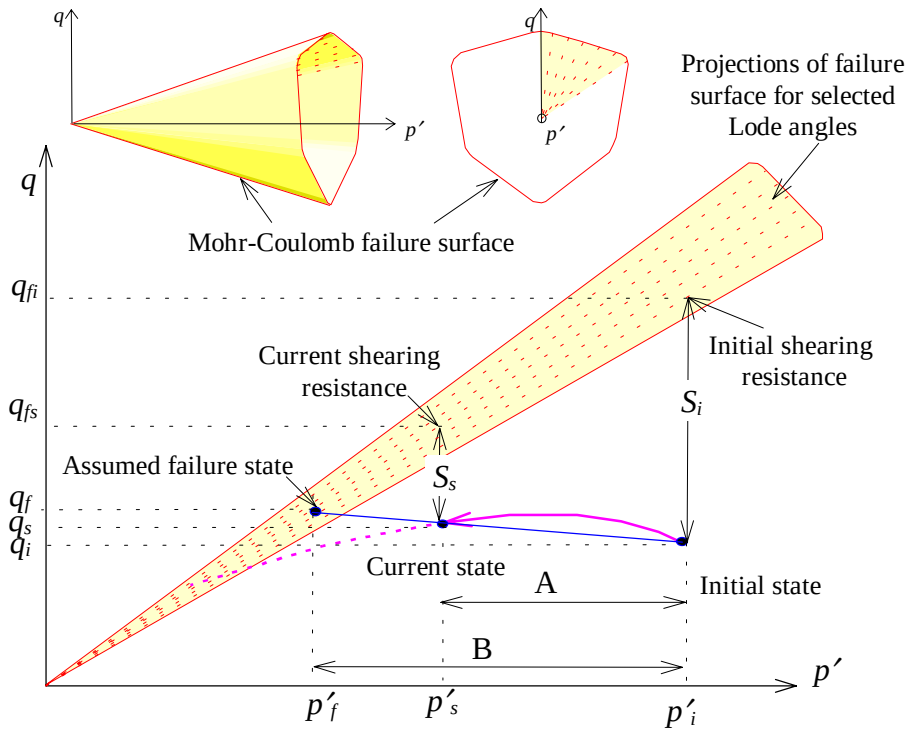

Fig. 6.2: Stress path in the Mohr-Coulomb failure surface

The damage done to the soil structure at any stage during cyclic loading can be evaluated by calculating the initial shear stress and shearing resistance of the soil, q_i and q_{fi}, and the current shear stress and shearing resistance of the soil, q_s and q_{fs}. Both q_{fi} and q_{fs} can be calculated from the elasto-plastic soil model. Since the stress paths in the field are not always similar to those applied in the laboratory, some assumptions are necessary in the evaluation of *DI*. For example, in cases where the current extra shearing resistance, S_s, becomes greater than the initial extra shearing resistance, S_i, it is assumed that no damage has been done to the soil, and therefore, the damage index is reset to zero. The maximum value of *B* is also limited to the initial mean effective stress, p'_i.

Comparison of Fig. 6.1 with Fig. 6.2 shows that the general definition for liquefaction is identical with the more traditional definition of liquefaction that was based on the results of laboratory tests.

6.2.5: Calculation of Pore Pressure

In a finite element liquefaction analysis, the pore pressures generated during application of each parcel of waves should be evaluated. The pore pressure can be calculated based on the level of damage previously done to the soil structure.

In laboratory undrained cyclic tests, the generation of pore pressure reduces the mean effective stress in the soil. As a consequence, the shearing resistance of the soil reduces. Therefore, the pore pressure can be seen as a measure of the damage done to the soil structure. The damage index, *DI*, can be interpreted as the ratio of the generated excess pore pressure to the maximum achievable pore pressure, i.e.

$$DI = u_c / u_{max} \tag{6.5}$$

The increment in pore pressure generated during each wave parcel can be calculated provided that the rate of damage is determined. The rate of damage done to the soil structure under undrained conditions can be taken as equal to the rate of the generation of pore pressure, determined from laboratory cyclic load tests. Considering the pore pressure generation function proposed by Seed *et al.* (1975a), for example, the rate of damage in a soil under undrained conditions can be evaluated as follows.

$$\frac{u_c}{u_{\max}} = \frac{2}{\pi} Arc\sin\left(\left(\frac{N}{N_l}\right)^{\frac{1}{2\alpha}}\right) \tag{6.6}$$

$$du_c = \frac{2u_{\max}}{\pi} Arc\sin\left(\left(\frac{N+\Delta N}{N_l}\right)^{\frac{1}{2\alpha}}\right) - u \tag{6.7}$$

$$\frac{du_c}{u_{\max}} = \frac{2}{\pi} Arc\sin\left(\left(\frac{N+\Delta N}{N_l}\right)^{\frac{1}{2\alpha}}\right) - \frac{u}{u_{\max}} \qquad (6.8)$$

$$dDI = \frac{2}{\pi} Arc\sin\left(\left(\frac{N+\Delta N}{N_l}\right)^{\frac{1}{2\alpha}}\right) - DI \qquad (6.9)$$

where dDI is an increment of damage due to the application of ΔN load cycles, N is the number of cycles of load applied previously to the soil, N_l is the number of cycles required for liquefaction, α is a pore pressure generation parameter, u is the present pore pressure, and DI represents the present value of the damage index. Under undrained conditions, the rate of damage can also be taken as $dDI=dA/B$ (Fig. 6.2), assuming $dB=0$. In this case dA is equal to the increment in pore pressure generated by cyclic loading.

Equation (6.9) can be used in a liquefaction analysis to calculate the increment in the damage index due to cyclic loading under undrained conditions, provided that the amplitude of the cyclic load does not vary during the analysis. In a more general case where the soil is under partially drained conditions and where the soil is subjected to cyclic loads of variable amplitudes, Equation (6.9) can be replaced by the following equation

$$dDI = \frac{2}{\pi} Arc\sin\left(R_N + \frac{\Delta N}{N_l}\right)^{\frac{1}{2\alpha}} - DI \qquad (6.10)$$

where

$$R_N = \left(Sin\frac{\pi\, DI}{2}\right)^{2\alpha} \qquad (6.11)$$

The cyclic ratio, R_N, represents the effects of previous cycles of loads of different amplitudes and the effects of any dissipation of pore pressures.

Equation (6.10) can be used to calculate the pore pressure generated by cyclic loading for general stress conditions in the soil. After application of ΔN cycles of load, the value of the increment of the damage done to the soil, dDI, is calculated from Equation (6.10). Then dA is calculated as:

$$dA = dDI \times B \qquad (6.12)$$

dA can be seen as the increment in the pore pressure generated due to cyclic loading under undrained conditions, du_c, and used in the finite element formulation, Equations (5.9) and (5.10). Furthermore, the finite element equations of consolidation, explained in Chapter 5, can be solved for any dissipation of pore pressure, and therefore, any change in the value of pore pressure in the soil resulting from the combined effects of undrained cyclic loading and consolidation can be calculated.

In Equation (6.12), B is the difference between the initial mean effective stress and the mean effective stress corresponding to the failure state of the soil. The failure state can be predicted based on the initial and the current stress states, which also imply the probable stress path (Fig. 6.2). The value of B can be calculated from the properties of the similar triangles in Fig. 6.2 as follows.

$$B = \frac{A.S_i}{S_i - S_s} = \frac{(p'_i - p'_s)(q_{fi} - q_i)}{(q_{fi} - q_i) - (q_{fs} - q_s)} \qquad (6.13)$$

In some special cases, the value of B cannot be calculated from Equation (6.13). For example, at the beginning of a liquefaction analysis, where $A = 0$, the value of B is taken as the horizontal distance between the initial state of stress and the failure surface. Also at some stage, the damage index may be calculated as zero, or even negative. Examples are when the stress path moves parallel to the yield surface, i.e. S_i=S_s in Fig. 6.2, or when the mean effective stress increases. In these situations, the value of B is assumed to be equal to the horizontal distance between the initial state of stress and the failure surface. It is also considered to be a reasonable assumption if the maximum value of B is limited to the initial mean effective stress.

In the calculation of pore pressure, all of the effects of previous cyclic loading, such as the number of previously applied cycles, the change in the magnitude of the cyclic deviator stress, the dissipation of excess pore pressure, and the change in the total stresses can be considered by evaluating the cumulative damage, DI, done previously to the soil. DI is used to calculate the cyclic ratio, R_N in Equation (6.11), which represents the effects of cyclic loads applied previously to the soil.

6.3: METHOD OF ANALYSIS OF LIQUEFACTION IN THE FIELD

The procedure presented in Chapter 5, for elastic liquefaction analyses, can also be used for non-linear liquefaction analyses. The initial mean effective stress, p'_i and the initial deviatoric shear stress, q_i, are determined at the beginning of the analyses. Likewise, the cyclic deviatoric shear stress, q_c, can be determined at the beginning of the analyses and whenever any change occurs in the cyclic load amplitude. The cyclic deviatoric stress is obtained by calculating the difference between the initial deviatoric shear stress, q_i, and the deviator stress resulting from the application of combined ambient loads and cyclic loads, q_{i+c}. Since the cyclic deviatoric stresses obtained in this way for cyclic loads applied in two opposite directions are not always equal, the average cyclic stress, resulting from the application of cyclic load in both directions is used in the analysis, i.e.

$$q_c = \frac{(q_{i+c} - q_i) + (q_i - q_{i-c})}{2} \qquad (6.14)$$

where q_{i+c} is the deviator stress corresponding to the application of ambient load combined with cyclic load in the positive direction (increasing q), and q_{i-c} is the deviatoric stress resulting from the application of ambient load combined with cyclic load in the negative direction (see Fig. 5.22).

The potential for liquefaction at any point in the soil under the foundation can be evaluated by calculating the number of cycles of load required for liquefaction at that point, N_l. Considering ΔN cycles of load applied to the soil under undrained conditions during a time increment of Δt, the generated excess pore pressures are calculated from Equations (6.10) to (6.13). The excess pore pressures are then used in the finite element liquefaction analysis, where the equations of consolidation are solved for dissipation of pore pressures.

6.4: LIQUEFACTION ANALYSIS OF AN OFFSHORE FOUNDATION

The elasto-plastic method described in this chapter was used to analyse the foundation of the Ekofisk tank, constructed in the North Sea in 1973. The full description of the tank, the ambient and cyclic loads, and the storm histogram have been presented in Chapter 5. As mentioned, the Ekofisk tank has a diameter of *93 m* and a submerged weight of *1900 MN*. It rests on *26 m* layer of sandy soil which overlays a stiff clay. The coefficient of permeability of the sand is about 10^{-5} *m/sec*. The sand has a drained Young's modulus of $E' = 48000\ kN/m^2$, a Poisson's ratio of $\nu' = 0.25$, and a saturated unit weight of $\gamma_{sat} = 17.3\ kN/m^3$.

A typical value of the friction angle for the sand in the Ekofisk field, obtained in drained triaxial tests, is $\phi = 43^o$ (Bjerrum, 1973). The dilation angle for the sand is assumed to be zero. Therefore, a non-associated flow rule is assumed for the sand based on the elasto-plastic model. This implies that under drained conditions there will be no plastic volume change under monotonic shearing.

The liquefaction data corresponding to a relative density of $D_r = 100\%$ for the sand, obtained from triaxial tests by Lee and Focht (1975), presented in Fig. 5.23, are adopted in the elasto-plastic analysis. The design storm, defined by Rahman *et al.* (1977) and presented in Fig. 5.5, is used in this analysis. A finite element mesh similar to the one used in the elastic liquefaction study in Chapter 5 is also used here.

6.4.1: Liquefied Zones

The change in the state of the soil under the tank during the storm is shown in Fig. 6.3, where the zones of failed soil are presented sequentially. Under the ambient load, at *time=0.0*, the soil under the edge of the tank fails (becomes plastic) under compressive stresses while the soil close to the surface adjacent to the tank is predicted to fail in tension. After the application of cyclic load, the pore pressures inside the soil rise and cause redistribution of stresses in the soil elements and reduction of soil shearing strength. The redistribution of stresses may decrease the effective stresses in some elements and cause the elements to yield plastically. The reduction in the shearing resistance of some points in the soil may also result in the plastic failure of those points. Since both redistribution of stresses and reduction in soil shearing resistance originate from the application of cyclic loading, the failure zones which are produced during storm loading can be regarded as "liquefaction" or at least "liquefaction induced failure". From Fig. 6.3, it may be observed that the soil elements under the edge of the foundation and also the elements close to the surface adjacent to the tank are the most critical elements during storm loading.

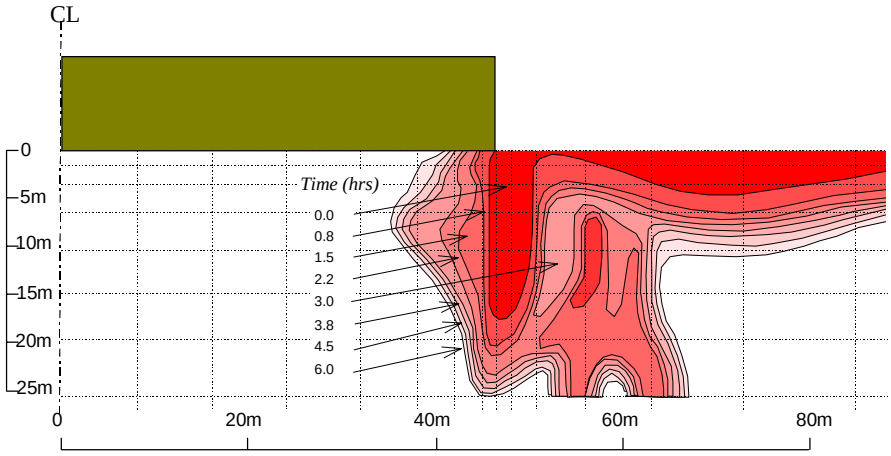

Fig. 6.3: Expansion of failure zone during the storm

6.4.2: Variations of Excess Pore Pressures

Variations of the excess pore pressures predicted during the storm for two points under the foundation are shown in Fig. 6.4. The pore pressure reaches *47 kPa* at the centre of the foundation, *3.8 hrs* after the beginning of the storm. The pore pressure under the edge of the footing, *1.5 m* below the soil surface, reaches a maximum value of about *9 kPa*, at the storm peak.

There is a fluctuation in the predicted pore pressure under the edge of the tank. This behaviour was observed for the points which reach the yield surface during cyclic loading and is an artifice of the numerical solution scheme. When the state of stress is on or near the yield surface, the isotropic increase in excess pore pressure due to cyclic loading decreases the

mean effective stress and causes the state of stresses to drift from the yield surface. The process of bringing the state of stresses back to the yield surface generally changes the stresses, which in turn affects the excess pore pressure. During cyclic loading, the continuous correction of stresses corresponding to a point on the yield surface results in the numerical fluctuation of the pore pressure at that point.

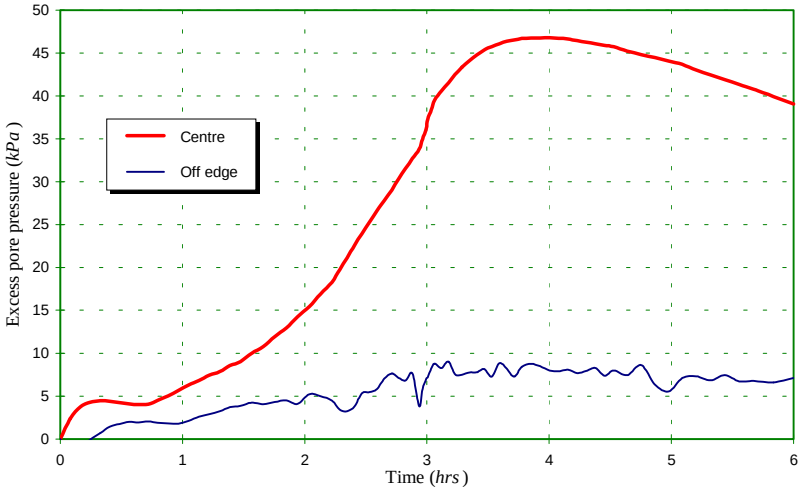

Fig. 6.4: Excess pore pressures generated during storm

Distributions of excess pore pressures in the soil are presented in Figs. 6.5 to 6.8 at *1.5 hrs*, *3.0 hrs*, *3.8 hrs* and *6.0 hrs* after the beginning of the storm. The maximum pore pressure at time *1.5 hrs* is about *38 kPa* which is generated close to the clay layer, about *55 m* away from the centre of the tank (Fig. 6.5). The predicted maximum pore pressure during the storm is about *51 kPa*, Fig. 6.6, which is generated at the same point *3.0 hrs* after the beginning of the storm. The pore pressure beneath the tank rises to *47 kPa* at time *3.8 hrs* (Fig. 6.7), and after that the pore pressure reduces. At the end of the storm there exists a substantial residual pore pressure under the tank (Fig. 6.8), with a maximum of *39 kPa* which is generated at the centre of the tank.

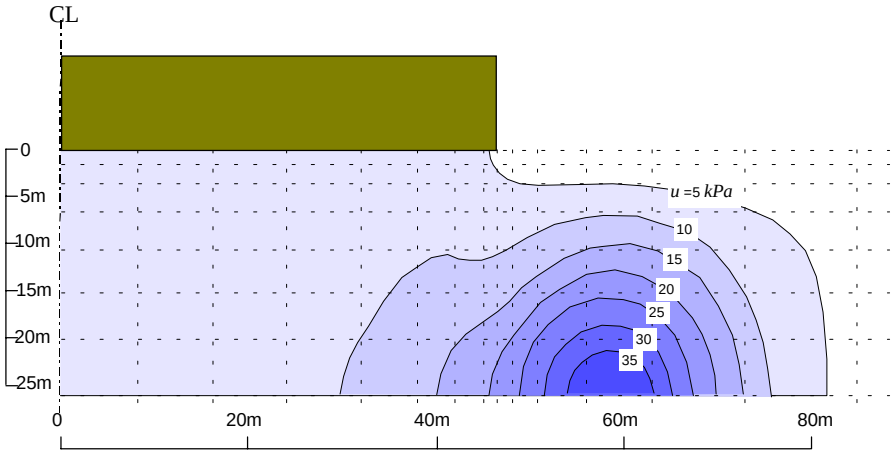

Fig. 6.5: Distribution of excess pore pressure at time=*1.5 hrs*

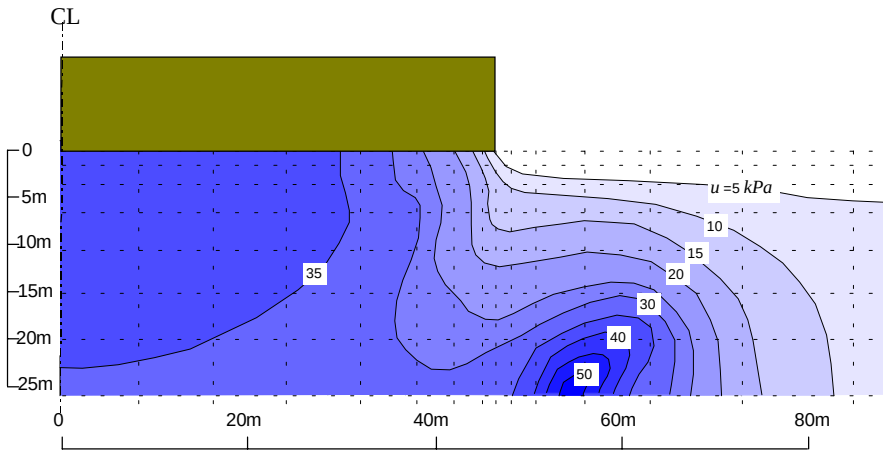

Fig. 6.6: Distribution of excess pore pressure at time=*3.0 hrs*

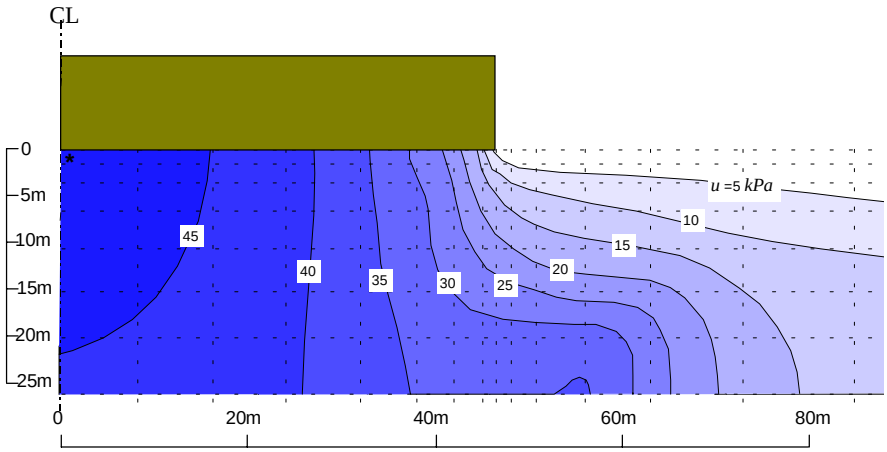

Fig. 6.7: Distribution of excess pore pressure at time=*3.8 hrs*

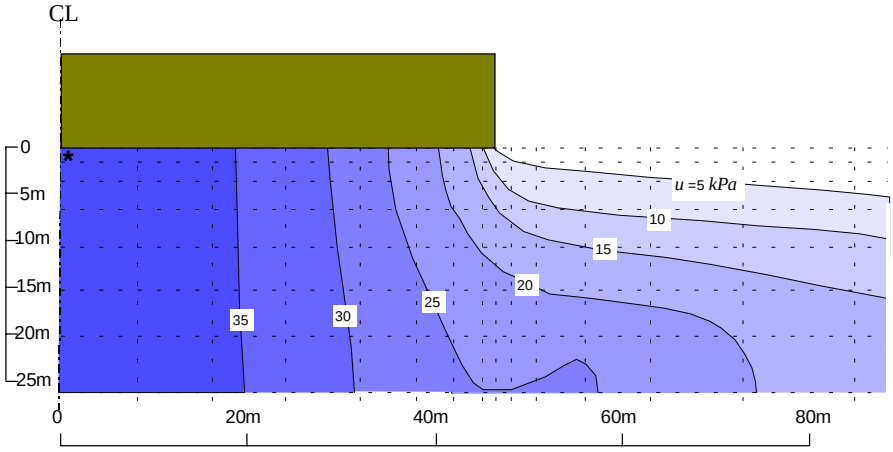

Fig. 6.8: Distribution of excess pore pressure at time=*6.0 hrs*

The value of the excess pore pressure under the edge of the tank is not very high. However, the soil elements under the edge are in critical conditions, since they experience relatively large deviator stresses and fail under the ambient loads. The model for liquefaction does not

generate any further pore pressure for elements of soil which are at the failure state. During cyclic load, pore pressures are only generated for the points where the soil elements have not yet failed. However, the diffusion of water from zones of high pressure under the tank toward the free drainage boundaries causes the pore pressure in the elements under the edge of the tank to be increased.

Variations of excess pore pressures during storm loading for some other representative points in the soil were also studied. The positions of these points relative to the tank are shown in Fig. 6.9. The variations of pore pressures for the representative points are presented in Fig. 6.10 to Fig. 6.12.

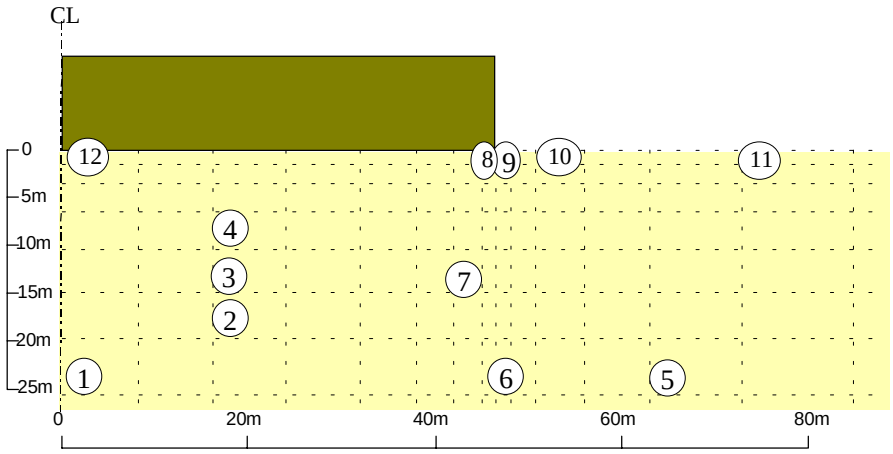

Fig. 6.9: Position of the representative points inside the soil

Variation of excess pore pressure at a point during cyclic loading can be related to the intensity of waves (the cyclic shear stress), the initial mean effective stress, and therefore, the position of the point in the soil relative to the foundation. The position of a point relative to the free drainage boundary also affects the variation of pore pressure at the point. When a point is far from the free boundary, dissipation of the pore pressure, generated during cyclic loading at that point, is retarded and incremental pore pressures are accumulated, increasing the total pore pressure at the point. Diffusion of water from zones of high pressure toward the free drainage boundary increases the pore pressures at the points close to the free boundary. Another factor which affects the variation of pore pressure at a point is the extra shearing capacity of the point, or in other words the position of its stress state relative to the failure surface, and the stress path during cyclic loading. Even the extra shearing capacity of the soil surrounding a point may affect the stress path of the point, and therefore, the variation of pore pressure at the point.

Variations of pore pressures for points (1) to (4) are presented in Fig 6.10. These points are situated under the tank, relatively far from the free boundaries. Therefore, the dissipation of pore pressures is retarded, causing relatively large pore pressures to be generated.

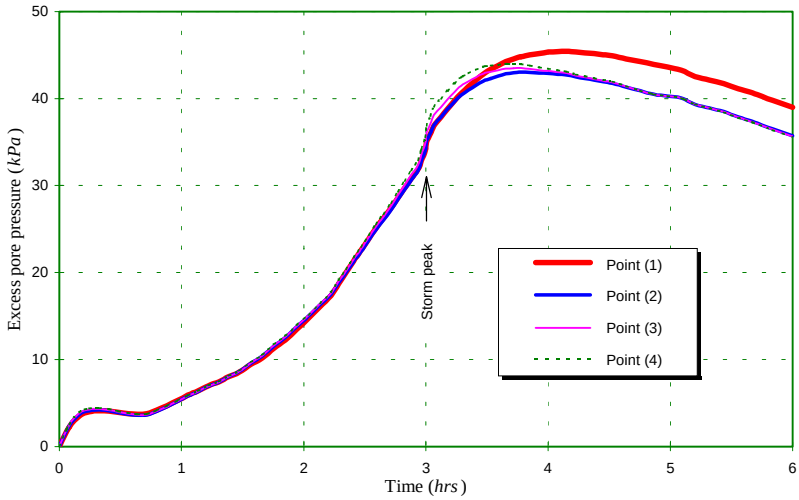

Fig. 6.10: Variation of pore pressures during storm for points (1) to (4)

Variations of pore pressures for points (5) to (8) are presented in Fig. 6.11. At the beginning of the storm the states of stresses of these points are inside the failure locus. However during the storm the stresses move toward the yield surface and eventually the points fail (see Fig. 6.3). After failure, there is a fluctuation in pore pressures predicted for the points, which is particularly pronounced for point (5).

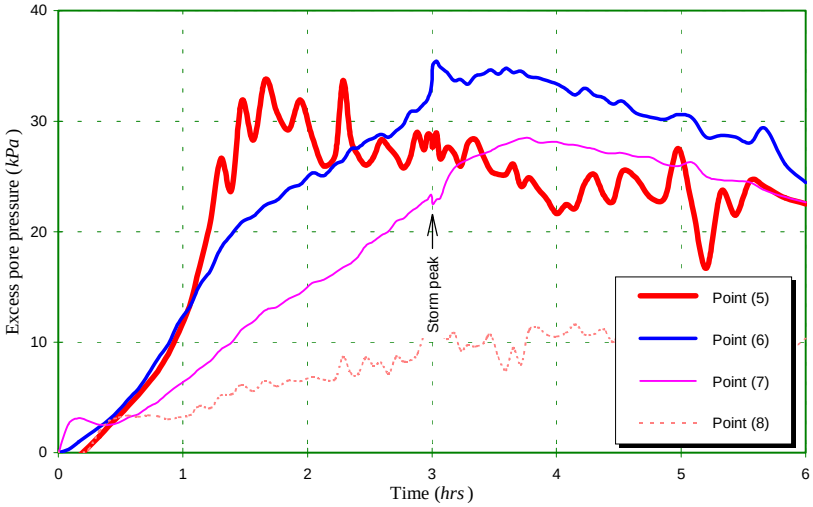

Fig. 6.11: Variation of pore pressures during storm for points (5) to (8)

Variations of pore pressures for the points close to the surface of the soil adjacent to the foundation, points (9) to (11), are presented in Fig. 6.12. All of these points fail under the ambient loads, and therefore, the changes in pore pressures at these points are mainly due to the flow of water from other parts of the soil. The influence of the flow of water from zones of high pressure toward the free drainage boundary is illustrated in this figure. The initial and cyclic stresses of the points are very similar. However, the pore pressure of the closest point to the foundation, point (9), is greater than the pore pressures predicted for the other points. Point (9) is influenced more by the flow from the soil elements under the foundation.

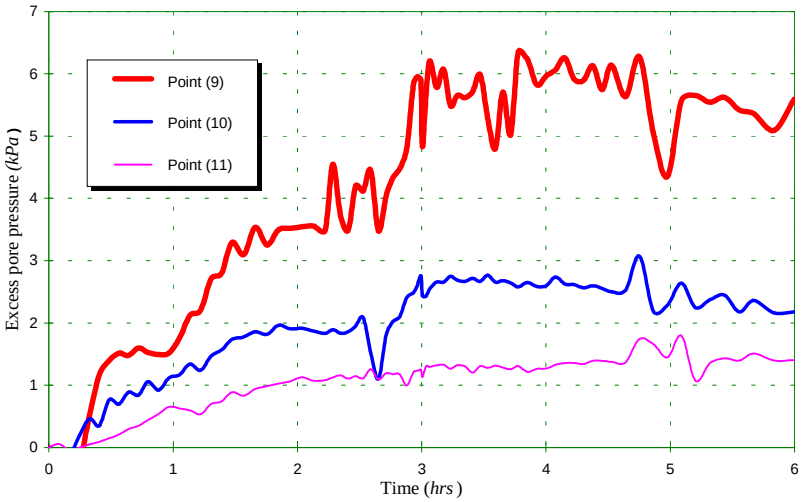

Fig. 6.12: Variation of pore pressures during storm for points (9) to (11)

6.4.3: Stress Paths

The effective stress paths of representative points during storm loading were studied. The stress paths of points (1) to (4), under the middle part of the tank, are presented in Fig. 6.13. The Mohr-Coulomb failure surface is also shown in this figure. Only a portion of the failure surface, which is between the extreme ranges of the Lode angles corresponding to the stresses, is presented. The states of stresses at these points are all inside the yield locus at the beginning of the storm and stay elastic during cyclic loading. The stress paths show upward movements with an increase in the deviator stresses. The mean effective stresses at these points decrease slightly and then increase later during the storm.

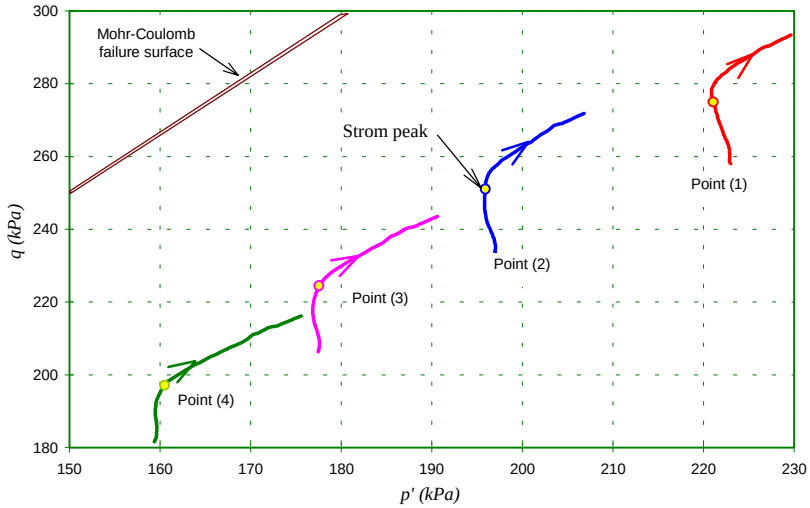

Fig. 6.13: Stress paths for points (1) to (4)

Stress paths for points (5) to (8), are presented in Fig. 6.14. The states of stresses of these points are inside the yield locus at the beginning of the storm. However, the stress paths move toward the failure surface during the storm, decreasing the mean effective stresses, and

therefore the shearing resistance of the soil, and eventually the points fail. (refer to Fig. 6.3). The intersections of the stress paths with the failure surface are marked by circles in Fig. 6.14. After failure, the stress paths move down, along the failure surface, decreasing both the mean effective stresses and the deviatoric shear stresses. There is a fluctuation in the predicted stress paths, when the stresses reach their minimum values, which is attributed to the numerical process of correcting the stresses back to the yield surface.

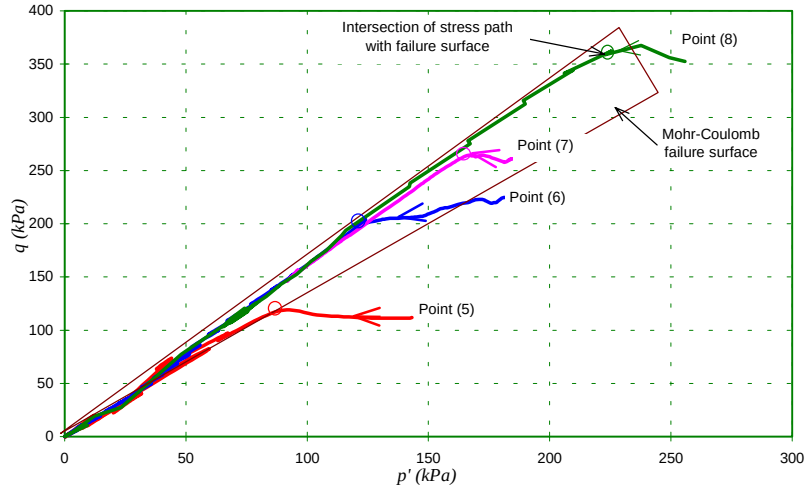

Fig. 6.14: Stress paths for points (5) to (8)

The stress paths of the points situated close to the surface adjacent to the tank, Points (9) to (11), are presented in Fig. 6.15. As noticed in Fig. 6.3, all of these points have failed under the ambient load. The subsequent fluctuation of stress paths can also be noticed clearly for these points.

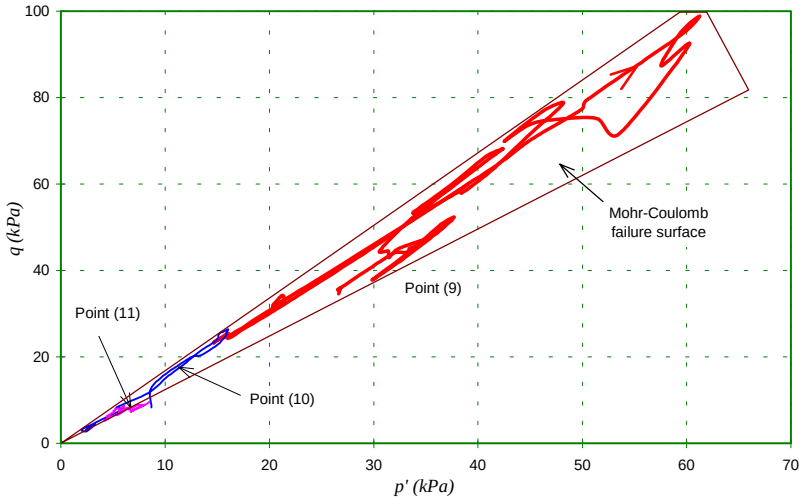

Fig. 6.15: Stress paths for points (9) to (11)

Stress redistribution in the soil under a foundation is an important aspect of cyclic loading. If the total stress in the soil does not change, the mean effective stress should be reduced during pore pressure build-up. However, the results of the present analysis show that the mean

effective stresses increase in some elements of the soil. To illustrate the stress redistribution in the soil during cyclic loading, the stress path for a point close to the centre of the foundation, point (12) in Fig. 6.9, is plotted in Fig. 6.16, together with the variation of the excess pore pressure versus the mean effective stress at that point. It can be seen that the mean effective stress and the deviatoric shear stress continuously increase during the storm. Even the sharp increase in the excess pore pressure before the storm peak does not reduce the rate of increase in the mean effective stress. The predicted variations of the mean effective stress, the pore pressure, and the total mean stress for this point are shown in Fig. 6.17. The total mean stress increases sharply before the storm peak, indicating a substantial transfer of stress from other parts of the soil to this point. After the storm peak, the rate of increase in the mean total stress reduces, which indicates that the increase in the mean effective stress after the storm peak is mostly due to the dissipation of excess pore pressure from the point.

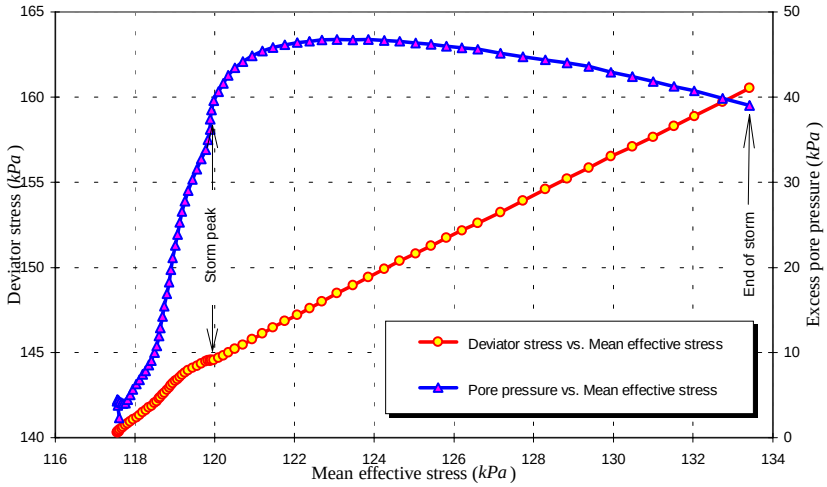

Fig. 6.16: Variations of the deviatoric stress and the pore pressure with the mean effective stress for a point at the centre of the foundation

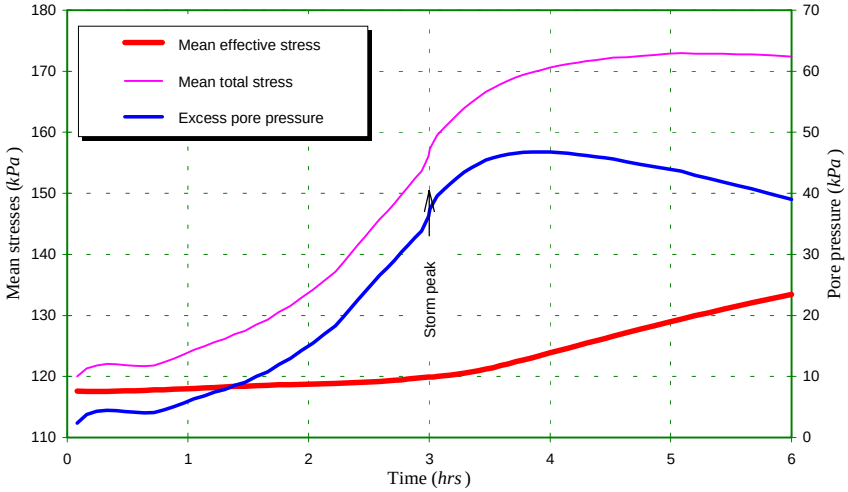

Fig. 6.17: Variations of the mean effective stress, the total stress and the excess pore pressure for a point at the centre of the tank

6.4.4: Settlement

The predicted vertical displacement of the tank during the storm loading is presented in Fig. 6.18. During the storm, specially during the application of wave loads with high intensities, the displacement increases. The foundation continues to settle up to *10 hrs* after the end of the storm. The settlement of the foundation is predicted to increase by approximately *0.052 m* during the storm.

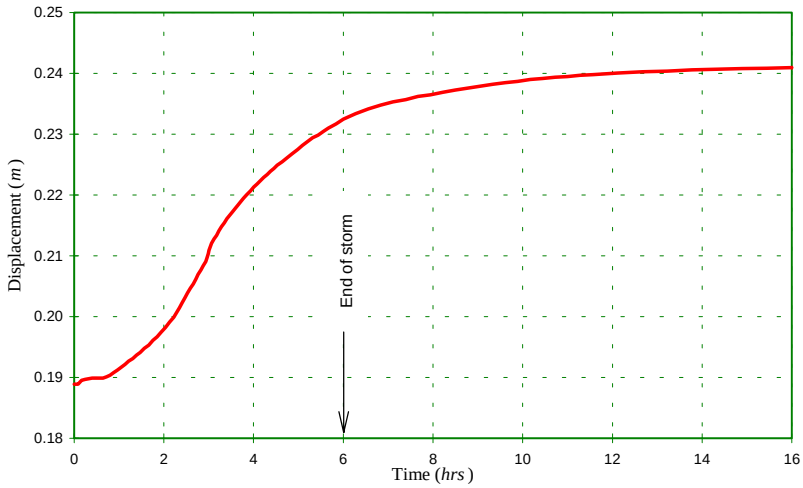

Fig. 6.18: Displacement of the tank during cyclic loading

6.5: EVALUATION OF THE RESULTS

The results of the analysis of the tank can be compared with the observed responses of the tank during two major storms. One of the major storms occurred on 6 November 1973, during which the performance of the foundation was measured. The storm had a maximum wave height of about *16 m* and caused the pore pressure in the upper layer of the sand to be increased by *10-20 kPa* (Clausen *et al.*, 1975). The most severe storm occurred on 19 November 1973 during which, as mentioned previously, the recording system was out of operation. The severity of the storm was estimated based on visual observations from a weather ship *100 km* away from the tank. The maximum wave height generated by this storm was probably *21 m*. During the first storm on 6 November, the tank probably settled *0.02 m* (Clausen *et al.*, 1975). During the period of severe storms, 15-20 November, the tank settled an additional *0.03-0.05 m*. Assuming that the excess pore water pressures are proportional to the settlements, Clausen *et al.* estimated that a maximum pore pressure of about *40 kPa* was generated under the tank on 19 November.

The liquefaction analysis reported here was performed for a *100* year design storm. The design storm has three maximum waves with a height of *24 m* and, therefore, is probably more severe than the storm that occurred on 19 November. The predicted pore pressures under the tank reached *51 kPa* during the storm. The additional settlement of the tank due to the storm loading was also predicted as *0.052 m*. Taking into account the severity of the design storm, in comparison with the storms on 6 and 19 November, the predicted pore pressures and the settlement of the tank are considered satisfactory.

6.6: CONCLUSIONS

A simple elasto-plastic model for soil was presented in this chapter which is suitable to be used in a liquefaction analysis. The model is based on the Mohr-Coulomb failure criteria. To incorporate the effects of cyclic loading, additional plastic volumetric strains are included in the model by incorporation of data obtained from laboratory cyclic tests on soil. A new definition for liquefaction was given in the framework of the elasto-plastic model.

The elasto-plastic model was employed in a liquefaction analysis of the Ekofisk tank. Considering the observed behaviour of the tank during major storms, the predicted performance is considered to be satisfactory. The pore pressure predicted at the centre of the tank is about *20%* greater than the estimated pore pressure generated by a severe storm with a probable maximum wave height of about *21 m*, corresponding to *90%* of the *100* year design storm wave. The predicted settlement of the foundation is also slightly larger than the maximum “observed” settlement during the severe storm. Therefore, the performance of the finite element model can be regarded satisfactory.

Application of the elasto-plastic soil model represents an improvement on more traditional methods of liquefaction analyses of offshore foundations. Comparison of the results of the modified elastic analyses, performed in Chapter 5, with the results of the elasto-plastic analysis shows some of the advantages of the latter method. The stress paths in the elasto-plastic analysis remain in the range of possible states, whereas in the modified elastic analyses, some points exhibit unrealistic stress paths, with negative mean effective stresses, a situation that is unlikely to be sustained in the ground. Another improvement in using an elasto-plastic analysis is the prediction of the settlement of the foundation. The predicted settlement in the elastic analysis was less than the minimum “observed” value, while the elasto-plastic analysis shows an excellent prediction of settlement for the foundation.

The results of the elasto-plastic analysis may be further improved if a more accurate soil model is employed. The generalized equation describing the stress-strain relationship in a

liquefaction analysis, explained in Chapter 5, can be used with any kind of soil model. The yield criteria and the flow rules offered by any model can be associated with the experimental data and used in liquefaction analyses. However, it is believed that the experimental data usually include some of the non-linearity associated with the cyclic behaviour of soil. Therefore, a simple elasto-plastic formulation, such as the one presented in this chapter, is probably adequate in representing soil behaviour under cyclic loading, at least for the solution of many practical problems.

In the next chapter, comparative studies of offshore foundations subjected to cyclic loading will be presented. The effects of the amplitude of cyclic load and the level of ambient load on the behaviour of the foundations will be considered.

Chapter 7

LIQUEFACTION RESISTANCE OF OFFSHORE FOUNDATIONS

7.1: INTRODUCTION

It was explained in the preceding chapters that the major loads experienced by offshore structures always include important cyclic components. When a wave passes an offshore structure, the wave force first acts in one direction and a few seconds later in the opposite direction with approximately the same magnitude. The stability of offshore foundations can be strongly affected if the seabed sediments have the potential to liquefy under wave induced cyclic loading. It is thus essential to check the stability of the foundations for cyclic loading.

There are various factors which may affect the cyclic behaviour of a foundation on granular soil. The liquefaction properties of the soil strata under the foundation are probably the prime factor. The magnitude of the ambient and cyclic loads acting on the foundation as well as the shape of the foundation are other factors that should be considered by the geotechnical engineer.

The shape of an offshore foundation has an important influence on the cyclic behaviour of the foundation. Some types of foundations may exhibit more resistance to cyclic load than others. An appropriate choice of foundation may reduce the risk of liquefaction and often reduces the cost of the construction. It is therefore of interest to study the behaviour of various types of foundations when they are subjected to cyclic loading.

In this chapter, the numerical method presented in Chapter 6 for elasto-plastic liquefaction analysis is employed to examine the resistance of some offshore foundations to cyclic load. The effects of various factors, such as ambient load, cyclic load, and the shapes of the foundations will be considered.

7.2: DEFINITION OF THE PROBLEM

Liquefaction analyses of offshore foundations resting on potentially liquefiable granular soil were performed to investigate the behaviour of the foundations under cyclic loading. Three

different hypothetical foundations have been used in this study, a shallow circular foundation, a cylindrical caisson, and a shallow circular foundation with a short pile at its axis, termed the "piled foundation". The effects of cyclic horizontal and vertical loads with different amplitudes, the magnitude of ambient loads, and the physical shape on the cyclic responses of these foundations were investigated.

Material properties

The liquefaction properties of granular soil used in this study are similar to the Ekofisk sand with a relative density of 77% (Lee and Focht, 1975). The cyclic strength of the sand is shown in Fig. 7.1. The pore pressure generation function proposed by Seed *et al.* (1975a), Equation (5.11), with a pore pressure parameter of $\alpha = 0.7$ was used in all analyses. It was assumed that the sand has a coefficient of permeability of $k = 10^{-6}$ *m/sec*, a Young's modulus of $E' = 50000$ *kN/m*^{2}, a Poisson's ratio of $\nu = 0.25$, a friction angle of $\phi = 45^o$, a zero dilation angle, and a saturated unit weight of $\gamma_{sat} = 17$ *kN/m*^{3}. The coefficient of lateral earth pressure in the seabed prior to the application of the foundation loads was assumed to be $K_o = 0.5$.

The foundations were assumed to be rigid. This condition was approximated by assigning a Young's modulus of $E = 10^8$ *kN/m*^{2} to all foundation elements.

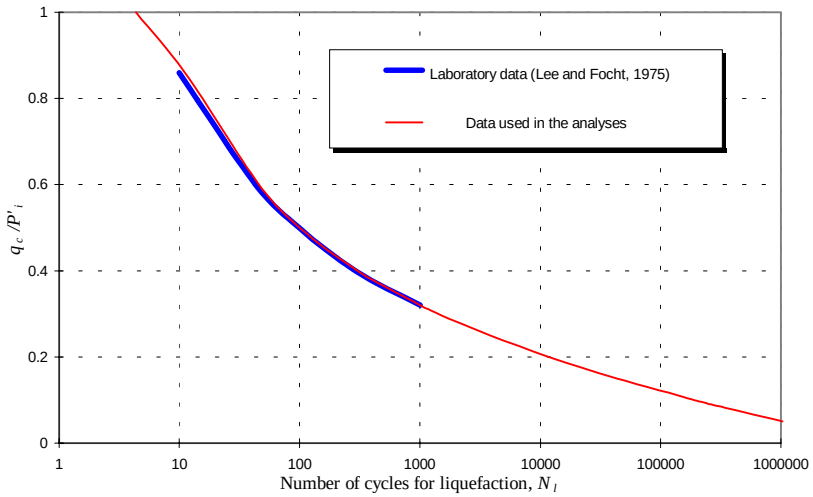

Fig. 7.1: Cyclic strength of the Ekofisk sand with a relative density of *77%*

Geometry

The finite element mesh used in the analyses is presented in Fig. 7.2, which also shows the geometry of the shallow foundation. The mesh can be modified for other types of foundations by changing the properties of some soil elements to those of the "rigid" foundation elements. The geometries of the other types of foundations are shown in Fig. 7.3. The number of wedges in the cylindrical finite element model used in the analyses was *8* (see Chapter 3)

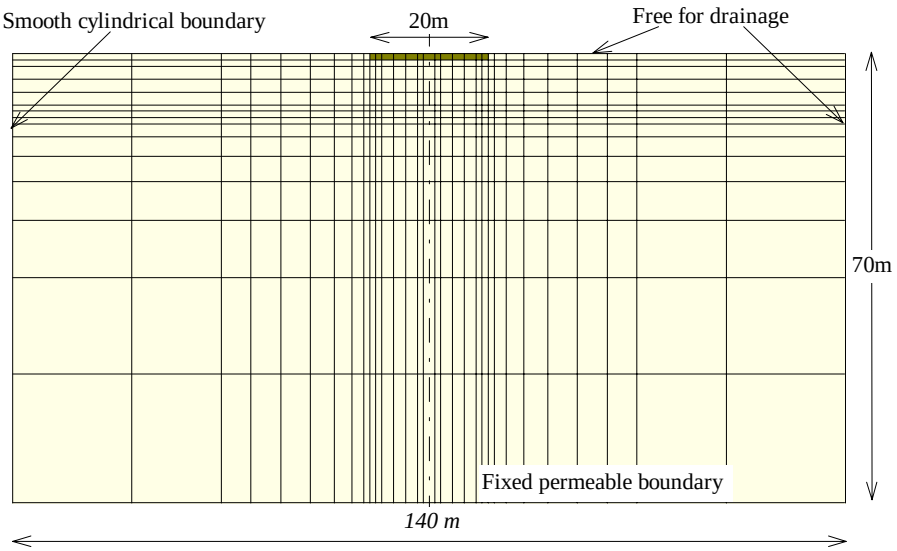

Fig. 7.2: Finite element mesh

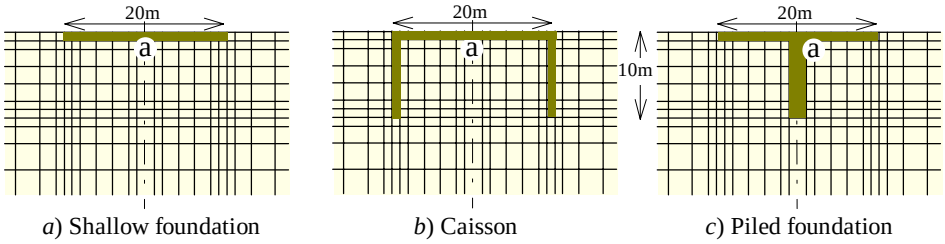

Fig. 7.3: Geometry of the foundations used in the analyses

Loading

Various values of the ambient loads and cyclic loads have been used in the analyses to evaluate the effects of load intensities on the behaviour of the foundations. It was assumed that the ambient loads act only in the vertical direction, i.e. the horizontal component of the ambient load was assumed zero. In each case the magnitude of the cyclic loading was held constant throughout the loading period, which was usually greater than *500* cycles or *5000* seconds. It was assumed that all cyclic loads, regardless of their amplitudes, have a constant period of *10 sec*.

7.3: CYCLIC RESPONSE OF SHALLOW FOUNDATIONS

The numerical scheme presented in Chapter 6 for liquefaction analyses was utilized to study the response of a shallow foundation to cyclic loads. The foundation has a radius of *10 m*, as shown in Fig. 7.3*a*. The cyclic responses of the foundation under various cyclic loads and ambient loads were compared.

7.3.1: Response of Shallow Foundations Subjected to Cyclic Horizontal Loads

Cyclic loads introduced by waves usually have a relatively large component in the horizontal direction. The response of the shallow foundation under a cyclic horizontal load was studied. It was assumed that the foundation is subjected to an ambient vertical traction of $V=400\ kPa$ and a cyclic two-way horizontal traction of $H_c=100\ kPa$, i.e. the horizontal traction was cycled about zero with an amplitude of $100\ kPa$. Variations of the settlement and pore pressure generated at the centre of the foundation are used as measures of the cyclic response of the foundation. The response of the foundation under the cyclic horizontal load is presented in Fig. 7.4. The maximum value of the predicted pore pressure is about $79\ kPa$ which is generated after application of about 350 cycles of load to the foundation. At this stage, the rate of pore pressure generation becomes almost equal to the rate of pore pressure dissipation. After application of 350 cycles of load, the pore pressure reduces slightly. This behaviour may be attributed to the diffusion of pore water from the zones of high pressure at the centre of the foundation. It also indicates that the rate of pore pressure dissipation at the centre of the foundation exceeds the rate of pore pressure generation. The settlement of the foundation continuously increases with increasing the number of cycles, which is a result of continuous densification of some part of the soil under the foundation. After application of 500 load cycles the settlement of the foundation increases by about 45% of the initial settlement produced under the ambient load. Application of an additional 500 load cycles increases the settlement by only 6% of its initial value. If the analysis is proceeded further, the cyclic load will result in indefinite densification of some elements in the soil. This phenomenon is not realistic since the densification may influence the cyclic properties of the soil, as well as the soil permeability, and eventually increases the cyclic strength of the soil. A more realistic solution to the liquefaction problem could have been achieved if the effects of densification on the cyclic properties of the soil were considered in the analyses.

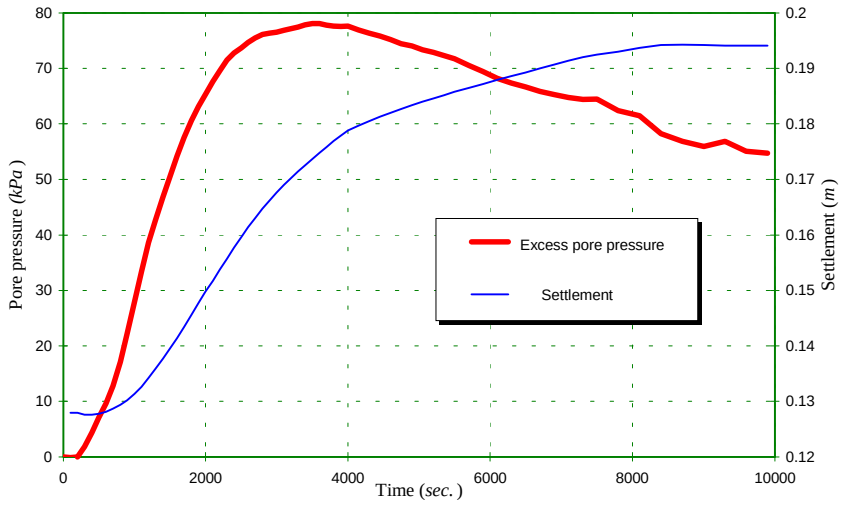

Fig. 7.4: Variations of excess pore pressure and settlement predicted at the centre of the shallow foundation, $V=400\ kPa$, $H_c=100\ kPa$

Distribution of pore water pressures under the foundation in the vertical plane of the applied cyclic horizontal load after application of *100* load cycles is presented in Fig. 7.5. The maximum pore pressure predicted at this stage is about *41 kPa*, which is generated at a depth of about *9 m* below the seabed and about *5 m* away from the foundation centre. Another zone of high pore pressure is also predicted off the foundation edge, about *8 m* below the seabed. The distribution of pore pressures after application of *300* load cycles is also shown in Fig. 7.6. The zones of high pore pressure have been expanded and extended deep into the soil, about *25-30 m* below the seabed. The maximum pore pressure at this stage is produced beneath the centre of the foundation with a value of about *76 kPa*. Another zone of high pressure is also predicted at a depth of about *25 m*, about *20 m* away from the foundation centre, with a maximum pore pressure of about *56 kPa*.

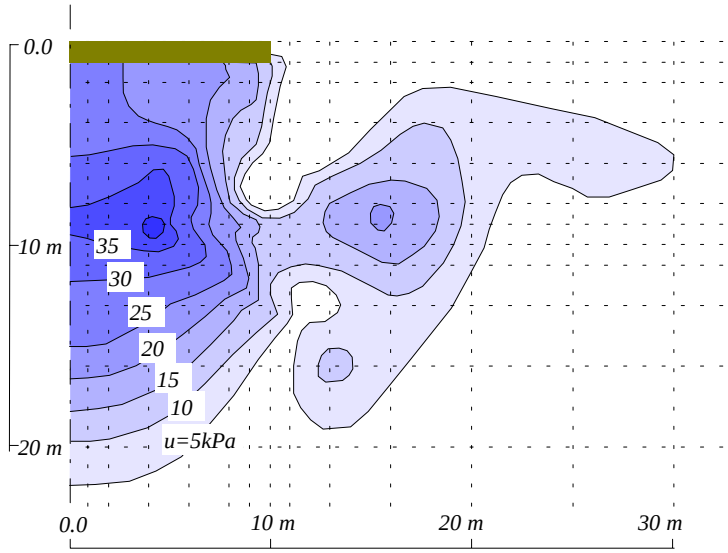

Fig. 7.5: Distribution of pore pressures predicted under the shallow foundation after *100* cycles of horizontal load, *V=400 kPa, H_c=100 kPa, Time=1000 sec.*

The soil elements under the edge of the foundation, up to about *15 m* under the seabed, do not generate significant pore pressures, since these elements have failed plastically under the ambient load. The failed zone affects the distribution of pore pressures, as may be noticed from Figs 7.5 and 7.6. Prediction of the zones which have failed under ambient load, together with the sequential expansion of the failed zone during cyclic loading are shown in Fig. 7.7. After application of about *300* cycles of load, the failed zone remains virtually unchanged. At this stage, only a small portion of the soil under the foundation, which has not failed previously, has the potential to generate pore pressures under cyclic loading.

Effects of cyclic horizontal load amplitude

The effects of the amplitude of cyclic horizontal load on the response of the shallow foundation were investigated. The amplitude of the cyclic horizontal traction was varied from

H_c=*10 kPa* to H_c=*200 kPa*. The foundation was assumed to be subjected to an ambient vertical traction of *V=400 kPa*.

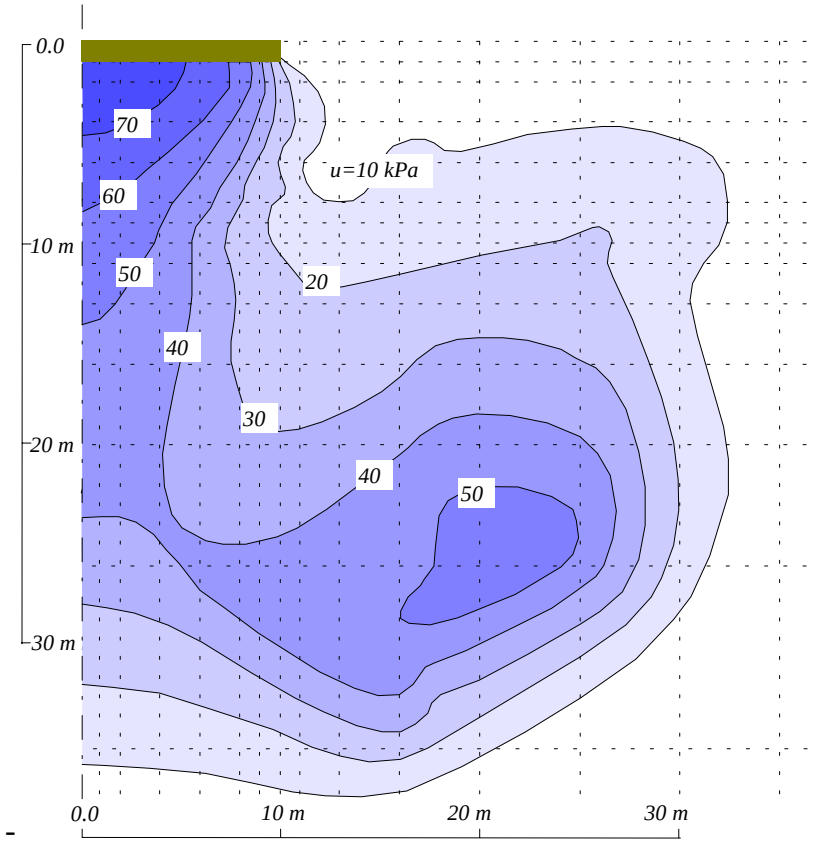

Fig. 7.6: Distribution of pore pressures predicted under the shallow foundation after *300* cycles of horizontal load, *V=400 kPa, H_c=100 kPa, Time=3000 sec.*

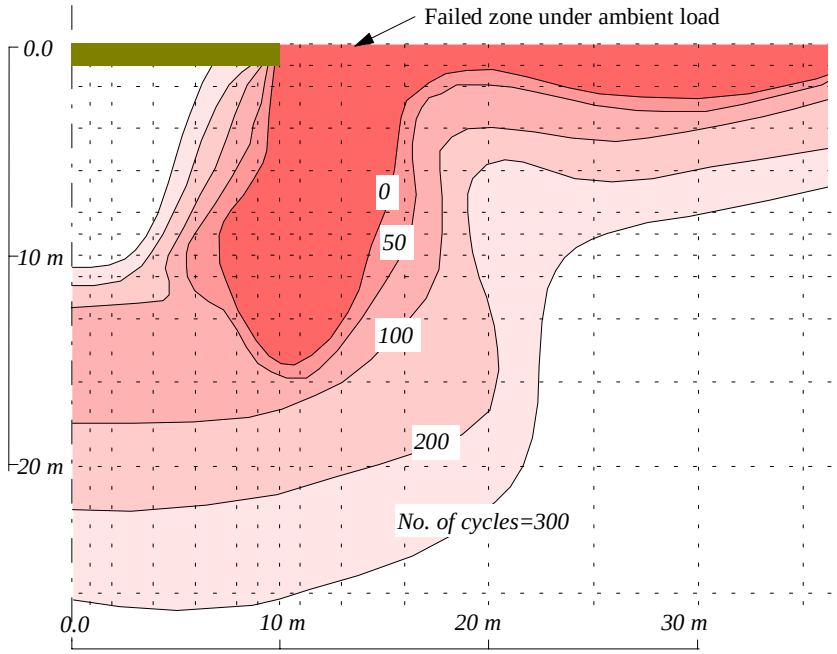

Fig. 7.7: Expansion of failed zone during cyclic horizontal loading of the shallow foundation, *V=400 kPa, H_c=100 kPa*

The pore pressures predicted at the centre of the foundation under various cyclic loads are presented in Fig. 7.8. As the magnitude of cyclic load increases, the pore pressures generated under the foundation increase. The pore pressures predicted at the centre of the foundation under cyclic horizontal loads of $H_c=50\ kPa$ and $H_c=100\ kPa$ are very similar. However, the greater cyclic load results in larger pore pressures at other points in the soil. There is a limit on the maximum value of the pore pressure generated at any point in the soil, above which the soil fails. For example, under cyclic horizontal loads of $H_c=150\ kPa$ and $H_c=200\ kPa$, the soil elements beneath the foundation fail quickly after the application of the cyclic loads.

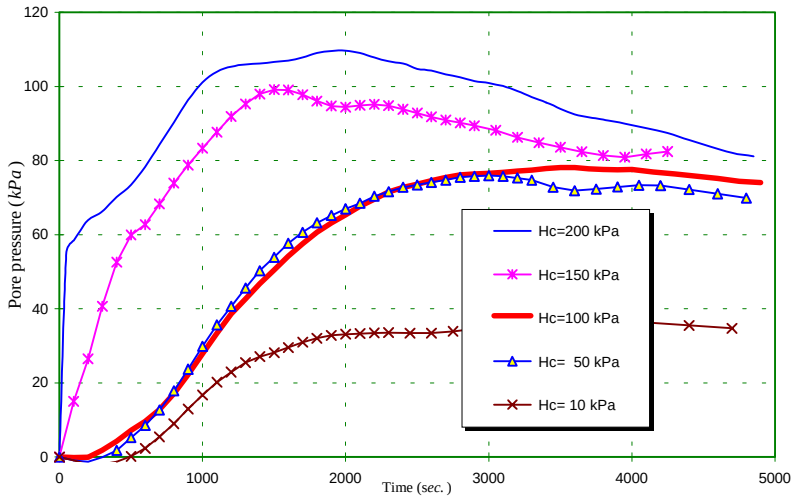

Fig. 7.8: Effects of cyclic horizontal load amplitude on the pore pressure generated at the centre of the shallow foundation, *V=400 kPa*

The predicted settlements of the foundation under different cyclic loads are presented in Fig. 7.9. Generally, the settlement at any time increases as the cyclic load amplitude increases. After *500* cycles of horizontal load of $H_c=200\ kPa$, the settlement of the foundation increases by about *75%* of the initial settlement produced under the ambient load.

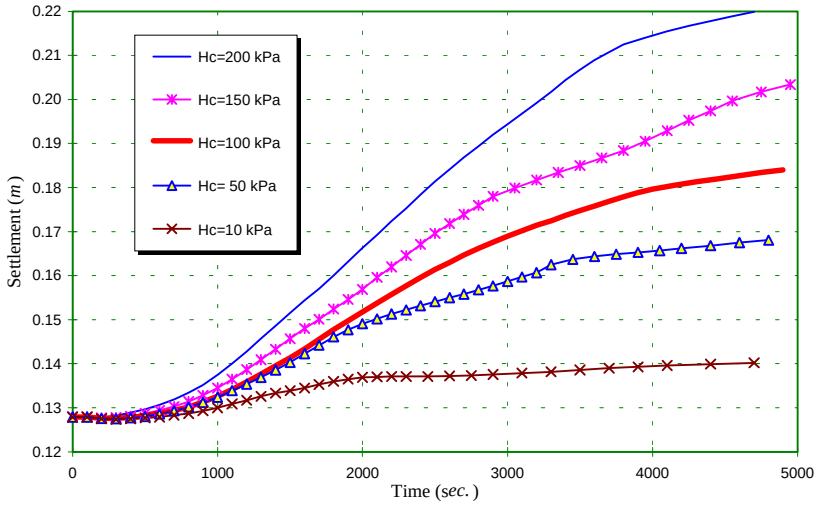

Fig. 7.9: Effects of cyclic horizontal load amplitude on the settlement of the shallow foundation, *V=400 kPa*

7.3.2: Response of Shallow Foundations Subjected to Cyclic Vertical Loads

Wave forces often apply cyclic vertical loads to some offshore foundations. The cyclic vertical loads are usually applied to the foundations as a series of consecutive tension and compression force increments. The responses of the shallow foundation subjected to cyclic vertical loads are presented in this section.

A cyclic vertical load with a constant amplitude of $V_c=100\ kPa$ is applied to the shallow foundation which is under an ambient vertical traction of $V=400\ kPa$, i.e. the load varies from $300\ kPa$ to $500\ kPa$. Variations of the settlement and pore pressure predicted at the centre of the foundation are presented in Fig. 7.10. For comparison, the response of the shallow foundation under a cyclic horizontal load of $H_c=100\ kPa$ is also shown in this figure. The variations of pore pressures predicted at the centre of the foundation under both loadings are very similar. However, the settlement of the foundation under the cyclic vertical load is generally larger than the settlement predicted under the cyclic horizontal load. A reason for this difference is that the distribution of pore pressure, and hence the effective stress distribution, produced in the soil due to the cyclic vertical load is different from that predicted under the cyclic horizontal load. The distributions of pore pressures after application of *100* cycles and *300* cycles of vertical load are presented in Figs 7.11 and 7.12, respectively. Comparison of these figures with the pore pressure distributions under the cyclic horizontal load, Figs 7.5 and 7.6, shows that under the vertical load, the zones of high pore pressures extend deeper into the soil, which result in a larger final settlement.

The maximum pore pressure generated after *100* cycles of vertical load is *46 kPa*, which is predicted at a depth of about *8 m* under the foundation. The maximum pore pressure after *300* load cycles is about *76 kPa*, which is generated at the centre of the foundation. Another zone of high pore pressure is also predicted at a depth of about *35 m* under the edge of the foundation. The maximum pore pressure in this zone reaches *68 kPa*.

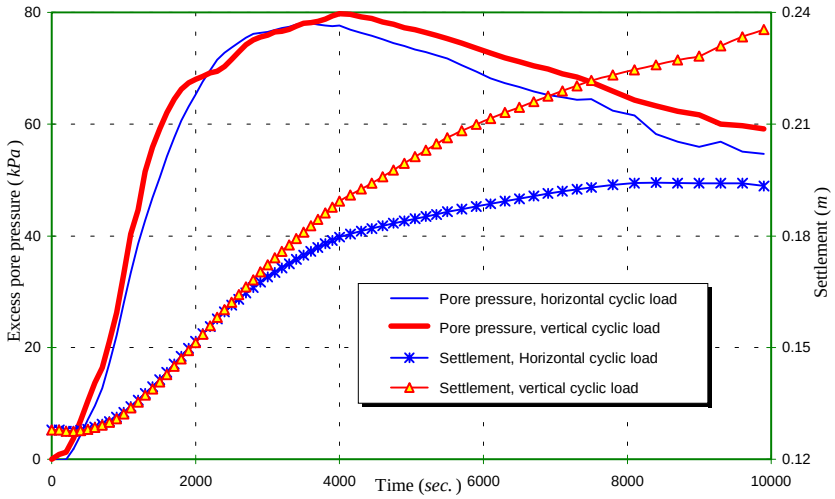

Fig. 7.10: Comparison of the responses of the shallow foundation under horizontal and cyclic vertical loads, $V=400\ kPa$, $H_c=100\ kPa$, $V_c=100\ kPa$

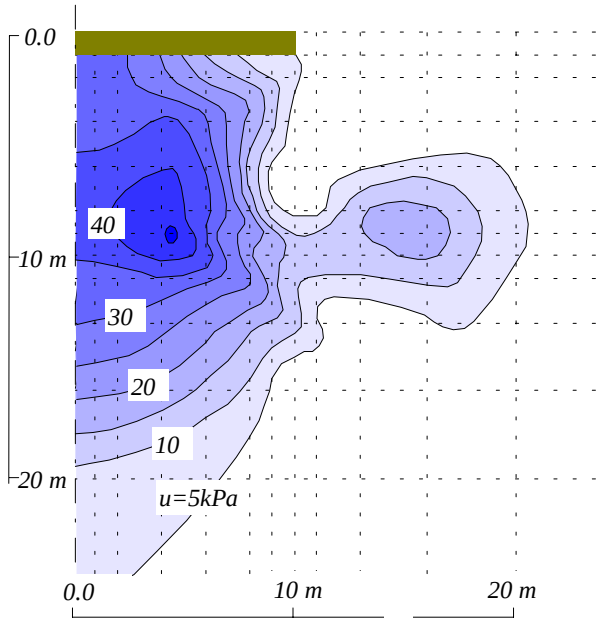

Fig. 7.11: Distribution of pore pressures predicted under the shallow foundation after *100* cycles of vertical load, *V=400 kPa, V_c=100 kPa, Time=1000 sec.*

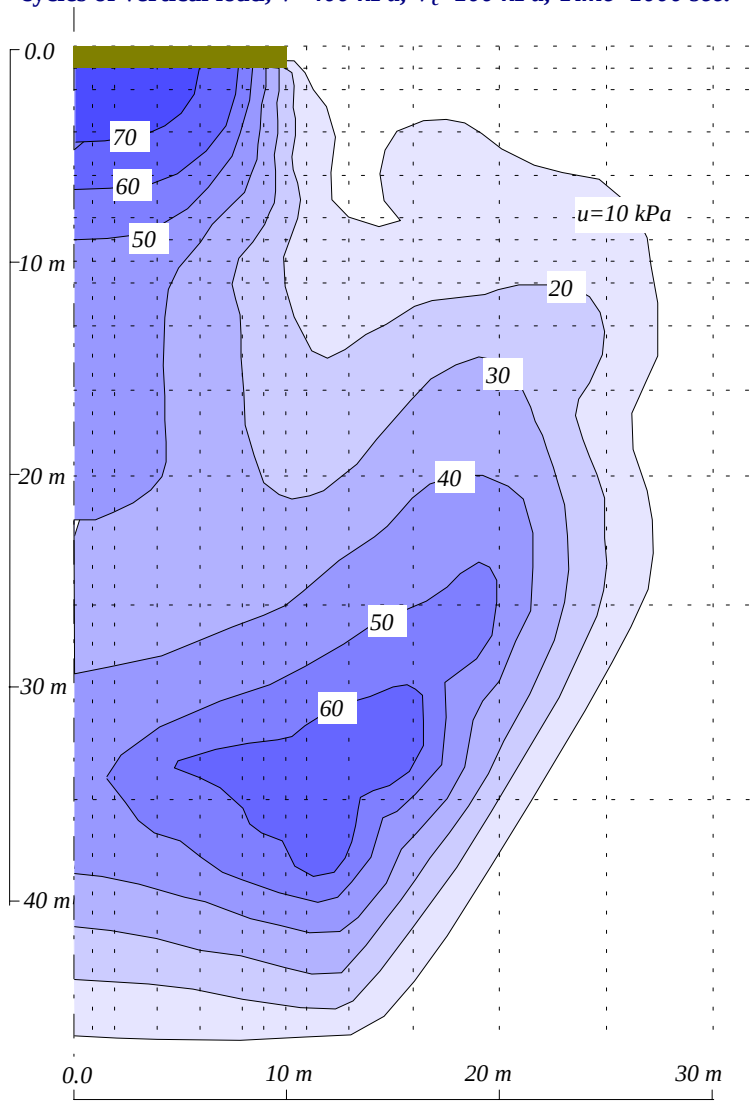

Fig. 7.12: Distribution of pore pressures predicted under the shallow foundation after *300* cycles of vertical load, *V=400 kPa, V_c=100 kPa, Time=3000 sec.*

Effects of cyclic vertical load amplitude

The effects of the amplitude of cyclic vertical load on the response of the shallow foundation were investigated. The amplitude of cyclic vertical traction was varied from $V_c=10\ kPa$ to $V_c=200\ kPa$. The ambient vertical traction on the foundation was kept constant at $V=400\ kPa$.

The excess pore pressure predicted at the centre of the foundation and the settlement of the foundation under various cyclic vertical loads are plotted in Figs 7.13 and 7.14, respectively. The pore pressure and settlement generally increase with increasing the cyclic load amplitude. The soil elements beneath the foundation fail quickly after the application of the cyclic vertical loads of $V_c=200\ kPa$. The initial settlement of the foundation increases by about *90%* after application of *500* cycles of vertical load of $V_c=200\ kPa$.

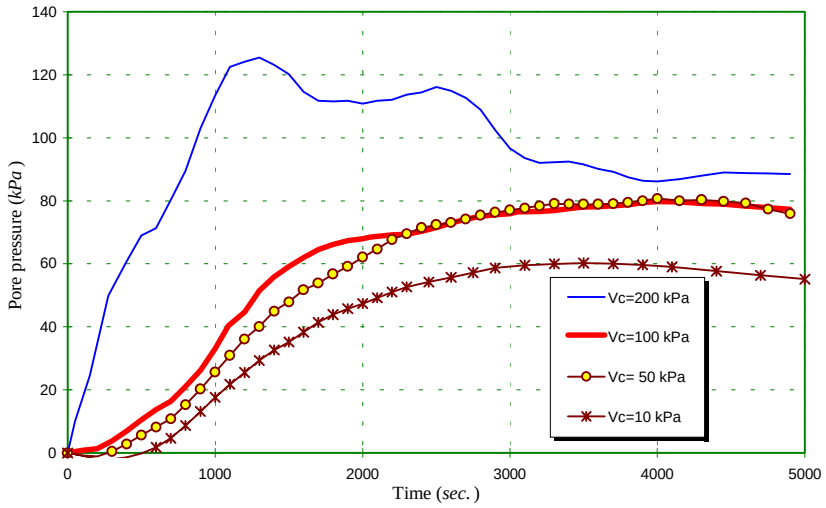

Fig. 7.13: Effects of cyclic horizontal load amplitude on the pore pressure predicted at the centre of the shallow foundation, *V=400 kPa*

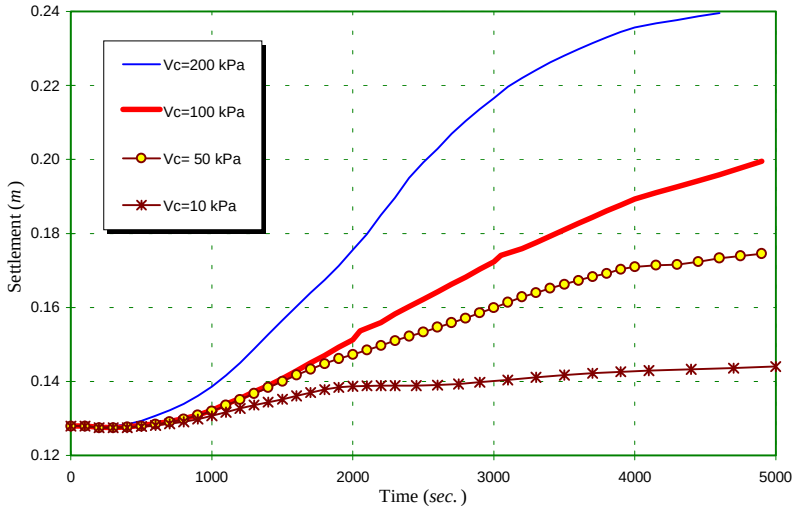

Fig. 7.14: Effects of cyclic horizontal load amplitude on the settlement of the shallow foundation, *V=400 kPa*

7.3.3: Effects of Ambient Load Intensity on the Cyclic Responses of Shallow Foundations

The effects of the magnitude of ambient vertical load on the cyclic behaviour of the shallow foundation were studied. The intensity of the ambient traction was varied from *V=200 kPa* to *V=800 kPa*. Cyclic loads with an amplitude of *100 kPa* were applied to the foundation in both horizontal and vertical directions, separately.

Variations of pore pressures predicted at the centre of the foundation are presented in Figs 7.15 and 7.16 for cyclic horizontal and vertical loads, respectively. The maximum pore pressure generally increases as the intensity of the ambient vertical load increases. An increase in the ambient load increases the mean effective stresses, and thus the maximum achievable pore pressures in the soil elements under the foundation. Therefore, the pore pressures generated due to cyclic loading of a foundation under a larger ambient load are expected to be greater. In other words, the tendency of the soil for densification is greater under a larger ambient load, which results in greater potential pore pressures and settlement.

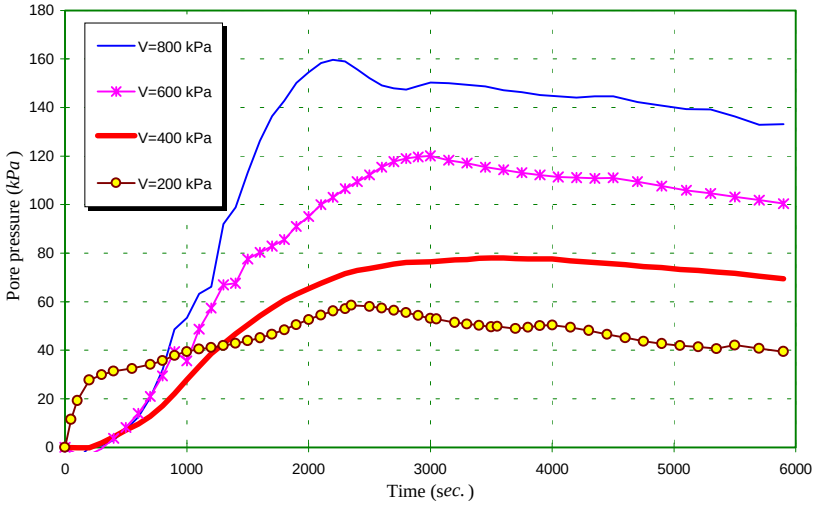

Fig. 7.15: Effects of ambient loads on the pore pressure generated at the centre of the shallow foundation subjected to a cyclic horizontal load of H_c=100 kPa

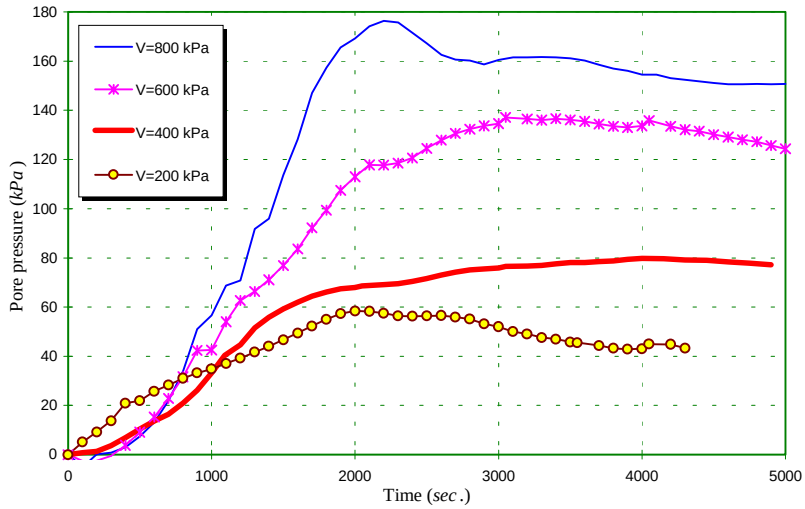

Fig. 7.16: Effects of ambient loads on the pore pressure generated at the centre of the shallow foundation subjected to a cyclic vertical load of V_c=100 kPa

An increase in the intensity of the ambient load has a great impact on the additional settlement produced during cyclic loading under the shallow foundation. The additional settlement is the increase in the initial settlement, produced under ambient load, during cyclic loading. The effects of ambient load intensity on the additional settlement are shown in Figs 7.17 and 7.18. Larger ambient loads generally result in greater settlements during cyclic loading. The settlement predicted due to a cyclic vertical load is generally greater than the settlement predicted due to a cyclic horizontal load with the same amplitude.

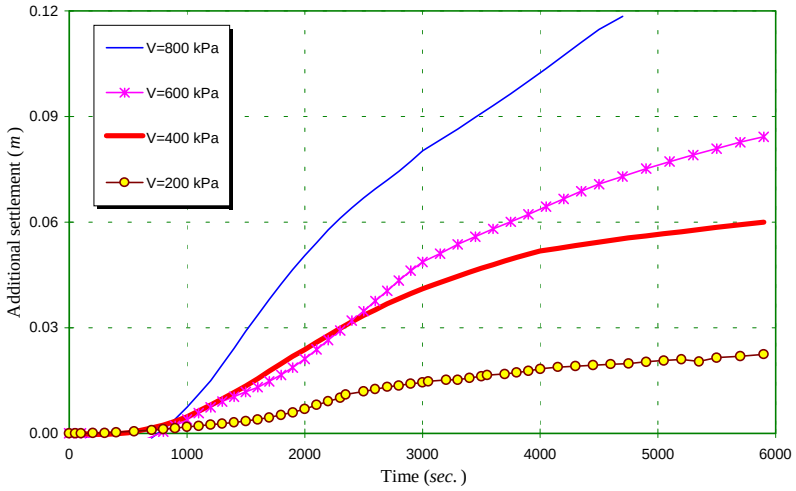

Fig. 7.17: Effects of ambient loads on the settlement of the shallow foundation subjected to a cyclic horizontal load of H_c=100 kPa

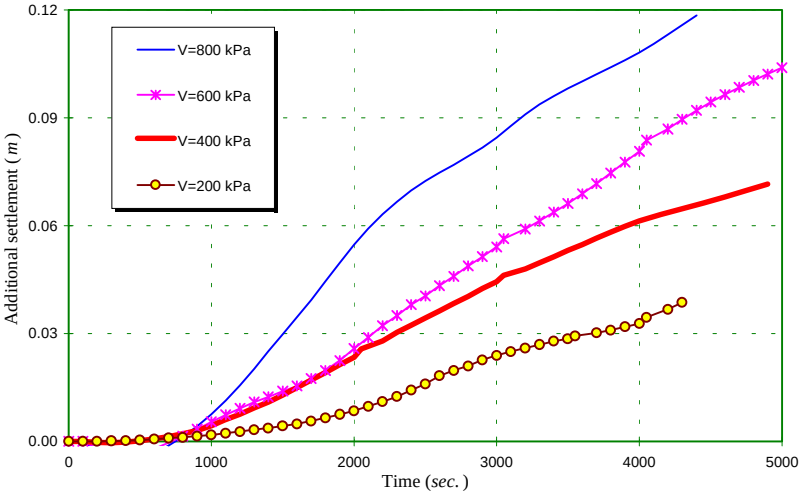

Fig. 7.18: Effects of ambient loads on the settlement of the shallow foundation subjected to a cyclic vertical load of V_c=100 kPa

7.4: CYCLIC RESPONSE OF CAISSONS

The effects of cyclic loads on a cylindrical caisson foundation with a physical shape as presented in Fig. 7.3*b* were studied. The caisson has an outside radius of *10 m*, and a depth of *10 m*. The thickness of the caisson wall is *1 m*. Various cyclic loads and ambient loads were used and the cyclic responses of the caisson were compared.

7.4.1: Response of Caissons Subjected to Cyclic Horizontal Loads

The response of the caisson to a cyclic horizontal load with an amplitude of H_c*=100 kPa* was studied. The caisson was subjected to an ambient vertical traction of *V=400 kPa*. Variations of the settlement and excess pore pressure predicted at the centre of the caisson, point (a) in Fig. 7.3*b*, are presented in Fig. 7.19. The pore pressure rises gradually to a maximum value of about *62 kPa* after application of about 55*0* load cycles. After this point the pore pressure at the centre of the caisson reduces slightly due to the diffusion of pore fluid from the zones of high pressure at the centre. At this stage the analysis reaches a steady state and no further change in pore pressure is predicted. At the beginning of the analysis, a small negative pore pressure is predicted at the centre of the caisson. However, the effects of the negative pore pressure on the overall behaviour of the caisson are considered to be insignificant. The settlement of the caisson continuously increases.

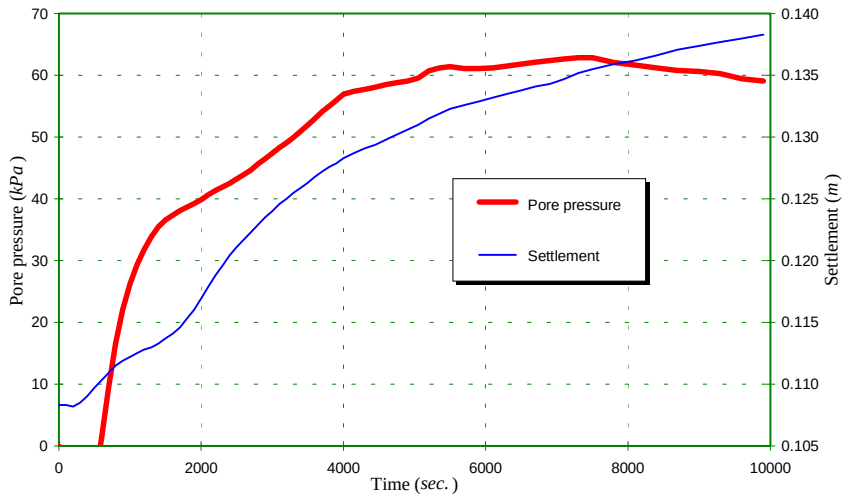

Fig. 7.19: Variations of excess pore pressure and settlement predicted at the centre of the caisson subjected to a cyclic horizontal load, *V=400 kPa, H_c=100 kPa*

Distributions of pore pressures under the caisson at times *1000 sec.* and *5500 sec.*, i.e. after application of *100* and *550* load cycles, are presented in Figs 7.20 and 7.21, respectively. The pore pressures inside the caisson are very large, since the drainage for the soil elements inside the caisson is relatively confined. After application of *100* load cycles, the maximum pore pressure inside the caisson reaches *49 kPa* which is predicted close to the caisson wall. The

maximum pore pressure increases to *62 kPa* after application of *550* load cycles. After application of *100* load cycles, the pore pressures predicted under the caisson are comparable with those predicted under the shallow foundation, Fig. 7.5.

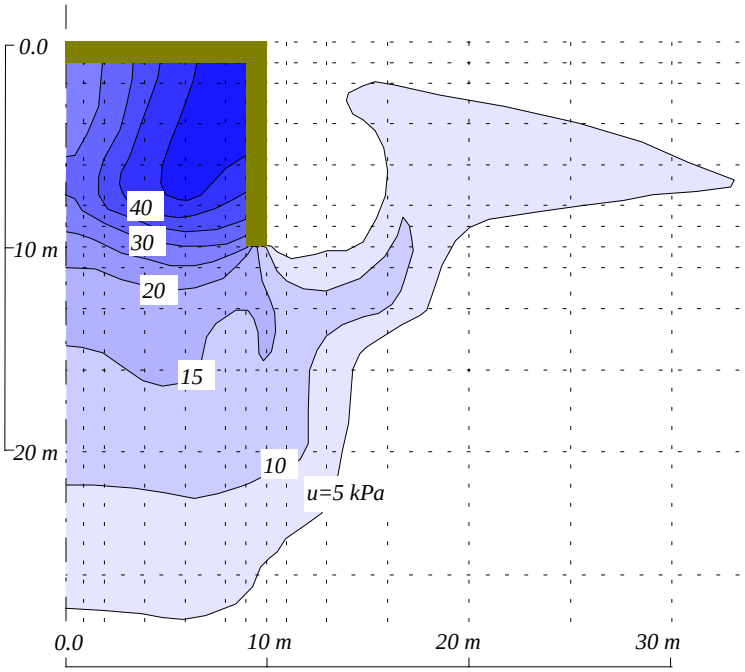

Fig. 7.20: Distribution of pore pressures predicted under the caisson after *100* cycles of horizontal load, *V=400 kPa, H_c=100 kPa, Time=1000 sec.*

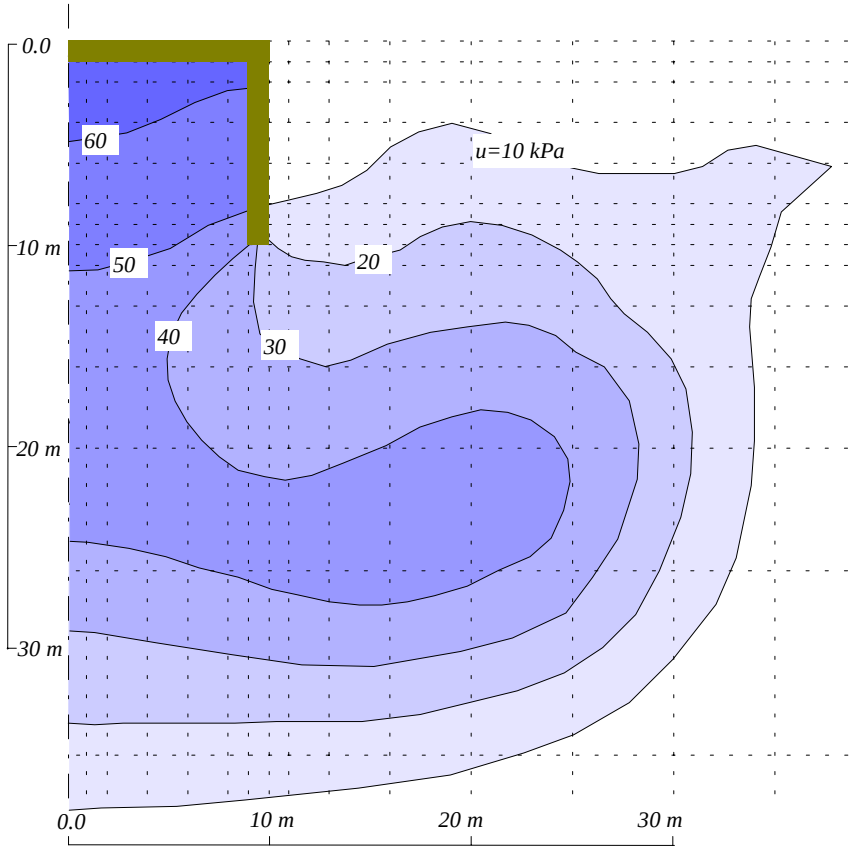

Fig. 7.21: Distribution of pore pressure predicted under the caisson after *550* cycles of horizontal load, *V=400 kPa, H_c=100 kPa, Time=5500 sec.*

The responses of the caisson and the shallow foundation under a cyclic horizontal load are compared in Fig. 7.22. Both foundations are subjected to similar cyclic and ambient loads. The settlement of the shallow foundation under the ambient load is about *18%* greater than the settlement of the caisson. However, the additional settlement of the shallow foundation produced during cyclic loading is about *2.2* times greater than the additional settlement predicted for the caisson. This difference shows the advantage of caisson foundations when they are subjected to cyclic loading. The difference in the settlements of the foundations is attributed to the difference in the pore pressure distributions in the soil for the period of time between *1000 sec.* and *4000 sec.* The pore pressure predicted at the centre of the shallow foundation is greater than the pore pressure under the caisson, for almost the whole range of time before *8000 sec*. However, since the drainage path for a point at the centre of the shallow foundation is shorter than that for a point at the centre of the caisson, the pore pressure is dissipated faster under the shallow foundation. As a consequence, the pore pressure at the centre of the shallow foundation becomes less than the pore pressure predicted under the caisson after *8000 sec*.

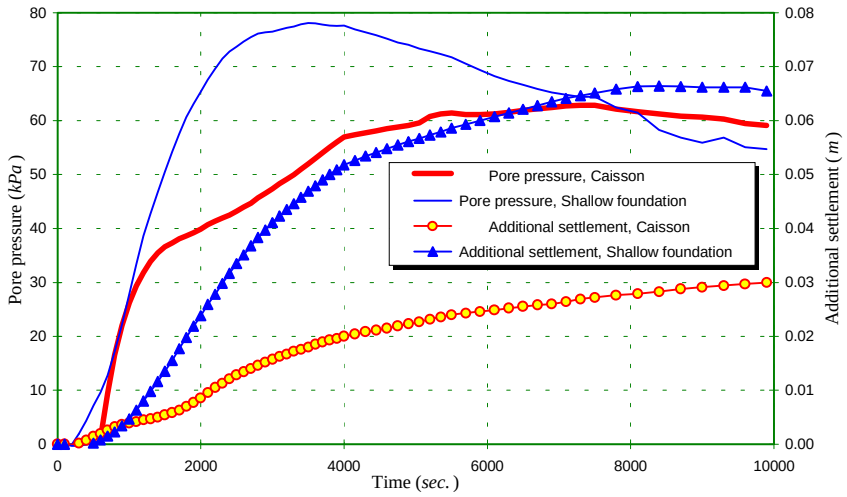

Fig. 7.22: Comparison of the responses of the caisson and the shallow foundation to a cyclic horizontal load, *V=400 kPa, H_c=100 kPa*

Effects of cyclic horizontal load amplitude

The effects of the amplitude of cyclic loads on the pore pressure and settlement predicted at the centre of the caisson are presented in Fig. 7.23. An increase in the cyclic load amplitude causes both the pore pressure and the settlement to be increased. These responses are similar to those predicted for the shallow foundation.

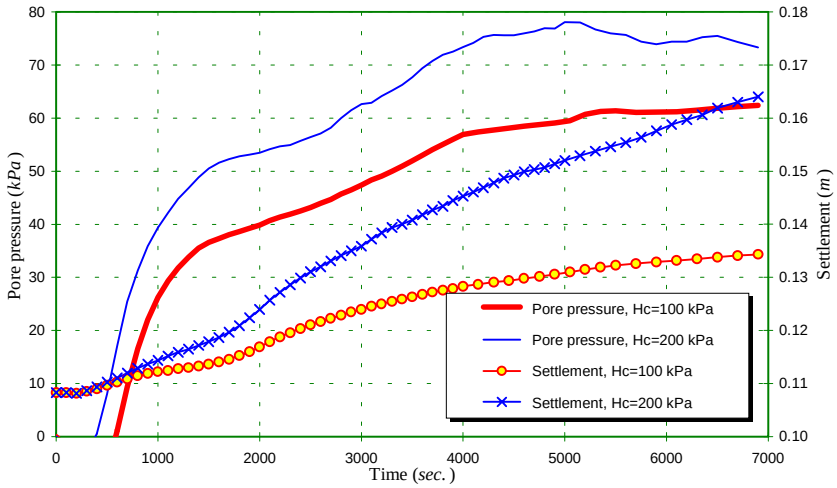

Fig. 7.23: Effects of the cyclic horizontal load amplitude on the pore pressure and settlement predicted at the centre of the caisson, *V=400 kPa*

7.4.2: Response of Caissons Subjected to Cyclic Vertical Loads

The response of the caisson to a cyclic vertical load was also studied. The caisson is subjected to a cyclic vertical traction of V_c=*100 kPa*, and an ambient vertical traction of *V=400 kPa*. The variation of excess pore pressure predicted at the centre of the caisson, point (a) in Fig. 7.3*b*, is presented in Fig. 7.24. For comparison, the variation of pore pressure predicted at the centre of the shallow foundation under the same loading, and the variation of pore pressure at the centre of the caisson under a cyclic horizontal load of H_c=*100 kPa* are also shown in this figure. The cyclic vertical load generates a larger pore pressure under the caisson in comparison to the cyclic horizontal load. The pore pressure predicted under the shallow foundation is greater than that predicted under the caisson for a period of time between *1000 sec.* to *6300 sec.*

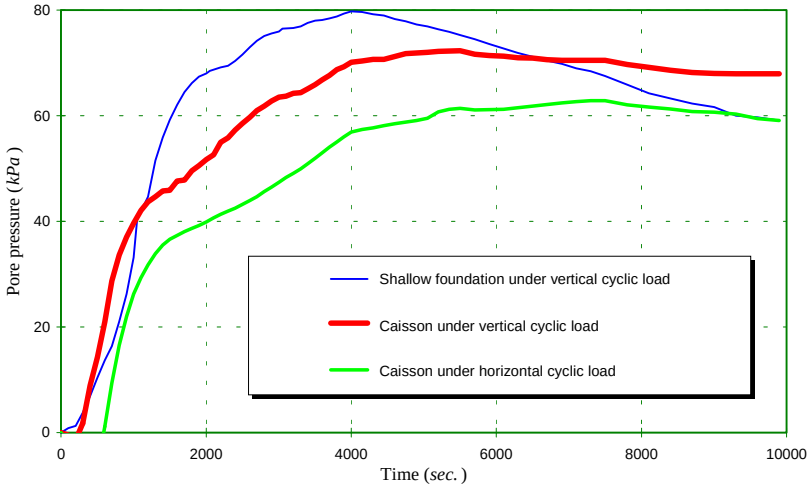

Fig. 7.24: Comparison of the pore pressures generated under the caisson and the shallow foundation, *V=400 kPa*

The additional settlements produced during cyclic loading for the caisson and the shallow foundation are compared in Fig. 7.25. The settlement of the caisson under the cyclic vertical load is greater than the settlement predicted under the cyclic horizontal load. The settlement of the shallow foundation is about *2* times greater than the one predicted for the caisson under a similar cyclic load.

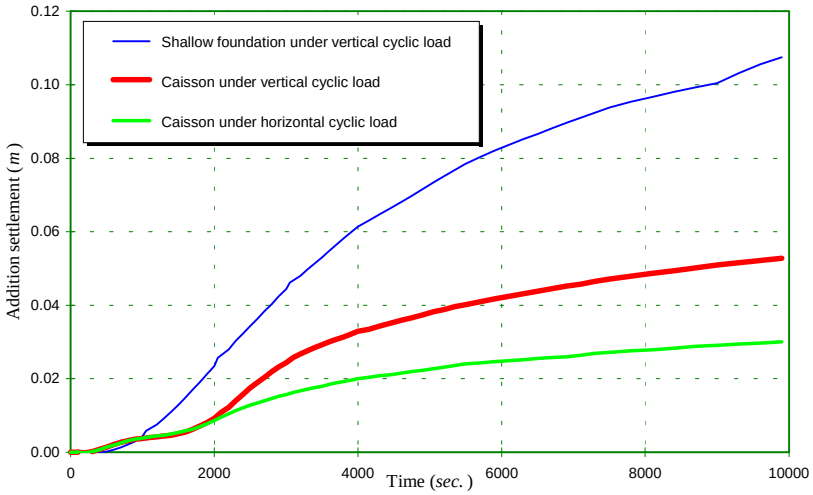

Fig. 7.25: Comparison of the settlements predicted for the caisson and the shallow foundation, *V=400 kPa*

Distributions of pore pressures generated under the caisson at times *1000 sec.* and *5500 sec.*, after application of *100* cycles and *550* cycles of the vertical load, are presented in Figs 7.26 and 7.27. Comparison of these figures with the pore pressure distributions for the caisson under a cyclic horizontal load of H_c*=100 kPa*, Figs 7.20 and 7.21, shows that under the cyclic vertical load, the zones of high pore pressures extend deeper into the soil. The pore pressures are also greater in most of the soil under the cyclic vertical load.

7.5: CYCLIC RESPONSE OF PILED FOUNDATIONS

Shallow foundations are often constructed together with piles in order to increase the lateral as well as the vertical resistance of the foundation system. It is therefore of interest to study the responses of a shallow foundation with a short pile. The short pile has a length of *10 m* and a radius of *1 m* which is connected to the centre of the shallow foundation. The shallow foundation has a radius of *10 m*. The geometry of the piled foundation was presented in Fig. 7.3*c*.

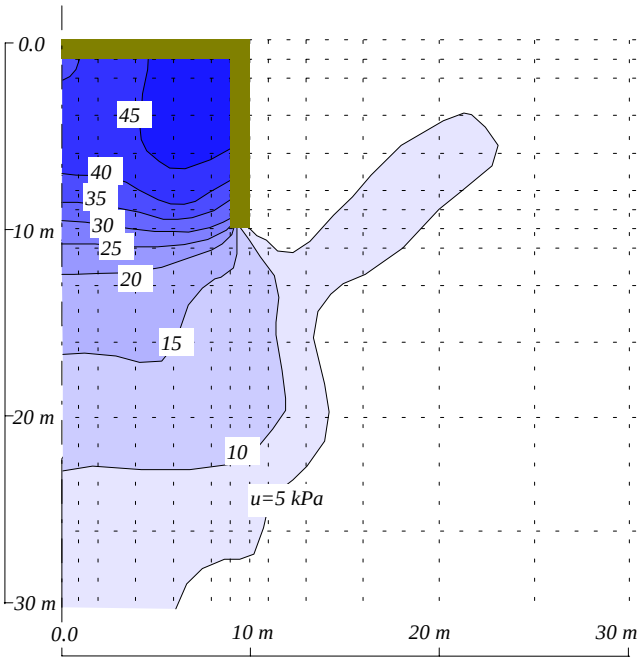

Fig. 7.26: Distribution of pore pressures under the caisson predicted after *100* cycles of vertical load, *V=400 kPa, V_c=100 kPa, Time=1000 sec.*

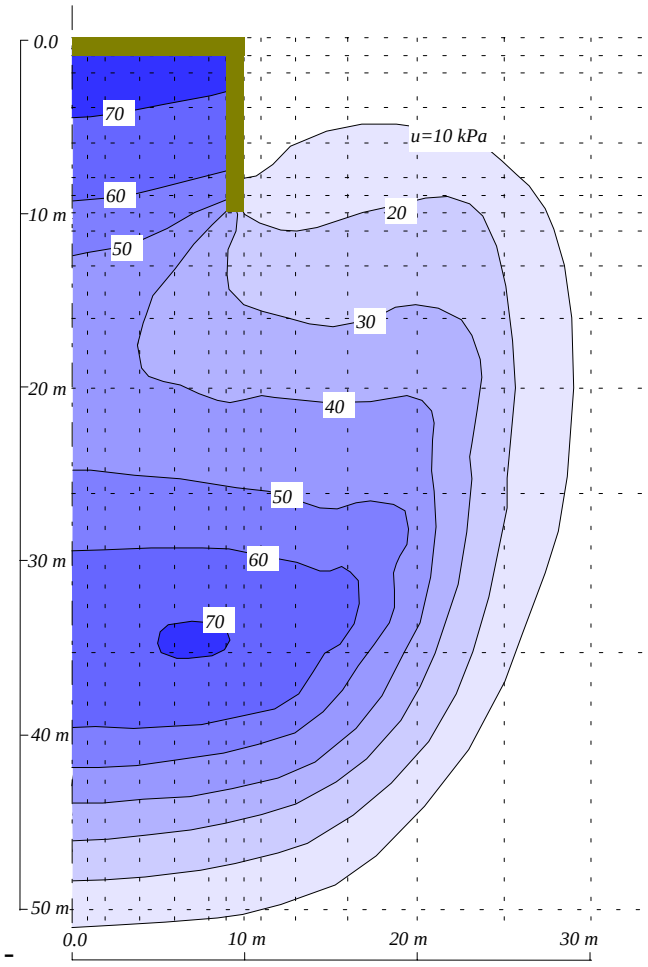

Fig. 7.27: Distribution of pore pressures predicted under the caisson after *600* cycles of vertical load, *V=400 kPa, V_c=100 kPa, Time=6000 sec.*

7.5.1: Response of Piled Foundations Subjected to Cyclic Horizontal Loads

The response of the piled foundation to cyclic horizontal loads was studied. The foundation was subjected to an ambient vertical traction of $V=400\ kPa$. Cyclic horizontal loads with two different amplitudes of $H_c=100\ kPa$ and $H_c=200\ kPa$ were applied to the foundation in the analyses. Variations of settlements and excess pore pressures predicted at the intersection point of the pile and the foundation, point (a) in Fig. 7.3*c*, are presented in Fig. 7.28 for both cyclic loads. The pore pressures rise to their maximum values at about *2000-2500 sec.* After that the pore pressures reduce. The settlements continuously increase. However, after about *600* load cycles the rate of increase in the settlements reduces substantially. The greater cyclic load generates larger pore pressure and settlement of the foundation

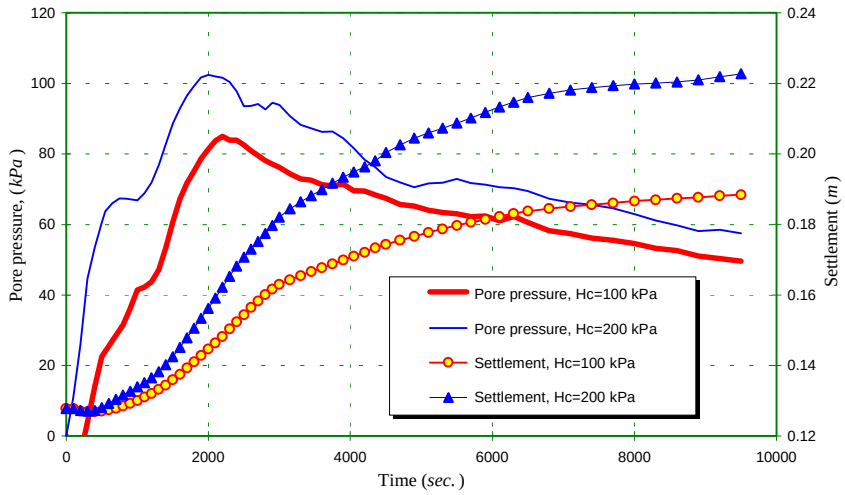

Fig. 7.28: Variations of pore pressures and settlements of the piled foundation under two different cyclic horizontal loads. *V=400 kPa*

The distributions of pore pressures for the piled foundation under the cyclic horizontal load of $H_c=100\ kPa$ are presented in Figs 7.29 and 7.30 for times *1000 sec.* and *2500 sec.*, i.e. after application of *100* and *250* cycles, respectively. A maximum pore pressure of *42 kPa* is predicted at point (a) after *100* load cycles. The maximum pore pressure reaches *83 kPa* after application of *250* load cycles. A zone of high pore pressure is also predicted at a depth of about *25 m*, about *23 m* away from the centre, with a maximum of about *59 kPa*. Figs 7.29 and 7.30 can be compared with Figs 7.5 and 7.6, which show the distributions of pore pressures for the shallow foundation under the same loading. The pore pressure distributions under the piled foundation are similar to those under the shallow foundation.

The variations of the pore pressures and settlements predicted for the piled foundation and the shallow foundation are compared in Fig. 7.31. Both foundations were subjected to an ambient load of $V=400\ kPa$ and a cyclic horizontal load of $H_c=100\ kPa$. The responses of both foundations to the cyclic loading are very close, indicating that the length of the pile is

probably too short to have a significant effect on the cyclic behaviour of the shallow foundation.

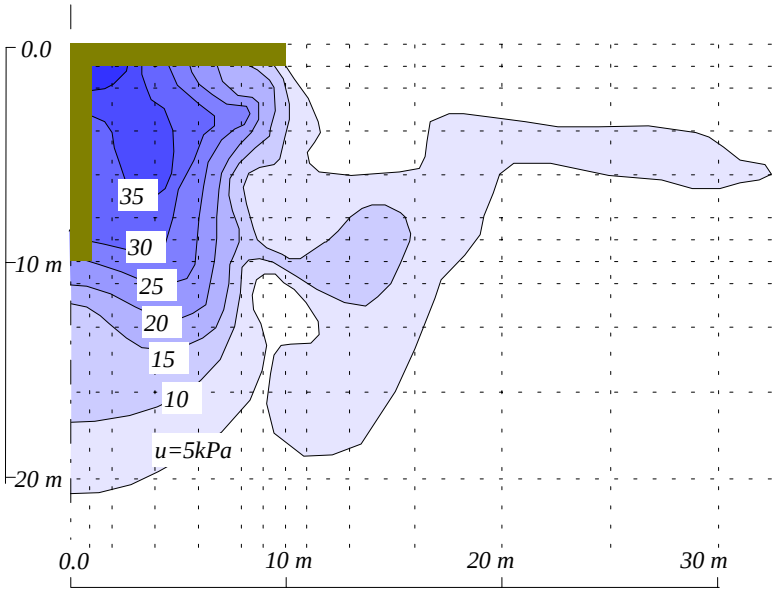

Fig. 7.29: Distribution of pore pressures predicted under the piled foundation after *100* cycles of horizontal load, *V=400 kPa, H_c=100 kPa, Time=1000 sec.*

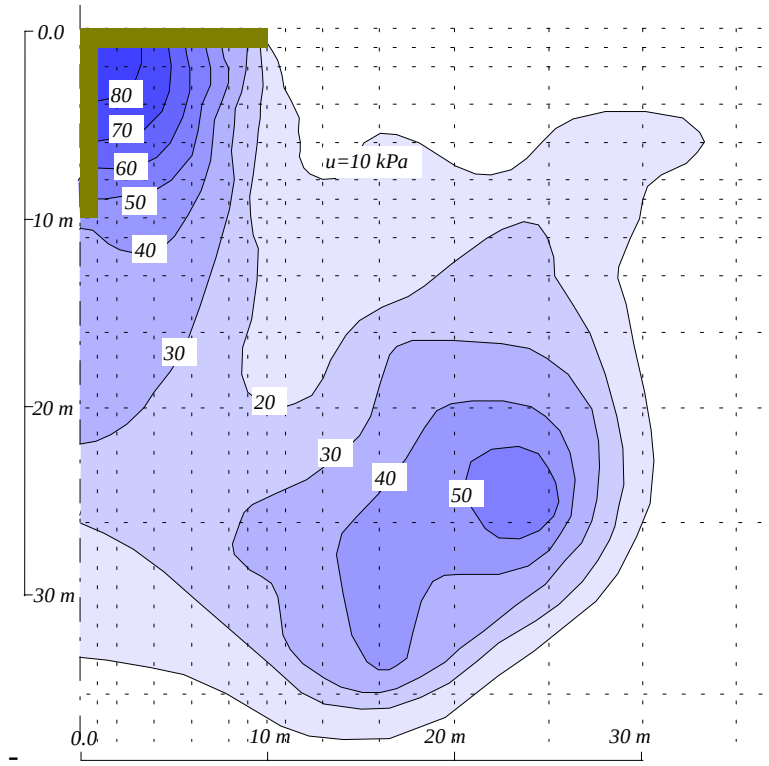

Fig. 7.30: Distribution of pore pressures predicted under the piled foundation after *250* cycles of horizontal load, *V=400 kPa, H_c=100 kPa, Time=2500 sec.*

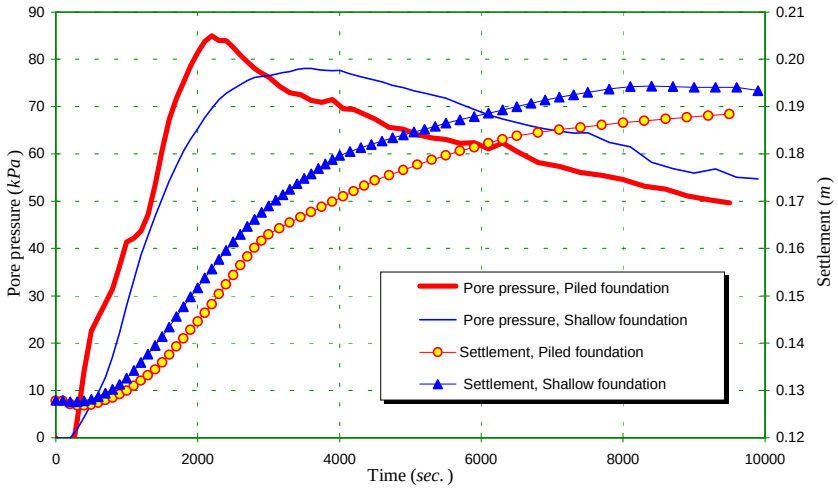

Fig. 7.31: Comparison of the responses of the piled foundation and the shallow foundation to a cyclic horizontal load, *V=400 kPa*, H_c*=100 kPa*

7.5.2: Response of Piled Foundations Subjected to Cyclic Vertical Loads

The response of the piled foundation under a cyclic vertical load was also studied. The cyclic vertical load has an amplitude of V_c*=100 kPa*. The foundation is subjected to an ambient load of *V=400 kPa*. The variation of pore pressure predicted at point (a) during cyclic loading is presented in Fig. 7.32. For comparison, the variation of pore pressure predicted for the shallow foundation under the same loading, and the variation of pore pressure predicted for the piled foundation subjected to a cyclic horizontal load of H_c*=100 kPa* are also presented in Fig. 7.32. The cyclic responses of the foundations are very close to each other. The maximum pore pressure predicted for the piled foundation under the cyclic vertical load is greater than the one predicted under the cyclic horizontal load. The pore pressures under the piled foundation are slightly greater than the pore pressure predicted at the centre of the shallow foundation at the beginning of the analysis, before *3000-4000 sec.* The settlements predicted for the foundations are presented in Fig. 7.33. The settlement of the shallow foundation is very close to the settlement of the piled foundation under the cyclic vertical load, and the settlements of both are greater than the settlement of the piled foundation under the cyclic horizontal load.

7.6: A SIMPLE METHOD FOR EVALUATING THE CYCLIC STRENGTH OF OFFSHORE FOUNDATIONS

A comparative study of foundations under cyclic loading is usually required at an early stage in the design process in order to choose an economically efficient foundation. A simple method is presented here which may be used to compare the cyclic strength of different

offshore foundations. The method is then used to explain the reasons for some of the similarities and dissimilarities observed in the behaviour of the foundations analysed in the preceding sections.

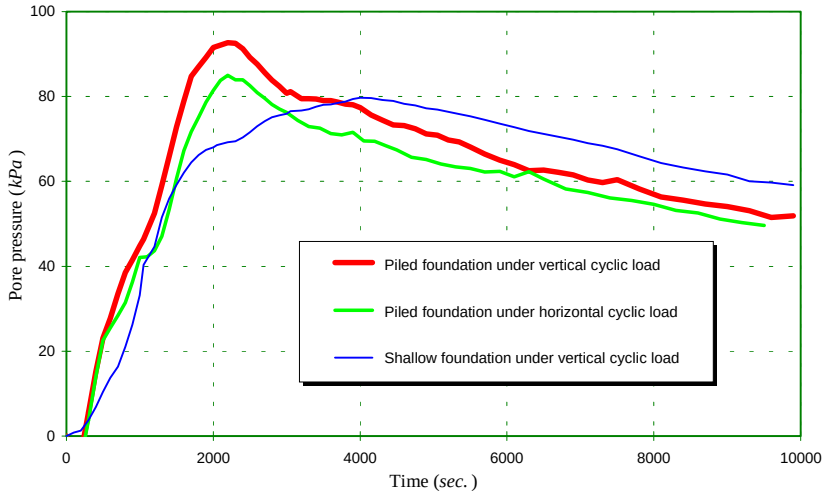

Fig. 7.32: Comparison of the pore pressures generated under the caisson and the shallow foundation, *V=400 kPa*

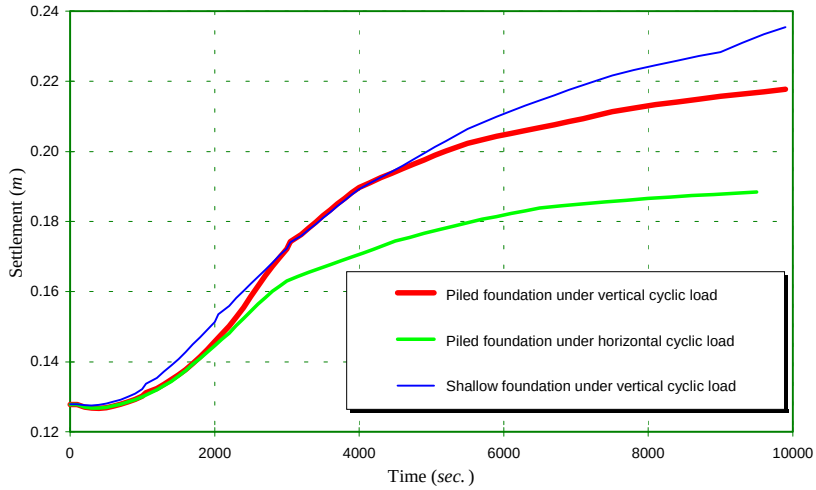

Fig. 7.33: Comparison of the settlements of the caisson and the shallow foundation, *V=400 kPa*

7.6.1: Method of Evaluation

Factors such as ambient loads, cyclic loads, shape and size of the foundations, cyclic properties of the soil, and soil strength parameters affect the cyclic behaviour of foundations. Inclusion of all of the factors in the evaluation process requires a complete cyclic analysis. However, for comparative study of offshore foundations, or for evaluation of the cyclic strength of a foundation, the effects of some of the factors may be ignored. In this way a simpler approach for the evaluation of cyclic behaviour of foundations can be obtained.

If liquefaction is deemed as being likely to occur in a soil under a foundation, then the cyclic stress ratio in the soil, q_c/p'_i (q_c is the cyclic deviatoric stress and p'_i is the mean effective stress under ambient loads), is the primary factor which determines the susceptibility of the soil to liquefaction. The generation of pore pressures in the soil is directly related to the cyclic stress ratio. Therefore, the distribution of the cyclic stress ratio in the soil under the foundation can be used as a qualitative measure for comparative studies of offshore foundations subjected to cyclic loading.

A distribution of the cyclic stress ratio produced under the shallow foundation is presented in Fig. 7.34. The dimension of the foundation was shown in Fig. 7.2. The foundation is subjected to an ambient load of *V=400 kPa* and a cyclic horizontal load of H_c*=100 kPa*, applied in both directions.

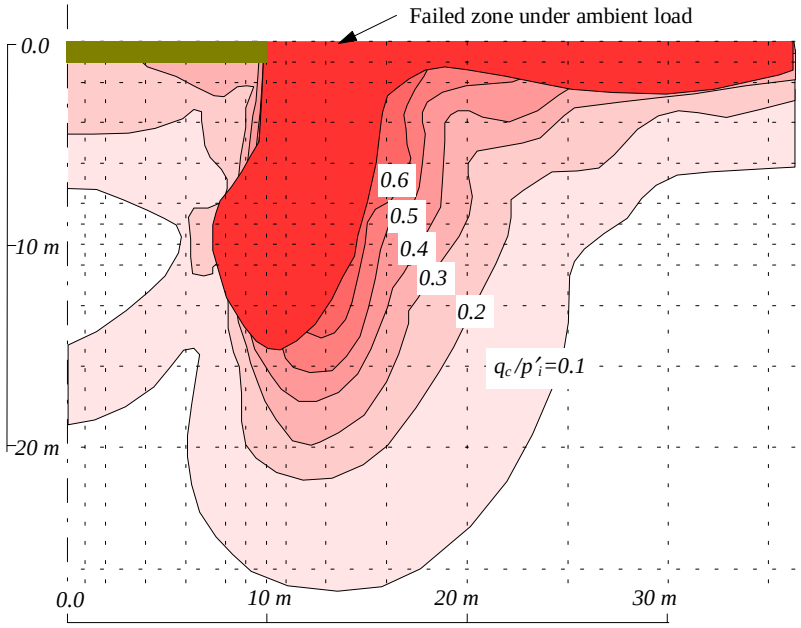

Fig. 7.34: Distribution of cyclic stress ratio under the shallow foundation subjected to a cyclic horizontal load, *V=400 kPa, H_c=100 kPa*

The distribution of the cyclic stress ratio in the soil includes the effects of ambient loads, cyclic loads, shape and size of the foundation. If the cyclic properties of the soil are available, then the extent of the possible liquefaction zone in the soil can also be determined. For example, if the cyclic properties of the Ekofisk sand, Fig. 7.1, are used for the soil, then the contours of the number of cycles required for liquefaction under undrained conditions can be obtained from the distribution of the cyclic stress ratio, as shown in Fig. 7.35. This figure also shows the failure zones under various numbers of cycles of the horizontal load under undrained conditions, if the redistribution of stresses in the soil during undrained cyclic loading is ignored. Based on Fig. 7.35, it may be concluded that soil elements with a high cyclic strength would never fail under partially drained conditions. However, these elements

may fail due to redistribution of stresses, as predicted during an elasto-plastic liquefaction analysis, bringing the state of stress to failure.

The significance of stress redistribution in an elasto-plastic analysis and its effects on the failure of soil should be emphasized. The generation of pore pressures during cyclic loading reduces the effective stresses in the soil, which may directly result in the failure of some elements of the soil. The stresses in the soil are then redistributed to satisfy the equilibrium conditions. Redistribution of stresses in the soil may cause the stress states in some other elements of the soil to reach the failure state. These elements then fail under the indirect effects of pore pressure generation. Redistribution of stresses causes soil elements to fail after application of a number of load cycles, well below the number determined from the distribution of the cyclic stress ratio. As an example, the failure zones predicted in the elasto-plastic cyclic analysis of the shallow foundation, which was presented earlier in Fig. 7.7, may be compared with the failure zones obtained from the distribution of the cyclic stress ratio under the foundation, Fig. 7.35. The results of the finite element analysis show that a large portion of the soil, with an initial cyclic strength greater than *100000* cycles, fails after the application of only *300* cycles of load. The failure zones obtained from the simple distribution of the cyclic stress ratio should therefore be considered only as a guide, which is, nevertheless, very helpful in a qualitative study of offshore foundations.

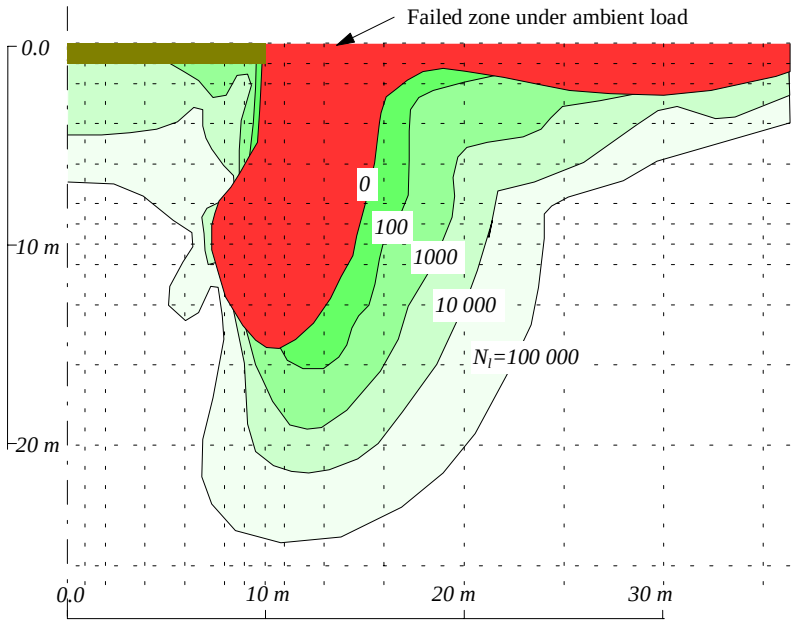

Fig. 7.35: Contours of the number of cycles required for liquefaction under the shallow foundation and undrained conditions assuming no stress redistribution, *V=400 kPa, H_c=100 kPa*

7.6.2: Evaluation of the Cyclic Responses of Offshore Foundations

The results of the cyclic analyses of offshore foundations, performed in the preceding sections, show some similarities and dissimilarities in the responses of the foundations. The simple method, explained in the previous section, is used here to illustrate some of the reasons for the distinct behaviour of the foundations when they are subjected to different cyclic or ambient loadings.

Shallow foundations subjected to cyclic horizontal and vertical loads

The results of the analyses show that cyclic vertical loads have greater effects on the responses of the foundations than cyclic horizontal loads of the same magnitude. This fact may also be concluded from the distributions of the cyclic stress ratio, q_c/p'_i, under the shallow foundation when it is subjected to cyclic vertical and cyclic horizontal loads. The distribution of the cyclic stress ratio for the shallow foundation under a cyclic vertical load of $V_c=100\ kPa$ is presented in Fig. 7.36. This figure can be compared with Fig. 7.34, which shows the distribution of the cyclic stress ratio for the shallow foundation under a cyclic horizontal load of $H_c=100\ kPa$. For both cases, the ambient load acting on the foundation is $V=400\ kPa$. Under the cyclic horizontal load, the zones of the high cyclic stress ratio are mainly concentrated under the edge of the foundation (Fig. 7.34). However, under the cyclic vertical load, the zones with a high cyclic stress ratio are directly under the foundation and extend deeper into the soil, which causes large cyclically induced pore pressures to be generated deep in the soil. The difference in the pore pressure distributions resulting from the analyses can be found from a comparison of Figs 7.6 and 7.12. As a result of this difference, the settlement of the foundation under the cyclic vertical load is greater than the settlement under the cyclic horizontal load of equal amplitude.

A point at the centre of the foundation experiences a similar cyclic stress ratio both under the cyclic vertical load and under the cyclic horizontal load. Therefore, the variations of pore pressures predicted at the point during cyclic loading, Fig. 7.10, are very similar.

Comparison of the cyclic responses of the shallow foundation and the caisson

The distribution of the cyclic stress ratio in the soil for a caisson subjected to a cyclic horizontal load of $H_c=100\ kPa$ and a ambient vertical load of $V=400\ kPa$ is presented in Fig. 7.37. Comparison of this figure with Fig. 7.34 shows that zones with high cyclic stress ratios occupy a slightly larger area under the shallow foundation, in comparison to the caisson. This causes a greater additional settlement for the shallow foundation during cyclic loading.

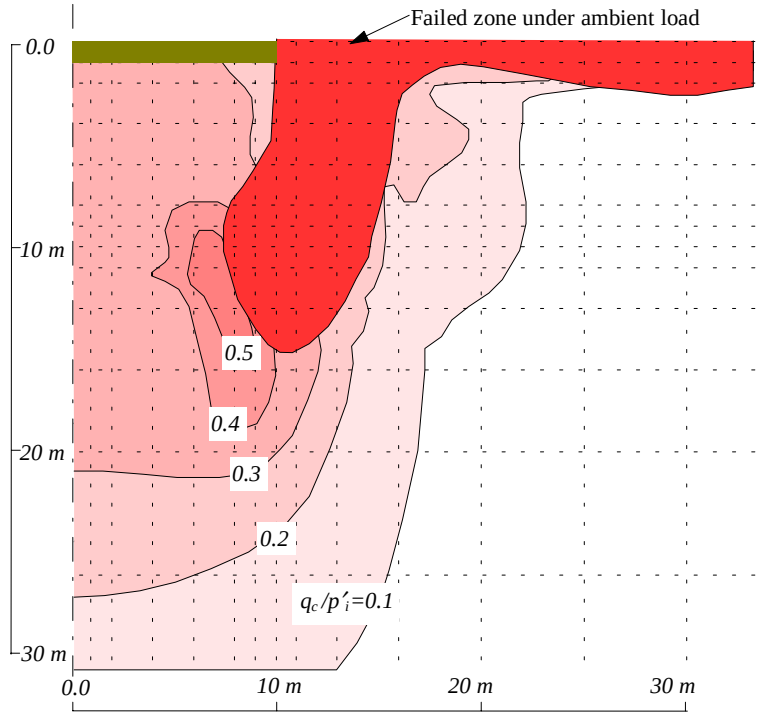

Fig. 7.36: Distribution of cyclic stress ratio under the shallow foundation subjected to a cyclic vertical load, *V=400 kPa, Vc=100 kPa*

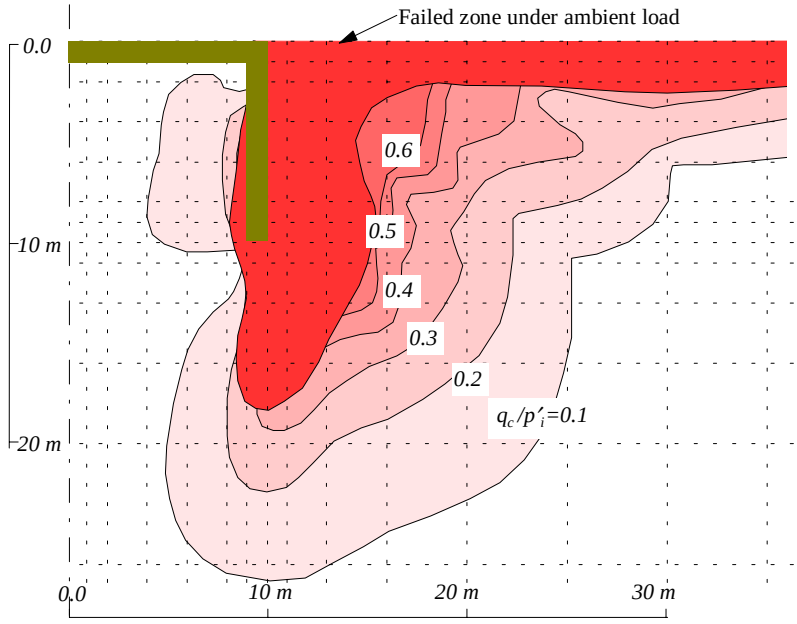

Fig. 7.37: Distribution of cyclic stress ratio under the caisson subjected to a cyclic horizontal load, *V=400 kPa, Hc=100 kPa*

The pore pressure predicted at the centre of the caisson, point (a) in Fig. 7.3*b*, is smaller than the pore pressure predicted at the centre of the shallow foundation. One reason for this fact is that the cyclic stress ratio immediately under the caisson is smaller. However, the maximum achievable pore pressure at the centre of the caisson is also smaller than that at the centre of the shallow foundation, since the initial mean effective stress at the centre of the caisson is

smaller. The length of the drainage path also affects the value of the pore pressure in the soil. The caisson wall blocks drainage of pore water to the free drainage surface in soil elements inside the caisson. Therefore, pore pressures rise inside the caisson close to the caisson wall.

Similarities between the cyclic responses of the shallow foundation and the piled foundation

The distribution of the cyclic stress ratio in the soil under the piled foundation is presented in Fig. 7.38. The foundation is subjected to a cyclic horizontal load of H_c=100 kPa and a ambient vertical load of *V=400 kPa*. The distribution of the cyclic stress ratio under the piled foundation is very similar to the cyclic stress distribution under the shallow foundation, Fig. 7.34, except in a small zone close to the pile. The zone around the pile contains a small volume of soil, and therefore, does not provide a significant contribution to the overall response of the piled foundation. This is the prime reason for the similarity between the cyclic performance of the two foundations.

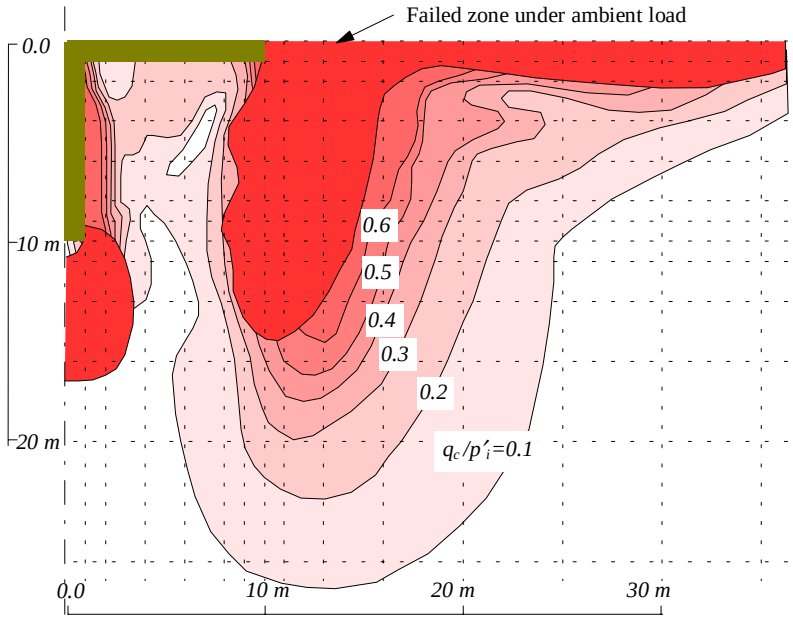

Fig. 7.38: Distribution of cyclic stress ratio under the piled foundation subjected to a cyclic horizontal load, *V=400 kPa, Hc=100 kPa*

7.7: EVALUATION OF THE NUMERICAL LIQUEFACTION ANALYSES

The numerical method presented in this thesis provides a valuable tool for the liquefaction analysis of offshore foundations. However, the capability of the tool is limited to the extent of the validity of the assumptions used in the elasto-plastic liquefaction model. The effects of these assumptions on the liquefaction analyses are explained in this section. There are also

some numerical problems which are probably associated with the elasto-plastic model and the numerical formulation of consolidation. These problems are also explained in this section.

7.7.1: Deficiencies Associated with the Elasto-Plastic Liquefaction Model

There are some theoretical deficiencies associated with the model used for liquefaction analysis. These deficiencies are described and their possible effects on a liquefaction analysis are discussed.

In the elasto-plastic model, the general governing equations presented in Chapter 5 are used. These equations have been obtained based on a series of assumptions. Most of the assumptions are valid for undrained cyclic loading. For example, in deriving the governing equations, only the volumetric strain corresponding to cyclic loading was included, assuming the cyclic strains are isotropic. While this assumption is true for undrained cyclic loading, its validity for general cases of partially drained conditions has not been proven.

In the elasto-plastic model, it was assumed that cyclic loading does not have any further effect on the soil when the state of stress is on the failure surface. This assumption has primarily been made to be able to cast the liquefaction phenomenon into an elastic-perfectly-plastic soil model. Incorporation of the effects of cyclic load after plastic failure of the soil into the model requires data related to the behaviour of the sand after failure. This data cannot be obtained easily from laboratory tests, especially ‘single element’ laboratory tests. Because of this assumption, the model does not predict the generation of any additional excess pore pressure for the points which have failed previously. As a consequence, during a liquefaction analysis of a foundation, as more soil elements fail, the global effects of cyclic load on the foundation gradually reduce with time. This means that the rate of generation of pore pressure due to uniform and indefinite cyclic loading decreases, and eventually becomes equal to the rate of dissipation of pore pressure, which indicates the development of a steady state throughout the soil body. After this point, additional load cycles do not change the stress state in the soil.

The liquefaction model may not provide good predictions for foundations with relatively large ambient loads. A large portion of soil usually fails under a large ambient load, before the application of cyclic loads. The cyclic load therefore affects only a small portion of the soil, which fails quickly and the problem may reach a steady state. This predicted behaviour may be in contrast to the actual behaviour of heavily loaded foundations. These foundations are expected to fail very soon after the application of cyclic loading.

7.7.2: Numerical Difficulties During Liquefaction Analyses

A series of numerical problems has been identified during the liquefaction analyses. Some of the problems are directly related to the formulation of the consolidation analysis. Some other

problems are also identified which may be associated with the non-associated flow rule adopted in the Mohr-Coulomb model, and its inclusion in the finite element solution scheme.

The results of the liquefaction analyses often exhibit oscillation of pore pressure. Large values of negative pore pressures may also be generated at isolated points in the finite element mesh. Both deficiencies are believed to be related to the numerical interpolation of pore pressure over a finite element. Three factors were identified which may contribute to this type of problem: the size of the finite elements in the mesh, the size of the time increment, and the loading. All of these factors change the gradient of pore pressure during cyclic loading. Vermeer and Verruijt (1981) showed that a solution for very small time steps generally requires a fine mesh. However, it has been found empirically that an oscillation during a liquefaction analysis will vanish by the use of a "time disturbance". A time disturbance can be introduced to the solution algorithm by changing the size of a few time steps when oscillation occurs. The size of the time disturbance does not necessarily need to be larger than the time step at which oscillation arises. Change in the size of the mesh often solves the problem. However, it has been found that a mesh which does not show any problem for a cyclic loading of a particular amplitude may exhibit oscillation of pore pressure for cyclic loading of another amplitude.

The solution algorithm often exhibits instability if a liquefaction analysis is continued for a large number of increments after the problem has reached steady state. The term "instability" here refers to a solution with unrealistic deformations. When the rate of generation of pore pressure becomes equal to the rate of dissipation of pore pressure, the stress state in the soil should remain unchanged. Application of additional cyclic loads results in densification of some elements of the soil, and therefore settlement of the foundation. However, the solution algorithm may not be continued for an infinite number of increments of cyclic loading, because instability will often occur, as indicated by unrealistic deformations and pore pressures. Although this problem was not investigated thoroughly, it is most likely linked to the non-associated elasto-plastic Mohr-Coulomb routine which was adopted in the analyses. It was noticed that for the problems used in this chapter instability typically occurs when the solution algorithm iterates for more than *20* times after the equilibrium was first attained. The instability is usually in the form of very large, unrealistic deformations. If the dilation angle of the soil is increased above zero, a more realistic answer can be achieved but of course the soil no longer deforms plastically at constant volume, as ultimately required.

7.8: CONCLUSIONS

The numerical tool for liquefaction analyses, presented in the preceding chapters was utilized to investigate the cyclic responses of three types of offshore foundations, shallow foundations,

caissons, and piled raft foundations. Various cyclic loads and ambient loads were applied to the foundations and the performances of the foundations were compared. A simple method for a comparative study of offshore foundations was also introduced. Finally, some problems and difficulties related to the liquefaction analyses were discussed.

The results of the analyses show that, for any foundation, an increase in the intensity of cyclic loads or ambient loads applied to the foundation usually generates a greater pore pressure in the soil and a larger displacement for the foundation. The resistance of the caisson foundations to cyclic loads is generally greater than the other types of foundations considered. The settlement due to cyclic loads is smaller for the caisson. Perhaps surprisingly, the model predicts that the cyclic performance of the shallow foundation does not improve significantly if a relatively short pile is attached to the centre of the foundation. The option of a longer pile was not investigated.

The results of the analyses also show that, in general, cyclic vertical loads have greater effects on the cyclic performances of the foundations than cyclic horizontal loads. Application of cyclic vertical loads generally results in larger displacements for the foundations, in comparison to cyclic horizontal loads of the same amplitude.

A simple method for qualitative evaluation of the cyclic performance of offshore foundations was introduced. The distribution of the cyclic stress ratio in the soil under a foundation is used as a measure which qualitatively determines the cyclic strength of the foundation. The method was applied to the different types of foundations, which were also analysed by the finite element liquefaction procedure, to explain the distinct cyclic performance of each foundation.

Some of the deficiencies related to the elasto-plastic liquefaction model were identified. For example, only the volumetric strain produced during cyclic loading is included in the model. The model may not provide a good prediction for the cyclic performance of the foundations subjected to large ambient loads. These deficiencies arise mainly because of the assumptions required to simplify the liquefaction phenomenon in the context of an elastic-perfectly-plastic soil model. A three-dimensional liquefaction analysis may not be possible without such simplifications.

A series of problems often arises during liquefaction analyses. Some of the problems are related to the finite element formulation of consolidation. Although they were not investigated in great detail, it is believed that these problems are related to the numerical interpolation scheme used in the analyses. There are also some other problems which are probably related to the adoption of highly non-associated plastic flow rule in the Mohr-Coulomb model adopted in the analyses. However, it was found that a careful application of the method to a liquefaction analysis provides a satisfactory result in most cases.

Chapter 8

SUMMARY, CONCLUSIONS, AND RECOMMENDATIONS FOR FURTHER STUDIES

8.1: SUMMARY

Three-dimensional numerical analyses of liquefaction problems of offshore foundations founded on granular soils have been presented in this thesis. Great emphasis has been laid on the practicability of the techniques used in the analyses. Some of the outcomes of the studies are briefly presented below.

The literature related to the liquefaction problem of offshore foundations has been reviewed in Chapter 2. The cyclic nature of environmental loads on offshore foundations, and the effects of cyclic loading on granular soils have been presented. It was shown that the generation of pore pressure in the soil under the foundations during storms is a great concern that should be taken into account in the design procedure. A chronological review of the development of the numerical techniques used in the prediction of pore pressure under offshore foundations has been presented. It has been shown that, in almost all of the liquefaction studies, the three-dimensional stress distribution under the foundations was simplified to a two-dimensional distribution, by application of either an axi-symmetric or a plane strain finite element method. Some of the difficulty associated with the application of a three-dimensional finite element method was perhaps the enormous time required for such an analysis. Furthermore, generalization of the data obtained from experimental tests on “single element” samples of soil in the laboratory to a three-dimensional stress space is also another major difficulty. A review of the mathematical models proposed for liquefiable soil has also been presented. However, no evidence has been found on the practicability of any advanced model in a three-dimensional liquefaction analysis. It was concluded that a three-dimensional liquefaction analysis requires an efficient analytical tool based on the finite element method. Also, given the lack of a complete liquefaction model for soil, attempts should be made to develop a simple mathematical model for soil that permits inclusion of the experimental data in the analysis.

An efficient three-dimensional elasto-plastic finite element for consolidation analysis has been developed in Chapter 3. By representing the field quantities of an axi-symmetric body as a discrete Fourier series, a three-dimensional problem is reduced to a number of smaller problems. Overall the solution to all the smaller problems requires less computational effort and time than the time required for a standard three-dimensional finite element analysis. The discrete Fourier series has an advantage over a continuous Fourier representation, since it gives an exact representation after a finite number of terms. Development of this method largely removes some of the restrictions on the application of three-dimensional finite element analysis to the study of the complicated problem of liquefaction and other topics in soil mechanics.

The bearing capacity of shallow foundations has been studied in detail in Chapter 4. A simple case of homogeneous cohesive soil was adopted for the studies. The numerical scheme presented in Chapter 3 has been extensively used in this chapter to find the failure locus of the foundations under all imaginable combinations of vertical load, horizontal load and moment. Based on the results of the numerical analyses, a unique three-dimensional failure surface has been obtained for the foundations. A new bearing capacity equation has also been proposed which may be used to calculate the bearing capacity of the foundations under three-dimensional loading. The accuracy of the results in special cases with known solutions provides confidence in the use of the newly developed numerical scheme to solve problems with as yet unknown solutions.

Liquefaction analysis of offshore foundations is described in Chapter 5, with the development of generalized equations of liquefaction. A procedure for liquefaction analysis of offshore foundations subjected to storm loading has also been introduced. The equations have then been modified for an elastic soil model and used in a series of liquefaction analyses of an offshore foundation. The foundation of the Ekofisk tank, which has been constructed on the North Sea, was adopted for the analyses. The effects of various factors, such as the flexibility of the foundation, different liquefaction criteria, soil liquefaction data, and storm histograms, on the elastic performance of the foundation have been studied. The results have been compared with the observed performance of the tank during some major storms. It was shown that the modified elastic model is very good in predicting the pore pressures generated during cyclic loading in the soil under the foundation, but it has deficiencies in predicting the settlement of the foundation. Investigation of stress paths during cyclic loading has also revealed some other deficiencies associated with the modified elastic soil model, and the need for an elasto-plastic soil model suitable for liquefaction analysis.

A relatively simple elasto plastic model for liquefiable soil has been proposed in Chapter 6. This model is based on the elastic-perfectly-plastic Mohr-Coulomb model which is modified

to be used in liquefaction analyses. In this model, the effects of cyclic loading are considered by including some plastic deformations in the Mohr-Coulomb model when the state of stress is inside the yield locus. The plastic deformations can be obtained from the results of experimental studies on samples of soil under cyclic loading. Application of the method to the analysis of the foundation of the Ekofisk tank has shown great improvements in the stress paths and the prediction of the settlement of the tank during storm loading.

The cyclic resistance of three different offshore foundations has been studied in Chapter 7 and the cyclic responses of the foundations have been compared. A simplified method has also been introduced in this chapter that may be used for comparative studies of offshore foundations. The performance of the elasto-plastic model proposed for liquefaction analyses has been explored in this chapter. Some of the deficiencies associated with the model have been identified. Despite the promising performance of the model in analyses of foundations subjected to moderate loading, the model is possibly deficient in analyses of foundations subjected to large cyclic or ambient loads.

8.2: CONCLUSIONS

The material presented in this thesis was mainly related to the behaviour of offshore foundations subjected to cyclic loading. However, the subjects of Chapters 3 and 4 are related to wider topics in soil mechanics.

The efficient finite element method for consolidation analysis provides a convenient tool to explore the behaviour of foundations subjected to three-dimensional loading. Application of the method to the bearing capacity of shallow foundations on cohesive soil, presented in Chapter 4, shows the efficiency, the accuracy, and the power of the tool in dealing with one of the fundamental problems in soil mechanics.

The method presented in Chapter 5 provides a solid basis for liquefaction analyses of offshore foundations. Application of the method to the liquefaction analysis of an offshore foundation resting on a soil that behaves elastically under static loading showed some promising results. However, it also revealed some of the problems related to the elastic soil model and the need for an advanced elasto-plastic model for liquefiable soil.

The elasto-plastic model proposed in Chapter 6 presents a significant improvement in liquefaction analyses of offshore foundations. The relatively simple formulation of the model is clearly an advantage, which has made application of the model to the analysis of offshore foundations possible. Application of the model to the analysis of the foundation of the Ekofisk

tank showed realistic predictions. The elasto-plastic model may well predict the behaviour of offshore foundations subjected to moderate loading. However, the performance of the model for heavily loaded foundations may not be satisfactory.

8.3: RECOMMENDATIONS FOR FURTHER STUDIES

The method presented in this thesis for liquefaction analysis is a suitable tool for investigation of the behaviour of many offshore foundations subjected to cyclic loading. The cyclic responses of some of the foundations have already been investigated in the thesis. However, there are other types of offshore foundations, in particular pile foundations, whose cyclic responses are also of interest. The method can also be used to evaluate the effectiveness of vertical dowels often used with some types of offshore foundations to improve the performance of the foundations.

The performance of the liquefaction analysis may be improved if some other features of cyclic behaviour of sand are included in the analysis. For example, sand exhibits strain softening during cyclic loading. The softening behaviour of sand can be easily included in the liquefaction analysis of offshore foundations, if a suitable softening function is adopted. A softening function may be in the form of a relationship between the shear modulus of a sand and the pore pressure generated in the sand. Inclusion of the softening function into the elasto-plastic model may improve the results of the liquefaction analyses.

The effects of soil densification on the cyclic strength and permeability of sand have been ignored in the studies presented in this thesis. These effects can easily be included in the process of liquefaction analysis, if the required data on the cyclic strength of the sand and the relationship between the permeability and the relative density of the sand are provided. There is a need for further experimental data defining such behaviour.

The accuracy of the liquefaction predictions may be improved if one of the assumptions made in deriving the governing equations is altered for general cases of drained and undrained conditions of sand. In deriving the governing equations it was assumed that the pore pressure generated by cyclic loading under undrained conditions would result in isotropic strains under drained conditions. While this assumption may be true for undrained conditions, results of experimental tests on drained sands indicate that both volumetric and deviatoric strains develop during cyclic loading. The deviatoric shear strain should also be included in governing equations. This is clearly not an easy task for the case of three-dimensional stress and strain. Therefore, it is suggested that any improvement in this regard is first evaluated for a simpler case of an axi-symmetric problem, and then extended for fully three-dimensional

analyses. This improvement may also require further experimental work to provide the essential data for any improved soil model.

In the proposed elasto-plastic model, it was assumed that cyclic loading does not have any effect on the behaviour of soil if the stress state reaches the failure locus. This assumption cannot be altered in the context of an elastic-perfectly-plastic soil model. However, the liquefaction phenomenon may be described in the context of strain hardening soil models, such as the critical state model. In that case, a new model will be obtained that may be suitable for more heavily loaded foundations.

The three-dimensional finite element method presented in this thesis is a convenient tool for exploring the behaviour of foundations under three-dimensional loading. The method has already been used to find a failure surface for shallow foundations resting on homogeneous cohesive soil. The behaviour of other types of foundations on various soil profiles may also be of interest. The method can be used for the bearing capacity of a shallow circular footing resting on frictional soil as well as on non-homogeneous soil profiles. It may also be applied to explore the behaviour of pile foundations and caissons under three-dimensional loading conditions.

Formulation of two-dimensional joint elements, suitable to be used in conjunction with three-dimensional solid elements, is another interesting area for future work which would certainly enhance the finite element modelling of the interface between soil and foundations.

REFERENCES

Anandarajah, A. (1994) 'Procedure for elasto-plastic liquefaction modeling of sands', *J ournal of Engineering Mechanics*, 120, 7,1563-1587.

Andersen, K. H. (1991) 'Foundation design of offshore gravity structures', *Cyclic Loading of Soil: From Theory to Design*, Eds O'Reilly & Brown, Blackie, 122-173.

Aubry, D., Kodaissi, E. and Meimon, Y. (1985) 'A viscoplastic constitutive equation for clays including a damage law', *Proc. 5th Int. Conf. on Numerical Methods in Geomechanics*, Nagoya, 421-428.

Baguelin F., Frank R. and Saïd, Y. H. (1977) 'Theoretical study of lateral reaction mechanism of piles', *Geotechnique*, 27, 3, 405-434.

Bhatia, S. K. and Nanthikesan, S. (1987) 'The development of constitutive relationship for seismic pore pressure', *Soil Dynamics and Liquefaction*, Ed. Cakmak, Elsevier, Oxford, 19-30.

Biot, M. A. (1941) 'General theory of three dimensional consolidation', *J ournal of Applied Physics*, 12, 155-164.

Bjerrum, L. (1973) 'Geotechnical problems involved in foundations of structures in the North Sea', *Geotechnique*, 23, 3, 319-358.

Bolton, M. (1979) *A Guide to Soil Mechanics*, MacMillan Publishers, London.

Booker, J. R. (1996) Private communication.

Booker, J. R. and Small, J. C. (1975), 'An investigation of the stability of numerical solutions of Biot's equations of consolidation', *Int. J ournal of Solids Structures*, 11, 907-917.

Booker, J. R., Rahman, M. S. and Seed, H. B. (1976) *GADFLEA- A Computer Program for the Analysis of Pore Pressure Generation and Dissipation During Cyclic or Earthquake Loading*, Report No. EERC 76-24, Earthquake Engineering Research Centre, The University of California, Berkeley.

Booker, J. R. and Small, J. C. (1979), 'Finite element analysis of the consolidation of layered soils', *Proc. 3rd Int. Conf. in Australia on Finite Element Methods*, Sydney, 485-500

Bouckovalas, G. (1991) 'Ekofisk tank: Performance prediction during the storm of Nov. 6, 1973', *Deformation of Soils and Displacement of Structures, Proceeding of 10th European Conference on Soil Mechanics and Foundation Engineering*, 1311-1314.

Bowles, J. E. (1982) *Foundation Analysis and Design*, 3rd Edition, McGraw-Hill, New York.

Bransby, M. F. and Randolph, M. F. (1997a) *Combined Loading of Skirted Foundations*, Research Report No. G1269, The University of Western Australia.

Bransby, M. F. and Randolph, M. F. (1997b) 'Finite element modelling of skirted strip footings subjected to combined loadings', *Proc. 7th Int. Offshore and Polar Engineering Conference*, Honolulu, 791-795.

Britto, A. M. and Gunn, M. J. (1987) *Critical State Soil Mechanics Via Finite Elements*, Ellis Horwood, New York.

Broms B. B. (1964) 'Lateral resistance of piles in cohesive soils', *J ournal of the Soil Mechanics and Foundations Division, ASCE*, 90, SM2, 27-63.

Butterfield, R. and Gottardi, G. (1994) 'A complete three-dimensional failure envelope for shallow footing on sand', *Geotechnique*, 44, 1, 181-184.

Carter, J. P., Booker, J. R. and Wroth, C. P. (1982) 'A critical state soil model for cyclic loading', *Soil Mechanics, Transient and Cyclic Loads*, Eds. Pande & Zienkiewicz, John Wiley & Sons, 219-252.

Carter, J. P. and Booker, J. R. (1983), 'Consolidation of axi-symmetric bodies subjected to non-axi-symmetric loading', *Int. J ournal for Numerical and Analytical Methods in Geomechanics*, 7, 273-281.

Carter, J. P. and Balaam, N. P. (1995) *AFENA Users' Manual*, Centre for Geotechnical Research, The University of Sydney.

Casagrande, A. (1936) 'Characteristics of cohesionless soil affecting the stability of earth fills', *J ournal of the Boston Society of Civil Engineers*; Reprinted in *Contributions to Soil Mechanics, 1925-1960*', Boston Society of Civil Engineers.

Chen, L. and Poulos, H. G. (1993), 'Analysis of pile-soil interaction under lateral loading using infinite and finite elements', *Computers and Geomechanics*, 15, 189-220.

Chen, W. F. and McCarron, W. O. (1991) 'Bearing capacity of shallow foundations', *Foundation Engineering Handbook*, Ed. Fang, 2nd Edition, Van Nostrand Reinhold, New York, 144-165.

Christian, J. T. and Boehmer, J. W. (1970), 'Plane strain consolidation by finite elements', *J ournal of the Soil Mechanics and Foundations Division, ASCE*, 96, SM4, 1435-1457.

Chu, J. (1993) 'Liquefaction of dilating granular soils', *Soil Dynamics and Earthquake Engineering, VI*, Eds Cakmak & Brebbia, Elsevier, London, 333-347.

Chugh, A. K. and Thun, L. V. (1985) 'Pore pressure response analysis for earthquakes', *Canadian Geotechnical J ournal*, 22, 466-476.

Clausen, C. J. F., Dibiagio, E., Duncan, J. M. and Andersen, K. H. (1975) 'Observed behaviour of the Ekofisk oil storage tank foundation', *Proc. 7th Offshore Technology Conference*, Houston, 3, 399-413.

Cook, R. D. (1974), 'Improved two-dimensional finite element', *J ournal of the Structural Division, ASCE*, 100, ST9, 1851-1862.

Cook, R. D. (1975), 'Avoidance of parasitic shear in plane element', *J ournal of the Structural Division, ASCE*, 101, ST6, 1239-1253.

Cook, R. D., Malkus, D. S. and Plesha, M. E., (1989), *Concepts and Applications of Finite Element Analysis*, 3rd Edition, John Wiley & Sons, New York.

Cox, A. D. (1961) 'Axially-symmetric plastic deformation in soil - II. Indentation of ponderable soils', *Int. J ournal Mech. Sci*, 4, 371-380

Dafalias, Y. F. and Herrmann, L. R. (1982) 'Bounding surface formulation of soil plasticity', *Soil Mechanics, Transient and Cyclic Loads*, Eds. Pande & Zienkiewicz, John Wiley & Sons, 253-282

Desai, C. S., Park, I. and Shao, C. (1998) 'Fundamental yet simplified model for liquefaction instability', *Int. J ournal of Numerical and Analytical Methods in Geomechanics*, 22, 721-748.

Dobry, R., Ng, T., Ladd, R. S. and Reese, L. C. (1988) 'Modelling of pore pressures and shear moduli in calcareous soils by strain-controlled cyclic triaxial testing', *Engineering for Calcareous Sediments*, Eds. Jewell & Khorshid, 531-539.

Evans, M. D. (1993) 'Liquefaction and dynamic properties of gravelly soils', *Soil Dynamics and Earthquake Engineering, VI*, Eds Cakmak & Brebbia, Elsevier, London, 317-331.

Evans, M. D. and Harder, L. F. (1993) 'Liquefaction potential of gravelly soils in dams', *Geotechnical Practice in Dam Rehabilitation*, ASCE Specialty Conference, Raleigh.

Ewing, J. A. (1970) 'The generation and propagation of sea waves', *Proc. Conf. Dynamic Waves in Civil Engineering*, Eds Howells *et al.*,Wiley Interscience, London, 43-55.

Figueroa, J. L. (1993) 'Unit energy level associated with pore pressure development during liquefaction', *Soil Dynamic and Earthquake Engineering VI*, Eds Cakmak & Brebbia, Elsevier, London, 413-427.

Finn, W. D. L., Bransby, P. L. and Pickering, D. J. (1970) 'Effect of strain history on liquefaction of sand', *J ournal of the Soil Mechanics and Foundations Division, ASCE*, 96, SM6, 1917-1934

Finn, W. D. L., Pickering, D. J. and Bransby, P. L. (1971) 'Sand liquefaction in triaxial and simple shear tests', *J ournal of the Soil Mechanics and Foundations Division, ASCE*, 97, SM4, 639-659.

Finn W. D. L., Lee, K. W. and Martin, G. R. (1977) 'An effective stress model for liquefaction', *J ournal of the Geotechnical Engineering Division, ASCE*, 103, GT6, 517-533.

Herrmann, L. R. (1973), 'Efficiency evaluation of a two-dimensional incompatible finite element', *Computers and Structures*, 3, 6, 1377-1395.

Hsi, J. P. and Small, J. C. (1992), 'Simulation of excavation in a pro-elastic material', *Int. J ournal for Numerical and Analytical Methods in Geomechanics*, 16, 25-43.

Ishibashi, I., Kawamura, M. and Bhatia, S. K. (1985) 'Effect of initial shear on cyclic behaviour of sand', *J ournal of Geotechnical Engineering, ASCE*, 111, 12, 1395-1410.

Ishihara, K. (1993) 'Liquefaction and flow failure during earthquakes', 33rd Rankine lecture, *Geotechnique*, 43, 3, 351-415.

Ishihara, K. (1996) *Soil Behaviour in Earthquake Geotechnics*, Clarendon Press, Oxford.

Ishihara, K. and Li, S. I. (1972) 'Liquefaction of saturated sand in triaxial torsion shear test', *Soils and Foundations*, 12, 2, 19-39.

Ishihara, K. and Yamada, Y. (1981) 'Liquefaction tests using a true triaxial apparatus', *Proc. 10th Int. Conference on Soil Mechanics and Foundation Engineering*, Stockholm, 3, 235-238.

Jessberger, H. L. and Jordan, P. (1981) 'Soil reaction under offshore structure' *Proc. 10th Int. Conference on Soil Mechanics and Foundation Engineering*, Stockholm, 3, 243-248.

Kaggwa, W. S. (1988) *Cyclic Behaviour of Carbonate Sediments*, Ph.D. Thesis, The University of Sydney, Australia.

Kooijman, A. P. and Vermeer, P. A. (1988) 'Elasto-plastic analysis of laterally loaded piles', *Proc. 6th Int. Conference on Numerical Methods in Geomechanics*, Innsbruck, 1033-1042.

Lai, J. Y. (1989) *Stability and Deformation Analysis of Caisson and Block Foundations*, Ph.D. Thesis, The University of Sydney, Australia.

Lai, J. Y. and Booker, J. R., (1991) 'Application of Discrete Fourier series to the finite element stress analysis of axi-symmetric solids', *Int. J ournal of Numerical Methods in Engineering*, 31, 619-647.

Lane, P. A. and Griffiths, D. V. (1988), 'Computation of the ultimate pressure of laterally loaded circular pile in frictional soil', *Proc. 6th Int. Conference on Numerical Methods in Geomechanics*, Innsbruck, 1025-1031.

Lee, C. Y. and Poulos, H. G. (1988) 'Influence of excess pore pressures on axial offshore pile response', *Behaviour of Foundations in Calcareous Sediments*, Bulletin GB6, The University of Sydney, 73-93.

Lee, C. Y. and Poulos, H. G. (1990) 'Behaviour of offshore piles subjected to storm loading', *Behaviour of Foundations in Calcareous Sediments*, Bulletin GB6, The University of Sydney, 1-32.

Lee, K. L. and Seed, H. B. (1967*)* 'Dynamic strength of anisotropically consolidated sand', *J ournal of the Soil mechanics and Foundations Division, ASCE*, 93, 169-190.

Lee, K. L. and Focht, J. A. (1975), 'Liquefaction potential at Ekofisk tank in North Sea', *J ournal of the Geotechnical Engineering Division, ASCE*, 101, GT1, 1-18.

Liu, L. and Dobry, R. (1997) 'Seismic response of shallow foundation on liquefiable sand', *J ournal of Geotechnical and Geoenvironmental Engineering, ASCE*, 123, 557-567.

MacCamy, R. C. and Fochs, R. A. (1954) 'Wave Forces on piles: A diffraction theory', *Technical Memo No. 69, US Army Corps of Engineering, Beach Erosion Board*.

Marr, W. A. and Christian, J. T. (1981) 'Permanent displacements due to cyclic wave loading', *J ournal of the Geotechnical Engineering Division, ASCE*, 107, GT8, 1129-1149.

Martin, C. M. (1994) *Physical and Numerical Modelling of Offshore Foundations Under Combined Loads*, Ph.D. Thesis, The University of Oxford.

Matasovic, N. and Vucetic, M. (1993) 'Cyclic characterization of liquefiable sands', *J ournal of the Geotechnical Engineering, ASCE*, 119, 1805-1822.

Meissner, H. E. (1976), 'Laterally loaded pile in cohesionless soil', *Proc. 2nd Conference in Numerical Methods in Geomechanics*, Virginia, Ed. Desai, C. S., 1353-1365.

Meyerhof, G. G. (1980) 'Limit equilibrium plasticity in soil mechanics', *Proc. Symposium on Application of Plasticity and Generalized Stress-Strain in Geotechnical Engineering. ASCE*, 7-24.

Mulilis, J. P., Seed, H. B., Chan, C. K., Mitchell, J. K. and Arulanandan, K. (1977) 'Effects of sample preparation on sand liquefaction', *J ournal of the Geotechnical Engineering Division, ASCE*, 103, GT2, 91-108.

Murff, J. D. (1994) 'Limit analysis of multi-footing foundation systems', *Proc. Computer Methods and Advanced Geomechanics*, Morgantown, Eds Siriwardane & Zaman, 233-244.

Nishizaki, S., Saito, I. and Ohira, A. (1982), 'Some finite elements for consolidation analysis', *Proc. 4th Int. Conf. Numerical Methods in Geomechanics*, Edmonton, 69-78.

O'Reilly, M. P. and Brown, S. F. (1991) 'Cyclic loading in geotechnical engineering', *Cyclic Loading of Soil: From Theory to Design*, Eds O'Reilly & Brown, Blackie, London, 1-18.

Osborne, J. J., Trickey, J. C., Houlsby, G. T. and James, R. G. (1991) 'Findings from a joint industry study on foundation fixity of jackup units', *Proc. 7th Offshore Technology Conference*, Houston, 3, 517-533.

Pillai, V. S. (1985) 'Effects of initial shear on cyclic behaviour of sand', *J ournal of Geotechnical Engineering, ASCE*, 111, 1090-1094.

Poulos, H. G. (1988) 'Soil behaviour under cyclic loading', *Marine Geotechnics*, Chapter 3, Unwin Hyman, London.

Poulos H. G. and Davis E. H. (1980) *Pile Foundation Analysis and Design*, John Wiley & Sons, New York.

Prager, W. and Hodge, P. G. (1951) *Theory of Perfectly Plastic Solids*, John Wiley & Sons, New York.

Prandtl, L. (1921) 'Uber die eindringungsfestigkeit plastisher baustoffe und die festigkeit von schneiden', *Z eitschrift fur Angewandte Mathematik und Mechanik*, 1, 1, 15-20.

Rahman, M. S., Seed, H. B. and Booker, J. R. (1977), 'Pore pressure development under offshore gravity structures', *J ournal of the Geotecnical Engineering Division, ASCE*, 103, GT12, 1419-1436.

Randolph, M. F. and Houlsby, G. T. (1984) 'The limiting pressure on a circular pile loaded laterally in cohesive soil', *Geotechnique*, 34, 4, 613-623.

Reed, M. B. (1984), 'An investigation of numerical errors in the analysis of consolidation by finite elements', *Int. J ournal for Numerical and Analytical Methods in Geomechanics*, 8, 243-257.

Reese. L. C., Wright, S. G., Roesset, J. M., Hayes, L. H., Dobry, R. and Vallabhan, C. V. G. (1988) 'Analysis of piles subjected to lateral loading by storm-generated waves', *Engineering for Calcareous Sediments*, Eds Jewell & Khorshid, 647-654.

Reissner, H. (1924) 'Zum erddruckproblem', *Proc. 1st Int. Conference on Applied Mechanics*, Delft, 295-311.

Roscoe, K. H. and Burland, J. B. (1968) 'On the generalised stress-strain behaviour of wet clay', *Engineering Plasticity*, Eds Heyman & Leckie, Cambridge University Press, 535-609.

Rose, G. A., Seed, H. B. and Migliaccio, R. R. (1969) 'Bridge foundations in Alaska earthquake', *J ournal of the Soil Mechanics and Foundations Division, ASCE*, 95, 1007-1036.

Runesson, K. & Booker, J. R. (1982), 'Efficient finite element analysis of 3-D consolidation', *Proc. 4th Int. Conference in Numerical Methods in Geomechanics*, Edmonton, 359-364.

Runesson, K. & Booker, J. R. (1983), 'Finite element analysis of elastic-plastic layered soil using discrete Fourier series expansion', *Int. J ournal for Numerical Methods in Engineering*, 19, 473-478.

Sandhu, R. S. and Wilson, E. L. (1969), 'Finite element analysis of seepage in elastic media', *J ournal of the Engineering Mechanics Division, ASCE*, 95, EM3, 641-652.

Sandhu, R. S., Liu, H. and Singh, K. J. (1977), 'Numerical performance of some finite element schemes for analysis of seepage in porous elastic media', *Int. J ournal for Numerical and Analytical Methods in Geomechanics*, 1, 177-194.

Saran, S. and Agrawal, R. K. (1991) 'Bearing capacity of eccentrically obliquely loaded footing', *J ournal of Geotechnical Engineering, ASCE*, 117, 1669-1690.

Seed, H. B. (1968) 'The fourth Terzaghi lecture: Landslides during earthquakes due to liquefaction', *J ournal of the Soil Mechanics and Foundations Division, ASCE*, 94, SM5, 1053-1122.

Seed, H. B. (1976) 'Evaluation of soil liquefaction effects on level ground during earthquake', *Liquefaction Problems in Geotechnical Engineering, ASCE Annual Convention and Exposition*, 1-104.

Seed, H. B. and Lee, K. L. (1966) 'Liquefaction of saturated sand during cyclic loading', *J ournal of the Soil Mechanics and Foundations Division, ASCE*, 92, SM6, 105-134.

Seed, H. B. and Peacock, W. H. (1971) 'Test procedure for measuring soil liquefaction characteristics', *J ournal of the Soil Mechanics and Foundations Division, ASCE*, 97, SM8, 1099-1119.

Seed, H. B., Martin, P. P. and Lysmer, J. (1975a) *The generation and dissipation of pore water pressure during soil liquefaction*, Report No. EERC75-26, Earthquake Engineering Research Center, The University of California, Berkeley.

Seed, H. B. Idriss, I. M., Makdisi, F. and Banerjee, N. (1975b), *Representation of irregular stress time history by equivalent uniform stress* series *in liquefaction analysis*, Report No. EERC75-29, Earthquake Engineering Research Center, The University of California, Berkeley.

Shahrour, I. and Meimon, Y. (1992) 'Application of the homogenization method to the calculation of marine foundations subjected to periodic loads', *Numerical Methods in Geomechanics*, Eds Pande & Pietruszczak, 601-608.

Shahrour, I. and Meimon, Y. (1995) 'Calculation of marine foundations subjected to repeated loads by means of the homogenization method', *Computer and Geotechnics*, 17, 93-106.

Sirovich, L. (1996) 'In-situ testing of repeatedly liquefied gravels and liquefied overconsolidated sands', *Soils and Foundations*, 36, 4, 35-44.

Small, J. C., Booker, J. R. and Davis, E. H. (1976), 'Elasto-plastic Consolidation of Soil'. *Int. J ournal of Solids Structures*, 12, 431-488.

Small, J. C. and Booker, J. R. (1977), 'Finite element analysis of primary and secondary consolidation', *Int. J ournal of Solids Structures*, 13, 137-149.

Small, J. C. and Booker, J. R. (1982), 'Finite layer analysis of primary and secondary consolidation', *Proc. 4th Int. Conference of Numerical methods in Geomechanics*. Edmonton, 365-371.

Smith, I. M. (1982) 'Analysis of fixed offshore platforms 1972-1982', *Proc. 4th Int. Conference of Numerical methods in Geomechanics*. Edmonton, 1165-1179.

Stamatopoulos, C. A., Bouckovalas, G. and Whitman, R. V. (1991) 'Analytical prediction of earthquake-induced permanent deformations', *J ournal of Geotechnical Engineering, ASCE*, 117, 1471-1491.

Symes, M. J., Shibuya, S., Hight, D. W. and Gens, A. (1985) 'Liquefaction with cyclic principal stress rotation', *Proc. 11th Int. Conference on Soil Mechanics and Foundation Engineering*, 1919-1924.

Tani, K. and Craig, W. H. (1995) 'Bearing capacity of circular foundations on soft clay of strength increasing with depth', *Soils and Foundations*, 35, 4, 21-35.

Taylor, R. L., Beresford, P. J. and Wilson, E. L. (1976), 'A non-conforming element for stress analysis', *Int. J ournal for Numerical Methods in Engineering*, 10, 1211-1219.

Terzaghi, K. and Peck, R. B. (1948) *Soil Mechanics in Engineering Practice*, 2nd Edition, John Wiley & Sons, London.

Vaid, Y. P. and Finn, W. D. L. (1979) 'Static shear and liquefaction potential', *J ournal of the Geotechnical Engineering Division, ASCE*, 105, GT10, 1233-1246.

Vaid, Y. P. and Chern, J. C. (1983) 'Effects of shear on resistance to liquefaction', *Soils and Foundations*, 23, 47-60.

Vermeer, P. A. and Verruijt, A. (1981), 'An accuracy condition for consolidation by finite elements', *Int. J ournal for Numerical and Analytical Methods in Geomechanics*, 5, 1-14.

Verruijt, A. and Song, E. X. (1991) 'Finite element analysis of pore pressure build-up due to cyclic loading', *Deformation of soils and displacement of structures, Proc. 10th European Conference on Soil Mechanics and Foundation Engineering*, 277-280.

Vesic, A. S. (1973) 'Analysis of ultimate loads of shallow foundations', *J ournal of the Soil Mechanics and Foundation Division, ASCE*, 99, SM1, 45-73.

Vesic, A. S. (1975) 'Bearing capacity of shallow foundations', *Foundation Engineering Handbook*, Eds Winterkorn & Fang,Van Nostrand Reinhold, New York, 121-147.

Vucetic, M. (1994) 'Cyclic threshold shear strains of soils', *J ournal of Geotechnical Engineering, ASCE*, 120, 2208-2227.

Whitman, R. V. (1985) 'On liquefaction', *Proc. 11th Int. Conference on Soil Mechanics and Found. Engineering*, 1923-1926.

Wilson, E. L. (1965) 'Structural analysis of axi-symmetric solids', *J ournal of American Institute of Aeronautic and Astronautics*, 3, 2269-2274.

Wilson, E. L., Taylor, R. L., Doherty, W. P. and Ghaboussi, J. (1973), 'Incompatible displacement models', *Numerical and Computer Methods in Structural Mechanics*, Eds Fenves *et al.*, Academic Press, New York.

Winnicki, L. A. and Zienkiewicz, O. C. (1979) 'Plastic (or visco-plastic) behaviour of axi-symmetric bodies subjected to non-symmetric loading, semi-analytical finite element solution', *Int. J ournal for Numerical Methods in Engineering* 14, 1399-1412.

Wood, D. M. (1991) 'Approaches to modelling the cyclic stress-strain response of soil', *Cyclic Loading of Soils: From Theory to Design*, Eds O'Reilly and Brown, Blackie, London, 19-69.

Yoshimi, Y., Tokimatsu, K., Kaneko, O. and Makihara, Y. (1984) 'Undrained cyclic shear strength of a Niigata sand', *Soils and Foundations*, 24, 4,131-145.

Yoshimi, Y., Tokimatsu, K. and Hosaka, Y. (1989) 'Evaluation of liquefaction resistance of clean sands based on high quality undisturbed samples', *Soils and Foundations*, 29, 1, 93-104.

Young, A. G., Kraft, L. M. and Focht, J. A. (1975) 'Geotechnical considerations in foundation design of offshore gravity structures', *Proc. 7th Offshore Technology Conference*, Houston, 367-386.

Zen, K., Umehara, Y. and Ohneda, H. (1985) 'Evaluation of drainage effect in sand liquefaction', *Proc. 11th Int. Conference on Soil Mechanics and Foundation Engineering*, San Francisco, 1931-1935.

Zienkiewicz, O. C., Taylor, R. L. and Too, J. M. (1971), 'Reduced integration technique in general analysis of plates and shells', *Int. J ournal for Numerical Methods in Engineering*, 3, 275-290.

Zienkiewicz, O. C. and Bettess, P. (1982), 'Soils and other saturated media under transient, dynamic consolidations; general formulation and the validity of various simplifying assumptions', *Soil Mechanics, Transient and Cyclic Loads*, Eds Pande & Zienkiewicz, John Wiley & Sons, New York, 1-16.

Zienkiewicz, O. C., Leung, K. H., Hilton, E. and Chang, C. T. (1982) 'Liquefaction and permanent deformation under dynamic conditions, Numerical solution and constitutive relations", *Soil Mechanics, Transient and Cyclic Loads*, Ed. Pande & Zienkiewicz, John Wiley & Sons, New York, 71-103.

Zienkiewicz, O. C. and Mroz, Z. (1984) 'Generalised plasticity formulation and applications to geomechanics', *Mechanics of Engineering Materials*, Eds Desai & Gallagher, John Wiley & Sons. New York.

Zienkiewicz, O. C. and Taylor, R. L. (1989) *The Finite Element Method*, 4th Edition, McGraw-Hill, New York.